UNIVERSITY OF GLASGOW

DOCTORAL THESIS

Design, Fabrication and Characterisation of Thermally Optimised Novel SThM Probes

---

Author:
Rory LAMBERT

Supervisor:
Dr. Jonathan WEAVER

A thesis submitted in fulfillment of the requirements
for the degree of Doctor of Philosophy

in the

AFM Group
College of Science and Engineering

August 24, 2020

Declaration of Authorship

I, Rory LAMBERT, declare that this thesis titled, "Design, Fabrication and Characterisation of Thermally Optimised Novel SThM Probes" and the work presented in it are my own. I confirm that:

- This work was done wholly or mainly while in candidature for a research degree at this University.
- Where any part of this thesis has previously been submitted for a degree or any other qualification at this University or any other institution, this has been clearly stated.
- Where I have consulted the published work of others, this is always clearly attributed.
- Where I have quoted from the work of others, the source is always given. With the exception of such quotations, this thesis is entirely my own work.
- I have acknowledged all main sources of help.
- Where the thesis is based on work done by myself jointly with others, I have made clear exactly what was done by others and what I have contributed myself.

Signed:

_____

Date:

_____

"Today I pulled three baby snakes out of moss and dirt
Where the wild strawberry vines toss and turn
I told them, "You will grow to be something inventive and electric;
You are healthy, you are special, you are present"
Then I let them go"

Ian Bavitz

UNIVERSITY OF GLASGOW

Abstract

School of Electronics and Nanoscale Engineering

College of Science and Engineering

Doctor of Philosophy

Design, Fabrication and Characterisation of Thermally Optimised Novel SThM Probes

by Rory LAMBERT

Novel scanning thermal microscopy probes have been presented, along with the design choices and fabrication challenges associated with realising them. The probe's performance was characterised as a resistance thermometer (passive mode) and as a self-heated thermal conductance measurement device (active mode). Frequency domain measurements demonstrated that improved performance in both operating regimes was the result of changes to the cantilever which made measurements less sensitive to the thermal properties of the cantilever.

The commercial KNT Scanning Thermal Microscope (SThM) probe has become ubiquitous in scanning thermal microscopy thanks to its commercial availability, high spatial resolution and relatively high reproducibility. However, no published studies have been performed with the aim of optimising this probe for a specific type of thermal metrology. The commercial probes are fabricated in the same cleanroom which is used for research fabrication, providing a unique opportunity to fabricate and test novel, optimised SThM probes based on the same technology.

Improvement of the existing probes requires a proper understanding of the complex thermal network which governs their operation. The typical lumped model based upon the thermal-electrical analogy is useful, but contains no information on

the temperature distribution within the device itself, data which is crucial for informing the design of new probes. This thesis presents a lightweight distributed model which is capable of computing, and comparing the temperature distributions of probes with arbitrary layout. The performance of novel probe designs may be assessed by simulating their response to contacting upon materials with various thermal conductivities. The model is tightly integrated with the design process to inform probe manufacture.

Tests undertaken with this model indicated that the placement and layout of the sensor should be optimised, and that the sensor should be thermally isolated from the body of the cantilever. Realising such changes required various improvements to the electron beam lithography process used to pattern the sensors. In particular, an increase in the positional accuracy of feature placement between writing layers and an optimisation of the focus of the beam were required for proper lift-off of narrow, sub-micron features.

A matrix of probe designs were fabricated and tested to investigate which designs could be realised with high yield, and of those, which would have the best performance for each application. Probes with material removed from their apices were found to give a signal which was less dependent on thermal loading through the air. All probe types were demonstrated to have greater sensitivity than the commercial probe to materials of varying thermal conductivity when used in the active mode. The source of the improvements was experimentally confirmed using a two-pole frequency response model, where it was demonstrated that their output was substantially insensitive to the influence of the temperature of the cantilever body.

Acknowledgements

Completion of any PhD project is not the result of a single person's efforts. The following are those people and groups who deserve special recognition for their support during this process.

- **Professor Jonathan Weaver** It has been an immense privilege to work alongside John for the duration of this project. I have had the pleasure of tapping into has vast and varied experience at a moments notice. I have yet to ask for John's advice on some topic, professional or personal, for which he has not had some kind of useful input. Thank you John, for broadening my horizons in every way imaginable.

- **Dr Phil Dobson** Phil's role in the success of this project cannot be overstated. From outset to completion, Phil's unwavering support and inquisitive mind have shaped the direction of this work immeasurably. Phil has consistently made the effort to go above and beyond for his students. His frequent visits to the office have been equal parts informative and enjoyable. The value of having a supervisor drop in mid-way through your work and open himself to questions large or small is immense. Thank you for encouraging me to believe in myself and my ideas, and for keeping spirits high throughout the difficult times.

- **Staff at Kelvin Nanotechnology** Completing my Masters' project with Kelvin Nanotechnology laid the foundations for my transition into this PhD project. I could not have asked for a better introduction to the world of micro and nano fabrication. The valuable experience I gained from their expert staff was my superpower throughout this project. Particular thanks go to Sara and Mary for introducing me to the probes fabrication process. Special thanks are extended to Kevin Docherty for his imparting his immense wisdom about all things Electron Beam Lithography, and to Corrie Farmer for many in depth discussions regarding all things resist processing. Thank you to Johnny and Ravish for valuable discussions about all things fabrication related, and for being excellent company throughout the Quantiheat project. Finally, thanks to Gordon

Mills and Brendan Casey for affording me the opportunity which started me along this road.

- **Dr. Stephen Thoms** Stephen's help has been invaluable throughout this project. It is especially appreciated given the many demands on his time from all of the Electron Beam Lithography users in the facility. Without Stephen's assistance, none of the work presented in Chapter 5 would have been possible.

- **Dr. Yuan Zhang** Yuan's extensive experience with novel SThM design, fabrication, and testing has been of immeasurable help. Yuan taught me all the intangibles and best practices that only a seasoned expert can impart on someone new to the field, and for that I am extremely appreciative.

- **JWNC Staff and users** The JWNC is an incredible facility to have been a part of. The vast wealth of knowledge contained by the community is incredible, and the willingness of other users to share their expertise has made this project so much smoother. It takes a great deal of effort to curate such a sense of community, and this community has not been taken for granted. It has been an honour to be part of it. Special thanks are extended to those members of technical staff who keep the multitude of different machines and processes running as intended. Without their efforts, this work would not have been possible.

- **The AFM Group Students**

  Yunfei - thanks for blazing the trail and writing such an excellent thesis. If I can impart as much wisdom to the next students as Yunfei passed on to me, then this endeavour may be considered a success.

  Zarina and Francesca - No one was more uniquely qualified than Zarina and Francesca to empathise with and support me throughout the duration of this project. I could not have asked for better colleagues to join me for this experience. Thanks for always being there to share ideas with, and for being up for a bit of banter when a break from work is required. Both have been an inspiration, particularly during the thesis writing stage, and they will remain dear friends.

Lukas, Chris, David, Hao - the next generation! I feel like I aged a thousand years in this process; but my thanks are extended to my these guys for keeping me young and keeping my spirits high. It has been a privilege to watch them all grow into mature and confident researchers. I am encouraged in the direction in which the group is headed. It's hard to leave a research group after what feels like an eternity, but I am cannot imagine a better group of people to which the torch should be passed.

- **Glasgow University Judo Club** It cannot be understated the value which I gained from training with the judo club. I have learned that it is impossible to be concerned about anything else in your life when one of these savages is doing their best to throw you half way across the room. Thanks for helping me to blow off steam in those times I needed it most. My dear friends in this club have helped in this process more than they can ever know.

- **My Parents** To my wonderful parents I extend the sincerest of thanks. They have supported me in every way imaginable, and have believed in me during those times when I could not believe in myself. My gratitude extends beyond what can be expressed in words.

- **Katherine McAinsh** Finally, my heartfelt thanks to my loving partner, Katherine, who has supported me each and every moment, from the first day to the last. This PhD has been a huge part of both of our lives, and completing it would have not been possible without her unwavering support.

Contents

List of Figures

List of Tables

List of Abbreviations

AFM	**A**tomic **F**orce **M**icroscopy
AMM	**A**coustic **M**ismatch **M**odel
BSS	**B**eam **S**tep **S**ize
CLSM	**C**onfocal **L**aser **S**canning **M**icroscopy
CVD	**C**hemical **V**apour **D**eposition
DMM	**D**iffuse **M**ismatch **M**odel
EBL	**E**lectron **B**eam **L**ithography
FEA	**F**inite **E**lement **A**nalysis
iSTM	**i**mmersion **S**canning **Th**ermal **M**icroscopy
LPCVD	**L**ow **P**ressure **C**hemical **V**apour **D**eposition
MFP	**M**ean **F**ree **P**ath
MNA	**M**odified **N**odal **A**nalysis
RIE	**R**eactive **I**on **E**tching
RO	**R**everse **O**smosis
SNOM	**S**canning **N**ear-Field **O**ptical **M**icroscopy
SEM	**S**canning **E**lectron **M**icroscopy
SPICE	**S**imulation **P**rogram with **I**ntegrated **C**ircuit **E**mphasis
SPM	**S**canning **P**robe **M**icroscopy
STM	**S**canning **T**unelling **M**icroscopy
SThM	**S**canning **Th**ermal **M**icroscopy
TCR	**T**emperature **C**oefficient of **R**esistance
TERS	**T**ip **E**nhanced **R**aman **S**pectroscopy
VB6	**V**ector **B**eam **6** Ebeam Lithography Tool

For those students who wish to build upon this work. I hope this may serve as a useful reference.

Chapter 1

Literature Review

1.1 Introduction

This thesis is concerned with the advancement of Scanning Thermal Microscopy (SThM), a technique which enables high resolution imaging of various thermal phenomena. In this chapter, we outline how this particular technique fits into the thermal characterisation space, and how it compares to other microscopy methods, especially those adjacent techniques which also employ scanning probes. Particular attention is paid to the design and fabrication of these scanning probes, since the technical challenges involved in creating functionalised probes are a focal point of this work.

An overview of key techniques within the family of micro-scale thermal measurements is presented, alongside the key advantages and application areas of SThM analysis. Finally, a discussion involving the state of the art, and the current challenges in SThM measurement is presented.

1.2 Thermal Microscopy

'Microscopy' refers to an area of metrology concerned with the imaging of objects at resolutions far greater than can be achieved by eye. While this term implies micron-scale, microscopy has since been co-opted as a catch-all for even nanometric or atomic scale imaging. There are many varieties of microscopy, each one imaging a different property of the sample or employing different contrast mechanisms. It

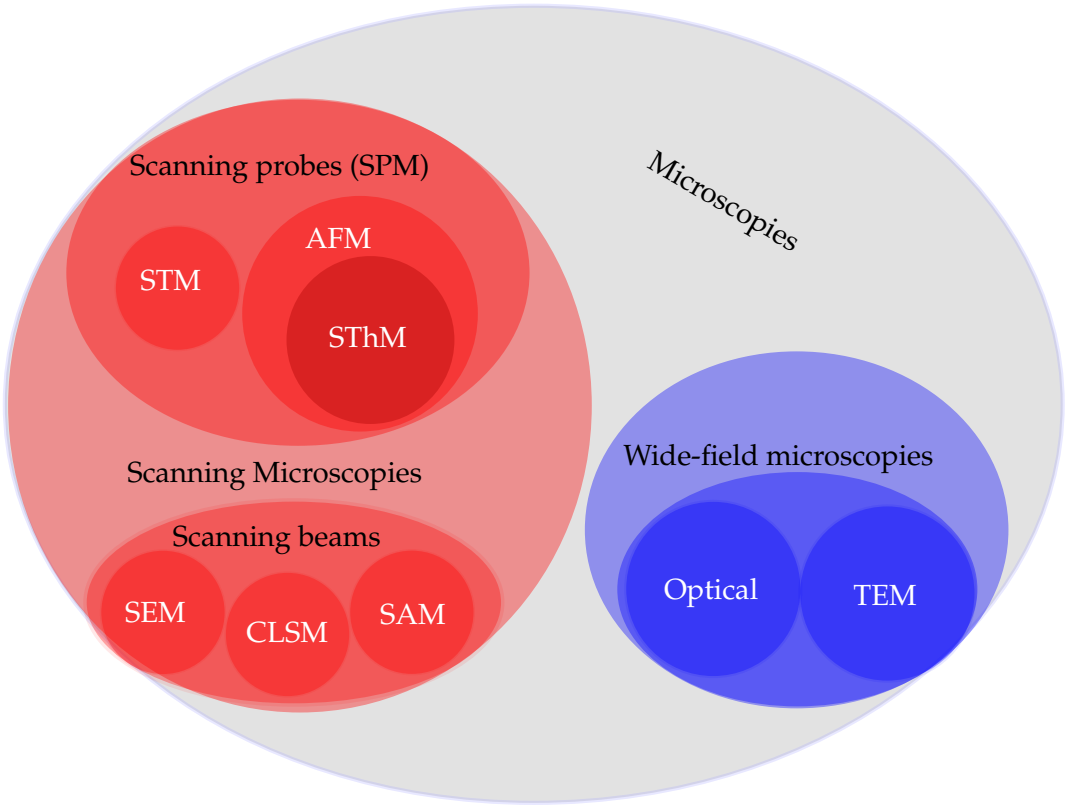

FIGURE 1.1: Venn diagram highlighting the relationship between various microscopy methods

is convenient to categorise microscopy techniques into different families. One distinction we may use to do so is whether or not the technique images a wide area simultaneously with wide field irradiation (such as optical microscopy), or point by point. Any technique which relies on the latter is regarded as a scanning microscopy. These techniques exploit the fact that any spatially distinct point measurements may be stitched together to form an image, in which the value of each pixel is a function of the parameter being measured. Within the family of scanning microscopies, it is useful to make a further distinction as to 'what' is being scanned. The first category involves the use of focussed beams, as is the case in Scanning Electron Microscopy (SEM), Confocal Laser Scanning Microscopy (CLSM) and Scanning Acoustic Microscopy (SAM). The second group of techniques are the Scanning Probe Microscopies (SPM), which measure near-field interactions between a sample and a nano-scale probe tip. The scanning mechanism of such techniques involves mechanical actuation of the probe across the sample. The positional accuracy of such actuators is suitably high that they impose no limit on the spatial resolution of the probes. Rather, resolution is governed by the contact or interaction area between the probe and sample. Figure 1.1 shows the position of our research topic, Scanning Thermal Microscopy, amongst the various families of microscopy.

In this thesis, specific attention is paid to those microscopy methods which feature temperature contrast. In the upcoming section, we will present some of the most prevalent thermal microscopies and their applications, comparing their merits and drawbacks.

1.3 Micro-scale measurement of thermal phenomena

Thermal microscopy methods may be categorised based upon the contrast mechanism of the measurement, or by the thermal phenomena being measured. It is important to note that, while thermal microscopy methods image temperature distributions, some methods measure alternate phenomena, such as thermal conductivity [1] or diffusivity [2]. In the following, various thermal measurement methods are reported, grouped by the contrast mechanism of the technique in question.

1.3.1 Optical Methods

IR thermography [3]

All objects of non-zero temperature emit electromagnetic radiation. If the object is a black body, or closely approximates a black body (i.e. the object has an emissivity close to 1), then the spectrum density of its thermal radiation is a function of temperature alone. This relationship is expressed through Planck's law. Infra-red Thermography employs an infra-red detector or camera to monitor this radiation.

The black body assumption central to quantitative measurement with this technique does not hold, even approximately, for a vast number of materials. In such cases, prior knowledge of the emissivity of the surface is required for accurate thermometry. An additional challenge is faced in the isolation of a given surface's thermal radiation. Since all non-zero temperature objects radiate to some degree, careful set-up is required to ensure that all other sources are rejected.

Due to the use of optical imaging and infra-red emission, this method is inherently limited in its spatial resolution. The diffraction limit of these wavelengths prevents sub-micron resolution imaging at room temperature, where the peak emission occurs at a wavelengths on the order of 10 µm.

Thermo-reflectance [4]

When a solid surface is struck by a photon, it may either be reflected, absorbed or transmitted. The ratio of its reflection to the other two possible events is known as the material's reflectivity. This property is known to be temperature dependent, and has thus been employed in the technique 'thermoreflectance' for the measurement of local temperature. A detailed discussion of the physics from which the temperature dependence of reflectivity arises has been presented in [4].

Thermo-reflectance measurements may be realised using a monochromatic laser beam scanning point-by-point across a surface, or through wide illumination and multiplexed detection [5]–[7]. In the latter approach, acquisition time is sufficiently fast that real-time imaging may be performed [8].

Thermo-reflectance measurements are not limited to the infra-red part of the spectrum, allowing for the use of visible through to near - UV illumination. This increases the attainable spatial resolution to the order of hundreds of nanometres [9].

For quantitative measurement, accurate knowledge of the relationship between the rate of change of reflectivity and temperature is required. The thermo-reflectance coefficient is introduced as a scaling factor, and is typically found through calibration. The value of this coefficient is typically on the order of 10^{-5} to $10^{-3}K^{-1}$ [7]. Due to this small signal, this technique is best suited to the measurement of modulated temperature fields, where lock-in detection techniques can be utilised [9]. The thermo-reflectance coefficient is also dependent upon a number of external factors, which precludes simple acquisition of quantitative data. For example, the wavelength of probing light for which the thermo-reflectance coefficient is maximised is different for each material that comprises the sample surface. Matters are further complicated by the fact that any encapsulating layers such as thin films cause significant optical interference that must be accounted for. Reflection coefficients for bare materials previously calculated or taken from the literature are not appropriate once the surface has been coated [5]. The surface texture of the coating, or even the bare material also has a significant influence on the reflection coefficient [8].

The same measurement principle may also be used for the determination of sample thermal conductivity. The technique, known as "time domain thermoreflectance" (TDTR), uses periodic pump and probe lasers to heat and measure the temperature of the sample respectively. The delay between pump pulse and probe temperature acquisition is used to inform the thermal conductivity measurement. An excellent review of the setup is presented in [10]. TDTR has been demonstrated as useful for the thermal characterisation of both thin films and bulk materials and is capable of measuring thermal conductivities across a wide range (0.03 to 2000 $\mathrm{W\,m^{-1}\,K^{-1}}$) [11]. Like all optical techniques, TDTR is diffraction limited, and therefore its spatial resolution remains limited to the range of hundreds or thousands of nanometres [12].

Raman

Raman thermometry exploits certain thermally dependent characteristics of the phenomenon known as Raman scattering. This is the term used for any occurrence of inelastic scattering of an incident phonon by the atoms or molecules of a material.

Predominantly, scattering events between photons and atoms are elastic, which is termed Rayleigh scattering. Very occasionally however, an incident photon will excite an energy carrier in the molecule (usually an electron), which will enter a more energised vibrational state. From this virtual state, the carrier absorbs some of the energy of the photon, and upon relaxation returns to a vibrational mode rather than its ground state. In this case, known as Stokes - Raman scattering, a photon is emitted with lower energy than that of the incident photon. Alternatively, the excited species may absorb an additional carrier and become further energised. When this species returns to ground state, it emits a photon of higher energy level (shorter wavelength) than the incident phonon. This is known as Anti-Stokes Raman scattering.

As the measured object's temperature increases, more carriers are above the ground state, and the probability of anti-Stokes transition occurring increases with respect to Stokes transitions. This ratio is exploited in Raman thermometry, which compares these peaks in the emission spectra to evaluate sample temperature.

Note that the Stokes - Anti-Stokes shift is not the only thermally dependent phenomenon that is observed in the spectra. Both the Stokes shift and line-width have a temperature dependence that has been used for thermometry. An excellent summary of the physics behind these interactions, and on the typical experimental setup is presented by Beechem et. al [7].

Raman thermometry typically employs a coherent, monochromatic light source that is focussed onto the sample with spot sizes (and therefore resolution) down to around 1 µm [13]. As with the thermo-reflectance method, it is possible to convert this point measurement technique into a 2D thermograph by employing an accurate motorised stage.

Raman thermography is capable of interrogating samples without any need for sample preparation, and can be used on both solids and liquids. Present challenges for this method involve slow acquisition time of around 2s per point, and low signal levels. [14]. In addition, not all materials show a clear Raman response, and some experience variations in their scattering characteristics based upon mechanical strain and thermal expansion [7]. The relationships between each must be well calibrated if accurate thermometry is desired.

1.3.2 Electrical

Contrast mechanisms - Resistance

Electrical resistivity is an intrinsic property of a material, and quantifies the opposition to the flow of charge carriers within that material. When considering solid metals, resistance to the flow of electrons is caused through various scattering events between mobile electrons and the atomic lattice. Scattering events are caused by irregularities in the lattice structure, which may arise through impurities, dislocations or mechanical strain within the structure [15]. Additional sources of lattice irregularities include grain boundaries in polycrystalline materials, and surface scattering, whose effect is more pronounced in low-dimensional nano-structures). All of these are substantially temperature independent.

A second class of scattering occurs in the form of phonon scattering, which occurs due to thermally-induced lattice displacements. This type of scattering has a direct temperature dependence, since the phonon concentration is increased by the addition of heat. The higher the vibrational energy of the lattice atoms, the greater the probability an electron will strike it. (i.e. The mean free path of the electron is reduced, i.e the resistance is increased)

The sum of scattering events may be approximated using Matthiessen's rule;

$$\rho(T) = \rho_0 + \rho_p(T) \tag{1.1}$$

In which ρ_0 represents the resistivity contribution by impurity scattering, and ρ_p the resistivity of the pure material at that temperature. The former is nominally

temperature-independent, while the latter is dictated by phonon scattering [15].

This temperature dependence may be exploited for thermometry if the relationship between the material's temperature and resistivity is known. Typically, this relation is characterised as an n-th order polynomial [16];

$$\rho(T) = \rho_0(1 + \alpha(T) + \beta(T)^2 + ...) \tag{1.2}$$

In which ρ_0 is the same as in Equation 1.1, T is the temperature, and α, β and so on are the temperature coefficients of resistance (TCR) for first, second and n-th order temperature variations. The values of these terms are determined experimentally. When this relationship is employed for thermometry, it is preferable to use a material with an approximately linear TCR across the range of operating temperatures. This is the case for the Platinum and Palladium resistive elements used throughout this work. As such, Equation 1.2 may be reduced to use only one temperature coefficient of resistance, α. It is also possible to change the reference temperature from 0K to room temperature, and present the equation in terms of resistance rather than resistivity, for a given structure of uniform material;

$$R(T) = R(T_0)(1 + \alpha(\Delta T)) \tag{1.3}$$

The transformation from resistivity to resistance is valid provided the material in question has constant cross-sectional area in the plane normal to current flow, and that it's dimensions are significantly larger than the electrons' mean free path. For objects approximating wires ($L >> w$), it has the following equation;

$$R = \frac{\rho L}{A} \tag{1.4}$$

Where L is the length of the material in the direction of current flow, and A is the cross sectional area. Devices which exploit this relationship between resistance and temperature are known as resistive temperature detectors (RTDs). Such devices are easily scalable, and so are popular both on the macro and micro-scales. Resistive

temperature detectors have a very fast response, and are relatively easy to calibrate, making them an attractive option for many applications

Joule Heating

RTDs biased above a certain current will begin Joule heating; a term which describes the transfer of energy from mobile electrons to the atomic lattice through scattering events. Frequent bombardment of the lattice structure results in increased phonon generation, increasing the device temperature. This is the dominant mechanism of heat generation in the vast majority of electronic devices. For purely resistive materials, Joule heating is characterised as follows;

$$Q = j^2\rho \tag{1.5}$$

In which j denotes current density, ρ resistivity and Q the generated heat per unit volume, which is sometimes termed thermopower. For thermometric measurements, Joule heating should be minimised for the most accurate measurements. However, an RTD may also be used as a heat source by increasing its current such that significant Joule heat is generated. RTDs may therefore be used for simultaneous heat delivery and temperature monitoring. A Joule heated RTD biased with constant current will provide a resistance which is proportional to the device temperature. The heat may be removed from the RTD by, for example, contact upon a material with high thermal conductivity, and the RTDs resistance may then be monitored as a proxy for the measurement of the efficiency of heat abstraction. This is the core principle in 'Active mode' SThM, in which the probe is heated and its resistance monitored as it scans a sample surface. A more thorough treatment of this technique as it pertains to SThM is given in Chapter 4.

Contrast mechanisms - Thermoelectric effects

An isolated conductive material subjected to a temperature gradient, ∇T, along its length will generate a corresponding electrical potential through the absolute Seebeck effect [17]. This occurs due to the migration of energetic electrons from the

warmer end to the cooler end of the material. At steady state, (zero current density throughout), one may describe the conductor's Seebeck coefficient as the rate of change of potential with respect to temperature;

$$S(T) = -\frac{\nabla V}{\nabla T} \tag{1.6}$$

In which ∇T denotes the temperature gradient experienced by the material, ∇V is the voltage gradient generated within the materials as a response to this temperature gradient. $S(T)$ is then the temperature dependent Seebeck coefficient. It has SI units of $\mathrm{V\,K^{-1}}$ however it is more commonly given in $\mu\mathrm{V\,^{\circ}C^{-1}}$ due to the magnitude of the generated voltages.

The Seebeck coefficient is unique to each material, meaning that subject to the same temperature distribution, each will exhibit a different voltage gradient. When two dissimilar materials are joined at one end, their voltages are forced into equality. The free ends must then exhibit non-equal voltages as a result of their differing voltage profiles. This open-circuit potential may be measured, and is proportional to both the temperature difference and the difference in the materials' absolute Seebeck Coefficients [18]. Such an arrangement is termed a thermocouple. These devices are frequently formed out of a pair of dissimilar metal wires, ideally with maximally dissimilar Seebeck coefficients. Thermocouples may be employed for thermometric measurements if one of the junctions is maintained at a fixed temperature. Typically, this junction is termed the reference junction while the other is termed the measuring junction. With a fixed reference, the temperature difference, and consequently the generated thermo-voltage is a function of the temperature of the measuring junction [19].

Thermocouples are a popular thermometry tool due to their low cost, small size, high sensitivity and wide variety of operating temperatures [18]. Thermocouples may be constructed from a variety of metals or alloys. Typically they are designed to adhere to a particular thermocouple 'Type', each of which having a different characteristic function that describes the temperature-voltage relationship. Data on the

standard thermocouple types and their temperature responses is available from the US National Institute of Science and Technology's (NIST) website [1]

How Electrical methods are used

Monitor the properties of an IC

Electrical methods such as the two methods described above have found particular usage for the temperature measurement of integrated circuits and their components. It should be noted that any temperature-dependent phenomenon may be used for a measurement of device temperature; for example, the forward voltage bias or reverse leakage current of a P-N junction [20]. This is a convenient method if one is interested in the average temperature of a specific component. Such electrical methods have very fast temperature response. Because temperature is inferred directly from the operation of the object under test, there is no wait time for thermalisation. Obviously however, this is a point temperature method at non-arbitrary fixed position, which provides very little information of the diffusion of heat through the sample.

Fabricate thermometers on chip

An alternative to the above method is to fabricate sensors (thermocouples or RTDs) directly onto the substrate to be tested. This offers a number of advantages compared to probing the operation of an active component, not least in that there is no requirement to electrically load the circuit under test. The transient response is excellent, as above

By integrating multiple sensors in different locations, it is possible to generate a low resolution, or interpolated temperature field. In addition, a set of differential sensing points will allow for measurements that are insensitive to changes in ambient temperature. [21]. The disadvantages for this method arise due to the significant area overhead, and processing challenges involved with integrating RTD or thermocouple sensors to the circuit under test.

[1] https://srdata.nist.gov/its90/main/

Conductivity measurement using the 3ω method. [22]

The 3ω method employs radial heat flow from a single element that is simultaneously used as the heating element and the thermometer. Heaters may be patterned directly onto any dielectric substrate, and have been fabricated from Silver and Platinum thin films for the operation at low and high temperatures respectively. When the heating/sensing region is biased with some AC signal at frequency (ω), it generates heat through the Joule effect at frequency 2ω. Since the thin film's resistance changes with temperature, the temperature of the sensor can be measured from the third harmonic of its voltage, 3ω. The full derivation of the 3ω method is presented in Appendix B.

1.3.3 Thermal Expansion based measurements

The thermal expansion of materials is a well-known phenomenon that is frequently exploited for macroscale temperature measurement. The same phenomenon may be scaled down to the micron and sub-micron scales provided the existence of an instrument with high resolution height measurement capability.

Scanning Joule Expansion Microscopy (SJEM) utilises a standard atomic force microscope to detect small height oscillations from an electrically active sample which are the result of periodic Joule heating [23]. Material expansion has also been reported using laser interferometry [24] and tunnelling current [25] as the measurement mechanism. While these methods have imaging capability beyond the diffraction limit, they require electrically conductive samples. Thermal expansion based measurements also face challenges in calibration if the sample is inhomogeneous.

1.3.4 Scanning Thermal Microscopy

The primary disadvantage of the contact electrical methods presented in Section 1.3.2 is the fact that they are limited to a single location. Scanning Thermal Microscopy overcomes this limitation by incorporating these sensors on to a mobile scanning platform. Thermocouples or RTDs may be fabricated upon, or fashioned into, scanning probes for use in an Atomic Force Microscope. Since the principle of the measurement is the same, it is even possible to perform 3ω measurements

with SThM. This method as it pertains to SThM is presented in Section 3.7.4 and in Appendix B.

Once loaded into an AFM, SThM probes are brought into solid contact with a sample, and scanned across a small area (typically <100 μm^2) with precision actuators. The probe signal is recorded throughout, yielding a two dimensional thermal map upon completion. This is in conjunction with the standard topographic map that is the result of standard contact AFM measurement. The spatial resolution of this technique is extremely high, limited only by the thermal interaction area [26], which is closely related to the tip-sample contact area ($\approx$ 50 nm [27]). SThM's ability to image samples with resolution far beyond the optical diffraction limit makes it an attractive technique in the nano-thermal characterisation space.

Just as a thin film RTD on a sample surface may be used for temperature or thermal conductivity measurement without any modification to the sensor, so too may an SThM probe be operated in both modes. In the field, these are typically referred to as Passive and Active modes. Further information on the instrumentation of the SThM system, and the electronics required to drive and monitor the probe in each of these operational modes is presented in Section 3.7.

Thermometry issues

SThM is not without its difficulties. Migrating the sensor from substrate to probe adds significant complexity to the thermal network. In the case of a monolithic sensor, the sensing element is part of the system, having a strong and consistent thermal coupling between itself and the substrate. Although providing only a static point of temperature reference, it is reasonable to assume that the measure is accurate, given that the sensor and surface share a large contact area, and are thus intimately coupled. When performing SThM measurements, the sharp tip that allows for such high resolution measurements also imposes a significant thermal resistance, since thermal conduction across a contact is proportional to the interaction area. The mathematics of contact resistance, especially as related to SThM, is discussed in Section 4.3.4. Since the contact area is unique for every probe-sample contact, and its measurement is non-trivial [28], contact resistance is a variable that cannot be easily eliminated

from the measurement.

Accurate sample temperature measurement is also precluded by the contributions of heat sources other than the tip-sample contact. The laser, which is used for deflection detection, has been observed to increase the probe temperature. Critically, it is not a constant temperature source, as the position of the laser and the optical properties of the sample underneath the probe have all been observed to alter the degree of laser heating [29].

In ambient operation, a further confounding heat source has been observed. It manifests as a temperature asymmetry in the scanned image, which arises due to air conduction between a heated sample and the probe. When the probe's cantilever is positioned above the sample, the feature appears hotter due to increased coupling. This artefact is discussed further in Section 4.3.6, and addressed in Section 7.3

Thermal Conductance issues

As with the on-chip electrical methods, SThM may be used to infer information about the thermal conductivity of a sample. To do so, whether using 3ω or steady state methods, the probe must provide heat to the sample. However, since the probe is thermally coupled much more strongly to the base of the chip than the sample, only a tiny fraction of the generated heat is delivered to the sample across the nanocontact. Limiting the heat available with which to probe sample thermal properties reduces contrast of this imaging mode. Much of this work is concerned with minimising the parasitic losses down the cantielver and to the environment, with in-depth discussions of the problem beginning at 4.10.1.

Complex thermal network

An additional complication that arises when moving the sensor from device to probe is the question of what exactly the probe measures. Whereas previously the sensor was bound to the device on at least one face, now the sensor is bound to a cantilever (which acts as a heat sink) on one side, and exposed to the environment on all other faces, the only exception being the small area at the apex of the probe which is in mechanical and thermal contact with the sample. However, given the tiny fraction of the sensor which this contact comprises, what is the dominant heat transfer

mechanism that defines the temperature of the sensor? If the heat transfer across the solid-solid contact is small and local, it is reasonable to assume that only the very apex of the probe is affected by this property. It should be apparent that if the temperature of the sample is the desired measurand, that the influence of all other heat transfer routes should be minimised.

During ambient operation, heat exchange occurs readily between bodies of non-uniform temperature, for example a heated sample and room temperature probe. In such cases, the heat transfer from heated sample to cantilever body through the air as the probe moves over the heated region results in an asymmetry in the thermal image. These effects have been well documented in the literature [30]–[32], and have been discussed later in this Thesis (Section 4.3.6). In the case of a heated probe, operation in air (other any other fluid medium) results in an unknown quantity of heat being abstracted from the probe into the medium. This prevents quantitative measurement of the heat transfer across the solid-solid contact, which is the desired measurand. Even in vacuum operation, any heat generated at the sensor has a low thermal impedance path to ambient temperature through the body of the cantilever. Without knowing which proportion of the generated heat travels which path, it is difficult to quantify any active mode thermal measurement.

Distributed sensor

In both the active and passive modes of operation, the signal of the probe is the result of its temperature-dependent resistance. If the sensor has a large area, then this number is actually the average of the temperature distribution along its extent. This temperare averaging problem is a significant focus of this thesis, and is described fully starting at Section 4.10.2

Topographic artefacts

The SThM reports only one measurement definitively, which is the average temperature across its sensor. This temperature is dependent upon the heat flux between the probe and the other heat sources and/or sinks within the network. A key variable in the heat flux between the probe and the sample is the contact resistance, which varies with contact area. As the probe scans a sample, the contact area may vary due

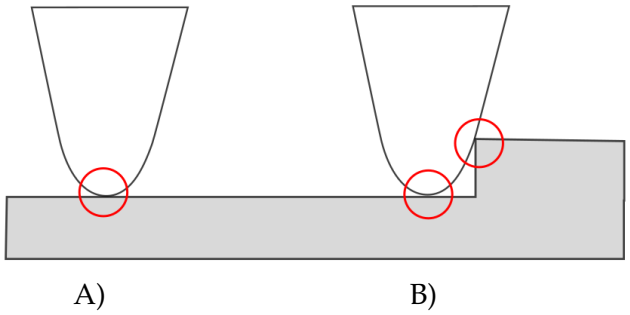

FIGURE 1.2: Diagram presenting the source of topographically induced thermal artefacts. In **B**, the side-wall of the raised feature contacts the probe and opens up an additional pathway for heat flux. Despite the substrate being homogeneous and isothermal, **A** and **B** will present different contact resistances, influencing the measurement. In passive mode, the edge of the feature will appear hotter thanks to the increased coupling into the probe. In active mode, the edge will appear cooler, since the reduced contact resistance will increase heat flux from tip to sample.

to variations in the compliance or roughness of a sample surface [28]. Frequently, the probe may form an additional contact with the side of a raised feature, as demonstrated in Figure 1.2. Thankfully, the SThM records the topography of the substrate simultaneously when scanning. Research on methods to decouple the true temperature by consideration of the topography is the subject of present work by Klapatek et. al [33], [34]

1.4 SThM as the research direction and the organisation of the thesis.

The advantages and challenges of SThM have been discussed. The technique is an attractive area for further study due to its unique position; its excellent spatial resolution is very appealing, but also appears to be the cause of one of the method's largest drawbacks; its poor thermal coupling across the tip sample contact. SThM measurements are further confounded by the thermal interactions involving the cantilever body - the temperature sensor is not simply an isolated measurement device, but mounted upon a mobile scanning platform whose thermal properties must also be considered. While the signal due to the tip-sample interaction is minimised due to the small contact area, and confounded by other heat sources/sinks, it is possible

to improve the signal to noise sensitivity of the probe through thermally informed design.

Glasgow University's Atomic Force Microscopy Group have developed a thin film silicon nitride SThM probe, which was commercialised through Kelvin Nanotechnology and subsequently became a leading probe for thermal nano-characterisation [26]. As such, the institution is uniquely positioned to realise novel Scanning Thermal Microscopy probes on this technology platform.

In this thesis, the design, fabrication and testing of novel probes to address the problems of SThM is described. The work is organised as follows;

- Chapter 2 outlines a few of the key fabrication technologies which are used in the manufacture of SThM probes.
- Chapter 3 presents the development of scanning probe technologies, beginning with standard AFM probes and culminating in integrated sensor AFM probes. Additionally, a review is presented of the different types of SThM probe, and the various approaches to instrumentation. A review of the present state-of-the-art Glasgow SThM probe is performed, and limitations in the fabrication process (and the resultant design decisions) are addressed.
- Chapter 4 details the complex heat transfer network typically employed when discussing SThM measurements. A critique of the lumped-element model is presented, and an alternative is demonstrated in the form of a one dimensional modified nodal analysis approach. Finally, the developed model is used to perform a series of case studies to understand how the various properties in the probe design affect its performance.
- Chapter 5 Details the work performed to improve the quality of pattern transfer of features written using Electron Beam Lithography onto the challenging topographic substrates required for fabricating SThM probes. Novel algorithms were deployed on the EBL tool which have been demonstrated to improve the accuracy of layer to layer alignment and improve the focus of the

beam at exposure locations. These changes are intended to address the limitations discovered in Chapter 3, and facilitate the improvements which are suggested by Chapter 4.

- Chapter 6 presents the design, manufacture and test of the novel probes, which incorporate the design changes suggested in Chapter 4, and utilise the fabrication improvements described in Chapter 5.

- Chapter 7 presents the results from various experiments designed to characterise the performance of the novel SThM probes developed in the previous chapter. Experiments comparing them to the standard commercial devices have been performed in both the Active and Passive modes of operation. Finally, we comment on the implications of these results in the field, and summarise our recommendations on future work and outlook of the field.

Chapter 2

Methods

2.1 Introduction

This section reports the tools and techniques that have been used in the fabrication of SThM probes, and in other projects discussed throughout this thesis. This chapter is intended to give an overview of the technologies used. Some aspects of the work performed require in-depth description of the specifics of a technique, more so than is appropriate for this chapter. In such cases, references to the relevant sections are given. The full process sheet for manufacture of the standard SThM probes is given in Appendix A. References to particular steps of the process will be given where appropriate.

2.2 Photolithography

Photolithography has been used throughout this project for the pattern transfer of large (>5 µm) features. This technique involves the exposure of a photosensitive medium to ultraviolet irradiation. A bright lamp which generates light of known wavelength and intensity forms the radiation source. This method of exposure has sufficient coverage that entire samples would be exposed, if not they were not masked. Most often however, a 'mask-plate' is introduced to enforce selective exposure. These plates are formed of transparent slides coated with an opaque metallic film. The plate's design is etched into the metal film, opening up areas of transparency. The mask-plates used in this work are Chromium plated Quartz, and have been patterned in-house using electron beam lithography and wet etching.

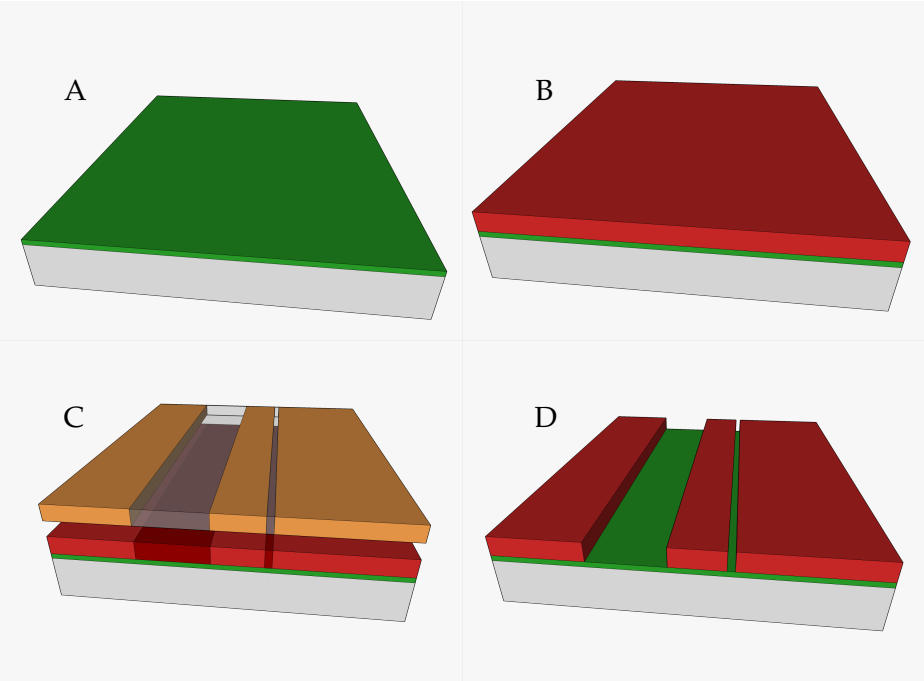

FIGURE 2.1: **A:** Blank (100) orientated silicon wafer with SiN thin film (green). **B:** Photoresist (red) is applied to the wafer using spin coating. **C:** The wafer is placed in close proximity to a mask plate and exposed to UV light. **D:** The exposed areas are removed in developer solution.

2.2.1 Resists

Samples to be exposed are coated in a photosensitive image transfer medium known as a 'photoresist'. These solutions are typically applied via spin coating, and are engineered with a specific viscosity such that the relationship between spin speed and film thickness is well-defined. Curves containing this data are usually available in the resist manufacturer's data sheet. For most of this work, Microposit S1800 series of photoresists have been used.[1].

This series is comprised of 'positive' photoresists, in which UV exposure causes polymer chain scission that makes the irradiated areas more soluble to the developer (in this case, MF319[2]). Negative photoresists work in the opposite manner due to cross-linking of polymer chains, however no such photoresists have been used in the course of this work.

One other resist was employed during this work, which was required due to the difficulty in spin coating large topographic features. AZ4562[3] is a very viscous resist

[1]Datasheet available here: http://microchem.com/products/images/uploads/S1800_Photoresist.pdf
[2]Datasheet available here: http://microchem.com/products/images/uploads/MF_319_Data_Sheet.pdf
[3]Datasheet available here: https://www.microchemicals.com/micro/az_4500_series.pdf

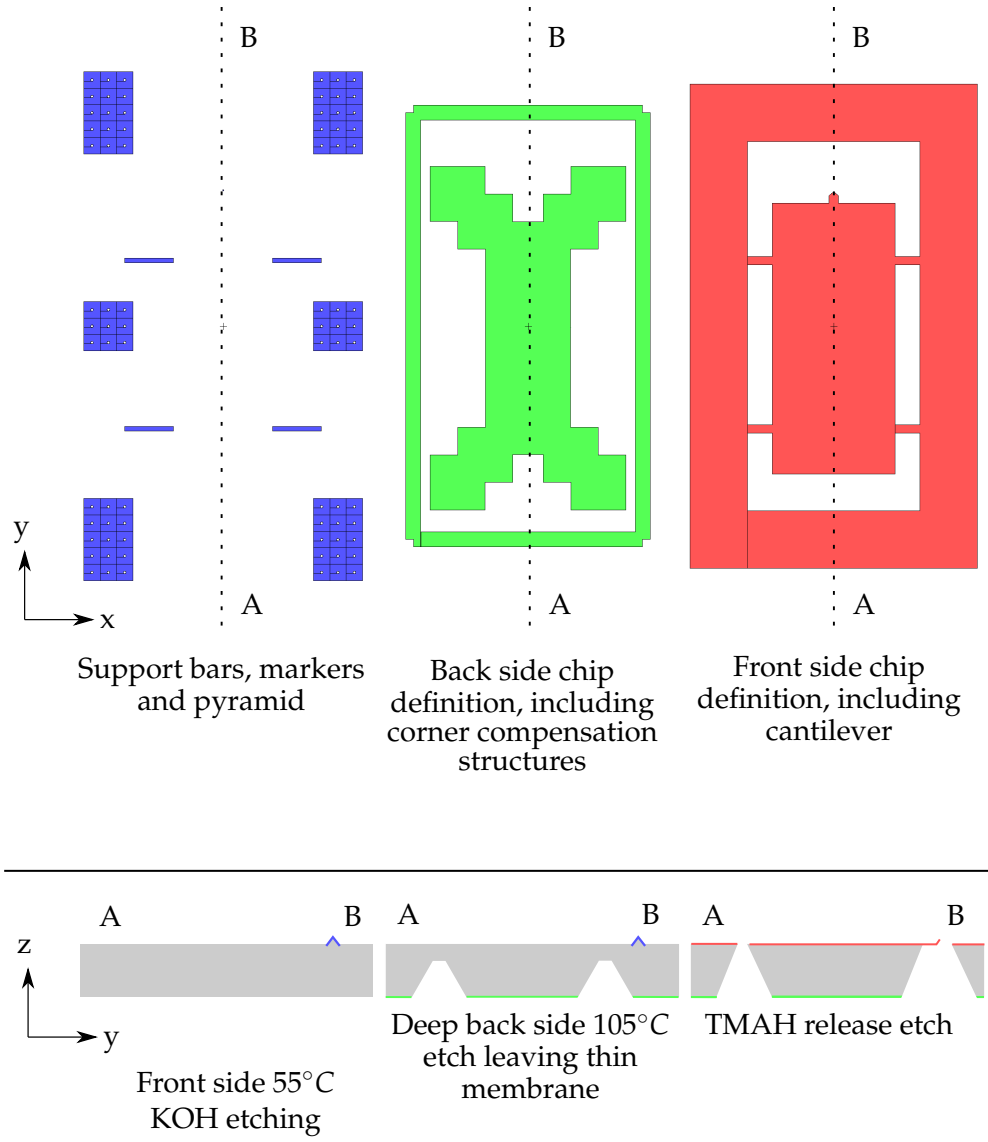

FIGURE 2.2: CAD drawings of the masks used in each of the photolithography stages (above), and sectional view of the substrate after their subsequent wet etches and follow on processing (below). The sectional views are not to scale.

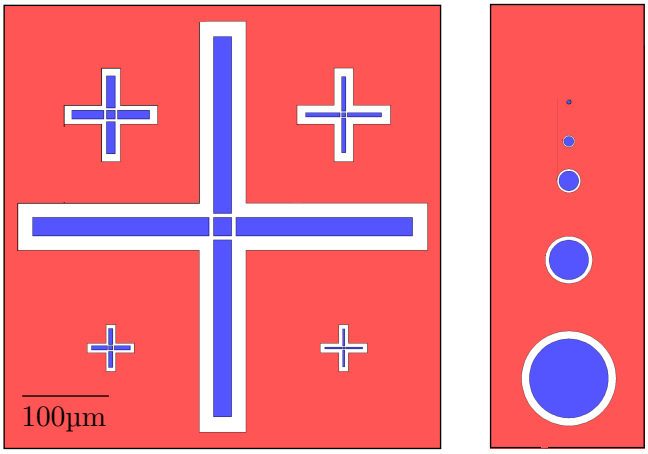

FIGURE 2.3: Schematic of two types of photolithography marker used in this project. The blue layer is transferred onto the sample in the first level of photolithography. The red layer represents the Chrome of the mask plate of another lithography level which we wish to align to the first. Features such as these are positioned at the wafers extremities to maximise rotational alignment accuracy.

that is particularly suited to such applications. The process for coating tall features with this resist was developed during the author's Master's project and is outlined in the Master's thesis. [35]. The process is outline in steps 31 through 41 of Appendix A.

Figure 2.2 presents the three layers that are defined by photolithography in the process of creating an SThM probe.

2.2.2 Alignment and markers

Markers: use and fabrication

In photolithography, alignment is achieved through the inclusion of dedicated registration features known as 'markers' at the extremities of the substrate. With knowledge of their position, it is possible to define the relative points of corresponding features on different mask-plates. In this work, both photo and electron beam lithography markers are etched into the sample during the first round of patterning (The blue drawing in Figure 2.2, step 12 of Appendix A). A tool known as a mask aligner is used to manipulate the substrate such that the registration features on are it observed to be in good alignment with those on the mask plate. An example marker strategy is given in Figure 2.3. Mask aligners typically feature a microscope, moveable sample chuck and the exposure lamp. For this work, a SUSS MA6 was used

[4]. The chuck allows for x and y movement with sub-micron precision, and allows for rotating the sample to within half a degree of accuracy. Note that no z, or tilt, alignment is required. In contact mode (used in this work), the substrate is brought into physical contact with the mask-plate and tilt is negligible. Even in modes where no contact is made, the resolution of photolithography is low such that typical wafer tilts of a few $\mu m\,mm^{-1}$ have little effect on the resulting pattern.

In addition to the standard alignment process described here, front-to-backside alignment has also been employed. Note from Figure 2.2 that the second phase of lithography and etching occurs on the rear of the wafer. This allows for deep Si etching to be performed prior to patterning any metal layers, which would sustain damage during such an prolonged/aggressive etch. If the same etch were initiated from the front side, the resulting deep etch trenches would prevent proper resist coating which is required for subsequent lithography steps. The process of front to back alignment on the MA6 is as follows;

Twin cameras are positioned under the wafer chuck, facing upward. The mask plate is loaded first, before inserting the sample. The cameras' position is adjusted such that the marker features are within view and an image is captured. This image is displayed on a screen at partial transparency, and the camera positions are locked. Next, the sample is loaded, and a live feed is merged with the mask image. The sample stage is positioned until the features are well aligned, at which point the exposure can be performed.

Alignment accuracy

Typical alignment accuracy for photolithographic processes is about 5 µm for a skilled operator and well defined alignment marks, however this is significantly diminished when performing back-side alignment due to the low resolution of the camera feed. Similarly, when topographic markers are coated with thick resist (such as in the cantilever definition level) alignment becomes more challenging due to the growth of marker features and a tolerance of 10 µm is observed.

[4]https://www.suss.com/en/products-solutions/mask-aligner/ma-ba-6

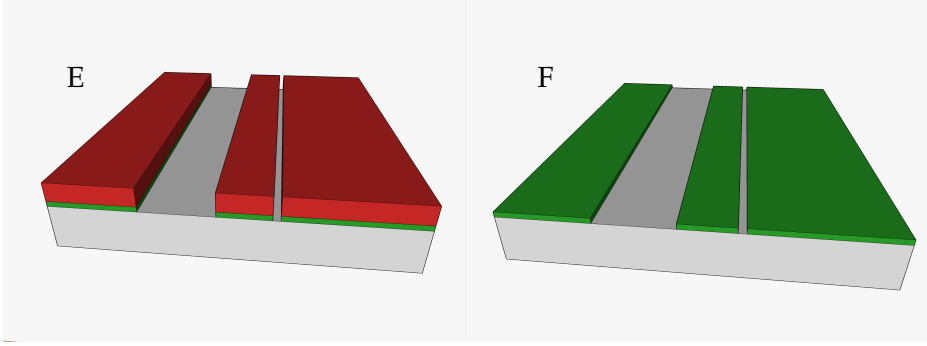

FIGURE 2.4: **E:** The patterned photoresist (from Figure 2.1) is used as a mask for dry etching. SiN is etched away in the exposed areas using fluorine chemistry. (see Table 2.1) **F:** Photoresist is removed with solvent cleaning and oxygen plasma.

2.3 Dry Etching

2.3.1 Overview

The most common use of photolithography in this project has been to selectively mask areas of the sample for "dry" (or, "plasma-phase") etching. In these processes, a sample is exposed to an RF energised plasma etchant. Dry etching is a versatile etching technique, capable of producing a variety of side-wall profiles and chemical selectvities [36]. This is achieved through fine control of the various process parameters, such as RF power, gas flow rate and process pressure. There are two mechanisms by which dry etch removes material from the sample [36].

2.3.2 Types of dry etch process

In the first, known as sputtering, energetic ions from the plasma bombard the sample. Material is removed by the momentum transfer between particle and sample. Physical etching of this type is slower than alternatives, and yields a characteristic non-vertical etch profile that may not be desirable. Plasmas of noble gasses are often used for sputtering, since their ions undergo no reactions with the target material. Unreacted substrate material removed via sputtering may redeposit on the sample.

When non-noble gases are used to strike a plasma, they generate radicals which chemically react with the surface. Free radicals of the etchant are created in the plasma, travel towards the wafer, and are adsorbed by the material on the wafer's surface. This area then undergoes a localised chemical reaction, and the by-products

are desorbed from the material before diffusing back into the plasma. If the products of the reaction are volatile, the reactants may be pumped out, resulting in a cleaner process than sputtering. Note that reactive ions may also sputter material from a target surface and physically etch the surface before inciting any chemical reaction. Reactive etch profiles are isotropic, since the reaction occurs in all directions. The active ingredient in these recipes is typically a Halogen, with fluorine being a common choice for silicon substrates, due to the volatility of SiF_4 [37]. Different combinations of physical and chemical etching are employed by varying the proportions and flow rate of the gasses involved, and varying the electrical field within the chamber. These parameters can be altered to create etches with varying degrees of anisotropy.

2.3.3 How we have employed dry etch

Fluorine-based dry etching has been used to pattern the SiN layer for hard-masking in wet etch, and Oxygen based plasma to strip resist and clean wafer surfaces of organic contamination via 'ashing'. This work has been performed in two machines, the BP80 RIE and the RIE 80+, both from Oxford Instruments. These tools are operated by technical staff. Dielectric etching of the type required in this body of work is routinely performed in the JWNC, and as such a number of standard processes are available. Table 2.1 lists the different etches used throughout the fabrication process.

2.4 Silicon Micro-machining

2.4.1 Overview

All bulk silicon micro-machining has been performed via anisotropic alkaline etching. This includes both the definition of individual chips, and the creation of the 'pyramid' upon which the cantilever is made. This procedure involves submerging the sample in basic solution at elevated temperature for a controlled duration. The chemical reaction is as follows;

$$Si + 2\,OH^- + 2\,H_2O \longrightarrow SiO_2(OH)_2{}^{2-} + 2\,H_2 \text{ [38]}$$

Etch Number	1	2	3	4
Role	Front side patterning	Front side clean	Back side chip definition	Front side chip definition
Material	SiO2/SiNx	Polymer residue	LPCVD SiN Rear	LPCVD SiN Rear
Thickness (nm)	60/40	N/A	400	400
Tool used	BP80	80+ RIE	80+ RIE	80+ RIE
Gas	C2F6	O2	CHF3/O2	CHF3/O2
Flow Rate (sccm)	20	50	50/5	50/5
Power (W)	100	10	150	150
Pressure (mT)	23	50	55	55
Temperature (C)	23	23	23	23
Duration (mins)	5	5	27	25†
Etch Rate	57/50nm	N/A	80-90*	80-90*
Selectivity (to Si)	2:1	N/A (inf)	10:1*	10:1*

TABLE 2.1: Dry etch recipes used in probe manufacture. * The reported values for etch rate and selectivity are for in-house grown SiN. The LPCVD Nitride employed in probe manufacture is known to exhibit higher etch resistance. † This etch uses an interferometer to monitor the removal of Nitride. After observing a steady trace, which indicates the Nitride has been removed, we typically etch for another 150% to ensure complete removal.

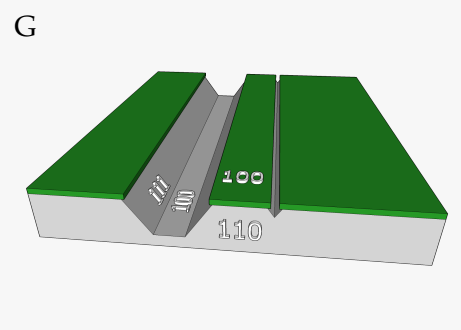

FIGURE 2.5: **G:** Those areas of the wafer surface not masked by SiN are subjected to a timed wet etch in KOH or TMAH, resulting in sloped side-walls. These are the {111} planes, which etch much slower than the {100} planes. The angle formed between the two is 54.7°. Note the difference between the two openings in the same etch time. The left opening continued to etch the {100} surface, while the right has self-terminated on the slow etching {111} planes. A slight undercutting of the mask occurs due to slow etching of the {111} planes.

Anisotropic etches refer to those in which the substrate is etched at different rates in specific directions, as opposed to isotropic etching in which all directions are attacked uniformly. While the above process is indeed anisotropic, the term crystallographic etching may be more appropriate, since it is the different planes of the Si crystal lattice which experience different etch rates. This phenomenon arises due to differences in bond energies between Si atoms in different crystal planes. Common etchants include Potassium Hydroxide (KOH), Tetramethylammonium Hydroxide (TMAH) and Ethylenediamine Pyrocatechol (EDP) [39] . The latter is not preferred however since it is highly toxic and a suspected carcinogen [40]. For CMOS applications, KOH cannot be used due to the risk of mobile ion contamination [39], [41]. Etchant compatibility with the metals required in a device is also an important consideration, for example, both KOH and TMAH are known to attack common metals such as Aluminium and Titanium [42], [43]. In addition, each etch chemistry offers different plane selectivity and surface finish [41].

2.4.2 Masking material

Wet etching requires a chemically durable mask, so resists are not typically appropriate. Furthermore, TMAH is a developer for some photoresists, meaning the these materials would be degraded as the etch progressed. In this work, LPCVD silicon nitride has been employed as a hard mask, since it has very good etch resistance to

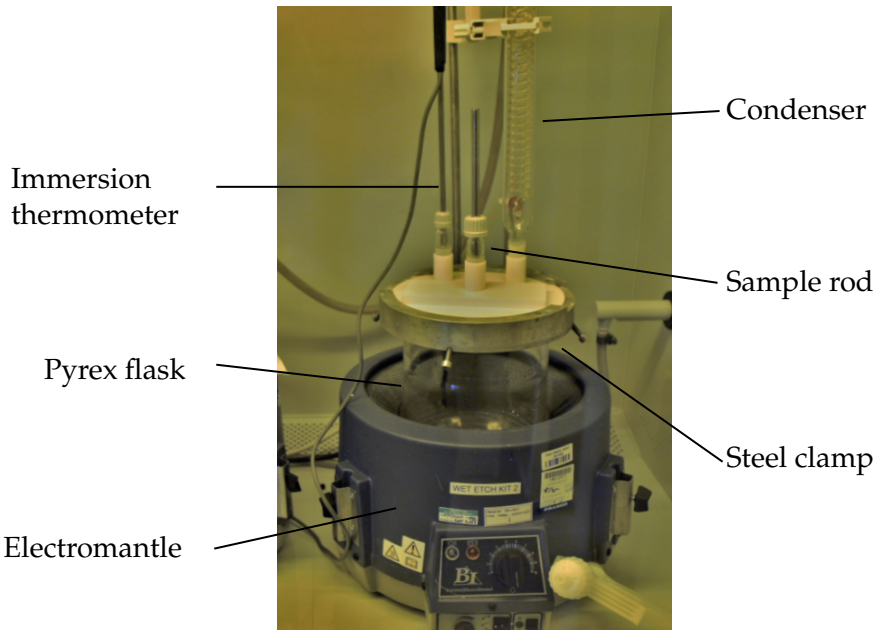

FIGURE 2.6: Annotated photograph detailing the different parts of the wet etch kit used throughout this work.

the chemicals listed above. The SiN is patterned using the combination of photo, or electron beam lithography alongside dry etching (Section 2.3, Figure 2.1)

2.4.3 Etch kit

Wet etching is performed in a custom-made bath consisting of a 2L Pyrex reaction flask, which sits in a heating electro-mantle that features magnetic stirring capability. The temperature is monitored by an immersion thermometer, whose output provides feedback to the mantle's temperature controller. To ensure that the heated mixture does not evaporate and change concentration, the lid is sealed using a Teflon cover with a corrosion resistant steel clamp. In addition, a water cooled reflux condenser is inserted into the lid to condense any escaping vapours. Teflon holders have been created at the university workshop for a variety of standard sample sizes, including 3", 4", quarter wafer and small rectangular pieces.

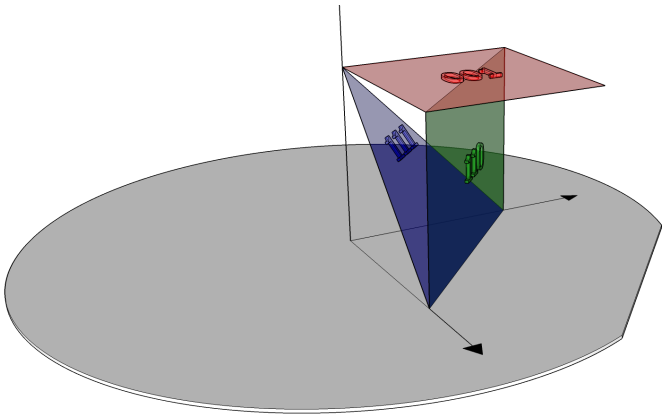

FIGURE 2.7: (100) Silicon wafer with graphic highlighting a few pertinent crystal planes, denoted by their Miller index.

2.4.4 Timed etching

The above equipment is employed with the aim of ensuring that the temperature and concentration of the etching solution remains constant, to keep the etch rate constant. Due to these measures, the etch rate is reasonably uniform and repeatable, and the desired etch depth can be achieved with sufficient accuracy simply by timing the sample's immersion in the kit. The immersion time, and desired etching depths for each wet process are presented in Appendix A.

At room temperature conditions with typical humidity levels, silicon is known to form a thin (single nm order) native oxide on its surface. Since alkaline etches demonstrate a high selectivity between Si and SiO_2 (roughly 500:1 [44]), even thin oxide layers can significantly inhibit the commencement of silicon etching. This 'induction time' introduces non-negligible process variability which must be avoided. To this end, Hydrofluoric Acid (HF) dips have been employed immediately prior to wet etching. HF is an SiO_2 etchant with excellent selectivity between SiO_2 and Si, and is able to quickly strip any native oxide. Details of the process, indlucing HF concentrations are provided in steps 12 and 24 of Appendix A.

2.4.5 Miller Indices

As described in Section 2.4.1, alkaline wet etching of Si exhibits selectivity related to the crystal planes of the silicon substrate. All bulk micro-machining performed in

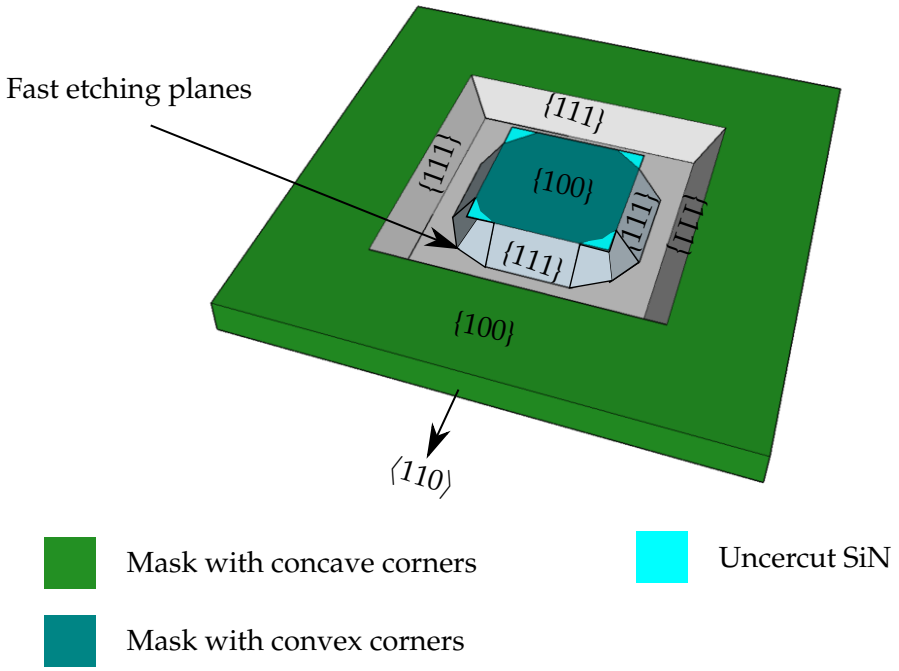

FIGURE 2.8: Whether pits or asperities are formed in the wet etch depends on the layout of the mask. The blue feature has only convex corners, and will etch with 'outwardly' sloping side-walls. The green masking layer is made up of concave corners. Etching this feature forms a pit with 'inwardly' sloping walls. Exposed silicon at the convex corners is comprised of fast etching planes, which leads to their preferential etching. This effect is termed 'convex corner undercutting'. [46]

this work has employed this type of processing, and in the case of the pyramid etch (Section 3.3.2 and Appendix A Step 12), the unique properties of this type of etch have been exploited to form important structures for AFM probe fabrication.

When discussing crystalline substrates, it is common to refer to the various crystal planes by their Miller indices, which are sets of indices denoting a vector that is normal to a crystal plane [45]. Different styles of brackets are used to refer to different things, as summarised below;

- [hkl] - Represents a direction
- ⟨hkl⟩ - Represents a set of equivalent directions by symmetry
- (hkl) - a plane with the normal vector [hkl]
- {hkl} - the set of planes equivalent to (hkl) by symmetry

2.4.6 Relation between different planes and wafer orientation

Wafers used for this work are (100) orientated, which refers to the plane that comprises its top and bottom surfaces. A flat edge is ground out of the wafer such as to expose the (110) plane. Figure 2.7 presents a (100) orientated wafer with the relationships between relevant crystal planes highlighted. When performing anisotropic wet etching, the orientation of mask openings on the wafer surface will define the planes initially exposed to the etchant and dictates how the etch will proceed. The vast majority of features patterned onto our wafers have been aligned to the $\langle 110 \rangle$ directions; parallel and perpendicular to the flat. In this configuration, the (100) plane etches quickly, and sloped {111} side-walls emerge. It is estimated that these {111} planes etch more than one order of magnitude slower than the other planes [45]. The angle formed between the {111} planes and the surface is 54.7 $^\circ$. Whether these planes form an asperity or a groove depends on the tonality of the mask. A square opening in a mask will produce and inverted pyramid or its frustum, depending on the duration of the etch and size of the opening. Figure 2.8 shows an example etch in which both convex and concave mask features were aligned to the {110} planes. The resultant etch planes are highlighted.

2.4.7 Self-terminating etches and undercutting.

A 'v' (1D) or 'pyramid' (2D) shape occurs when the etch is 'self-terminated', a term used to indicate that all the exposed facets are {111} and the etch has practically ceased. An example of a self-terminated feature is presented in Figure 2.1G. Note that the {111} planes do still etch slightly, which causes undercutting of the mask. This is also shown in Figure 2.1. Undercutting of the mask is particularly evident when features are slightly misaligned with respect to the $\langle 110 \rangle$ directions, as the etch will 'correct' the misalignment such that the trench will have $\langle 110 \rangle$ aligned edges, even if the mask did not. For this reason, rotational alignment in the initial photolithography level is very important. By aligning the flat to a grating in the mask-plate, we are able to minimise errors to within a few tenths of a degree.

Etch	Etchant(s)	Temp. (C)	Time (mins)
1 - Pyramids, bars, markers	7 molar KOH: IPA, 0.8:0.2	55	60
2 - Deep back-side etch	7 molar KOH	110	75
3 - Release etch	25% TMAH: IPA, 0.8:0.2	80	135 (variable)
4 - Undercut	7 molar KOH	N/A*	9

TABLE 2.2: Process parameters for the different wet etches used in this work. * Etch 4 is performed in a Beaker, rather than the wet etch kits. As such, the temperature is not controlled. Preparing the KOH solution is an exothermic reaction, and we perform the etch at whatever temperatures are reached in this process.

2.4.8 Modification of etchant by surfactants

In addition to the unmodified etchants described throughout this section, there has also been much discussion on their performance when surfactants are added [47]–[50]. Alcohols and other amphiphilic molecules, when added to KOH or TMAH alter the etch ratios of different crystallographic planes, and have been demonstrated to improve the surface finish on certain facets [51]–[55]. A reduction in roughness on those slow etching arises planes because the addition of IPA promotes dissolution of material on fast etching planes. The etch rate selectivity in unmodified anisotropic etching is $R_{100} > R_{110} >> R_{111}$,while the above modifications result in an altered selectivity of $R_{110} > R_{100} >> R_{111}$ [54]. In this work, IPA has been added to all but the deep back-side etch to improve the surface roughness and to promote fast etching of higher order planes.

2.4.9 Tip Formation

Designing masks that do not align with the (110) plane yields more exotic results upon anisotropic etching. AFM probes have long been fabricated using anisotropic wet etching [56], [57] since crystallographic etches yield multi-faceted, reproducible 3D structures that could not be achieved through dry etching. A variety of different mask shapes have been employed to create tips of different shapes and aspect ratios [44], [47], [56], [58]–[61].

For non-functionalised AFM probes, tip sharpness is the highest priority. In functionalised AFM, this is not always the case, as properties other than sample topography are the primary focus. The resolution of the measurement may be defined by the size of the functionalising sensor.

The following Chapter details the development and design decisions of integrated sensor probes, while Section 3.6 discusses the development of the particular integrated sensor AFM technological platform upon which this work builds. As such, the discussion of tip formation on these samples is reserved until Section 3.6

2.5 Electron Beam Lithography

2.5.1 Introduction

Electron Beam Lithography (EBL, e-beam) is a vital technology for the production of the functionalised AFM probes presented here, as it is used to define the sensing elements and the cantilever itself. EBL is a 'direct-write' form of lithography, and as such, no mask is required. Patterns are generated in software and translated into machine operable commands. Whereas photolithography employs UV light to expose a resist, EBL uses a focussed beam of electrons. A series of lenses, apertures and other electronics make up the tool's optical system, which controls the current, diameter, and placement of the beam. The optical system of our tool is presented in Figure 2.9.

2.5.2 Tooling

Electron Gun

The electron gun uses a thermal field emission cathode to generate a steady beam of electrons. It is consists of a sharp Tungsten tip, which is coated with Zirconium Oxide. This coating forms a Schottky emitter, reducing the work function of the surface and making it easier for electrons to tunnel free [62]. The tool employs the standard suppressor/extractor electrode configuration [63], with the latter being held at sufficient potential (few kV) to allow electrons to escape the surface (Figure 2.10). Once freed, the electrons are accelerated by the anode. The energy of the electrons is usually referred to in terms of the 'accelerating voltage' of the anode. In this work, 100kV accelerating voltages have been used throughout. High accelerating voltages yield smaller spot sizes, greater positional accuracy of the beam, and reduced line edge roughness in the resulting pattern [64]. The accelerated electrons pass down the column, where a series of electrostatic, or electromagnetic lenses act to align, deflect and focus the beam (Section 2.5.2), as well as to combat various aberrations of the beam, such as astigmatism [65].

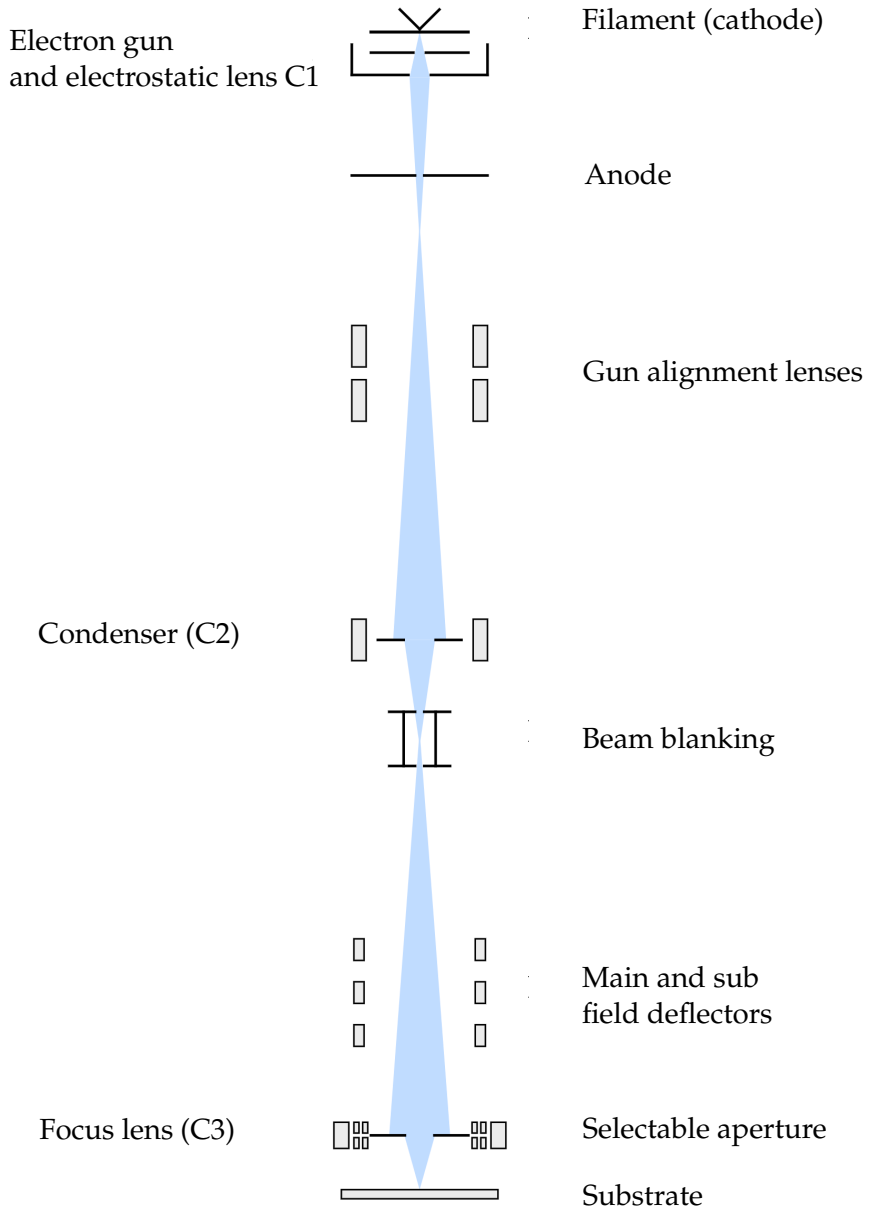

FIGURE 2.9: Optical system of the VB6. This entire layout is housed within the column of the tool and held at high vacuum.

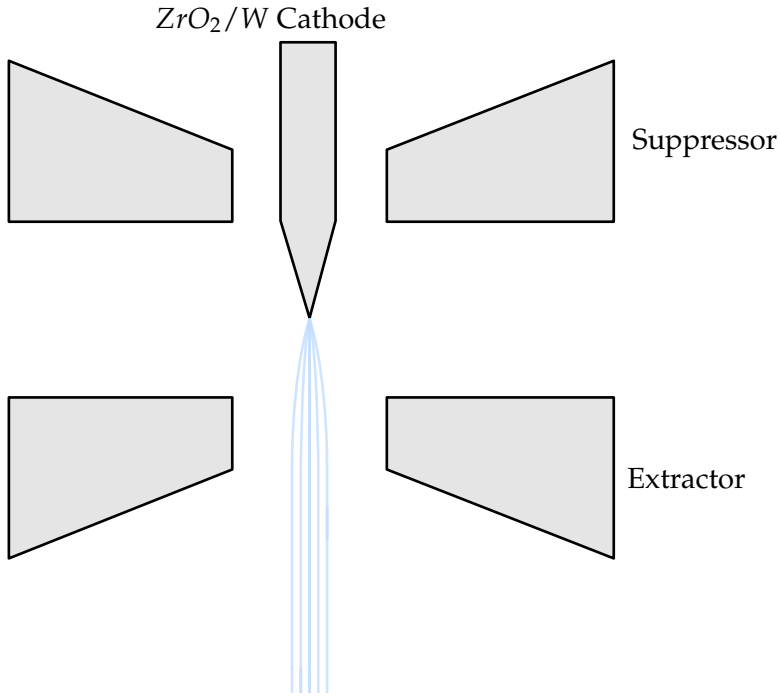

FIGURE 2.10: Schematic of the Thermal Field Emission gun employed in the VB6 EBL tool.

Beam Blanker

The beam blanker is used to selectively toggle the beam on or off at high frequency. It is comprised of a set of electrostatic plates that, when activated, deflect the beam drastically such that electrons are diverted away from the openings in its aperture, and are blocked instead. The beam blanker is used heavily during pattern writing, where it defines which pixels are to be written. The specifics of this depend on the scanning strategy of the particular tool. Raster scanning involves scanning the beam in a series of parallel lines, and the beam is blanked and un-blanked corresponding to whichever pixels are required to be written in the present line. Its alternative, vector scanning, employs a serpentine beam deflection within the boundaries of the shape to be written, avoiding any unnecessary beam blanking and deflection. The VB6 EBL tool used in this work employs vector scanning exclusively.

Apertures

Apertures are employed throughout the column to control the divergence of the beam, blocking out any stray electrons. The final aperture before the substrate has

Aperture Size (µm**)**	**Spot Size (**nm**)**	**Beam Current (**nA**)**
40	4	1
40	6	2
50	9	4
50	12	8
70	19	16
70	24	32
100	33	64
100	45	100
100	50	128

TABLE 2.3: The relationships between aperture size, beam current and spot size

selectable size, and is used to define the convergence angle of the beam on the substrate, and also has an affect on the spot size and beam current. The beam current may also be adjusted using the condenser lenses C1 and C2 (Figure 2.9). The software for interfacing with our EBL tool, Belle (Section 2.5.3) allows for selection between a number of pre-set aperture and lens configurations for various spot sizes and energies. These are presented in Table 2.3. Both spot size and beam current are important parameters which have a significant impact on writing time and resolution. Their effect is best discussed in the context of how an e-beam tool constructs a pattern, a topic which is discussed in Section 2.5.3

Deflection and focussing

The position at which electrons strike the substrate is controlled by the deflection of the beam. This is achieved through a set of magnetic coils, which are positioned orthogonally to the beam. They provide X and Y axis deflection fields as required. The maximum extent the beam deflectors can cover is referred to as a single 'writing field'. In the VB6, the maximum field size is 1.31072mm. Deflecting the beam over the relatively large area of the main field requires significant time for the beam to settle. This is overcome by the inclusion of a second set of deflection coils, known as 'sub-field' coils, which split the main 'writing field' into a grid of 64x64 'sub-fields' (of side 24.8 µm). The main field coils address the centre of each sub-field while the sub-field coils perform any necessary deflections around these central points. Since these deflections are much smaller in magnitude, coils with a lower inductance may be employed. These operate at higher speeds and have reduced settling times when

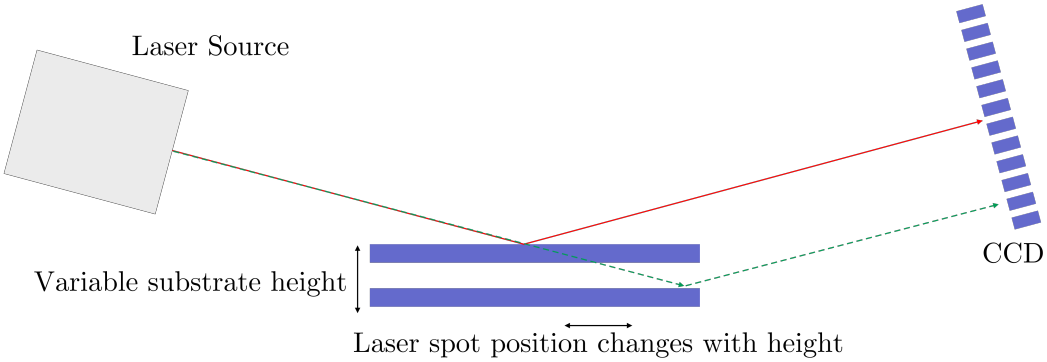

FIGURE 2.11: The laser height measurement system used in the VB6.

compared with their main field counterparts.

Stage

In the common situation that the desired pattern spans more than one main field, stage movements must be used. Different techniques for splitting up large patterns and ordering fields are available, a selection of which are presented in Figure 2.14. The VB6 features an automated, motor-driven stage. Its position is measured using integrated interferometers to a precision better than 1nm [66]. Small errors in stage positioning are compensated for by the beam error feedback system which adjusts the beam deflection to compensate.

Height measurement and stitch

The final set of coils in the optical system are the fast focus coils, which adjust the convergence of the beam such that it is focussed on the substrate surface. Substrates come in a variety of thicknesses, so a laser height sensor is employed to measure the distance from the final lens to the surface (henceforth 'substrate height'). In addition, substrate tilt or bow introduces height variation that must be accounted for at each exposure location on the substrate. The operation of the laser height sensor is presented in Figure 2.11. Correct height measurement is especially important when writing patterns spanning more than one field. Consider that maximal beam deflection occurs at the edges of each writing field. This high angle of incidence means the beams intercept position on the substrate is strongly height dependent. If the height

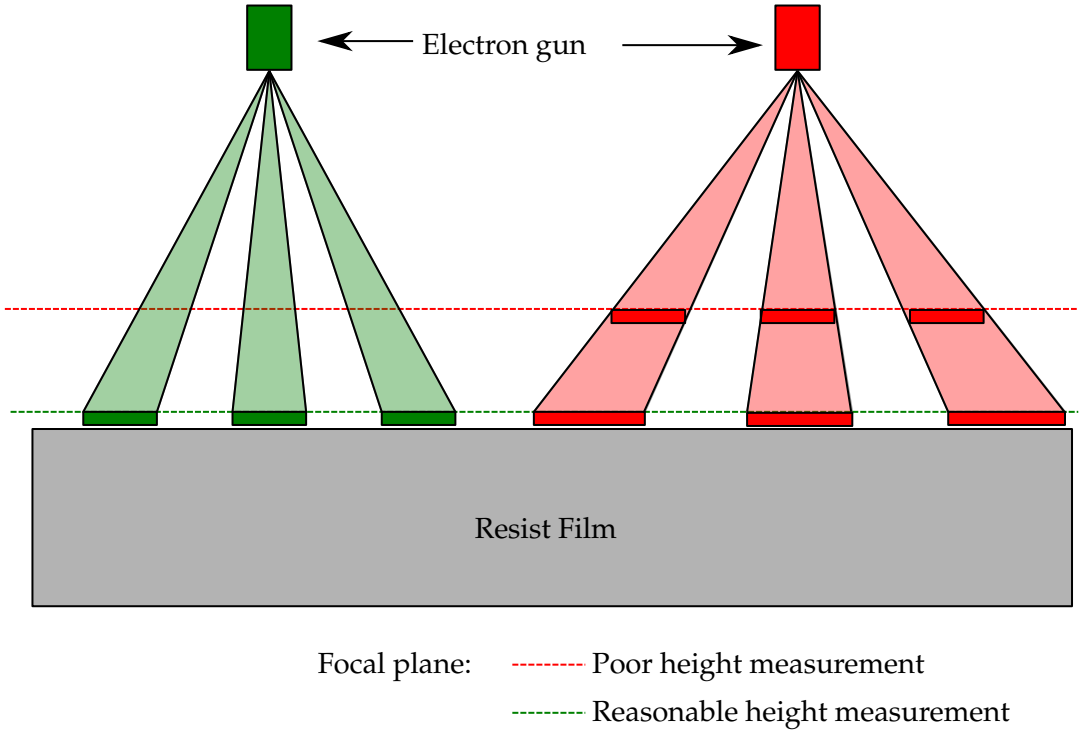

FIGURE 2.12: Diagram highlighting the 'bloating' artefact that may occur when exposing focused at the incorrect height. An incorrect height measurement has caused the red beams to focus above the surface of the resist. The area exposed by these beams will be larger than intended. Note that the effect is more pronounced at high beam deflection, which occurs at the edges of sub-fields.

of the substrate at each field is accurately measured, the beam lands where intended. However, even slight errors manifest strongly when the height measurement is not true to the surface. If the reported height is higher than the wafer's actual position, the writing field (and any features within it) will be bloated. Similarly, a reported height lower than the substrate surface will cause the resultant pattern to be shrunk. These effects are shown schematically in Figure 2.12.

This writing artefact is one form of 'stitch error', a term that covers any aberration that occurs when tiling adjacent writing fields. Other causes for stitch errors are numerous, since they can result from any errors in the projection system or stage positioning system. For flat samples whose height may be measured accurately, errors of this type are very small; on the order of 10 nanometres [67].

However, throughout this work we have observed significant writing errors on substrates with structured local topographic variation. This was attributed to poor

height measurement and beam focussing. As such, a distinct body of work was performed to mitigate this issue. More information on the problem, and our work towards its solution, is presented in Section 5.3.

Height offset The VB6 allows for setting a manual height offset. If enabled, the offset will be applied to the measured height reported by the laser height sensor. The tool will make the appropriate adjustments to re-focus the beam at the requested height, and re-scale the field size. This system was intended for resist thickness compensation, since, in some circumstances, the refraction of the laser in the resist film alters the apparent position of the surface [66]. In this work, it has been employed to compensate for the known topographic variation of the substrate.

2.5.3 Pattern generation and preparation

L-Edit

Patterns are drawn using the Tanner Suite's L-Edit CAD software [68]. It features multiple customisable layers, a hierarchical cell structure and arraying capabilities. Both nanometre sized features and centimetre sized chips can be manipulated easily and accurately using this software. In addition to all the usual drawing primitives, complex shapes can be created using chamfering, filleting or Boolean operations. A flexible grid structure allows for the snapping of different features to different intervals. For example, markers and other registration features can be snapped to a 100 µm grid, while curved polygons can be snapped to the 'manufacturing grid'. Once a design has been created, the desired layers can be isolated and exported to the common GDSII format.

BEAMER

Beamer - fracturing

GDSII files are next read into another software package, GeniSyS LayoutBEAMER. The primary function of this software is to perform 'fracturing', an operation which transforms complex pattern data polygons (of arbitrary shape) into trapezoidal primitives that the lithography tool can recognise.

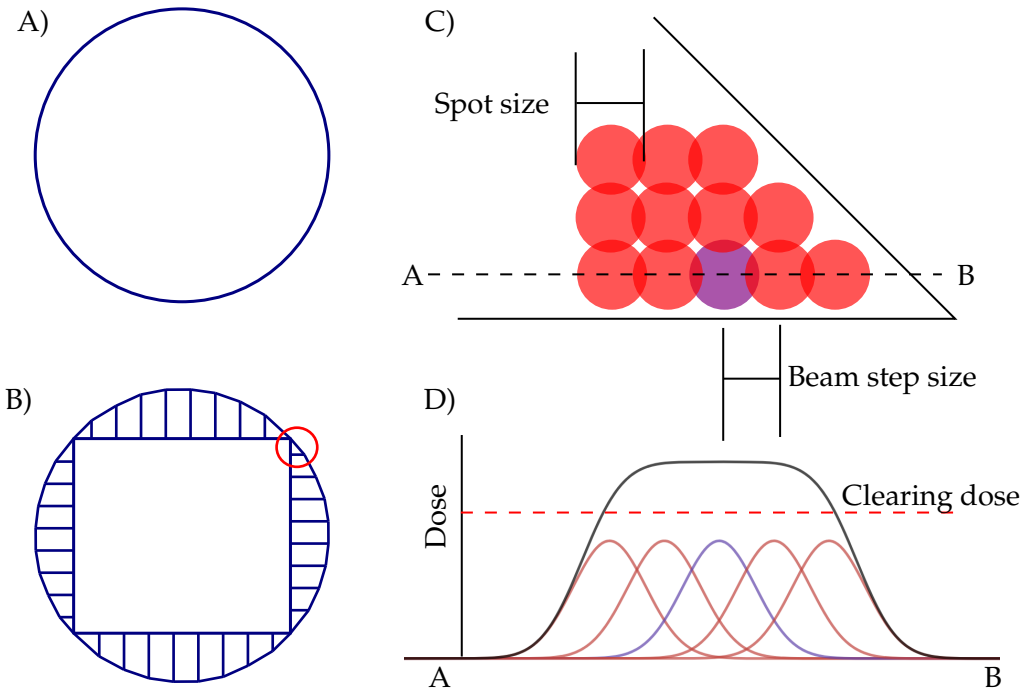

FIGURE 2.13: From complex pattern to individual shot distribution. **A:** The original unfractured shape. **B:** The complex polygon is fractured into a collection of rectangles and trapezoids. **C:** Magnified view of the trapezoid circled in **B**. Individual shots (red) are overlapped with one another to provide sufficient clearing dose. The total energy profile is shown in **D:** by a black line, while the clearing dose is indicated by a dashed horizontal line. A single shot has been highlighted purple in both **C** and **D** for clarity

Upon exposure, fractured primitives are drawn using individual 'shots' whose diameter is defined by the spot size of the beam. The beam's energy profile is non-uniform, typically being assumed to have Gaussian profile [69]. The 'spot size' is taken as the full width half maximum of the Gaussian beam, and the spacing between adjacent shots is known as the beam step size (BSS).

The number of electrons striking a given area of resist is known as the dose. The dose required to toggle the solubility of a resist film in a given region is known as the clearing dose. The clearing dose varies between resists and development procedures. In this work, features have not been written with single shots of the electron beam. Therefore, it makes sense to consider instead the area dose, which is the energy provided per unit area due to the interaction of multiple shots. Figure 2.13D compares the individual shot doses (red) to the area dose of their combined contribution.

The area dose may be described by the following;

$$\text{dose} = \frac{I_e}{fr^2} \tag{2.1}$$

In which I_e is the beam current (A), and is related to spot size Table 2.3, r is the distance between individual shots (BSS) and f is the frequency with which the beam moves between locations on the BSS grid. The lower the frequency of beam movements, the higher the dwell time at a given position, and the greater the dose. Careful consideration of all parameters within Equation 2.1 is required to optimise for write time, resolution or resist profile.

Beamer - Field Ordering and Floating

In addition to fracturing complex shapes into primitives, BEAMER is also used to define the field ordering of large patterns, and the placement of small patterns within the writing field. Typically, the tool places patterns however they may fall upon the fixed grid of main fields, however this may cause problems if small features are to be written at the edge of the writing field. This situation is depicted in the left image of Figure 2.14, in which the leads running up the cantilever are written at the very edge

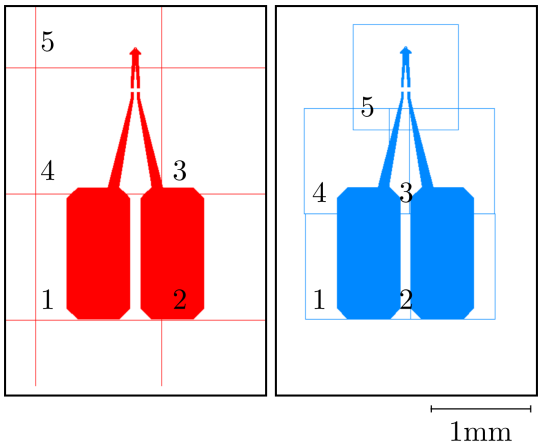

FIGURE 2.14: Two approaches to writing a pattern in the VB6. The numbered squares represent a main field. In the first image (red), a fixed field ordering is used. In the second pattern (blue), floating field ordering with the centre to sub-field option selected. This ensures that critical patterns are written on-axis, reducing the probability of deflection based aberrations and reducing the influence of any poor focus.

of field number 5. Recall from Figure 2.12 that errors in height measurement may manifest as positional/bloating errors that are worst at the high deflections. Height measurement has been a particular challenge for these substrates (see Section 5.3, meaning these devices are extremely susceptible to such errors. By using BEAMER's floating placement option with 'centre to sub-field' selected, we instruct the tool to deviate from the grid, and instead to align the writing field such that the maximal area of pattern is written on-axis. This is shown in the right of Figure 2.14, and has been successful in minimising stitch errors on our devices.

Beamer - PEC

A final noteworthy application of the BEAMER software is the implementation of proximity effect correction (PEC). The proximity effect is a common artefact when performing electron beam lithography. It occurs due to electron scattering in the resist and substrate materials, resulting in areas adjacent to the incident beam expe-riencing a non-zero dose. [70], [71]

The energy distribution with the resist for an example point exposure is presented in Figure 2.15. It has been described as the summation of two Gaussian contributions from two types of scattering effect [70]. The narrow Gaussian with greater magnitude represents the contribution from forward scattering.

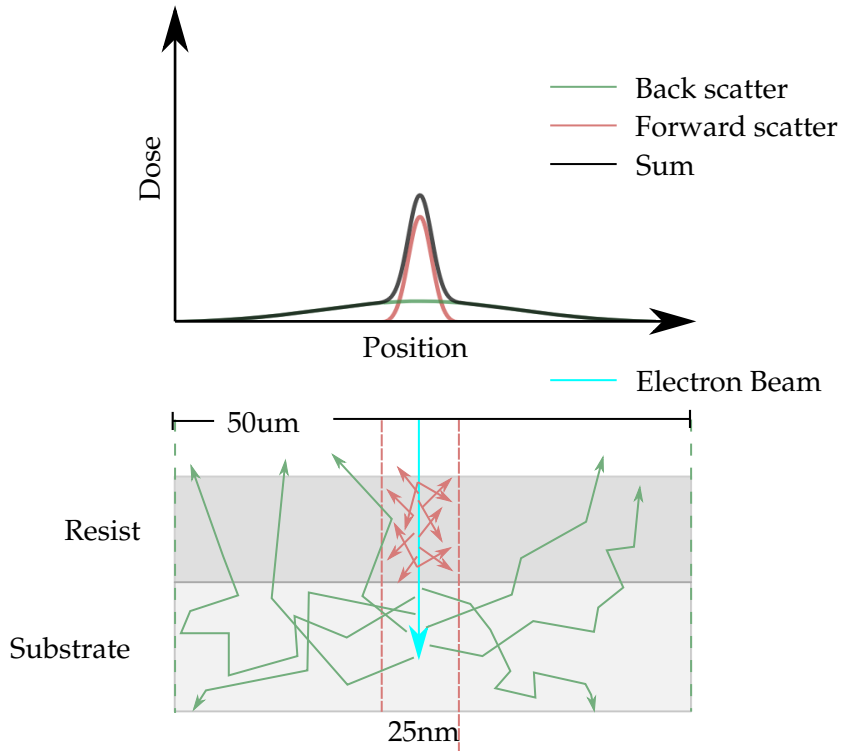

FIGURE 2.15: The effects of forward and back scattering on exposure in Electron Beam Lithography. **Top:** The exposure profile resulting from a single 'shot' by the electron beam. The total profile is the sum the forward and back scatter, which each have Gaussian form. **Bottom:** Diagram of the scattering events which result in the above dose distribution. Forward scattered and secondary electrons (red) contribute to the bulk of the desired exposure. Elastic collisions with substrate nuclei result in backscattered electrons (green), which may travel a few microns within the substrate. BSEs which exit the substrate through the top surface expose the resist as they pass through it. Note that the distributions are not to scale; forward exposure actually approximates a delta function.

In this event, an incident electron collides with an electron of the substrate or resist material. This inelastic collision deflects the incident electron through a small angle, while also exciting the atom with which it collided. The atom may then eject a secondary electron into the material. Secondary electrons make the greatest contribution to the intended exposure dose. Secondary electrons have low energy, and thus do not travel more than a few nanometres in the resist, therefore contributing very little to the proximity effect, except at extreme resolutions

Rather, it is the contribution of backscattered electrons (BSEs) that make up the majority of proximity effect artefacts. In BSE events, the electron undergoes elastic collisions with the more massive nucleus of the resist or substrate. The incident electron retains most of its energy, but has the possibility to scatter at a high angle. This type of scattering is referred to as Rutherford scattering [72]. An electron may experience many such scattering events within the substrate before exiting through the resist some distance (few nm to many um) away. Its exit causes additional, unintended resist exposure in these regions. It is these electrons which are responsible for the proximity effect.

The probability of each scattering event occurring is dependent on the substrate/resist materials and the properties of the beam. For example, a thick resist will increase forward scattering, while a substrate with high atomic number (heavier nucleus) will increase the probability of backscatter events [73]. Increased beam energy will reduce forward scattering width, but increase the backscatter width due to increased penetration into the substrate [74]. The energy distribution of a given materials/beam combination may be computed through Monte Carlo simulation or measurement.

This information is used to inform the PEC software of the point spread function (PSF) (dose profile for a single pixel exposure). If the pattern were written without any PEC, then the result would be the convolution of the desired pattern with the PSF, thresholded by the clearing dose [75]. This would lead to feature bloat, especially in those areas with dense patterning. Instead, PEC applies dose modifiers to select areas of the pattern. Alternatively, or additionally, polygons may be grown or shrunk. Both methods are chosen by the PEC algorithm to result in the correct shape when convolved with the provided PSF.

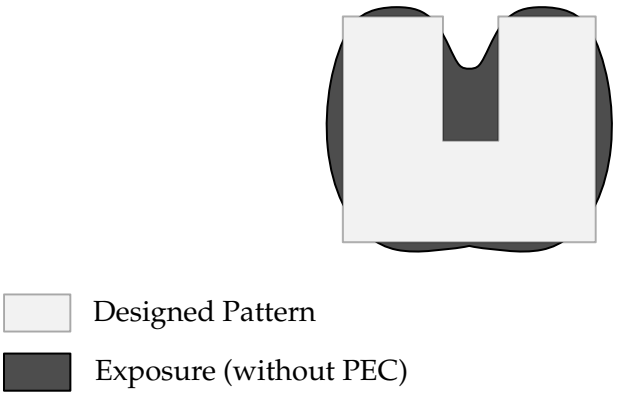

FIGURE 2.16: Example of the proximity effect in electron beam lithography. The designed shape (light grey) is convolved with the beam's PSF. Significant background dose from the BSE exposure results in feature bloat that is exacerbated at the 'notch' in the pattern due to the proximity of the exposed areas. The pattern shown is a split ring resonator as was presented in [71]

In addition, PEC software has been used here to maintain a sharp dose profile for high quality lift-off, using the 'undersize/overdose' option. This correction reduces the size of the pattern slightly, but increases the dose around the edges, enhancing the dose contrast of the features to which it is applied, resulting in better resist profile for metal lift off. This correction proved very useful for the definition of cantilever tips in non-uniform resist films, a topic which is discussed in Chapter 6.

Belle

Belle stands for 'Beamwriter Exposure Layout for Lithographic Engineers', and is the University's in-house method of creating jobs for the VB6. Belle files contain the specific machine operable commands required to run the VB6. The primary function of this software is to facilitate the accurate placement of patterns onto the substrate. This process is known as registration, or alignment. This is another area in which the non-standard samples used in this project have required additional effort, so this topic is given separate treatment in Section 5.2

In addition to the above, Belle allows the user to set dose, spot size and BSS. It also has built-in support for dose testing which has proven very useful throughout this work. Dose testing refers to an ebeam job in which the same pattern is arrayed out

with incremental changes to its dose each iteration. In this work, the beam current and beam step size are chosen first, and the dose is altered by the frequency with which the beam steps across the BSS grid.

It is good practice to perform a dose test when developing any new process, since the exact clearing dose for a given pattern is very challenging to estimate analytically, since it depends on the specific combination of;

- **Materials properties** such as the substrate atomic number, resist thickness and resist molecular weight.
- **Beam properties** such as the accelerating voltage, spot size, BSS
- **Pattern geometry concerns** such as minimum feature size (resolution), pattern density (proximity effect)
- **Development regime,** including development time and temperature [76]

In Belle, any array of patterns can be quickly set up as a dose test, by setting a dose multiplier. Throughout this work, dose arrays of $0.5\times$ to $1.5\times$ the best estimate of ideal dose have been used. Previous runs on similar materials stacks inform the initial estimation of ideal dose.

Belle files are typically created and edited in the GUI software, however it is also possible to manipulate the files using a text editor. In this body of work, we have implemented some new algorithms that have not been added to the GUI at the time of writing. As such, the calls to these novel routines are added manually in the belle file.

2.5.4 Resists and molecular weight

For this work, Poly(methyl methacrylate) (PMMA) has been used exclusively as the e-beam resist. PMMA is a high resolution positive e-beam resist with good sensitivity [77]. We make use of standard PMMA solutions that are prepared in-house through the mixture of PMMA granules with the solvent o-xylene. The resists used are presented in Table 2.4, alongside their molecular weight (mwt).

Resist Type	Molecular Weight (Da)
PMMA 8% 2010	84,000
PMMA 4% 2041	410,000,000
PMMA 1.5% 2041	410,000,000

TABLE 2.4: The electron beam lithography resists used in this project, and their corresponding molecular weight

Resists are comprised of polymer chains. In positive e-beam resists, the solubility of the resist is drastically increased below a certain chain length [78]. Exposure to the electron beam causes chain scissions, locally increasing the solubility. The relationship between exposure and solubility is described by contrast curves, which are typically presented in the resist datasheet. The molecular weight of a resist is indicative of its chain length. Thus, higher molecular weight resists require more exposure to toggle their solubility [79].

The stacking of higher molecular weight resists onto lower ones is a common practice in nanofabrication [80]. Exposed resists in this configuration result in an inwardly sloping (undercut) resist profile that is ideal for the 'lift-off' metallisation process (see Section 2.6.1). This profile occurs since for the same exposure dose, the high molecular weight resist does not develop as readily as the resist underneath it.

As with photoresists, the typical method of resist application is via spin coating, which has well defined speed to film thickness relationships (see datasheets for the resist in use). However, this method proves unreliable when working with samples of significant relief, whose raised features prevent normal distribution of resist when spin coated [81]. This is a major process challenge, which is discussed throughout Chapter 5 and Appendix G.

2.5.5 Development

Exposed PMMA may be developed using a mixture of Methyl isobutyl ketone (MIBK) and IPA, in which the former is the active ingredient. In this work, we have used a ratio of 1:1 for routine development due to its speed and reasonable contrast. 2.5:1 has also been employed where higher contrast development is required. This is particularly necessary for fabricating the cantilever to ensure high tip sharpness. In

addition to concentration, development of exposed patterns is temperature sensitive, a fact which becomes increasingly evident with reduced feature size. To this end, all development has been performed at a fixed temperature of 23.0 °C. Correct pattern transfer is dependent upon both exposure and development variables. In this work, we have chosen to fix the development parameters and adjust the dose when developing new e-beam processes.

Plasyss II	Ti	Ni	**NiCr**	Ge	**Au**	Mo	Al	Pt	x
Plasyss IV								x	**Pd**

TABLE 2.5: Metal deposition capabilities of Plassys II and IV

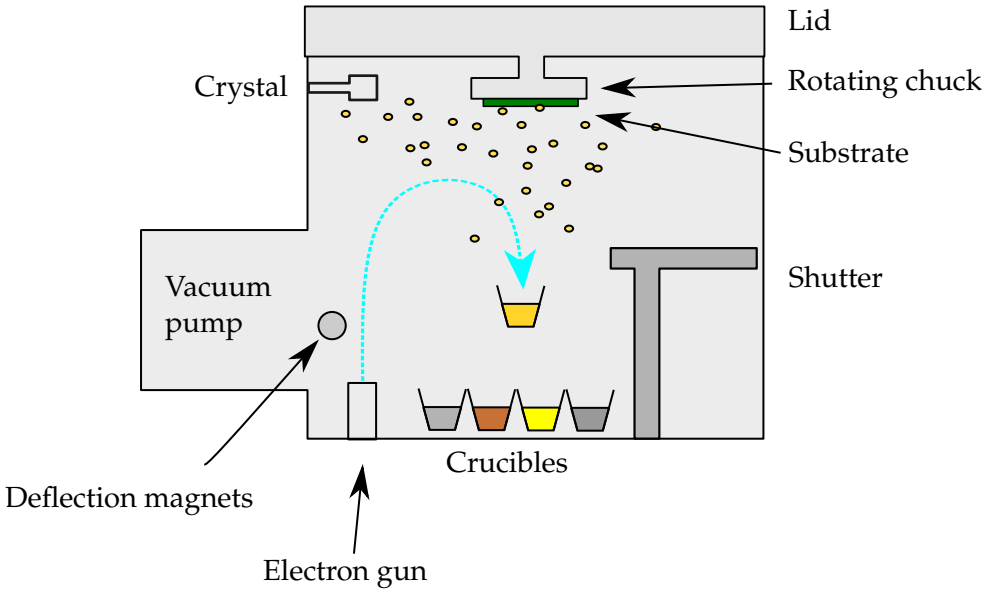

FIGURE 2.17: Simplified schematic of a Plassys metal evaporator

2.6 Metal Evaporation

Metal deposition has been performed using e-beam evaporation in the Plassys series of tools. These machines have the capability to deposit a variety of metals, since they each incorporate multiple crucibles. Table 2.5 presents the metals each tool is able to deposit, with those that we have used frequently highlighted in bold.

Once a metal has been selected, a 10kV electron gun is used to heat the source metal until evaporation occurs. The vapour rises and condenses on the wafer surface, which is upturned such that the face to be metallised is pointing downward. The entire process takes place under a vacuum to ensure the vaporised particles do not interact with any background gases. This gives them a high mean free path, and makes this method a highly directional deposition method, well suited to lift-off patterning. The thickness of the metal layer is monitored as a function of the resonant frequency of a quartz crystal, which decreases due to additional mass as metal

Metal	Etchant(s)	Etch Rate (nm/min)
NiCr	Ceric Ammonium Nitrate, 50C	∼150
Au	Aqua Regia, 60:40 HCl:HNO_3	∼500
Pd	Aqua Regia, 60:40 HCl:HNO_3	∼400

TABLE 2.6: List of metal etchants used in this work.

condensates build up on it. A diagram is presented in Figure 2.17

2.6.1 Pattern transfer of metal layers

Throughout this project, we have made use of the patterning technique lift-off, in which a thin film (in this case evaporated metal), is deposited on to a pre-patterned resist film. When considering a transfer medium for this technique, it is useful to employ a bilayer resist structure of differing molecular weights, such that an undercut profile emerges upon development. This is depicted in Figure 2.18, panel 4.

After deposition, the sample is submerged in Acetone causing the remaining resist to dissolve. Any metal deposited upon the resist is freed upon resist dissolution and is poured away with the solvent. Only metal deposited directly on the sample surface remains. Adhesion between remaining the metal and substrate is promoted by incorporating a intermediary 'sticky' layer, often NiCr or Ti. For this work, NiCr is always preferred since Ti is incompatible with the wet chemistries used in this process. Additional processes to promote adhesion include an oxygen plasma descum. This short, low power plasma process removes any resist residue or organic contamination, and is employed immediately prior to any metal deposition.

In addition to adding device layers, metals may be used as a hard-mask for subsequent etches, since they may offer better selectivity to the etch chemistry than the resist used to create the pattern. Once this action has been performed, they must be removed from the sample, typically with wet etching. Specific etchants are available that offer good selectivity between the metal to be etched and typical substrate materials. Those used in this work are listed in Table 2.6

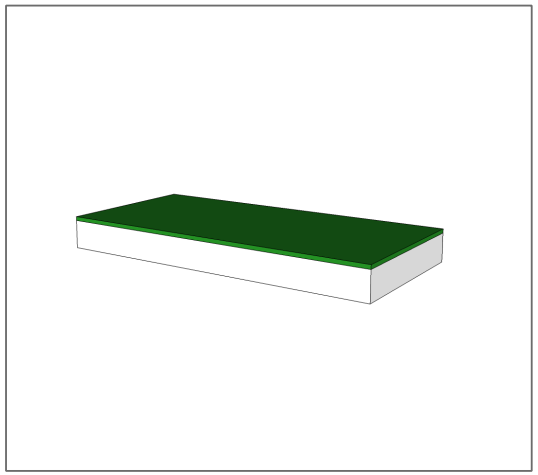

1) Silicon wafer with a thin film of Silicon Nitride

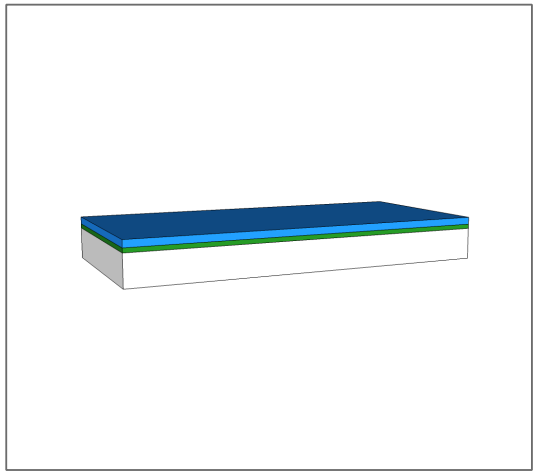

2) A layer of low molecular weight PMMA with high sensitivity is spun on and baked

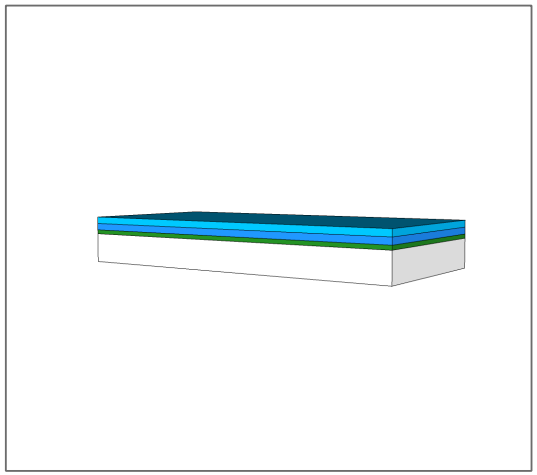

3) A second layer of PMMA with higher molecular weight and lower sensitivity is applied and also baked.

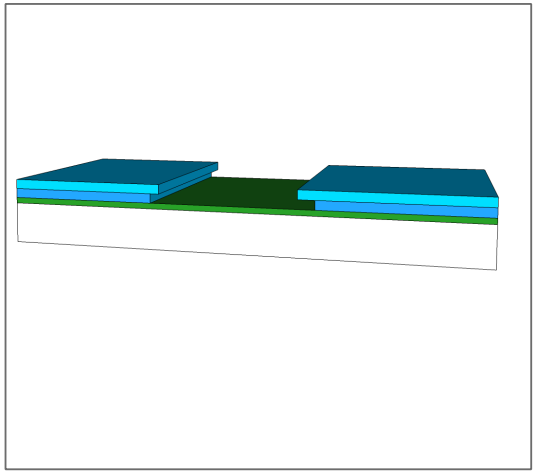

4) After e-beam exposure and development, an undercut profile is formed between the two resists

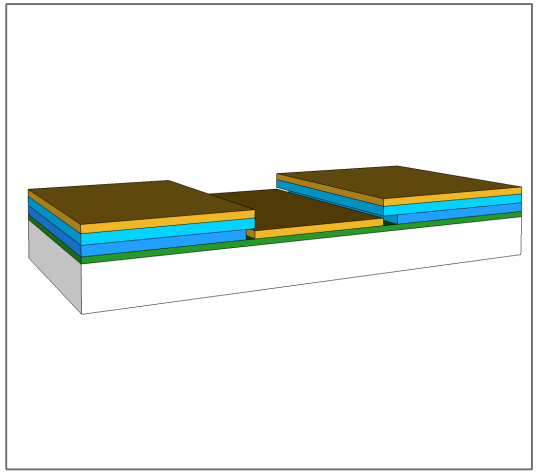

5) Metal is then evaporated onto the sample which gives a uniform covering across the surface. The undercut stops the film being continous.

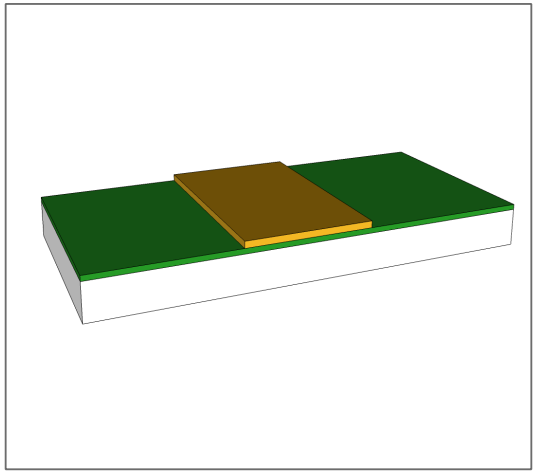

6) The resist is then dissolved away, leaving metal only in places where the resist was exposed by the electron beam. After cleaning and ashing the wafer is ready for further processing.

FIGURE 2.18: Pattern transfer using EBL, metal evaporation and 'lift-off'.

2.7 Analysis tools

2.7.1 SEM

Scanning Electron Microscopy has been used for the high-resolution inspection of small features. Two machines were used frequently; a Hitachi S4700 and an FEI Novasem. The former is a cold field emission microscope featuring a load-lock system for quick sample loading. The latter is capable of ultra high resolution imaging in both high and low vacuum, and has a variety of secondary electron detectors including TLD, ETD and helix. SEM is an invaluable tool not only for the inspection of sub-micron features, but also for the characterisation of 3D structures such as AFM pyramids and released cantilevers. Note that optical microscopy cannot easily be used to inspect features fabricated on the side of pyramids, since the angled surface prevents reflected light from returning up the column. As such, SEM is routinely performed after metal lift-off to asses the quality of pattern transfer and ensure no instances of tagging, peeling or poor adhesion have occurred. For new, or altered processes, SEM is performed even more frequently as a first point of characterisation.

2.7.2 Optical Microscopy

Throughout this thesis we present optical micrographs from one of the many microscopes available throughout the JWNC. All feature cameras for the easy collection of images. Typically, optical inspection is performed after each fabrication step due to accessibility and the non-destructive nature of this imaging method. Some of the applications where optical microscopy has proven invaluable include;

- Assessing the progress of resist development in lithographic processes
- Inspecting the appearance of thin films
- Measurement of dimensions, both x,y and z thanks to certain microscopes having calibrated stages.
- Inspecting the cleanliness of a surface after etching, ashing other layer removal methods.

- Inspecting metal films transferred by lift-off, in particular to ensure there is no tagging (i.e. extra bits of metal), and to check for any re-deposition of metal flakes.

2.7.3 Stylus Profilometry

Stylus profilometry has been used for the characterisation of step heights and surface uniformity, primarily as part of the spray coating project reported in Appendix G. This work was performed on the Bruker DektakXT[5]

A sharp diamond tip is contacted with a sample and maintained at constant force as the sample is moved underneath it using the tool's automated stage. This yields a line scan of the sample with up to nanometric z resolution. This technique is similar in principle to an AFM, however the profilometer is usually only used for a single line trace, and trades poorer z accuracy for increased data acquisition rate. The data generated by this tool were subject to data levelling to remove the influence of substrate tilt prior to exporting, since this is routinely required for these measurements. Aside from this operation, all data processing has been performed using the authors' own software.

[5]https://www.bruker.com/products/surface-and-dimensional-analysis/stylus-profilometers/dektak-xt/overview.html

Chapter 3

Development of Functionalised AFM

3.1 Scanning Tunnelling Microscopy

One of the earliest reported Scanning Probe Microscopy methods was the Scanning Tunnelling Microscope (STM). This technique exploits the quantum tunnelling effect to interrogate the surface of a conductive sample with around 0.2 Angstrom topographic resolution [82]. Tunnelling is used to describe the action of an electron passing through a barrier which would appear insurmountable in classical mechanics. In quantum mechanics however, there is a probability that the particle will appear on the other side of a potential barrier. This probability is exponentially dependent on the width of the barrier. In an STM, a sharp Tungsten or Molybdenum tip is brought into close proximity with a conducting sample, and it is the separation between the two which acts as the potential barrier. For metals with typical work functions of a few electron volts, an adjustment of the tunnelling distance of only 1 Å changes the tunnelling currents by about an order of magnitude [83].

The first demonstrations of this technique as a method for the measurement of sample topography involved scanning the tip across the sample surface while maintaining a constant tunnelling current. This was achieved through a feedback system, in which the height of the probe was modulated such as to maintain the set point of current. The probe was affixed to a piezo-drive which was used to lower and raise the probe in accordance with the feedback signal, and to scan it across the sample

in x and y [84]. If the material being scanned is homogeneous (has no variation in work function), then the voltage applied to the piezo is a direct measure of surface topography [84].

The piezoelectric effect was crucial to the success of STM. Piezoelectric actuators produce a small, measurable mechanical strain which is proportional to the magnitude and direction of the supplied input voltage [85]. Piezoelectric tubes, such as that presented by the STM inventors [86] are a popular choice for SPM due to their capability to perform precision 3D nano-positioning. These devices are used to dictate the position of the probe relative to sample, making them a fundamental part of a scanning probe system [87]. Either the probe or sample may be attached to the positioning system. While Piezos are used for small deflections required for z feedback and xy scanning, coarse positioning is typically employed through mechanical motors.

3.2 AFM

A limitation of the STM is its inability to measure non-conductive samples due to the nature of the quantum tunnelling. To overcome this, a flexible metal microcantilever was incorporated into the system. This cantilever is placed directly below an STM tip resulting in a tunnelling current that is a function of the cantilever's flexure as it scans a sample surface. This new tool was named the Atomic Force Microscope due to its ability to measure short range inter-atomic forces between the tip and the atomic structure of a sample surface [88]. This was facilitated through the development of a cantilever with spring constant weaker than that found between atoms and the sensing of the sub-nanometre displacements which arose when scanning such a soft spring over a surface [89].

The original AFM had transformed the STM into a technique capable of imaging insulating samples, however there was no necessity to use an STM for the deflection sensor. Although the STM demonstrated excellent sensitivity, it's performance was degraded if the tip or cantilever suffered from any insulating contamination [89].

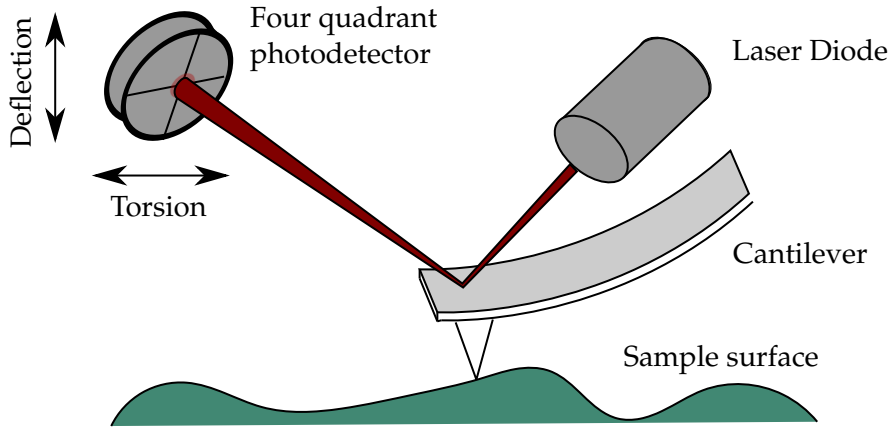

FIGURE 3.1: Schematic drawing of the optical lever feedback system employed in AFM. A cantilever with reflective top surface scans across a sample with topographic variation. A laser is reflected from the cantilever detected by a four quadrant photodetector. The beam is deflected up and down by cantilever deflection, and along the horizontal axis through cantilever torsion.

This is particularly problematic for imaging in ambient conditions, where metal oxides form readily [90].

3.2.1 AFM - Optical Detection

Optical detection methods were demonstrated to be an equally sensitive and more reliable method of deflection detection [89]. A popular approach is an optical lever system, which is depicted in Figure 3.1. A laser is aligned to reflect off the cantilever beam and land somewhere upon a position sensitive photodetector. The voltages output by this sensor are proportional to the position in x and y at which the laser spot hits the detector, which is a function of the cantilever's vertical and torsional displacement. One demand of this set-up is a reflective cantilever with large enough dimensions to reflect the laser spot without too much diffraction [91]. This is rarely a concern for traditional AFM probes, which are often uniformly coated with a highly reflective metal, however the requirement for such a coating poses significant design limitations on the SThM probes used in this work, since separation is required between the electrically active wires leading to the RTD.

While a number of modern AFMs use an optical lever system, it is also possible to use an interferometer [92]. Although optical levers technically measure the cantilever bending angle while interferometers measure the displacement, the two have been demonstrated as practically equivalent when calibrated accurately [93]. Interferometers are more expensive than using the optical lever method [94], however they are still preferred in some applications. Their reduced physical size may be advantageous in systems where space is at a premium, such as cryo or vacuum AFMs [95]. Additionally, the interferometer method does not require mirror-like reflecting surfaces [89]. All the AFMs available for this work employ the optical lever method, therefore the probes' reflective surface is a design constraint that could not be significantly altered.

3.2.2 Modes of AFM

An AFM may be operated in a number of 'modes' which govern the motion of the tip. Although there are many different combinations of tip motions and feedback controls, they may all be broadly categorised into one of two categories; contact (static) modes, and tapping (dynamic) modes.

Tapping/Intermittent contact

In tapping mode AFM, the probe is driven at, or near its resonant frequency. The amplitude of the cantilever's oscillation is damped by the interaction with close and long-range forces of a sample surface [96]. Feedback is employed to vary the tip-sample separation such that the oscillation remains constant. The amplitude is diminished as a function of tip-sample proximity, which forms the basis for height mapping in this mode of operation [97].

A key benefit of this dynamic mode operation is the reduced lateral forces with which the probe interacts with the sample. This can be especially beneficial when considering biological samples, or particularly complaint materials that may deform under the pressure of a contacting tip [98].

In this thesis, force-distance curves have been collected at fixed x-y position. This intermittent contact mode is not an imaging technique per-se, but rather is used for

the detailed interrogation of the probe's response as it approaches, contacts upon, and pushes into the sample at a single point. By monitoring the laser deflection signal as a function of piezo position, it is possible to assess the degree of bending the cantilever experiences for a given force with the sample. This metric describes the probe's mechanical deflection sensitivity. This operating mode has been used in this work for the mechanical characterisation of novel SThM probes with atypical cantilever geometries (Section).

For thermal probes, this mode of operation has been employed in ambient conditions to monitor the degree of coupling through the air as a function of tip sample separation. The probe's temperature response to approaching, contacting upon, and withdrawing from a sample is a key investigation of this work, which is described throughout Section .

Contact mode

Contact mode AFM describes a static operating regime in which the probe remains in continuous contact with the sample. In this mode, the probe is brought into contact with a sample, and a small force is applied, causing a deflection in the cantilever. This initial deflection is known as the set point. As the probe scans over a sample surface, the cantilever deflects further, or relaxes as it tracks over peaks and troughs respectively. While it would be possible to confer the sample height from this deflection alone, this would result in a non-uniform application of force across the sample surface, with the highest forces being experience by sample peaks, and low forces, or even tip disengagement occurring at valleys. [99]. This lack of force feedback would risk damaging the sample surface or blunting the sharp probe tip. To combat this, feedback control is often used to maintain a constant force between the probe and sample [100]. When the measured deflection is too great or too little, the z-piezo retracts or expands proportionally raising or lowering the tip so as the same degree of deflection is maintained. In contact mode measurements, it is common to receive three data channels: the surface height, the tip deflection and the friction, which is a measure of the probe's torsional bend caused by scanning across a surface. Contact mode is preferred for SThM, since the technique requires thermalisation between the

tip and sample at each measurement point. Since the probe remains in constant contact with the sample between adjacent pixels, the change in thermal signal between them is minimal and the thermalisation time is negligible. If one were to employ dynamic methods, one would have to ensure sufficient time in solid contact and contend with the fact that the probe's temperature would change significantly during the out-of-contact phase of the period. The limited oscillation frequency tapping SThM would significantly increase the acquisition time of the image. An alternative approach may be to employ an SThM probe with minimal heat capacity/thermal mass.

3.3 AFM probe manufacture

In all modes of operation, the design of the AFM probe is of great importance. We can consider an AFM probe to be comprised of two parts: the lever, and the tip.

The design of an AFM probe is dictated by its application, and there are countless varieties. A typical AFM probe can be thought of as the sum of two parts; the lever, and the tip - each having their own design requirements.

3.3.1 Lever

In tapping mode AFM techniques, resonance properties such as the spring constant, stiffness, Q factor and resonant frequency are primary concerns, since these dictate the dynamic properties of the probe. These properties are calculated based upon the plan view dimensions of the cantilever in conjunction with the properties of the material used in its fabrication [101]. The majority of cantilevers are rectangular in shape, however trapezoidal [102] or V-shaped [103] cantilevers are not-uncommon.

While early cantilevers consisted of sharp tips affixed to various metal foils [88], the majority of modern cantilevers are microfabricated using monolithic silicon substrates, due to the wealth of knowledge the semiconductor industry has in processing this material. Cantilever manufacture varies based upon material and geometry, but usually involves typical microfabrication processes such as photolithography and plasma etching, Often, patterning and etching is performed on both sides of the

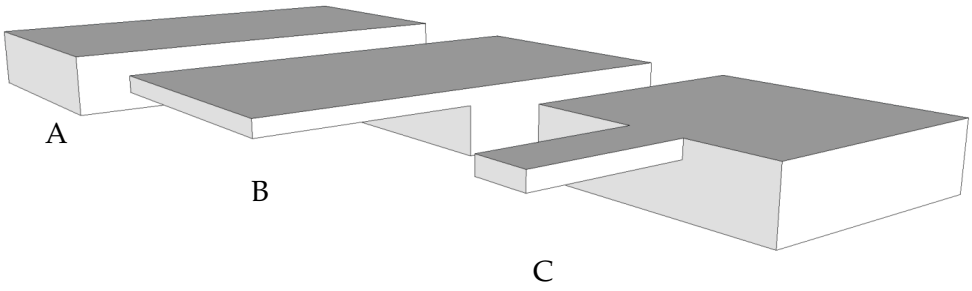

FIGURE 3.2: Simplified drawing of a double sided cantilever pattern/etch process. **A:** The unprocessed substrate. **B:** A deep etch is performed on the back side of the cantilever, introducing a thin membrane everywhere other than the chip. **C:** The front side is patterned and given a short etch, resulting in a free-standing cantilever attached to a full-thickness chip.

substrate to remove the bulk of the material before finally releasing the cantilever. This is depicted in Figure 3.2. Alternatively, thin films may be deposited over a sacrificial micro-machined Si substrate, and released upon dissolution of the Si using a wet release.

3.3.2 Tip

Tip fabrication methods may be classified as direct or indirect, depending on whether the tip material is made from the substrate or some other material. An example of each is given in Figure 3.3, which shows a tip made from a thin film deposited upon a trench of inverted pyramid shape, and another which has been fabricated using isotropic plasma etching. Another method of direct tip manufacture is by carefully designed crystallographic wet etches (see Section 2.4) that encourage the exposition of specific crystal planes such that a pyramid is formed. Accurate orientation of the mask structure to specific crystal planes governs the initial formation of the slower etching planes, which can yield reproducible, sharp pyramids. A variety of different masks layouts have been employed to create tips of different shapes and aspect ratios [44], [47], [56], [58]–[61]. The approach which forms the basis for this work is presented in Figure 3.4.

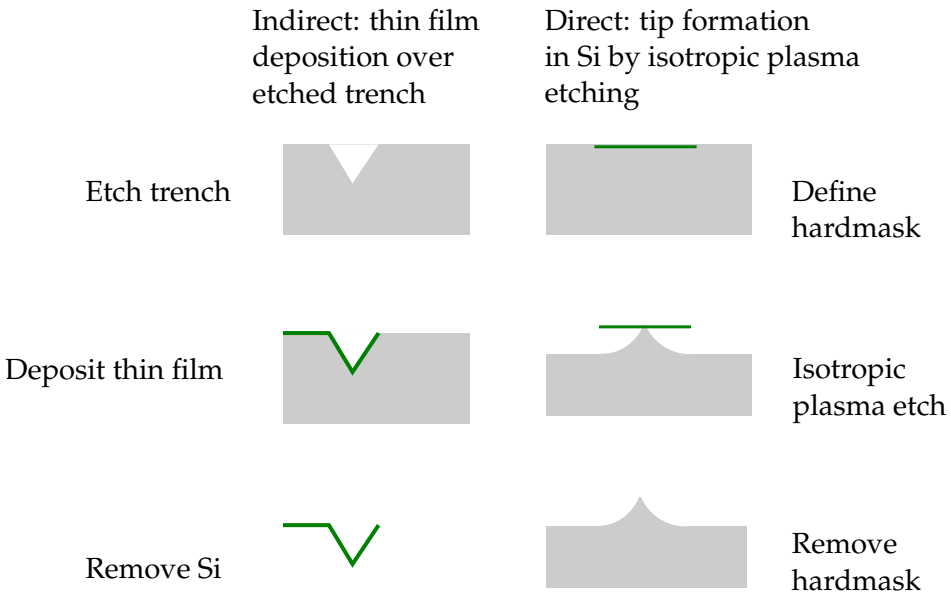

FIGURE 3.3: Diagram detailing a pair of methods for fabricating AFM tips. **Left:** The desired tip shape is etched into the substrate, which serves as a mould. The cavity is filled, or outlined with a thin film. The Si substrate is sacrificial, and is dissolved through wet etching [104]. **Right:** The tip is fabricated directly from the substrate material thanks to the undercutting of the mask by an isotropic plasma etchant (such as SF_6 for Si) [56]

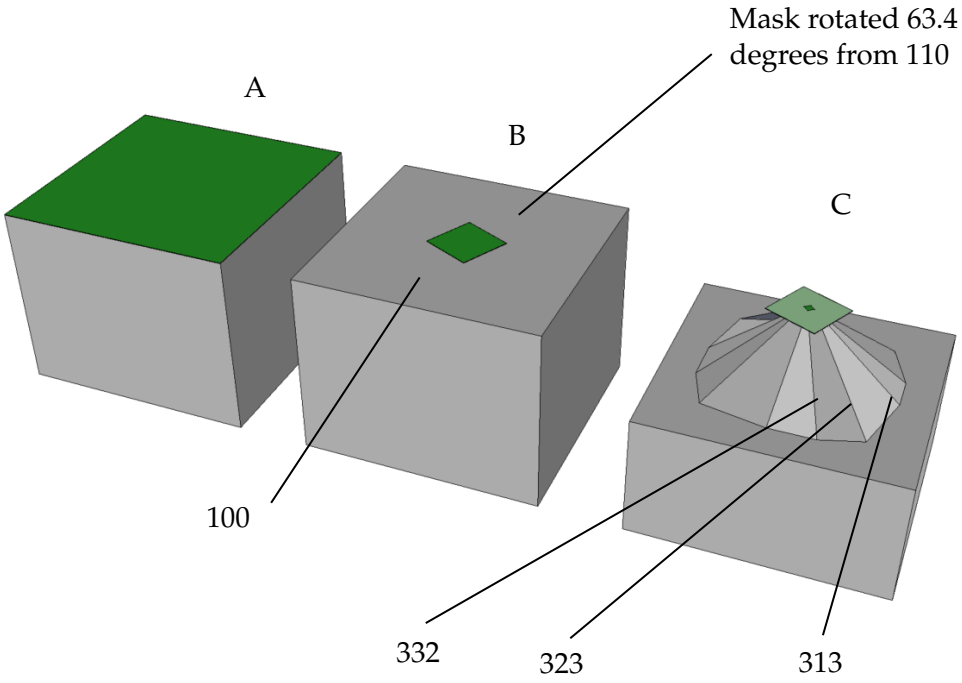

FIGURE 3.4: Drawing showing the emergence of a pyramid through crystallographic Si etching. This example follows the method of tip formation used in this work. **A:** A silicon substrate with silicon nitride hard mask. **B:** The thin film is patterned and etched to form a hard-mask, which is rotated 63.4° with respect to the 110 plane. **C:** As the etch progresses, a pyramid comprised of higher order fast etching planes is formed. This is enabled by the rotation of the mask. The mask is undercut by the etch, and would eventually fall of if the etch is let to progress to completion. This will result in an exposed Si tip, which can be further sharpened using a process known as oxide sharpening [44].

For non-functionalised AFM probes, tip sharpness is the highest priority. In functionalised AFM, this is not always the case, as properties other than sample topography are the primary focus. The following Chapter details the development and design decisions of integrated sensor probes, while Section 3.6 discusses the development of the particular integrated sensor AFM technological platform upon which this work builds. As such, the discussion of tip formation on these samples is reserved until Section 3.6

3.4 Integrated Sensor AFM

3.4.1 Introduction

The accurate nano-positioning system of the atomic force microscope made it an excellent platform for the development of other scanning probe microscopies. Modifications to the probe allow for the collection of images with completely different contrast mechanisms. A prominent example is that of chemical force microscopy (CFM), in which the tip is chemically modified with the addition of various species. Contrast in chemical imaging depends upon the chemistries with which the probe was functionalised. There are far too many different types of chemical imaging and therefore cantilever modifications than it is practical to discuss here, however an excellent overview is presented in [105]. In this work, we remark only that these functionalisations require no modification to the design or fabrication of these cantilevers. A notable exception is the uniform deposition of a thin film of gold, which is performed to promote the formation of thiol based monolayers [105], [106]. The functionalising, including gold deposition may be performed in-laboratory on standard commercial probes, or may be sold directly by vendors [1].

3.4.2 Electrical AFM, metallised probes

Thin film deposition is a common cantilever modification. It's integration with AFM is very mature, since this method is often used to metallise the rear of cantilevers and increase their reflectivity optical lever sensitivity. Conductive probes utilise the same

[1] https://www.nanoandmore.com/Functionalized-Chemical-Modified-AFM-Probes

Method	Contrast Mechanism
Kelvin Probe Force Microscopy (KPFM)	Work function of sample surface [107]
Electrostatic Force Microscopy (EFM)	Charges on sample surface [108], [109]
Scanning Capacitance Microscopy (SCM)	Probe-sample capacitance [110], [111]
Conductive AFM	Resistivity/conductivity mapping [112]
Piezoforce Microscopy	Ferroelectric domain mapping [109]

TABLE 3.1: A selection of electrical scanning probe microscopies.

deposition methods, but on the other side of the cantilever. Blanket metal evaporation (see Section 2.6) is possible even upon released cantilevers since the deposition itself poses no risks to the mechanically fragile beams. Selective metallisation typically requires some form of resist application, which risks damage to released cantilevers [31].

Conductive AFM probes offer an accurate method of delivering a local electrical impulse, or for measuring nanoscale spatial variations in electrical phenomena. Some scanning probe methods utilising a conductive probes with blanket metallisation are presented in Table 3.1.

3.4.3 Near Field Techniques, metallised probes

In addition to enabling the imaging of various electrical phenomena, metal-coated AFM probes have also been used for near-field optical imaging. These techniques are able to overcome the diffraction limit through probing the evanescent fields that exist only within a few nanometres of a sample surface. Introducing a sharp metal tip gives near field enhancements that have been exploited in the fields of Tip Enhanced Raman Spectroscopy (TERS) [113] and nano-FTIR [114]. Metallised tips have also been used for aperture-less Scanning Near Field Optical Microscopy (SNOM) [115]–[117]

3.4.4 Near Field Techniques, Aperture Probes, FIB

Aperture SNOM uses a pinhole as a near feild light source rather than an antenna for the enhancement of an existing field [117]. Traditional SNOM methods are based upon optical fibres that are etched to a fine point and metallised at an angle such that an aperture is formed [118]. Fibre probes are scanned across the sample using a

shear-force feedback mechanism which limits the lateral resolution of the technique [119].

An alternative approach is to create a cantilever - style probe that is compatible with standard AFM actuation. The high compliance of cantilever devices means they are less likely to damage the surface than a fibre probe [120]. Different approaches have been presented to perform realise an aperture within a scanning probe. A popular strategy has been the modification of commercial tips through Focussed Ion Beam (FIB) milling [121]–[123]. This technique is employed for the selective ablation of material from the probe apex to form a nanoscale aperture.

FIB milling is a high resolution technique that is capable of being performed while simultaneously imaging the sample at high magnification [124]. The precision and flexibility of this technique makes it an attractive tool for the modification of scanning probes. In addition to aperture-SNOM, FIB has been used for the fabrication of Hall Sensors on STM tips [125]. It has also been used for the production of high aspect ratio (regular) AFM tips [126], and sharp, high-resolution STM probes [127].

One appeal of FIB for SPM modification, is that unlike other forms of nano-patterning such as electron beam lithography, no resist is required. This is because FIB is a mask-less, direct etching method. This is particularly beneficial when working with fragile, and high aspect ratio micro-structures such as cantilevers and needles. The flexible cantilevers of released AFM probes are at risk of damage or destruction when subjected to typical methods of resist application such as spin, or spray coating [31], [128]. Similarly there are difficulties involved with coating surfaces with high aspect ratio features or significant topography [129], [130]. These substrates are common in SPM, because the tip is necessarily taller than the cantilever surface to ensure a single point of contact.

One of FIB's greatest advantages, flexible direct patterning, is also its greatest weaknesses for metrological applications. Modifications to probes must be performed on a per-probe basis, which introduces some variability between devices and lowers reproducibility [131]–[133]. It is also time consuming, and not amenable to batch fabrication.

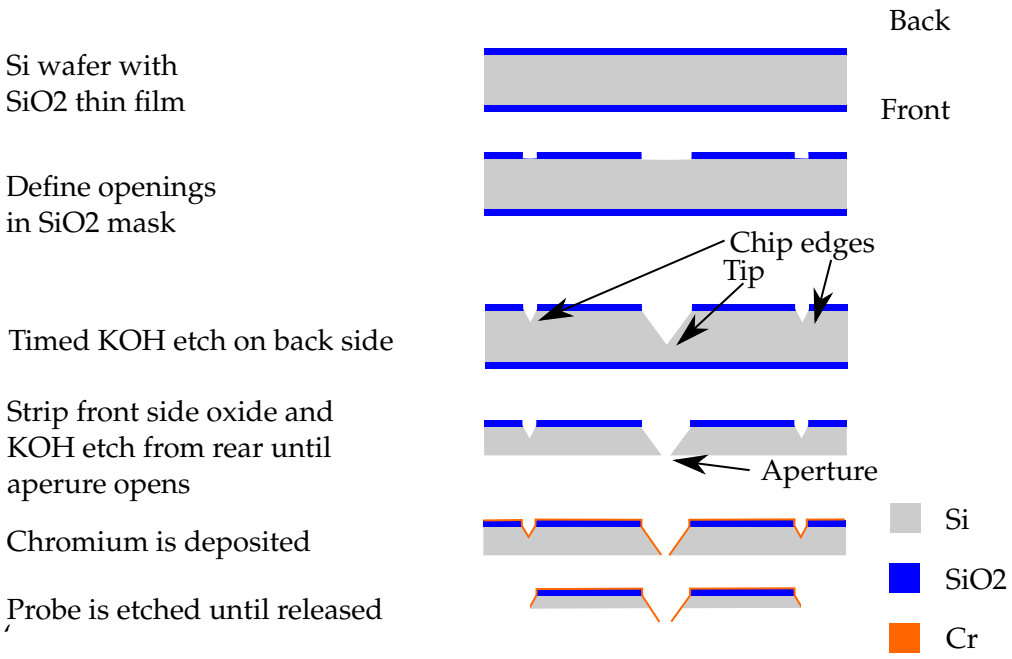

FIGURE 3.5: Process diagram of the self-aligned SNOM probe fabrication employed by Mihalcea et al. [134]

3.4.5 Batch-fabricated SNOM probes using self-alignment

Mihalcea et. al presented a method for the batch fabrication of bespoke aperture SNOM probes [134], without employing FIB or lithography on the tip. This was achieved through timed anisotropic etching of the silicon substrate to reproducibly create a hollow tip with an aperture at the apex. The procedure is presented in Figure 3.5.

The hole is formed by through-wafer etching a silicon substrate with an anisotropic wet etch processes, in a similar manner to that shown in Figure 3.3A. Because the relationship between etching planes is well known, it is possible to calculate the size of hole in a tip from the size of the mask opening on the reverse of the wafer. The side-walls of the etch pit are used as the pyramid of the probe, with the hole being present in the very centre of the feature.

The cantilever is uniformly coated with metal, including the inverted pyramid. The aperture is not coated, since there is no substrate upon when the evaporated metal may condense. The rear of the wafer is etched away, exposing the metal tip. The

nature of this process is such that the aperture is always perfectly aligned to the centre of the pyramid feature. This method has been introduced here as an example of 'self-alignment'; a process or set of processes which result in the ideal placement of a feature without requiring any sort of registration step.

3.4.6 More complex integrated sensor probes

Costa et. al have presented probes in which photolithography was used to pattern complex metal features onto a cantilever structure [135]. It should be noted however, that in this example these features were patterned before the cantilevers were released (using HF vapour). This approach allows for fabrication on a significantly more mechanically robust substrate, however one is only able to pattern materials which are compatible with the (usually) aggressive release methods.

Secondly, these probes did not feature any raised tips such as pyramids, rather the tapered point of the flat cantilever was used as the scanned region. This avoids a second problem of trying to perform lithography on AFM probes, which is the application of resist to 3D micro-structures.

3.5 SThM probes

The previous section highlighted some of the common methods employed to integrate sensors with scanning probes. In this section, the development of various types of SThM probes is considered. For the purposes of this review, only probes based upon the electronic methods presented in Section 1.3.2 are considered. Finally, a review of the state of the art of SThM manufacture at Glasgow is presented, with a particular focus on the unique technologies which enabled these devices.

3.5.1 Thermocouple type

The operation of thermocouples as temperature measurement devices was presented in Section 1.3.2. The usual method for microfabrication of thin film thermocouples is to use photo or electron beam lithography and metal deposition [136]. This is the case in the on-sample thermocouples described in Section 1.3.2. However, the requirement that the thermocouple junction be at the raised tip of an AFM probe presents a unique challenge due to the topographic variation of these unusual substrates. The difficulty in performing lithography on released cantilevers, and upon raised features has been described throughout this chapter. The following presents some of the alternative methods of integrating a thermocouple junction with a scanning probe.

Capped pyramid

In 1995, Luo et. Al. remarked that it was difficult to perform lithography on released AFM probes, and that it would be non trivial to simply pattern a thermocouple onto a commercial AFM probe. They therefore opted to perform custom probe manufacture [31]. The probes are fabricated such that a thermocouple junction is formed at the very tip of the probe. A similar probe was presented by Oesterschulze et. al [137], however they did not disclose their fabrication methods. Figure 3.6 presents the method demonstrated by Luo et al, reported in [138].

The challenge in this scheme is the penetration of the oxide layer to allow for the contact with the underlying metal in a subsequent deposition. A later method of performing this process was presented by Hwang et. al [139]. The tip was coated

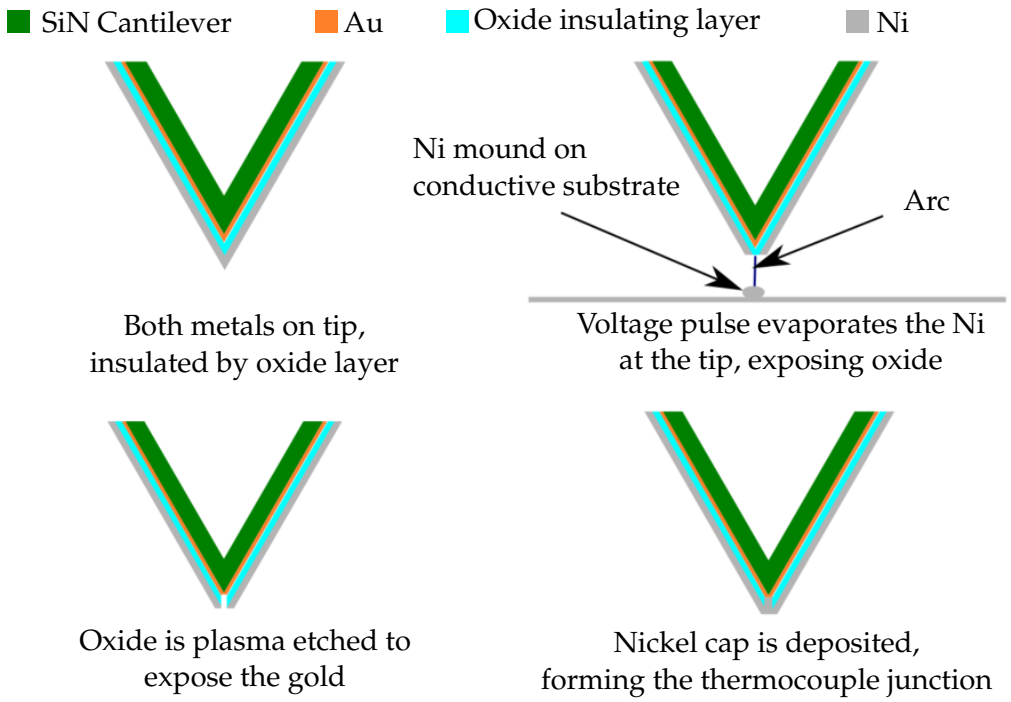

FIGURE 3.6: Capped thermocouple fabrication method employed by Luo et. al

with metal 1 and the insulating layer before being buried under photoresist. A Subsequent RIE processes removed the photoresist slowly until the probe apex emerged from beneath it, and was exposed for etching. With the tip oxide etched, the remaining resist was stripped, and the second metal was blanket deposited. A thermocouple junction was formed at the tip, where the oxide had been removed and the two metals are in contact. This has an advantage when compared to the method of Luo et. Al, since the process is performed on the wafer-scale pre-release. This batch-fabrication method results in probes with greater uniformity in junction size. This method of fabrication was first described in 2009 [139], and probes fabricated using this method have been used in multiple subsequent studies by the group [140]–[143].

Another batch-method of forming the thermocouple junction was presented by Zhang et. al, who identified that spinning photoresist onto topographic samples did not cover the raised pyramids. By tailoring the spin parameters, they exploited this fact to leave the probe apices exposed. They were able to remove the oxide in this region and form the necessary metal-metal junction [81].

In both the examples of Luo and Hwang above, note their employment of 'self-alignment'. Although achieved through different mechanisms, both exploit the fact that the tip protrudes. In the former, the protruding tip encourages arcing, while in the latter its height means it is the first part of the probe to become exposed as the photoresist is steadily removed.

At the time of writing, probes such as these are available commercially under the brand Vertisense Thermal Probes[2]

Wire thermocouples

In 1993, Majumdar et. Al first presented thermocouple-based SThM probes [144]. They were produced using alumel / chromel wires that were electrochemically etched to form a sharp tip, then welded together by discharging a capacitor to form a thermocouple junction (K-type) that also served as the AFM tip. Further etching was performed to reduce junction size and increase tip sharpness. The smallest reported junction diameter was $25\mu m$, however the tip contact was inferred to be much smaller by the quality of topographic imaging. To enable AFM-style optical feedback, an aluminium foil reflector was affixed between the wires. With this probe, they were able to map the temperature of an active MESFET device and observe heating under the gate, with estimated spatial resolution of 500nm.

Although these probes demonstrated the possibility of temperature mapping with micro-thermocouple probes, they were discovered to be mechanically unfit for contact mode operation with the feedback mechanisms available at the time due to the softness of the metals at the tip, as significant deformation would occur during scanning.

One particular modern realisation of micro-thermocouple SThM systems is that of the group at FEMTO-ST [145]. Rather than fashioning the thermocouple wires into a make-shift cantilever with optical feedback, they have attached the wires directly to a quartz tuning fork. The increased Q factor of the QTF allows for more sensitive force detection, which is valuable for the soft, wire probes [146]. In addition to improvements in the drive system, they have also increased the spatial resolution of

[2]http://www.appnano.com/product/category/vertisense-thermal-probes

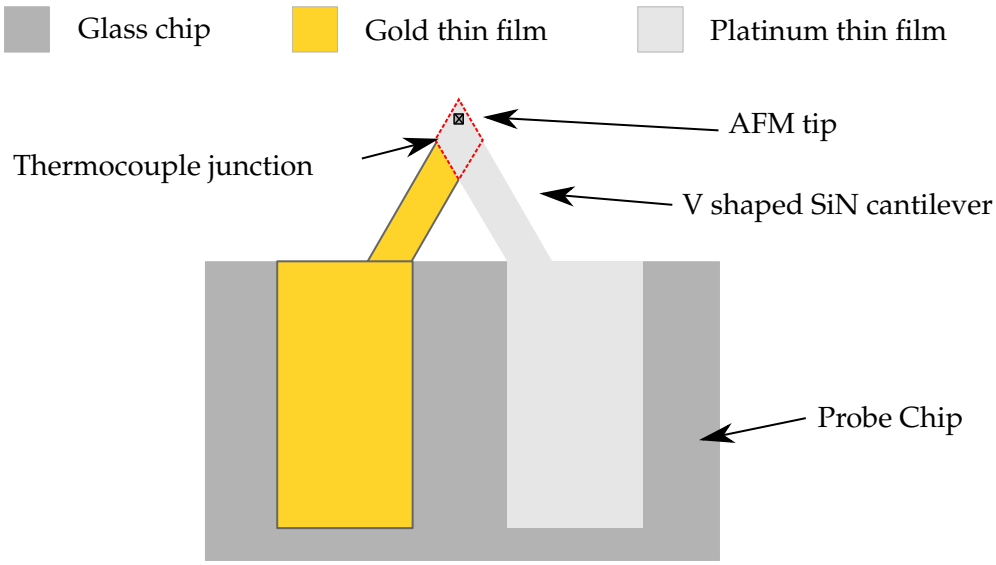

FIGURE 3.7: Drawing of the thin film thermocouple probes presented by Majumdar et. al [30]

the probes by sharpening them with FIB [147]. The disadvantages of modifying single probes was previously discussed, however this procedure results in very sharp tips exhibiting excellent spatial resolution. In addition, the low thermal mass of the micro-thermocouple probes means its response/thermalisation time is very fast.

Microfabricated Type

In conjunction with the development of micro – wire thermocouples described above, Majumdar et. al also experimented with fabricating thin film thermocouples [30]. They were motivated to do so in the hope that microfabrication techniques would prove more reproducible and yield more uniform probes – an important consideration when designing consumable devices for metrological applications.

A drawing of their probe is presented in Figure 3.7. They started with a commercial AFM probe with cantilever beams forming a V-shape. Physical masks were used to pattern gold and platinum onto each of the beams respectively, with the junction being formed at their overlap.

The motivation for using the V shape cantilever was most likely so that a degree of 'self-alignment' could be employed between the metal layers and the cantilever beams, since the alignment accuracy of physical masks is expected to be lower than

that of alternative pattern transfer methods such as photolithography, which could not be employed on a released cantilever. Although not explicitly stated, it is reasonable to assume the physical mask employed had openings for the leads wider than the cantilever beams. The increased width translates to misalignment tolerance – since within this area the metal will completely cover the beams.

This procedure resulted in devices with high reproducibility as desired, however the thermal performance of the probe was poor. As can be assessed from the Figure, the junction area is on the order of $40 \times 40 \mu m^2$, much larger than the cantilever tip. Given the small contact area (and thus high resistance) between cantilever tip and sample, this route for heat conduction was not particularly attractive. In air, the signal was dwarfed by conduction through the air, while in vacuum the probes suffered from poor spatial and temperature resolution. They remark that, while sharper probes can increase the resolution of thermal images, this should also be accompanied by smaller temperature sensors. It should be added that, as discussed later, the requirement is not only that the sensor be smaller, but be more localised to the tip.

3.5.2 Resistive Probes

Wollaston Wire

The other main type of SThM probes are those which incorporate resistive temperature detectors. The first demonstration of a resistive SThM was presented by Pylki et. al, who fashioned a probe from Wollaston process wire [148]. This material consists of a platinum core and silver sheath, having diameters of 5 µm and 75 µm respectively. By looping the wire and etching away a small (roughly $200 \mu m$) length of the silver cladding, the platinum core is exposed. This area represents the only significant resistance in the wire, and thus heating occurs primarily in this region. Similarly, the temperature dependent resistance change in platinum is well suited to resistance temperature detection due to its very linear Temperature coefficient of Resistance (TCR). Optical lever detection is achieved in the same manner as Majumdar's wire thermocouple probes [144].

Their commercial availability has meant that these probes are popular, and thus have been well characterised in the literature. However, the cause of their high contrast

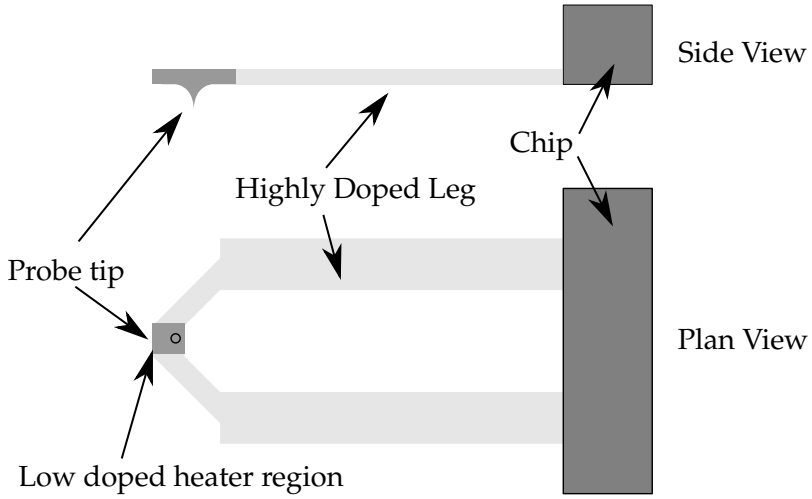

FIGURE 3.8: Diagram of a doped silicon probe.

is their large contact area, which precludes high spatial resolution measurement. Values of the thermal exchange radius have been published in the literature ranging from 200 to 2300nm [149]. As with other wire-probe microscopies, these devices are also not amenable to parallel production, introducing significant device to device variation.

Doped Silicon

Selective doping of semiconductor allows for local variation of the resistance of an otherwise monolithic structure. This property has been exploited in the fabrication of actively heated doped – Si AFM probes. By creating a probe with a high dopant concentration in the 'legs', and a low dopant concentration in the tip, a loop is created in which the highest resistance – and thus the most heat – is dissipated in the high resistance tip region. Such probes were initially developed for high density data storage by Despont et al. of IBM [150]. Nano-indentations were created by impressing the heated cantilever on a polymer film. The indentations could subsequently be detected ('read') by the same tip by exploiting the relationship between probe-sample distance and heat loss. In air, the extent to which the substrate acts as a heat-sink to the hot probe is modulated by their separation. Therefore the depressions caused by the 'write' operation indents could be observed in the thermal

signal. [150]

The operating principle of these probes necessitates two separate physical 'legs' to ensure proper electrical isolation between them. Such probes typically do not employ optical lever force feedback, since there is no suitably large plane for the reflector. Instead, such probes exploit the piezo-resistive property of doped Si, in which the resistance of these regions varies linearly with deflection. The fabrication of piezo-resistive Si cantilevers upon which the doped-Si thermal probes are based was presented by Tortonese et. al. [151]. The cantilever is formed using a 'silicon on insulator' substrate, using the oxide as an etch stop to define the cantilever thickness. The probe's tip is formed using isotropic dry etching and oxide sharpening, as discussed in Section 3.3.2 and shown in Figure 3.3 [140]. The layout of such a probe, including the selective doping to turn it into a heated cantilever, is presented in Figure 3.8.

These types of probes are capable of delivering a great deal of heat – up to 1000K [152]. This is the result of their comparably large heated region (roughly 8 x 16um) and high electrical resistance [153]. This makes them especially well-suited to applications where heat delivery is of importance, including micro-calorimetry and local thermal analysis of materials softening behaviour [154]. In a follow up paper to Despont's [150], King et. al. describe some of the design considerations for a second generation of heated cantilever probes. They remark that the heating of the probe may be increased by narrowing the legs leading to the heated region [155]. This simple geometric alteration increases the thermal resistance of heat flowing towards the cantilever. This encourages localisation of the heat to the tip region, which causes a greater fraction of the generated heat to travel across the tip sample contact, or to cross the air gap to the substrate.

In these probes, the latter is by far the dominant transfer mechanism. The tip has nanoscale contact radius comparable with that of non-functionalised AFM probes. The small solid-solid interaction area results in very poor thermal coupling due to this geometrically induced contact resistance. Meanwhile, the heated region is comparably large. The probe's resistance is the average of the temperature of the entire heater/sensor region, of which the tip contact comprises only a minute part [140]. In

addition, the raised tip (although doped in the same manner as the rest of the heater) carriers negligible current, since the circuit does not require electrons to travel to the end of the tip. Changes in sample temperature induce a tiny change in the probe resistance, making them unsuitable for thermometry. When the probe is heated instead, it has been shown that the dominant heat transfer mechanism is conduction through the air, rather than the tip - sample contact. Since this mechanism is separation dependant, rather than materials dependent, these probes cannot be used for thermal conductance contrast imaging (under ambient conditions [156]) either. They have however been identified as useful tools for calorimetry and nanolithography [157]. In addition, Kim et. al have used probes of this type to topographically image a sample using the thermal signal, and compared the results with optical deflection force feedback [158]. The contrast mechanism exploits the fact that the tip-sample solid-solid conduction is negligible. As the probe scans over some small feature with its sharp tip, the distance between the heated cantilever and the substrate is modulated. The tip scanned over a raised, isolated feature increases the cantilever – sample separation, which reduces coupling between the tip and sample through the air. Because the sample is now sinking the cantilever's heat less effectively, the cantilever resistance increases. In this paper, the authors demonstrated greater topographic sensitivity than was achieved using the traditional laser deflection method.

Additional applications for probes of this type are presented in the review paper of King et. al [159], which also outlines some of the challenges for these devices. Although these probes have not been actively developed for SThM applications, there are enough parallels in the design and characterisation of these probes to make their study of importance to this work. Subsequent chapters of this work draw upon some of the experimental conclusions and design principles presented throughout the references in this section.

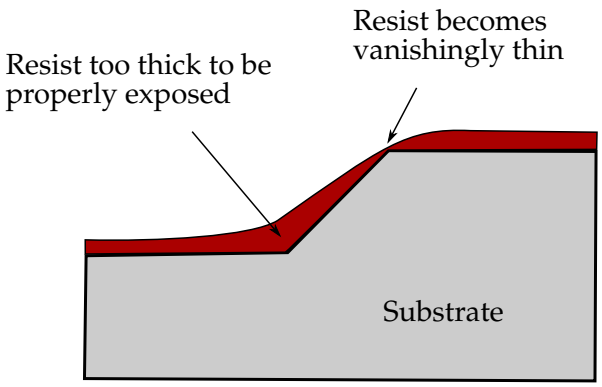

FIGURE 3.9: Diagram highlighting the resist profile resulting from spin coating over a topographic feature. The resist gathers at the base of the feature, and becomes very thin at the upper edge.

3.6 Prior Art at Glasgow

3.6.1 Ebeam lithography on micromachined substrates

Glasgow University has been involved in the development of integrated sensor AFM probes since the early 1990s. The group's novel contribution to the field was the integration of electron beam lithography with standard Si micromachining processes to create a robust technology platform for the batch fabrication of integrated sensor AFM probes with various sensors located at their apices. As has been previously argued in this chapter, the ability to repeatably batch fabricate probes at the wafer scale is of great importance when developing metrological devices. Similarly, through the examples of the various SThM probes presented in this section, it is reasonable to conclude that a probe that is intended for thermal imaging should have a sensor which is both small (order of magnitude of the contact radius [30], and aligned to the tip. While these criteria are met by the novel 'capped probes' of Oesterschulze et. al, these devices rely upon complex fabrication procedures which are unique to each device type. The ability to perform lithography on AFM probes allows for flexible pattern transfer of a variety of sensors simply by changing the pattern. However, the as has been remarked upon throughout this Chapter, patterning sensors onto AFM probes (especially the tips) is non trivial. As a review;

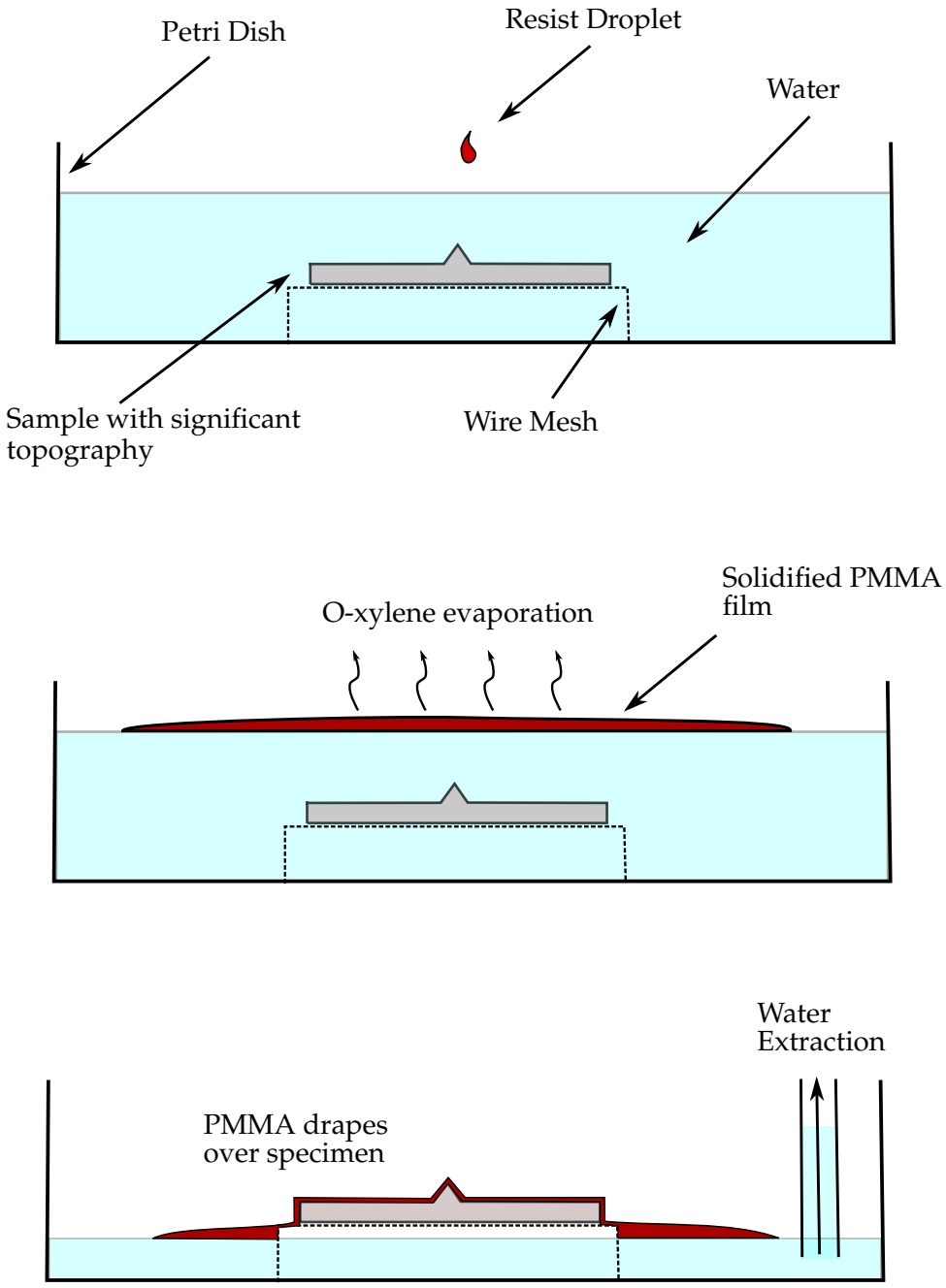

FIGURE 3.10: Diagram highlighting the process of float coating a wafer with significant topographic variation. The sample is submerged in cool water. A drop of resist is added, and the solvent is slowly evaporated, leaving a thin film of resist. Water is then extracted, resulting in a thin film of solidified resist which drapes over the sample, covering any topographic features

- Freestanding contact mode cantilevers are too mechanically fragile to withstand spin or spray coating of resist [31]
- Even before releasing the probes, spin coating (the typical method of resist application) does not properly coat the raised features the AFM tips (Figure 3.9). The non-uniformity resist thickness introduced by these features results in a variation in the critical dose of the resist, which severely diminished process latitude.
- Structures and device defined before release need to be compatible with the cantilever release etch which may be quite aggressive, since a lot of substrate material needs to be removed.

The innovation allowing the group to avoid such issues is termed 'float coating', and involves draping a solidified resist film over the top of the raised features. Figure 3.10 presents the principle of the technique. By combining spin and float coating, it was possible to ensure complete coverage of the AFM pyramids and perform direct EBL patterning on them for the first time [160].

Applications

An early application of this technique was for the EBL definition of the aperture in SNOM. Zhou et al. presented such probes based upon a SiN cantilever. The fabrication of the tip is similar of that of Figure 3.4 for the pyramid formation. The etch is stopped before completion, leaving the pyramid with a flat top. The mask is stripped, and a second thin film, either SiN or SiO_2 is deposited. Atop this is deposited the metal cladding of choice, (such as palladium [161] or aluminium [162]). E-beam resist is applied to the samples with a combination of spin and float coating applications, and the exposure and development are performed. The apertures are then etched into the metal films using dry etch with the ebeam resist as a mask. The specifics of the fabrication procedure change between publications as the technology progressed, but this is sufficient to describe the general principle. When compared with the other methods of creating aperture SNOM probes (see Section 3.4.4), this approach has the following advantages;

- Batch fabrication compatible, unlike FIB.
- Highly reproducible shape and location on the top, therefore throughput between probes is consistent.
- Arbitrary size and shape (others can only do circles or polygons defined by etch planes) [162]

Limitations

Alignment

A limitation of the electron beam lithography method was discovered when considering the accuracy of registration between device layers. Since electron beam lithography relies on automatic alignment after finding marker blocks, the accuracy is limited by the quality of the markers and the registration algorithm's handling of that data. The first lithography step must include the markers which will be used in all subsequent steps; in this case that means they are etched into the substrate during the pyramid level. The requirement for another film (SiO_2/ SiN) to be grown after the pyramid layer means that it is not possible to simply put down high resolution metal markers in the first step, since it is not permitted to contaminate the growth furnaces with metals. The alignment issues which result from these sub-optimal markers have persisted to the outset of this work, and are addressed in further detail in Chapter 5, where a method to combat this issue is discussed.

Non-uniform thickness

Although capable of mitigating some of the issues with spin-on deposition, float coated resist films typically features defects such as wrinkling and tearing, as highlighted in Figure 3.11. Tearing occurs infrequently enough to be tolerable, whereas wrinkling poses a more serious limitation. Local thickness variations of three times the nominal value require significant overdosing to ensure feature clearance. As above, this condition restricts minimum attainable line-width.

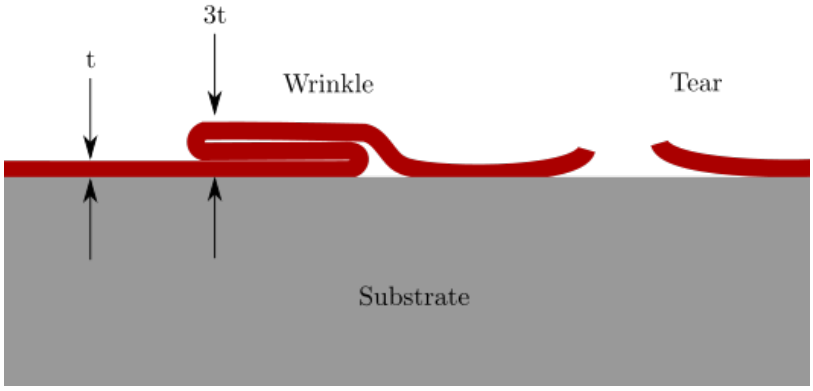

FIGURE 3.11: Graphic highlighting the common defects arising from the float coating technique. Wrinkling of the resist as the solvent evaporates results in a local thickness variation of three times the nominal thickness. Occasionally, the film may tear during processing leaving areas of no coverage.

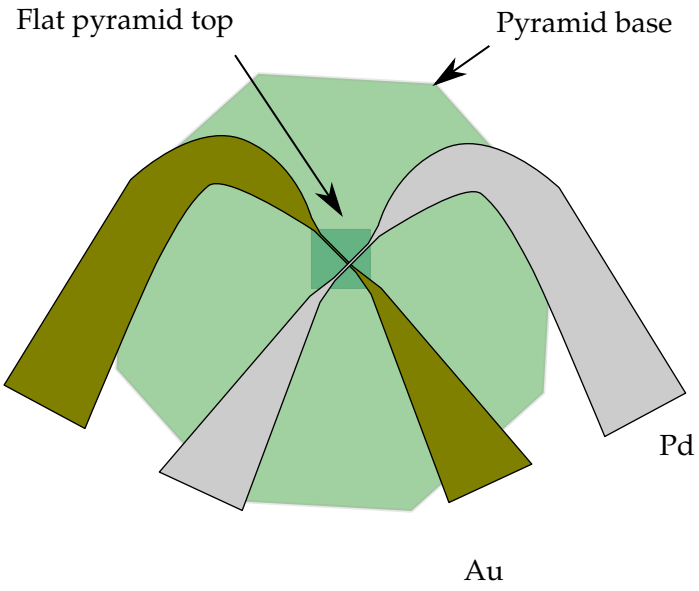

FIGURE 3.12: Drawing of the misalignment-tolerant cross thermocouple probe tips presented by Mills. The flat top is highlighted in darker green. Ebeam lithography and metal lift off are used to pattern the gold, and palladium layers, with the thermocouple junction being formed at their point of intersection. Each layer requires its own alignment operation which may result in some misalignment, however as long as both wires cross the pyramid a junction of the correct size will be formed.

Application to SThM

The first SThM probes fabricated by the Glasgow group employed the same generic substrate and resist stack as the SNOM probes described above. They were flat-apex, 'cross-thermocouple' probes, shown schematically in Figure 3.12 [163] . This design took into account the previously-encountered misalignment problems, since a junction is formed regardless of the relative positions of the wires. Failure through misalignment could only occur if either wire was patterned outside of the flat apex, which was rare. Development of these probes uncovered a number of challenges associated with performing lift-off on these substrates and their unconventional resist stack, with particular problem areas being atop the pyramid apex and at the base of the feature where resist would gather. Although float coating allowed for continuous film coverage, the resultant film is highly non-uniform, having thickness that varies from the centre to the edge of the film. Additionally, it varies upon a number of factors such as the droplet size, position, and solvent evaporation rate. A thorough treatment was presented by Rudnicki [164]. Spin coating was employed in conjunction with float coating to ensure the resist was of uniform thickness across the majority of the wafer. Sharp edges present in the pattern would cause tearing, and it was discovered that these should be rounded to encourage peeling off. Additionally, small, isolated features proved difficult to lift-off. Note that sonication is unsuitable for the probes after the back side etch (Appendix A, Step 24) has been performed, since the membrane is too fragile to hold the probes in place throughout agitation.

In the case of the cross thermocouple sensor design, it was possible to extend the wires beyond the slope of the pyramid and onto the flat plane. Here, the resist stack is expected to be more typical and the lift-off profile better defined. Metal lifted off more readily in this region can be used to initiate 'tearing' that propagates all the way to the tip. This approach is not appropriate for all devices however, since design restrictions may limit the flexibility in feature placement. In Chapter 6 of this work, we detail difficulties with this lift-off similar to those discovered here and how they were addressed through design changes. In Section 5.3 we outline work performed to improve the focus of the beam in an attempt to improve the lift-off

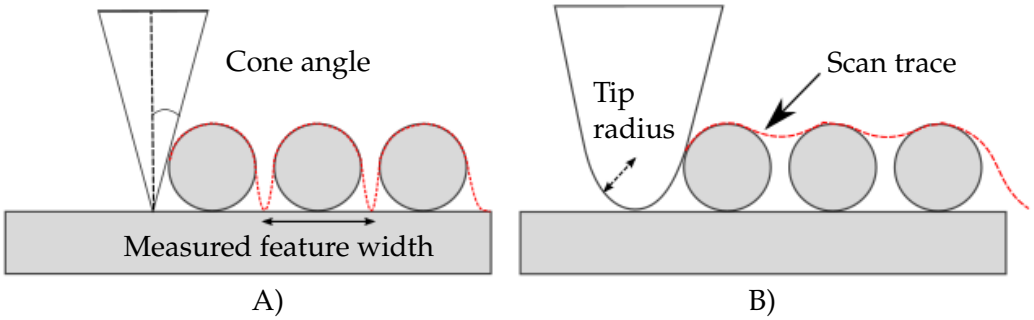

FIGURE 3.13: Diagram highlighting a common artefact in topographic AFM in which a blunt probe cannot fully resolve a high aspect ratio feature.

profile. Note that the non-uniform profile resulting from spin and float coating was considered during this work. A large body of work was performed in an attempt to transition to spray coating of e-beam resist. This is non trivial however, as equipment manufacturers do not support e-beam resist. Additionally, spray coating is typically used for thicker films than are suitable for high resolution electron beam lithography, in which sub-micron films are preferable. It was not possible in the duration of this project to deposit a suitably thin continuous film. A summary of this work is presented in Appendix G

3.6.2 Side Probes and 'Self-Alignment'

The flat apex probes described above proved a useful platform upon which sensors could be patterned. However, their wide opening angle and large tip radius prevents faithful reproduction of the sample topography, due to an artefact termed 'tip-sample convolution'. This is demonstrated in Figure 3.13. In addition to this issue, there is also some ambiguity as to which part of the tip is in physical contact with the sample. This is particularly problematic for thermal probes such as the cross thermocouples described above, as one cannot be sure if the sensor and the sample are in solid contact at any point. To combat these issues, 'improved access' or 'side' probes were developed [163]. These differ from traditional AFM probes in that no pyramid is present on the released cantilever. Instead, the pyramid is used as a sacrificial structure upon which a kink, or beak in the SiN layer is defined. This

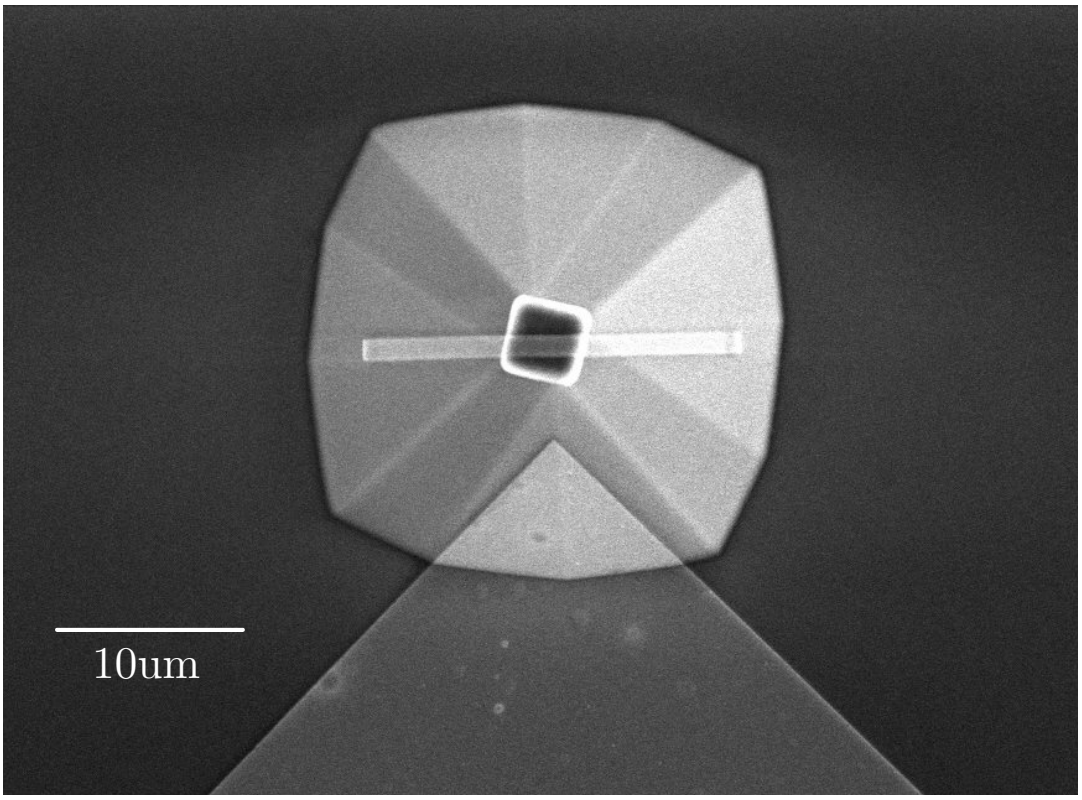

FIGURE 3.14: For 'improved access' probes, the tip is defined on the side of the pyramid. This image shows the NiCr mask which is used to transfer the cantilever into the SiN membrane.

cantilever definition can be seen in Figure 3.14. The cantilever apex is lithographically defined, a feat which is non-typical and necessitates high resolution electron beam lithography.

The pattern defined in EBL is lifted off into a NiCr thin film, which is used as a hard mask to transfer the pattern into silicon nitride through plasma etching. The process is detailed fully in Appendix A steps 25 through 44. The EBL pattern is a 'sleeve' which defines the outline of the cantilever with high resolution. The body of the cantilever is defined with photolithography, in a layer which is aligned to fall within the NiCr outline. Images of this procedure as it pertains to the novel cantilevers developed in this work may be found in Section 6.1.2 Figures 6.4 and 6.5

Sensor definition on these 'side' probes is achieved using EBL and lift-off, in a similar fashion to the cantilever definition. However, the reduced dimensions of the sensor mean that its placement relative to the cantilever level is much more critical than the alignment of the previous level - the cantilever to the pyramid. The earliest

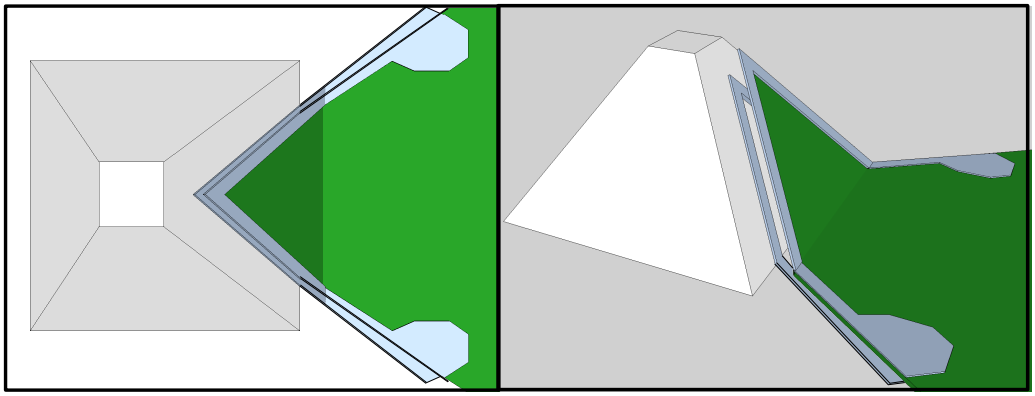

A) Top view B) Three quarters view

FIGURE 3.15: Illustration highlighting the 'self-alignment' principle as it pertains to GU-style 'side' probes. After defining the cantilever in SiN, the pyramid is given a short wet etch to reveal an undercut. The sensor feature is written deliberately larger than required and offset over the edge of the tip. Upon exposure, development and metallisation, some of the metal is deposited on the tip and the rest on the pyramid, however because of the undercut, the two are discontinuous. The deposited metal is always present at the tip, tolerant to any misalignment. This processes is amenable to thermocouple fabrication by employing two individual strips in their own lithography steps.

application of these 'side probes' were in the fabrication of thermocouple probes, in which 'self-alignment' between the metal films and the SiN beak is employed to ensure the junction is always located at the pyramid apex. In the context of these probes, 'self alignment' refers to the logical AND operation between the triangular SiN tip and the deposited metal thin films. The sensor pattern is written such that it overlaps the cantilever and the sacrificial Si substrate. Only that metal which lands upon the cantilever remains after release. By careful design of the EBL patterns, it was possible to reproducibly fabricate thermocouple junctions at the very apex of the side probe. While this strategy of self-alignment ensures that a junction is reliably formed at the wire intersection, a lack of accuracy in their relative positions meant that junction sizes were observed to vary significantly (250 nm $+/-$ 40%).

In addition to self-aligned thermocouple 'side-probes', Mills also presented resistive SThM probes using the same strategy. Rather than two levels of sensor definition EBL however, a single exposure and deposition was required. Figure 3.15 shows how self-alignment was employed in the fabrication of these devices. The central

part of the RTD is always present at the probe apex. Misalignment still occurs, and in these devices is manifest as a variation in resistance since the sensor width is altered by misalignment. A detailed treatment of the causes and implication is this misalignment is given in Section 5.2.3

Dual self alignment

While it is possible to 'self-align', using one edge only, Mills et al also identified the possibility of 'dual self alignment', in which both edges of the sensor are defined by the cantilever edges. This requires introducing a hole into the cantilever tip such that the tip is formed by the union of two beams. Since the beams are written in the same lithography stage, defining their width does not depend on the accuracy of alignment. A blanket metal deposition over these beams will yield a resistor of well defined and highly-reproducible width, completely tolerant to any misalignment between cantilever and sensor definition. The challenge with such a procedure is in the lift off of the bounded features to create the beams. If the hole fails to lift off, the RTDs are at risk of shorting; a critical failure. These devices were described and fabricated in Mills' thesis, but were abandoned shortly after, due to the difficulty in defining holes in the cantilever.

Commercialisation

The devices shown in Figure 3.15 represent the earliest thin-film resistive SThM probes. Since they are microfabricated, their reproducibility is high, when compared to the leading alternative; the Wollaston wire probes. The lithographically defined sharp tips offered greater spatial resolution, and the linear-response platinum resistance thermometer is easily as sensitive. These devices were subsequently commercialised by Kelvin Nanotechnology and have been used in numerous SThM studies in the literature [165]–[170] .

Since only one side self alignment is employed in these devices, their sensor resistance varies. To combat this, temperature insensitive NiCr trimming resistors are integrated into the wires leading to the pads. This increases the resistance of the probes from $100 \pm 50\,\Omega$ to $350 \pm 50\Omega$. The increased resistance ensures compatibility with customer's control circuitry despite any fluctuations in sensor resistance, at

the expense of sensitivity.

In addition to passive mode thermometry, resistive probes may also deliver heat to the sample through Joule heating. By monitoring the resistance of a heated probe as it scans over a sample, it is possible to correlate the degree of heat the sample is able to remove from the probe at a given position. In this manner, it is possible to qualitatively map probe sample thermal conduction, which is related to, amongst other things, the sample thermal conductivity. While this imaging technique is also achievable using Wollaston wire probes, they lack the spatial resolution of these microfabricated alternatives. The doped Si probes discussed in Section 3.5.2, are capable of delivering a great deal of heat, however are hardly sensitive enough to be used for conductance imaging (in air), thanks to the huge volume of heated air, and the lack of resistance at the point of solid-solid contact. The design of the Glasgow probe is such that the hottest, and highest resistance point of the RTD/heater is in direct contact with the sample. However, the thin film construction of these probes means they are less thermo-mechanically robust than monolithic probes, and have been shown to suffer from bi-metallic bending [171].

Thanks to the involvement of Kelvin Nanotechnology with the Quantiheat project, of which this work is a part, the process for the manufacture of the commercial probes has been made available. The process, as it was given to the author at the project's outset, is presented in full in Appendix A. The following Chapter presents a thorough analysis of the operation of these probes as a thermal transducer, considering their suitability for temperature and thermal conductivity imaging. With an understanding of how the probe's design affects it's function, it will then be possible to re-design the probe to maximise its sensitivity, accuracy and reproducibility. While many groups have presented thermal models of this popular probe, none have the capability to alter the design and manufacture of the probes. This presents a unique opportunity to understand and address the strengths and weaknesses of these probes. In support of this, we have developed generic, flexible and fast models to characterise numerous novel designs. The aim is to understand the relationships between certain design features (i.e film thickness) and thermal properties (i.e maximum heater temperature) of the probes, and then to apply this understanding to the

design of new probes, and the quantification of complex SThM measurements.

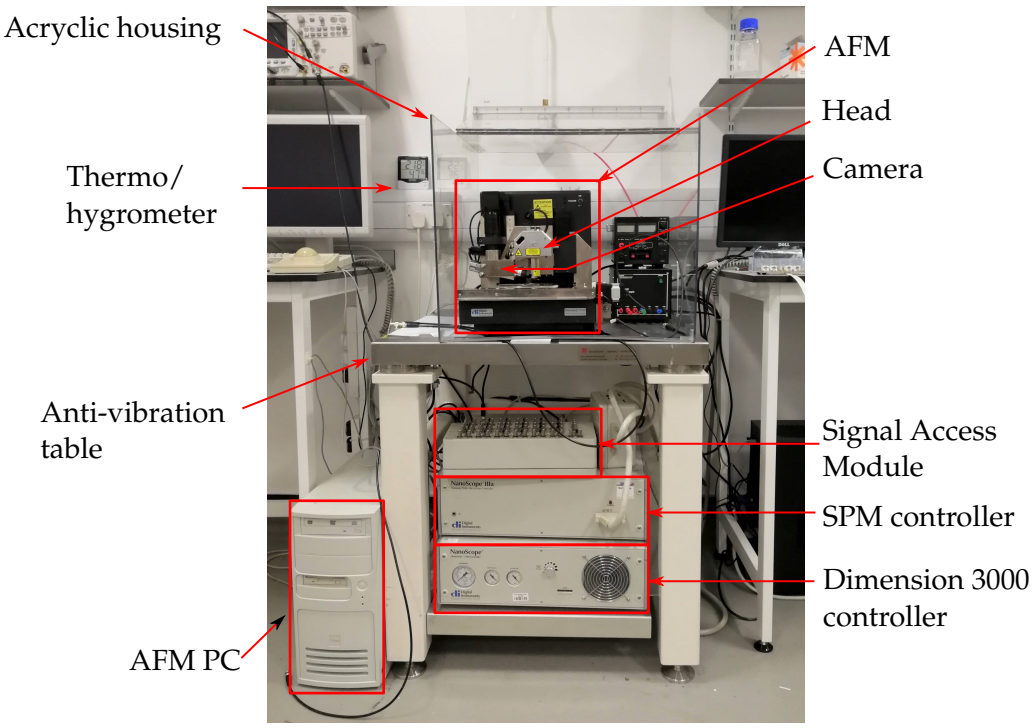

FIGURE 3.16: Annotated photograph highlighting various parts of the AFM used in this work

3.7 Instrumentation and Operation of resistive SThM

3.7.1 The AFM

All AFM data presented in this thesis has been captured using a Digital Instruments Dimension 3100 Atomic Force Microscope, presented in Figure 3.16. The tool is located within our temperature controlled laboratory, and is housed within a clear acrylic cube to reduce any environmental interference. The AFM sits on top of an optical table, to minimise vibration. Underneath the table houses the two microscope controllers, and the signal access module.

This AFM includes no special features for interfacing with integrated sensor AFM probes, therefore the signal access module is required. This box allows users to 'inject' a signal to various channels the AFM. In our case, the properly conditioned probe signal is used to override the horizontal deflection channel, which is used to produce the 'Friction' image in conventional AFM. In this manner, we are able to produce the complete 2D SThM image.

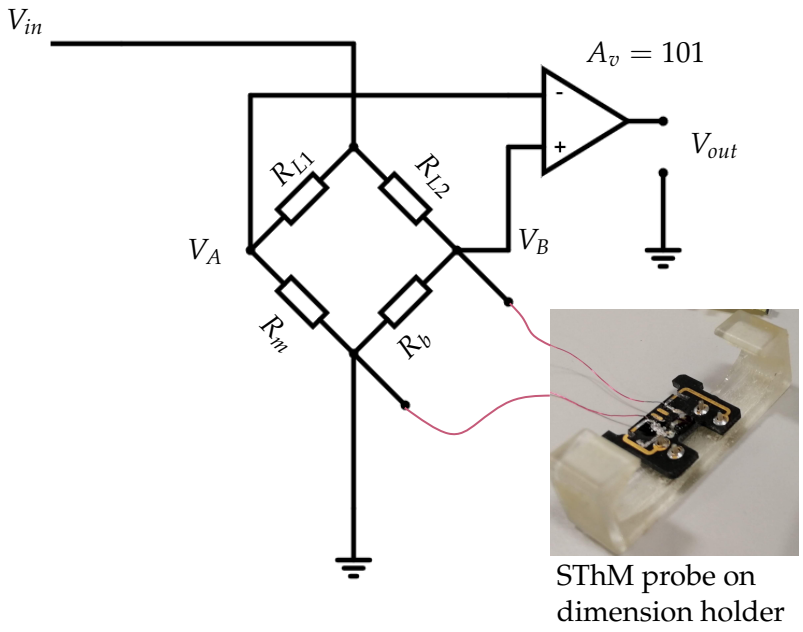

FIGURE 3.17: Simplified diagram of the circuit used to drive the SThM probes used in this work. The pairs of resistors on the left and right form two voltage dividers with voltages V_A and V_B respectively. When the bridge is perfectly balanced, the voltages are equal. Small changes in the probe resistance manifest as a difference between the two node voltages. R_{L1} and R_{L2} are equal. Their value is chosen to be sufficiently high to limit the current to maximum value tolerable by the probe, when the bias is at 5V. R_m is the matching resistor whose value is closest to that of the probe. R_b is the balance resistor, used to reduce the probe resistance sufficiently to match with R_m.

3.7.2 Bridges

The instrumentation required for driving and measuring the output of the probes has been designed and manufactured in-house. A simplified circuit diagram showing how this has been achieved is presented in Figure 3.17. The probe's resistance - temperature variation is typically on the order of $0.1\,\Omega\,\mathrm{K}^{-1}$ [172], therefore a Wheatstone bridge has been employed to accurately measure the small resistance variations. A low-noise instrumentation amplifier [3] with gain of $\times -101$ has been employed to increase the signal amplitude.

To facilitate simple, error-free bridge resistor calculation, a simple program was developed[4]. When provided with the probe resistance and desired maximum current,

[3] Analog Devices AD8429, `https://www.analog.com/media/en/technical-documentation/data-sheets/AD8429.pdf`

[4] Available as part of the 'SThMpackage' software available on GitHub: `https://github.com/RL-AFM/SThMpackage`

the software will return values for all necessary resistors. The layout of the circuit board is such that R_m should be chosen as the closest resistance **below** that of the probe. The resistance of the probe branch of the Wheatstone bridge is then reduced by the parallel sum of the probe and R_b. The program features a lookup table of E96 (1%) or E192 (0.1%) preferred value resistors so only available values of resistance can be chosen. The advantage of using fixed resistors over a potentiometer is increased accuracy and stability. The limiting resistors are calculated based upon the desired maximum current. A simple, battery-powered variable 0 to 5V isolated power supply was designed to drive the probes when using DC. Therefore, the maximum current was chosen to occur at 5V DC. The software calculates the limiting resistors using Equation 3.1:

$$R_{lim} = \frac{5V}{i_{max}} - R_p \tag{3.1}$$

The output of the circuit V_{out} in Figure 3.17 may be observed using a voltmeter or oscilloscope, and may be fed directly into the AFM's signal access module.

3.7.3 DC and AC/Lock-In detection

DC

In the passive mode of operation, probe temperature is frequently the reported measurand, and is arrived at through the conversion of probe signal to a temperature, achieved through calibration. This process is described in Section 3.7.5. In the active mode however, results tend to be reported in a fractional measure of the probe's initial signal, be that in terms of power, resistance, or voltage. Calculation of probe resistance from bridge output is trivial when the bridge resistances and bias voltage are known. The relationship is given in Equation 3.2, which may be used to convert datasets from voltage to resistance values. Note that Equation 3.2 assumes raw bridge output, therefore care must be taken to divide through by any gains performed by amplification circuitry. Power conversion is then i^2R, which is again known if the bridge resistors and bias voltage are known.

$$\left(\frac{R_1}{\frac{V_{out}}{V_{bias}} + \frac{R_1}{R_1 + R_m}} \right) - R_1 \tag{3.2}$$

3.7.4 AC

In active mode SThM, it is possible to increase the probe's sensitivity, and to remove the effects of ambient temperature drift and amplifier $1/f$ noise through the use of AC bias and lock-in detection. This is known as the three-omega (3ω) mode of SThM. In this setup, the probe is driven with some frequency, ω which results in periodic Joule heating at frequency 2ω. The multiplication of this 2ω resistance change with the 1ω current results in a voltage that contains a 3ω component. Monitoring this third harmonic is achieved through lock-in detection, and its isolation means that only changes in amplitude at this frequency are measured. Electrical drift or ambient temperature variation affect DC measurements, but because these phenomena do not occur at the specified frequency, they are discarded from the 3ω measurement. A further derivation of the 3ω mathematics is given in Appendix B

3.7.5 Probe TCR calibration

Conversion between probe signal and temperature requires some form of calibration to compute the probe's Temperature Coefficient of Resistance (TCR). The temperature - resistance relationship is shown in Equation 3.3:

$$R(T) = R(T_0)(1 + \alpha(T - T_0)) \tag{3.3}$$

in which R is the probe's resistance, T is the probe's temperature, with the zero subscript indicating room temperature, and α is the probe TCR. This calibration method relates the probe's resistance to the temperature changes it experiences. Some care must be taken when using this TCR value, as this is only valid for the case where the entirety of the probe's sensor changes homogeneously. This is a valid assumption for scanning large heated areas, but less so for small heated regions or active probe experiments. The calibration procedure as it is performed in our lab is presented in Figure 3.18

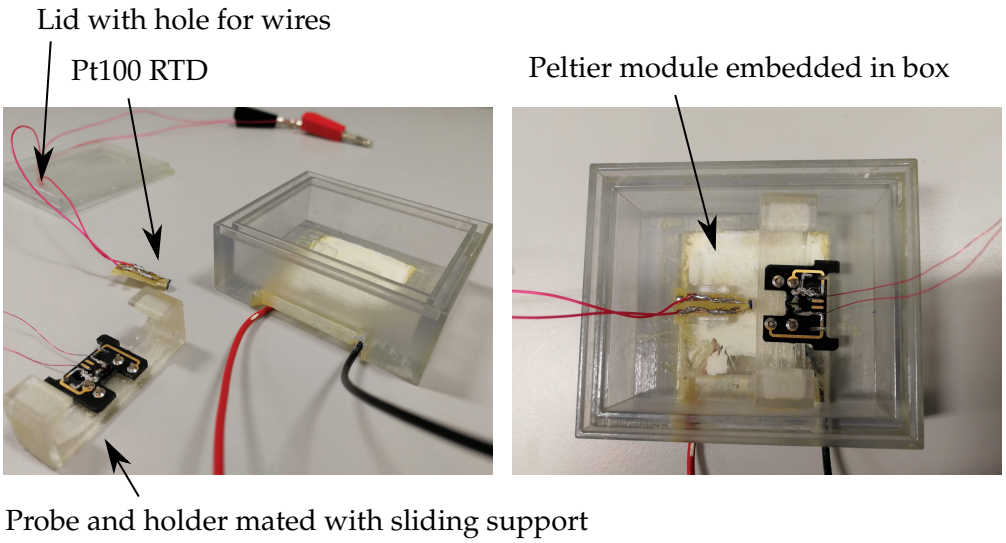

FIGURE 3.18: Photographs of the 3D printed enclosure used for probe temperature calibration. The enclosure is designed to hold a small (<50ml) volume of Flutek PP3, a chemically inert liquid with high ($60.4\,\mathrm{W\,m^{-1}\,K^{-1}}$) thermal conductivity and electrical resistivity. Because of its thermal conductivity and small volume, the liquid thermalises very quickly. Submersion in liquid ensures the entire probe is at uniform temperature. A Peltier module is recessed into the bottom of the enclosure, which has been made as thin as possible to ensure rapid thermalisation. A PT100 temperature sensor may be affixed into the enclosure using a T-shaped PCB and an inversely shaped female end in the enclosure. Because there is some risk of breaking probes during scanning, it is preferred to complete a body of work with the probe before calibrating. As such, probes for calibration are already bonded onto dimension holders. The enclosure includes a 3D printed sliding support with pins whose size and spacing matches that of the Dimension AFM. This allows the probe to be mated with the support outside of the enclosure before being inserted and slid into close proximity to the PT100 for accurate temperature calibration

Immersion of the probe in a small volume of fluid is intended to ensure that the entirety of the fluid, and thus the sensor, is isothermal. Therefore, the probe's resistance change is the result of the change in the uniform temperature across it's length. While this is a sensible approach considering the definition of TCR, this metric must be employed with caution when trying to calibrate probe output. Unfortunately, this procedure of immersion in uniform temperature fluid hardly mimics any of the probe's typical operating regimes. It may be somewhat appropriate for the situation in which the probe is scanned over a large heated region in ambient, such that the sample is able to heat the air surrounding the probe's sensor to a roughly uniform temperature. More often however, the temperature distribution of the probe is non-uniform across its length. Non uniformity may arise through probe self-heating, or through local heating of the sensor apex due to solid-solid conduction from a heated sample. In such cases, the TCR is not a valid conversion method, since the probe's resistance change is not the result of a uniform temperature change. [173]. Non-uniform heating and sensing is a key topic of this thesis, and is discussed in particular detail starting at Section 4.8.1. In particular, let us highlight that the assumption of uniform temperature distribution becomes more egregious for probes whose sensors span a larger area.

In this work, we have been careful to avoid any claim to the probe's absolute temperature in any of the experimental work. It is always more accurate, and often more appropriate to discuss the probe signal change, since this is the only metric which the probe is able to provide without a more robust calibration.

In leiu of a more representative method, isothermal fluid immersion has been employed in our lab, and has been found to be useful first approximation for probe TCR.

3.7.6 Image capture and post-processing

Images are gathered in the AFM using the nanoscope software, however this is not used for post-processing and analysis. For this work, the open source alternative, Gwyddion [174] was used due to the availability of information on all the algorithms

used[5]. The processing of SThM images requires careful consideration. A simple example highlighting the importance of this is that of tilted data. When considering topographic data, tilt is simply the physical tilt of the sample. This contains no useful information, and reduces the contrast of the features of the image, so tilt in this channel can safely be removed to produce a more useful image. When considering a thermal scan however, any apparent 'tilt' is the result of a systematic electrical or thermal variation and this should be understood before deciding whether or not to filter it from the image.

[5] http://gwyddion.net/

Chapter 4

Probe Characterisation and Model Development

4.1 Unpacking the SThM measurement

The SThM probe is a thermal transducer which converts the average temperature across its sensitive element into an electrical signal. The relationship between the probe output and the nanoscale thermal phenomena to be measured is not simple however. The sensor temperature is defined by several factors, including, but not limited to, those listed in Table 4.1. This is not problematic in and of itself, however, issues arise due to the fact that the probe's output does not contain any information about **which** effect has caused the temperature disturbance. To this end, one cannot make the distinction between 'useful' and confounding contributions to the thermal system. This prevents quantitative measurements, which is the aim of every metrological measurement.

Experimental factors
• The power supplied to the probe
• The temperature of the sample
• The ambient temperature and humidity
• The contact resistance between probe and sample
• The thermal conductivity of the sample
• The thermal resistance of the probe
• The probe - sample separation

TABLE 4.1: Selected experimental factors impacting probe output

A particular challenge to the formulation of a simple relationship between tip temperature and sample thermal measurements is the variety of ways with which the probe may thermally couple between the sample and the environment. This coupling is the result of the fact that it is very difficult to constrain the flow of heat. It travels not only through solid materials and interfaces between solids, but also flows freely through surrounding fluid mediums such as water and air. Consider that the difference between thermally insulating and conducting materials is about three orders of magnitude. This is in contrast to electrical flux, for which there is a distinct (20 order of magnitude) difference in the conductivity between insulating materials and conductive materials [175]. This example illustrates why it is so difficult to design an SThM system in which all the heat fluxes are constrained. This is especially true of experiments performed in ambient conditions. We observe that the thermal conductivity of air (k=0.024 $\mathrm{W\,m^{-1}\,K^{-1}}$) is only one order of magnitude lower than that of solid PMMA (k = 0.187 $\mathrm{W\,m^{-1}\,K^{-1}}$), a material which we have probed during this work), yet air surrounds the probe! The thermal confinement problem is not limited to coupling through fluids either; it also results in unintended and parasitic fluxes, such as the transfer of heat through the cantilever to the base of the chip.

Any thermal fluxes that are not accounted for will act as confounding variables to the measurement. Therefore, it is evident that the full network of thermal transfer routes should be described, and quantified, if quantitative measurements are to ever be performed.

Figure 4.1 presents a diagram of the multiple heat transfer mechanisms that exist between the probe and sample. The complexity of this system is such that its characterisation is non-trivial and quantification of the heat flux along any route is challenging. To this end, many in the field have utilised the thermal-electrical analogy to leverage the circuit diagrams employed in electronic engineering, and use them to describe equivalent thermal systems [26], [132], [138], [165], [176], [177]. With this approach, the different routes of thermal transport are transformed into 'branches' of an electrical circuit, with the opposition to these fluxes being represented by appropriate thermal resistances. If enough of the thermal resistances, temperatures or heat fluxes are known, it is possible to solve the network for the remaining unknowns. In

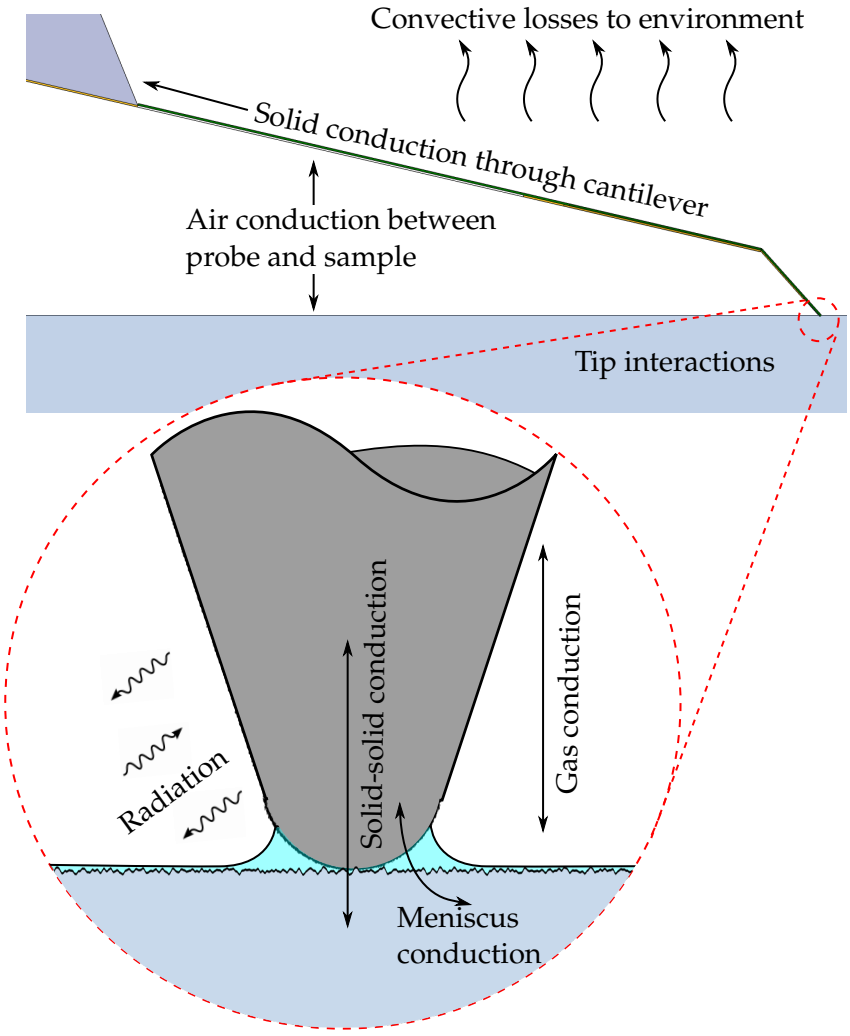

FIGURE 4.1: Schematic diagram indicating the many heat transfer routes between the probe, sample, and environment. Double headed arrows indicate that heat transfer can occur in either direction, depending on which is the hotter body.

the following sections we will discuss why this approach is favourable, before presenting an in-depth representation of the SThM thermal network as it is presently understood. With a detailed thermal network established, we will be able to more clearly explain the specific problems in SThM scanning that the work in this Thesis aims to address. Since it is our aim to design and fabricate an improved SThM probe, this network will help to communicate what would constitute an improvement; and how such improvements may arise.

4.2 Thermal-resistance modelling background

4.2.1 How a thermal-resistance model is constructed

Systems involving potentials, flows and resistances may be found in many fields. In each case, the flux is driven by a potential, and the opposition to a flux is affected by the geometry of the medium through which it flows. In structural mechanics, a displacement (potential) results in a load (flux), whose magnitude is influenced by the stiffness (conductance) of the medium. Similarly, in fluid dynamics, a pressure (potential) drives a flow rate (flux) with a rate determined by the resistance of the pipe through which it is being transferred.

When compared with the examples presented above, we note that electronics has received the greatest attention in the field of network analysis. The rapid scaling of components in micro-electronic circuits has driven demand for sophisticated computer aided simulation methods. Notably, the development of software suites built upon SPICE (Simulation Program with Integrated Circuit Emphasis) [178] simulations has been particularly impactful [179]. In addition, members of the scientific community typically have a working understanding of circuit diagrams and simple circuit analysis techniques. This makes the electrical analogy an attractive candidate for both communicating and evaluating networks in the thermal domain. This appeal is evidenced by a wealth of examples of thermal-electrical networks throughout the literature [33], [138], [153], [159], [170], [180], [181]. It should be noted that their use is by no means limited to SThM studies [182]–[184]

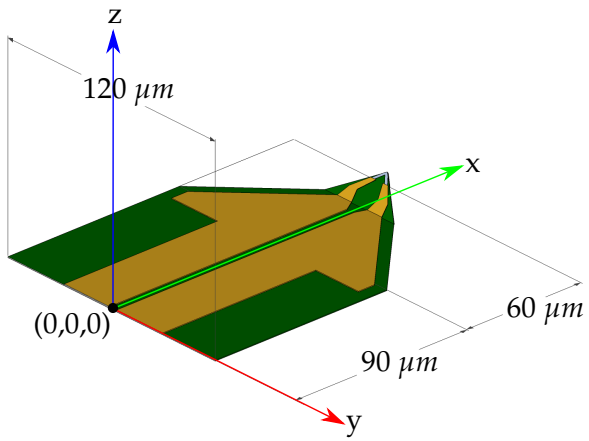

FIGURE 4.2: Schematic highlighting the co-ordinate system used to refer to the probe. We define the x direction as 'length', the y direction as 'width', and the z direction as 'thickness'. The probe thickness is 400nm, which is significantly smaller than the its extent in the other two dimensions.

The challenge in creating a thermal-resistive network for SThM concerns the correct representation of the resistances associated with the various modes of heat transport. In this section we will outline the relevant mathematics required for such transformations, alongside any assumptions which must be made to perform them.

4.2.2 1D conduction in solids

Conduction is the mode of thermal transport most prevalent within solid materials and between solids in thermal contact [185]. How easily thermal transport occurs within a material is dependent upon its thermal conductivity, which is an intensive material property. An object comprised of a particular material may be described in terms of its thermal conductance, which accounts for how the dimensions of the object influence its ability to conduct heat. This is an extensive property which is often reported in terms of its reciprocal; thermal resistance. Thermal resistance therefore is defined as the ratio of a temperature difference to a resulting heat flux. For materials of certain dimensions, it is reasonable to assume that conduction occurs in only one direction. This approach is valid when the dimensions of the object in question are such that the resistances across two of the object's dimensions are small when compared with the third [186]. In such systems, the temperature is considered uniform across two of the three dimensions. The spatial variation of temperature is then fully

described by one coordinate alone. In this work, the length, or x co-ordinate (see Figure 4.2) is chosen as the dimension across which temperature variation occurs.

Thermal probes such as those used in this work are 'thermally-thin' objects which are well-suited to description with 1D thermal conduction models [153], [176]. This assertion is validated by their having a Biot number far less than 0.1 [187]. When this condition is met, the assumption of a uniform temperature distribution is reasonable [185].The Biot number is a dimensionless quantity which is calculated using the following relation;

$$Bi = \frac{hL_c}{k} \tag{4.1}$$

Where h is the heat transfer coefficient of convection from the object's surface, k is the thermal conductivity of the object in question, and L_c is the characteristic length of the object, typically defined as the ratio of the object's volume to surface area [185]. For the probes used in this work, the Biot number is always far lower than 0.1, typically on the order of 10^{-8}.

In the following sections, diffusive heat conduction is discussed. However, it should be noted that in mesoscopic length scales, heat conduction through ballistic heat carriers becomes of importance. In this regime, heat carriers travel through the medium experiencing negligible scattering interactions, and therefore no temperature gradient within the medium may be observed. Ballistic transport occurs when the mean free path of the heat carrier is greater than the dimensions of the medium. The relationship between the two is quantified by the Knudsen number (Kn), which is defined as the ratio of the former to the latter. When $Kn << 1$ diffusive transport may be assumed and the influence of ballistic contributions omitted. The mean free path of phonons in SiN has been shown to be less than 2nm [188], which is two orders of magnitude smaller than the minimum characteristic dimension that has been considered in this work. The model developed in this work and outlined in this chapter is intended to be indicative of gross changes imparted by significant probe re-design. Beyond that, FEA tools with more advanced thermal transport models should be considered.

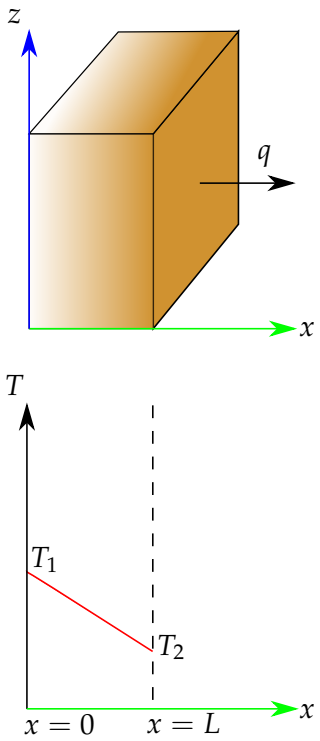

FIGURE 4.3: A plane wall constructed from homogeneous material. Heat flux, q, travels along the x direction. There is a linear gradient between temperatures T_1 and T_2

4.2.3 Derivation of 1D conduction

Under classical conditions, thermal conduction within a homogeneous body is governed by Fourier's Law [189];

$$\mathbf{q} = -k\nabla T \tag{4.2}$$

where $\mathbf{q}$ denotes the heat flux density ($\mathrm{W\,m^{-2}}$), k is the material's thermal conductivity ($\mathrm{W\,m^{-1}\,K^{-1}}$) and ∇ is the differential operator.

When considering 1D heat conduction, Equation 4.2 reduces to [185];

$$q = -kA\frac{dT}{dx} \tag{4.3}$$

In which q is the scalar heat flux, A is the cross section of the material orthogonal to the direction of heat flux, and $\frac{dT}{dx}$ is the rate of change of temperature along the x

direction.

In the case of a homogeneous material with uniform cross-section and thermal conductivity, exhibiting no internal heat generation, the temperature gradient across the object is linear [185]. Figure 4.3 shows a one-dimensional plane wall, which is an example of such an object. In this specific case, Equation 4.3 may be further reduced to [185];

$$q = -\frac{kA}{L}(T_2 - T_1) \tag{4.4}$$

Where L is the wall's length in the x direction, and T_1 and T_2 represent the temperatures at the left and right faces of the wall respectively. A schematic representation of this relationship is presented in Figure 4.3

As stated previously (Section 4.2.2), a resistance is, by definition, the ratio of a potential to a flux. Therefore, we can state the thermal resistance of 1D conduction in solids through the re-arranging of Equation 4.4:

$$\frac{T_1 - T_2}{q} = \frac{L}{kA} \equiv R \tag{4.5}$$

In which R denotes the thermal resistance of conduction through this object.

4.2.4 Composite plane walls and contact resistance

The 1D plane wall analogy has provided a method of calculating the thermal resistance of a single homogeneous material. Like their electrical counterparts, thermal resistors may similarly be arranged into a network in series or parallel arrangements. An example of when such a network may be used is presented in Figure 4.4, which shows a composite wall structure containing 4 distinct materials in thermal contact. The manner in which these materials are arranged with respect to the direction of heat flux defines their representation. Those which are butted against one another normal to the x direction may be treated as series resistances. Laminate materials, which are 'stacked' one atop the other, are represented as parallel thermal resistances. Recall that for the 1D thermal model employed here the laminated materials

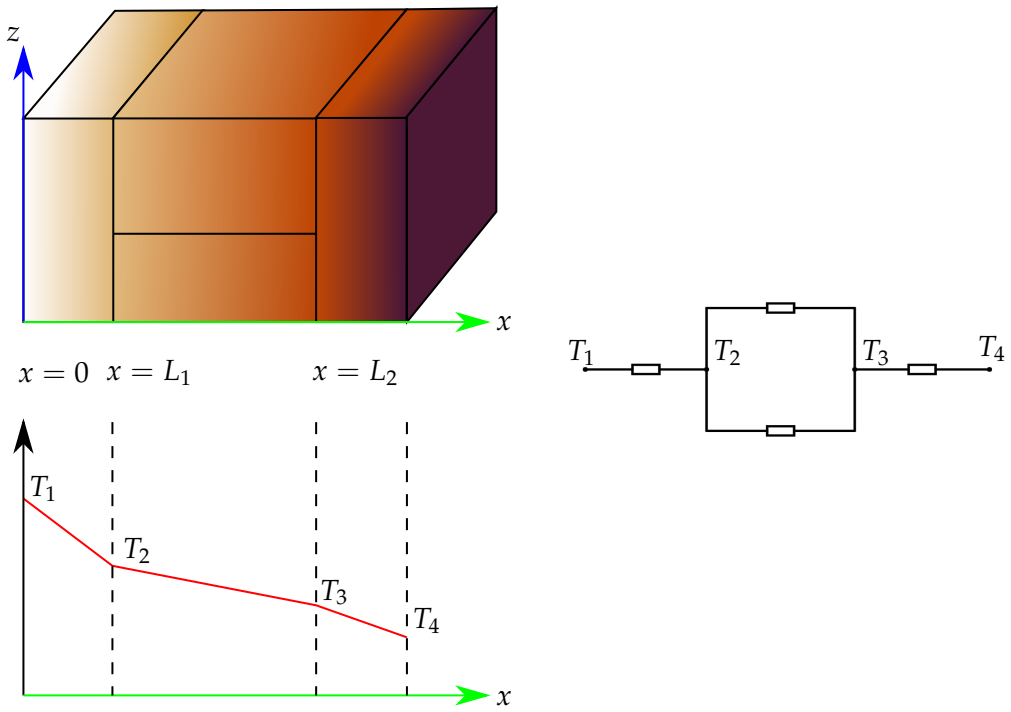

FIGURE 4.4: A series-parallel composite wall and its thermal circuit equivalent.

must be isothermal by definition, since heat may only flow in the x direction and they are stacked in z.

The validity of the composite plane wall system is conditional upon the assumption of perfect thermal contact between the adjacent materials. This assumption is predicated upon two factors; perfect mechanical coupling, and exact phonon coupling [186]. For all real surfaces, there exists some degree of roughness which precludes perfect mechanical contact. Rather, the joint is comprised of many nano-contacts; the number and distribution of which is dependent upon factors which include the pressure exerted upon the joint, the compliance of each material and the roughness of each surface [28]. In addition to conduction through the multi-asperity solid-solid contact, heat transfer also occurs through conduction through the gaps, for example through air in ambient conditions. The contact resistance is then the sum of the parallel contributions of the solid-solid condition and the conduction (or radiation) through the medium. It is typical to represent this resistance as an additional resistor in the thermal network at the interface between the materials, as shown in Figure 4.5.

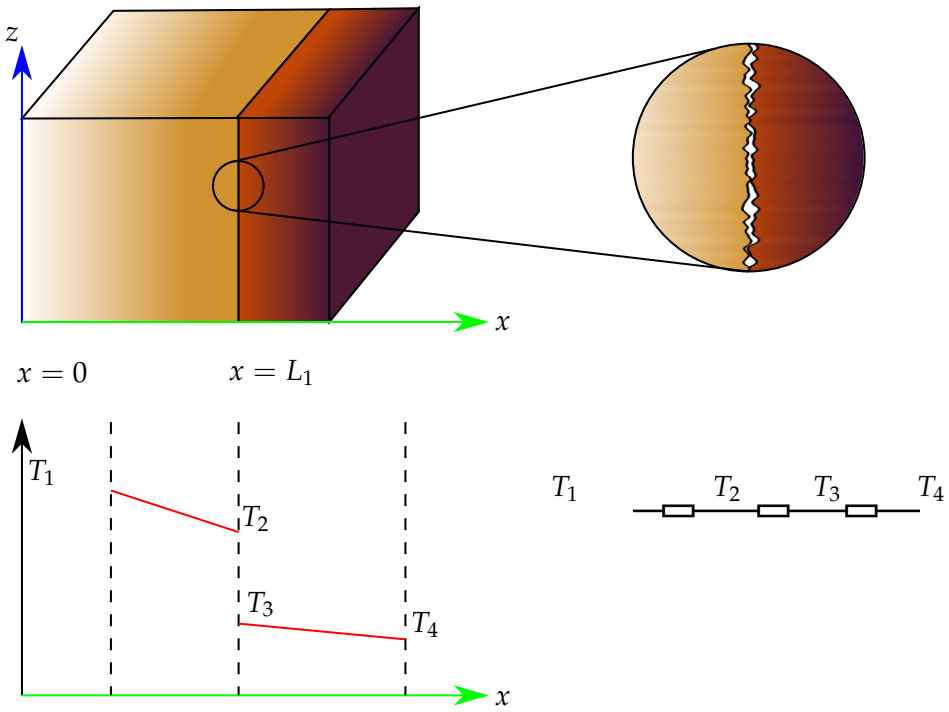

FIGURE 4.5: A contact resistance, R_c is present between the two materials which comprise this composite plane wall. It occurs due to lattice mismatching and nanoscale roughness on the sample surfaces. It results in a temperature drop at the boundary between materials.

Boundary Resistance

Thermal boundary resistance, also known as Kapitza resistance, R_b, has been observed between well thermally coupled materials [190], and is thought to arise due to differences in the atomic structure of the materials in contact. Phonons propagating through a regular crystal lattice are expected to encounter some impedance mismatching when crossing the boundary into materials with a dissimilar lattice period [177]. Two models have been developed to describe the thermal boundary resistance, each making different assumptions about the type of the phonon scattering that occurs [191]. The Acoustic Mismatch model (AMM) assumes specular reflection and transmission, while the Diffuse Mismatch model (DMM) assumes diffuse reflection. These differences result in each model being more appropriate at different temperatures, with the former being better suited to temperatures of < 10 K where specular scattering is more likely [192].

In this work, we use contact resistance, R_c, to refer to a single resistance which encapsulates the contributions from both phonon boundary scattering and the small contact area. It should be noted that this quantity is difficult to predict, so tends to be measured experimentally [28]. One reason why these terms are often grouped together is that the 'true' contact area is not possible to measure experimentally [28], therefore the two cannot be dis-entangled. In Section 4.3.4, we detail how contact resistance is treated in the specific context of SThM measurement.

Note that in the 1D thermal model, contact resistances between materials which are stacked perpendicular to the axis of heat flux (such as the central materials in Figure 4.4) are disregarded, since all layers are assumed isothermal.

4.2.5 Spreading and constriction resistances

The 1D thermal conduction model presented in this chapter is a suitable representation of heat flux through the probe, since the dimensions of cantilever structures are a reasonable approximation to a 1D system. However, it is not appropriate to employ a 1D model for the representation of heat transfer from a heated probe into a sample. To this end, we employ the familiar 'spreading resistance' calculation [26], [188], [193], [194], which represents this probe-sample heat-sinking with a single thermal resistance, that can easily interface with the rest of the 1D model.

Spreading resistance describes the resistance associated with the diffusion of heat into or out of an isotropic half-space, that is, a homogeneous solid whose dimensions are much greater than the characteristic length of the heat source. In this description, the free surface of the half-space is considered a perfect insulator apart from the source region, and is therefore adiabatic [194]. Whether the resistance is termed a 'spreading' or 'constriction' resistance depends upon the direction of the heat transfer with respect to the half space. Spreading resistance is used when heat flows into the half space and spreads out, while constriction describes transfer in the opposite direction; out of the half-space through the aperture-like opening [195].

As with all the prior resistances discussed, thermal spreading resistance is the quotient of a temperature gradient and a heat flux;

$$R_s = \frac{T_{source} - T_{sink}}{Q} \tag{4.6}$$

In which T_{Source} is the temperature of the source which is in thermal contact with the free surface of the half space. T_{sink} is the thermal sink temperature. Since the sink area of the half space is much larger than the source area, it is assumed isothermal. The heat transfer rate, Q, is dependent upon the type of contact between the source and half space, and is described in the general case in [194]. The specific case as it applies to SThM is detailed in Section 4.3.4 of this thesis.

4.2.6 Thermal resistance of convection

The thermal resistance representation is not only applicable to conductive transport. For example, Newton's law of cooling (Equation 4.7), which describes the heat loss of a body to its environment due to convection, may be rearranged similarly to yield a thermal resistance [185];

$$q = hS(T_s - T_{env}) \tag{4.7}$$

Where h is the heat transfer coefficient of the fluid environment, S is the surface area of the heated object which is exposed to the fluid, and T_{env} is the ambient temperature of the fluid, which is considered a heat sink. Re-arranging this equation yields the thermal resistance of heat transfer of this type;

$$R_{th,conv} = \frac{T_s - T_{env}}{q} = \frac{1}{hA} \tag{4.8}$$

Constructing a thermal resistance in this manner allows us to model the heat transfer from the surface of a solid to the environment through convection. The thermal resistance analogy allows the option to include this mode of thermal transport alongside the chain of resistors representing one dimensional conduction within the probe.

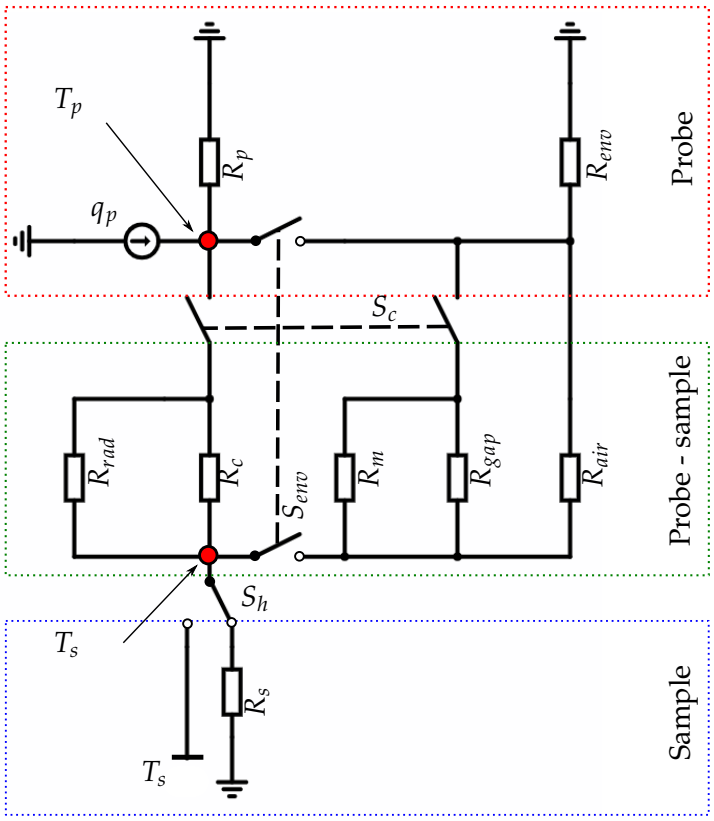

FIGURE 4.6: The full thermal-electronic equivalent circuit for the SThM probe-sample-environment network

4.3 The thermal resistive model of SThM probe - sample - environment interactions

4.3.1 Introduction: typical thermal resistance networks

Thermal resistive networks are commonly employed in SThM studies [138], [153], [159], [170], [180], [181], [196], however the number of components present in each network is different depending on the study being performed. For example, when studies are performed under vacuum, it is reasonable to discard resistances associated with air conduction or convection.

For the purposes of fully describing the network, we present here an equivalent circuit that may be used to describe the operation of the SThM probe in any environment, in any operating mode. The thermal circuit shown in Figure 4.6 features all of the routes for thermal transport between the probe, sample and environment, with their inclusion or isolation being controlled by switches. In this Section, we

will describe each element of the circuit and its significance to the measurement, before using this circuit to demonstrate the operation of the probe in a few common configurations.

4.3.2 Temperature Nodes

Temperature nodes are the analogue of voltage nodes in the thermal electrical analogy. In Figure 4.6, nodes of particular importance to the SThM system have been annotated and highlighted in red. These nodes are point measurements intended to describe the temperature at various locations throughout the system. Note that real systems may be more appropriately represented by a temperature distribution. However, the system is composed of a discrete set of elements having common thermophysical properties (i.e, probe, sample, environment), so a discrete lumped model is a natural and intuitive approximation.

Probe Temperature, T_p

In resistive SThM systems, the output of the probe is a signal which is proportional to the probe's electrical resistance. This is, in turn, a function of its sensor temperature T_p, with the relationship being described by the probe's Temperature Coefficient of Resistance (TCR). From this circuit, it is readily apparent that the temperature of this node is dependent upon every other element in the network simultaneously.

The probe may be driven in two different modes, and as such the probe temperature is intended to vary as the result of different thermal phenomena. In the passive mode of operation, the probe acts as a thermometer, and its sensor temperature is monitored as a function of the sample temperature, T_s. The accuracy of this method is limited due to the presence of a contact resistance, R_c which impedes the flow of heat from the sample into the probe. This results in the probe typically 'under-reporting' the temperature of hot samples, and prevents quantitative temperature measurement without some means to characterise R_c [28].

In the active mode of operation, the probe is heated to a temperature greater than ambient q_p and is brought into contact with the sample. Samples of different conductivities, Rs, abstract heat more or less efficiently from the tip, forming an image

whose contrast is related to sample thermal conductivity, k. In this mode, the change in probe temperature as a function of k is the desired measurand.

It is important to note that in thermal circuits of this type, the probe temperature is reduced to a single point, which discards some information regarding its temperature distribution. The appropriateness of this representation is discussed further in Section 4.10.2

In addition to heating via the sample or probe self-heating, the probe is also subject to heating from the laser, for the majority of systems which use optical lever deflection systems. Heating contributions from this source are particularly difficult to quantify, since they vary depending upon laser alignment, sample reflectivity and separation between the laser source and the probe. Laser heating has been demonstrated to be a significant source of uncertainty, especially in passive mode measurements [173] [29]. While the laser heating contributes to the probe temperature, its impact cannot represented with the lumped approximation, as it manifests as a temperature distribution along the cantielver. It is therefore not possible to define the proportion of laser heating that would need be added to the probe temeprature node, T_p.

Sample Temperature, T_s

This node represents the sample temperature, which may be elevated above ambient by internal or external heat sources. An example of the former is an active sample such as a heater, which may be represented in this circuit by closing the switch to voltage source T_s. The sample temperature may also be raised due to the abstraction of heat from a probe with elevated temperature, both through the solid contact and/or through the environment.

4.3.3 Sources and sinks

Source - Probe Joule Heating, q_p

q_p represents a heat flux generated by the probe due to Joule heating. It is manifest as an ideal current source, which is characterised by its ability to provide steady current no matter the load opposing it. This results in a source voltage which varies in

accordance with Ohms Law. The 'load' in this case is the equivalent resistance of the rest of the network to which the current source is attached. The ideal current source is therefore a fitting representation, since the probe's heat generation is constant, but its temperature is defined completely by the rest of the thermal circuit.

The magnitude of the heat flux provided is calculated using the following assertion; for purely resistive materials, it is reasonable to assume that all the electrical power is dissipated as heat [197]. The power is calculated by the Joule-Lenz law;

$$P = I^2 R \tag{4.9}$$

Where I is the current supplied to the probe and R is it's electrical resistance.

T_s The sample temperature, T_s, is represented by a 1-terminal voltage source, whose connection to the circuit is dependent upon the state of switch S_h. When connected, this source ensures that the sample temperature is driven to T_s. This models experiments in which the sample is held at elevated temperature relative to the probe and the environment. In passive mode, this value is typically unknown and it is this quantity we wish to measure. In active mode, S_h is opened, and this temperature is reached due to the influence of probe heating alone. Determination of the value of T_s is non trivial in this case however; in the active mode, losses are monitored by the probe signal (node T_p) alone, and it is typically unknown which quantity of the dissipated heat has affected T_s.

Sinks - Ground

In an electronic circuit, 'ground' represents a reference potential, which is given the value 0V and is used as a baseline against which the voltages in the circuit are measured. In the electrical domain, current flows from a high potential to a lower one, i.e. towards ground. This is mirrored in the thermal domain, where heat flows from a higher temperature to a lower one.

Much like the earth acts as an electron sink because it is a large, electrostatically neutral mass, heat sinks are bodies whose heat capacity is great that any of heat delivered to them will not appreciably alter their temperature. Heat may be sunk

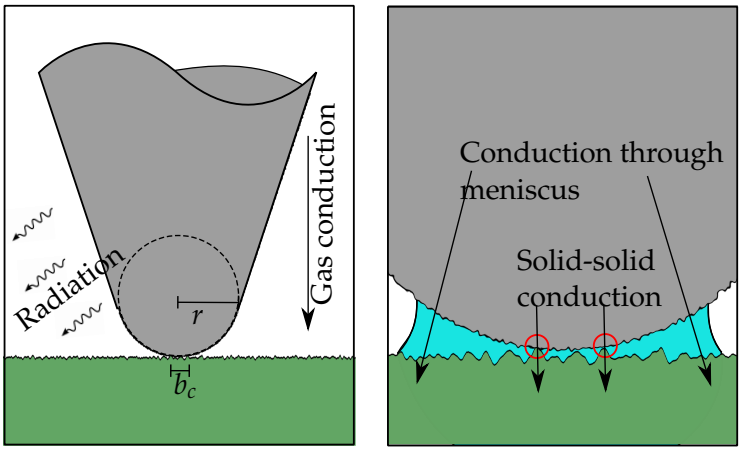

FIGURE 4.7: Magnified view of the tip-sample solid-solid contact, highlighting the various modes of thermal transport that occur. In the leftmost figure, we observe radiative transport, and conduction through the air. The view on the right is a further magnified version of the image on the left, and shows solid-solid conduction across a multi-asperity contact, as well as through a liquid meniscus that is present on all surfaces in ambient conditions.

into large solid objects, or into the environment if the system is operating outside of vacuum. For the systems in consideration in this work, their small physical size and modest power generation (order of µW) is such that the ambient air temperature will be negligibly affected by any heat generated within the system. Therefore, the environment itself may be considered an effective heatsink. This is modelled by the branch containing R_{env}, which represents the thermal resistance associated with heat transfer to the environment.

An important observation about 'grounds' in this circuit is that this reference temperature will be affected by fluctuations in ambient temperature. For this reason, strict environmental control is desirable when undertaking SThM measurements.

Throughout this thesis, we have considered ground to represent a room temperature of approximately 23 °C. In graphs which display the probe temperature, these values are given in terms of 'degrees above room temperature' unless otherwise stated.

4.3.4 Resistances

Thermal resistances dictate the rate of heat flux through each of the various pathways available in the system. These resistances may be described by different heat transfer mechanisms, such as conduction, convection or radiation. In this section, we

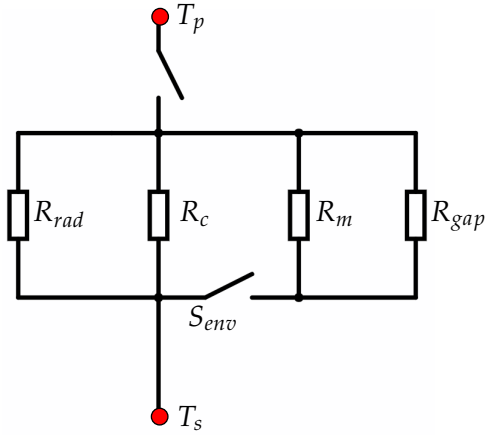

FIGURE 4.8: Reduced view of the thermal equivalent circuit showing only the resistances associated with the probe-sample contact. This is the equivalent circuit of the situation depicted in Figure 4.7

outline the heat transfer methods associated with each resistance and identify any phenomena upon which the values of these resistances are dependent. Any variation in these resistances will result in a change in the tip temperature, which may therefore be interpreted as representing a change in probe-sample conductance. To improve quantitative measurement, the influence of these external factors should be minimised.

Thermal resistances associated with the tip - sample contact region

As a contact thermal metrology technique, it is to be expected that a great deal of the thermal network is concerned with heat transfer in the tip-sample contact regime, which is highlighted by a green box in Figure 4.6. As such, we begin this section by discussing these resistances, before moving on to the other resistances in the system.

Contact Resistance, R_c

R_c represents the contact resistance that arises between the probe and sample. It arises due to imperfections in the mechanical coupling between the two solid surfaces and an interfacial thermal resistance associated with differences in lattice spacing (Section 4.2.4). These effects are exacerbated in SThM studies due to the nanoscopic contact area. An equation describing these effects is presented below [26], [32], [170];

$$R_c = \frac{R_b}{\pi b_c^2} \tag{4.10}$$

In which R_b denotes the interfacial thermal resistance, which describes the thermal resistance associated with heat transfer between dissimilar materials due to phonon mismatching [198]. It assumes a physical contact at the interface [170]. b_c is then a scaling factor which is related to the size of the mechanical contact of between the probe and sample. Treatment of this radius varies in the literature. One approach considers this contact radius to be roughly 3nm [170], a value which was calculated from the Derjaguin-Muller-Toparov model [199]. However, an alternative value was suggested by Ge et. al [32], who performed a body of work comparing the probe's experimentally-determined output against a detailed thermal model.

The experiment involved a passive probe which was scanned over an active device in ambient conditions. The primary unknown of the accompanying model was the tip-sample thermal resistance. Good agreement was found between the form of the curves measured experimentally and determined numerically. The value of R_c was then taken as the value which best minimised the offset between the two. This value was found to be $8.33 \times 10^5\,\mathrm{K\,W^{-1}}$. Various sources propose to consider the contact radius, b_c, to be equal to the probes radius of curvature, r [28], [149], [170], [200], which has been shown to be approximately 50nm [201]. This would yield an interfacial thermal resistance of $6.5 \times 10^{-9}\,\mathrm{K\,W^{-1}}$ which is in reasonable agreement with values for metal-metal interfaces found in the literature [202], [203].

Acceptable values of R_b for the type of interface formed between the probe and sample (Gold, in this case) range from $1 \times 10^{-9}\,\mathrm{K\,W^{-1}}$ to $5 \times 10^{-8}\,\mathrm{K\,W^{-1}}$ [32]. This range was used in conjunction with the 3nm contact radius predicted by the DMT model to solve Equation 4.10. The result is a range of contact resistance from 2×10^7 to $2 \times 10^9\,\mathrm{K\,W^{-1}}$, which was at least two orders of magnitude too large to prove a good fit for the thermal model.

In this work, we opt to use the value of contact resistance presented by Ge et. al ($8.33 \times 10^5\,\mathrm{K\,W^{-1}}$). The evidence provided by the author, alongside his appeal to Gotsmann's work [28] regarding the fact that a tip with nano-scale roughness may be treated as a flattened tip when experiencing the pressure induced by contact scanning, is one we find compelling. Therefore, we shall also consider the contact area to equal the tip radius of curvature, 50nm.

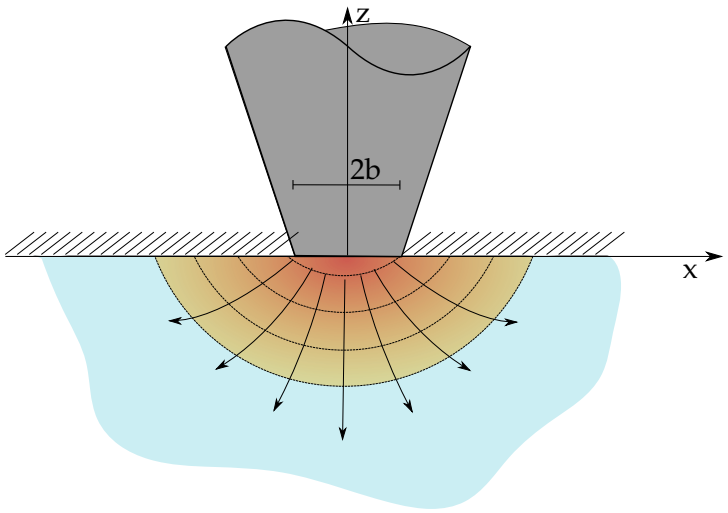

FIGURE 4.9: Schematic showing the probe sample contact as it considered in this model. We assume a flat, circular contact on the sample surface. For the radius of contact, b, we select a value of 50nm as suggested by Ge et al [32]. In this schematic, a heated probe touches a sample at lower temperature, the dimensions of which are much larger than the mean free path of heat carriers within the materials. We have highlighted the isotherms and heat flux lines associated with conduction from the probe into the material. The exposed surface of the material is adiabatic.

R_s, Spreading Resistance

An overview of spreading resistance was presented in Section 4.2.5. In SThM studies, the spreading resistance is used to represent the heat flow from a heated tip into a sample of lower temperature (typically taken to be room temperature), as demonstrated in Figure 4.9. This resistance is dependent upon the thermal conductivity of the sample being scanned, and it is this resistance which is the desired source of signal contrast in Active mode SThM studies. As discussed in the previous section, it is possible to model the probe as a conical frustum, in which the circular plane of the flat apex makes contact with the sample. As such, the spreading resistance may be modelled as a circular heat source in contact with an isotropic half-space. This assumption does not hold for those materials (such as quartz) exhibiting thermal conductivity anisotropy [204]. If the heat source is isothermal, the relation describing spreading resistance through the sample is [193], [194];

$$R_s = \frac{1}{4kb_c} \tag{4.11}$$

In which k represents the thermal conductivity of the material to which the probe has made contact, and b_c is the contact radius. The assumption of an isothermal heat source is reasonable given the small dimensions of the probe [149]

R_r Radiative Transfer

R_r represents heat radiative heat transfer that occurs between the probe and sample. While both near and far field radiative transfer has been observed [26], it has been acknowledged that radiation is never the dominant heat transfer mechanism and its affect is negligible in most cases [23], [26], [32], [132], [170]. Estimations of the effects of far-field radiative heat transfer places its thermal resistance in the order of $1 \times 10^8\,\mathrm{K\,W^{-1}}$, which is three orders of magnitude greater than that of convective heat transport [205].

Radiative heat transfer occurs regardless of the environment of operation. Under ambient conditions however, its contribution is difficult to distinguish from conduction through the gaseous medium. As such, its effects are sometimes encompassed in the calculation of the heat transfer coefficient, h (as seen in Equation 4.7) [26].

In this work, we make the assumption that radiative heat transfer is negligible and may be ignored.

R_m, Conduction through a liquid meniscus

R_m represents conduction through a liquid meniscus that forms between the tip and sample in ambient conditions due to capillary condensation [206]. In ambient conditions, a thin film of water is present on all surfaces [207]. When a probe tip is introduced, capillary condensation acts to form a meniscus with high radius of curvature between the two surfaces [206], [208]. It has been proposed that, under ambient conditions, this is a dominant mechanism for thermal transport [138]. These claims were recently investigated, and disproved, by Assy et. al. [180], [209]

Assy et. al have estimated the geometry of the meniscus using the Kelvin equation [180], [209], which considers the temperature and relative humidity, alongside the geometric properties of the tip (described by it's radius of curvature). They performed measurements of the capillary force experience by the probe as a function of

probe self-heating temperature. They observed a gradual evaporation of the meniscus as the probe's temperature was increased, and a corresponding reduction in stiction [180].

In [209] the authors present plots of the thermal conductance of the meniscus as a function of tip temperature for KNT probes such as those that form the basis of this work. They have observed the tendency $G_{meniscus} \rightarrow 0$ as T_p increases. The maximum operating temperature of the KNT probe is too low to fully remove the meniscus however. At any temperature, they found that the thermal conductance of this mode of transport was always greater than $20\,\mathrm{nW\,K^{-1}}$ ($R_{meniscus} = 5 \times 10^7\,\mathrm{K\,W^{-1}}$). This represents between 1-6% of the solid-solid conductance, and is therefore not the dominant heat transfer mechanism for probes of this type.

The authors note that the degree of heating required to successfully evaporate the meniscus (reduce pull-off force) was dependent on the sample thermal conductivity, as contact with a conductive sample effectively reduces the tip temperature due to their being more effective heat spreaders (low spreading resistance). [209]

The positioning of R_m in Figure 4.6 has been chosen to most closely represent the real situation. This route of thermal transport only exists in ambient conditions and when the probe and sample are in contact.

4.3.5 R_{air}, Conduction through the air to the probe tip in proximity

Correct treatment of air conduction in SThM remains a challenge due to the various length scales involved [26]. As such, both ballistic and diffusive conduction should be considered [32]. The resistance R_{air} is the final component in the probe-sample contact regime of the network (Figures 4.7, 4.8) and is used here to model the thermal interactions between the probe and sample facilitated by air conduction at close range (<10 µm).

If any significant portion of the probe's temperature sensor is closer to the sample than the mean free path of air (70nm at 1 bar [195]), then its reading will be dependent upon ballistic heat transfer [26]. Given the distributed nature of the resistive

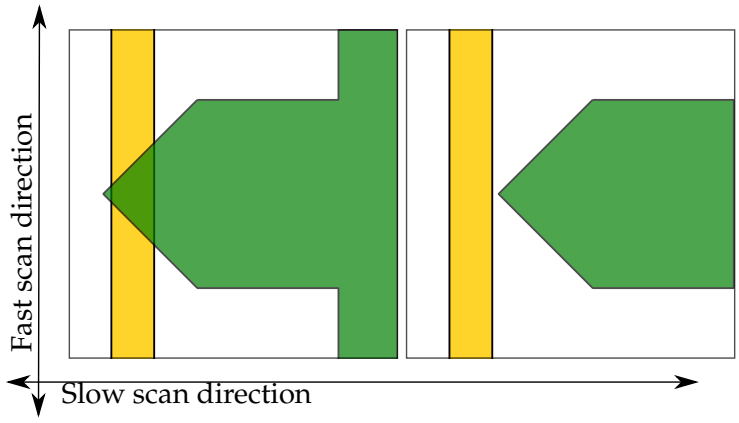

FIGURE 4.10: Illustration of the cantilever coupling problem leading to thermal profile asymmetry. A probe is scanned over a metal strip (yellow) that is Joule heated. The temperature profile around the heater is expected to be symmetric. The distance between to probe apex and the centre of the hot strip is the same in both images, however one probe has yet to reach the strip, while the other has already passed it. On the left, the body of the cantilever is positioned directly above the heated strip and will therefore be at a higher temperature than the cantilever on the right. This is due to conduction through the air. The temperature gradient induced in the cantilever by this heat transfer will increase its thermal resistance and increase thus increase the temperature present on the tip resistor.

element in the KNT probe, the 70nm section from the end of the tip is responsible for less than 0.1% of the total thermal resistance and therefore may be ignored. The slip regime, extending to roughly 7 µm from the tip apex must be considered however [32]. The thermal conductivity of air is modified to correct for slip regime conduction, and these values are used in conjunction with the tip sample separation to present am appropriate heat transfer coefficient for each region of the probe [172]

Because of the dependence of this resistance on probe-sample separation, it is not strictly appropriate to model it as a single component (lumped resistance) as we have done here and as is seen in the literature [26], [32], [170], [188]. Rather, it is included in thermal circuit diagrams simply to illustrate that this mode of transport does occur, and should be considered separately to air conduction via diffusive transport to the cantilever. Heat transfer to the environment is not the primary focus of this thesis however, and as such the reader is directed to the following studies in which this has been investigated more thoroughly; [32], [210]

4.3.6 R_{gap}, Conduction through the air to the cantilever body

R_{gap} is included to represent the existence of some thermal coupling between the probe and sample through the environment even when the two are far from contact (from hundreds of nanometres to tens of microns). This relationship is evidenced in this Thesis (Figure 4.12), and throughout the literature [156], [173], [211] in what we shall term thermal-distance curves. These are physically identical to AFM force-distance curves, but rather than monitoring the deflection signal, the probe temperature is recorded. The probe is oscillated such that it repeatedly makes, and breaks, contact with the sample. Probe-sample thermal coupling is identifiable in the non-contact regime of the curve as a second-order dependence. This can be directly attributed to air conduction, since this dependence is completely removed in vacuum. The reader is directed to Figure 3 of a recent publication by Spiece et al for an excellent demonstration of this phenomenon [173].

As with R_{air}, the distance dependence of this phenomenon means it cannot be calculated analytically for probes whose loading angle is not parallel to the sample (see Figure 4.14). Nelson et al. have calculated this resistance for doped Si probes in which the cantilever 'legs' do run parallel to the sample surface [154]. Once again, the inclusion of this resistance in the network should be considered illustrative only as we would not recommend a lumped treatment for this phenomenon. Numerical methods (finite-element) which consider this effect have been proposed by Shi et al [176], Kim et. al [140] and Ge. et al [32], [172]. Numerical models will be discussed in Section 4.4, and more detail on these sources will be found there.

This effect has been identified as the cause of the spatial asymmetry in temperature profiling as the probe is scanned over an active devices [30]–[32]. The situation in which this arises is depicted in Figure 4.10. Note that this only occurs when the temperature field being probed has significant variation over an area on the order of, or less than, the dimensions of the cantilever.

4.3.7 R_{env}, Convective losses to the environment

R_{env} describes the thermal resistance associated with convective losses from the probe to the environment. The derivation of a thermal resistance for this mode of

heat transfer was previously discussed Section 4.2.6. The heat transfer coefficient, h, required for this calculation has been reported as less than $10\,\mathrm{W\,m^{-2}\,K^{-1}}$ [32], [186].For reference, the KNT probe has a surface area of $1.44 \times 10^{-8}\,\mathrm{m^2}$

In Figure 4.6 this resistance has been presented as a single component due to lumped treatment. In reality, the thermal resistance associated with this mode of transport will vary along the length of the probe. This is because the probe has non-uniform temperature across its length, as well as a variable cross section. In [32], Ge et. al split the probe into a number of distinct regions depending on the length-scales of the relevant thermal phenomena. In this configuration they have reported values of the convective resistance, whose magnitudes range between $10^{12}\,\mathrm{K\,W^{-1}}$ to $10^{6}\,\mathrm{K\,W^{-1}}$. The parallel sum of the reported resistances is $6.8 \times 10^{6}\,\mathrm{K\,W^{-1}}$, which is an order of magnitude higher than the resistance of solid conduction along the cantilever body [32]. The parallel sum of convective resistances is dominated by the region with largest surface area, the rectangular body of the cantilever (E, in [32]).

The thermal convective resistance R_{env} between the probe and the air above, taken to be at room temperature, is given by Equation 4.8. The existence of this pathway for heat transport is not dependent on contact, but is dependent on the probe operating in a fluid environment, hence its dependence on S_{env}.

Most of the studies surrounding this value have been performed far from contact with the sample. Such a treatment is likely to overestimate the value of h that would be observed when the probe was is in contact. This is because the exchange area to the environment is reduced by the presence of a solid half-space [26].

R_p, Probe Thermal Resistance

The cantilever of the probe experiences a temperature gradient as heat travels through it to the base of the chip, which is considered a heat sink. R_p, the probe thermal resistance, is a measure of the opposite to conductance in this manner. The magnitude of this resistance is the result of the geometries and thermal properties of the materials which comprise the thermal probe. For the case of the nano-fabricated thin film

resistive probes used in this work, their complex geometry at lengths scales comparable to phonon mean free path prevents deduction of this value through analytical means.

In the literature, attempts have been made to quantify the thermal resistance of KNT probes using modelling (both lumped [32] and FEA [27]), and experiment [166], [180]. Estimates of cantilever thermal resistance range from 5.06×10^4 [27] to $2.26 \times 10^5\,\mathrm{K\,W^{-1}}$ [32].

A confounding factor in the determination of cantilever thermal resistance is the lack of agreement upon what it is that the term refers to. From the definition of thermal resistance, it is understood that a temperature gradient and heat flux may be described as a thermal resistance. In the case of thermal probes however, one should consider the source of the temperature, as the opposition to heat flux from an external source (such as an active sample) will not be the same as the thermal resistance associated with probe self-heating. This observation has recently been discussed in detail by Spiece et. al [173] at the University of Lancaster.

The correct determination and treatment of the cantilever thermal resistance is a core theme of this thesis, and is explored in more detail in Section 4.10.1

4.3.8 Switches

The thermal network presented in Figure 4.6 is similar to those found in the literature [138], [153], [159], [170], [180], [181], [196], but is designed to encompass all the possible modes of operation in a single circuit. This is facilitated by the use of various switches that model the addition or removal of certain heat transfer pathways to the thermal circuit. In this section we outline the operation of each switch, including why representation in this form is suitable. In each case, we shall defend the position that a certain choice is 'binary' enough to be implemented in this manner.

Throughout the upcoming sections, we have made use of 'voltage highlighting', a common feature in circuit simulation packages to qualitatively display the spread of heat throughout the network. We believe this is a novel and effective method of communicating how heat is distributed across this complex thermal system.

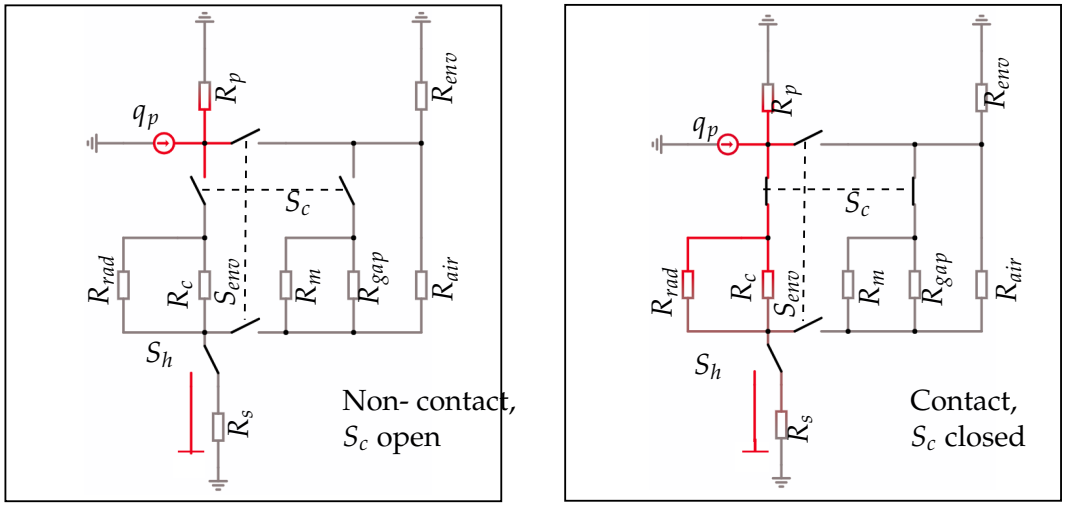

FIGURE 4.11: Comparison of the thermal network between non-contact (left) and contact (right) regimes in vacuum. The probe is operating in active mode in both cases. The intensity of red colouration indicates the temperature in that region of the system. In the first example, there is only one route for heat transfer, and the probe temperature dictated solely by the relationship between its Joule hating and the cantilever thermal resistance. In the second example, the probe experiences some heat loss due to the mechanical contact. Note that due to the high thermal resistance associated with this nano-contact, the sample temperature T_s is minimally increased. The majority of the heat is lost down through cantilever conduction, or through contact resistance.)

Contact switch, S_c

The difference between contact and non-contact regimes of probe operation are best understood through reference to thermal-distance plots, such as the one presented in Figure 4.12. In this figure, the probe is operating in active mode and is thus at elevated temperature compared to the sample. The probe is operating under ambient conditions. Prior to making contact we observe the temperature drop associated with increased proximity to the sample, resulting in increased conduction through the air. Upon making contact, we observe a drastic temperature change as the additional route for thermal transport by solid-solid contact opens up. The solid-solid contact has (relatively) high conductance, and signals an obvious change in the circuit.

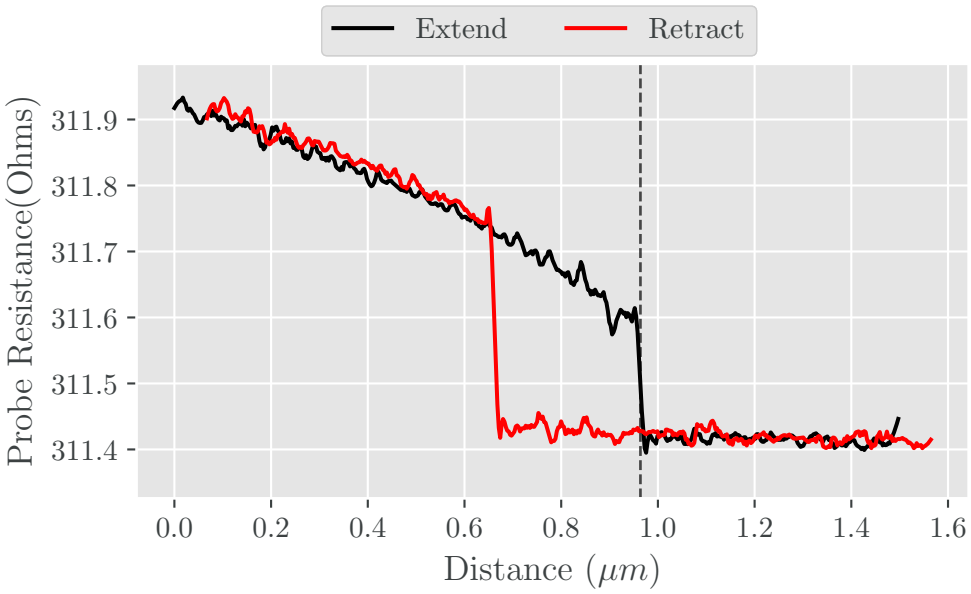

FIGURE 4.12: Thermal - Distance curve of a standard SThM probe coming into contact with a Si sample. There is a large signal change due to a temperature drop as the hot sample 'jumps' into contact with the room temperature sample.

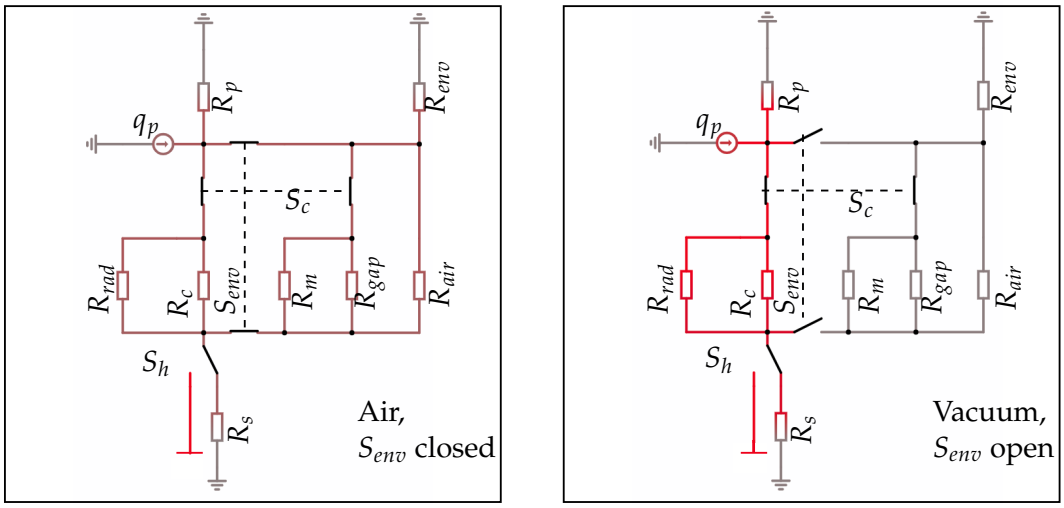

FIGURE 4.13: Qualitative example of the temperature distribution across the thermal circuit when the probe is operating in air (left) and under vacuum (right). In both cases, the probe is heated and is in contact with the room temperature sample. The intensity of the red colouration indicates the degree of heat experienced in this area of the network.

Environmental Switch, S_{env}

S_{env} represents the difference between operating in a vacuum or an ambient environment. This is modelled as the opening or closing of the thermal pathways associated with conduction through the air. The qualitative effects of toggling this switch are demonstrated using the thermal resistive analogy in Figure 4.13.

All of the resistors modulated by this switch are dependent upon the thermal properties of the environment, whether that be ambient air, under liquid or under vacuum. All of these resistors could be represented as variable resistors, in which case vacuum would simply be the result of $R \rightarrow \infty$. While this is a perfectly reasonable treatment, the difference between 'some fluid' being present and none is stark enough such that the switch representation is arguably more intuitive. This was exemplified by Zhang et al [212] who used who used novel - dual cantilever probes with 2 µm and 10 µm separation to investigate the influence of ambient pressure to thermal coupling between the two prongs. They noted that below 1mbar (far from high vacuum) negligible coupling between prongs was observed.

The distinction is generally made as a matter of experimental procedure. Many researchers prefer to perform experiments under vacuum as it significantly reduces the number of unknowns. Conversely, due to the expense and complexity of vacuum SThM systems, the vast majority of end-users will perform experiments under ambient conditions. It is not typical that researchers perform measurements at pressures in between ambient and high vacuum, unless studying the nature of air conduction itself.

Active/Passive Switch, S_h

Switch S_h is a single-pole double-throw (SPDT) type switch that is used to represent the distinction between sample behaviours in the passive and active modes of SThM. One terminal is connected to a heat source that is defined by the sample temperature, while the other connects to ground through the material's spreading resistance.

When probing the temperature of an active sample, it is reasonable to assume that the sample is isothermal in the region of the tip-sample contact due to its nanoscale

interaction area [203]. As far as the probe is concerned, there is no temperature gradient within the sample, and thus no spreading resistance. To model this behaviour we have employed a switch between sample temperature, T_s, a perfect heat source, and the spreading resistance, R_s. Recall from Section 4.3.4 that spreading resistance has been used to quantify the opposition to a hemispherical flux that is the result of imposing a local hot spot (introduced by probe - sample contact) onto the sample surface. R_s therefore cannot exist when the sample is at greater temperature than the probe.

4.4 Limitations of the lumped thermal network

The lumped thermal network is a useful tool for the communication and visualisation of the complex SThM thermal system. While this type of model has its merits, it cannot sufficiently inform probe design (which is the goal of this work), since it contains no information on the spatial distributions of the various thermal phenomena. Consider R_p, the probe cantilever thermal resistance. In the lumped model, it is represented as a single value which is connected between temperature nodes T_p and ground (room temperature). No information regarding the temperature distribution of the probe may inferred from this representation. Given the complex geometries and materials stack of the probe, it is likely to exhibit a non-linear temperature distribution. This information is of vital importance, since the probe signal is the spatial average of the sensor resistance [187], which is, in turn, a function of the temperature distribution along its length. This particular problem as it relates to the sensor placement and design is discussed in greater detail in Section 4.10.2

The following section reviews another thermal resistance that is ill-represented with the lumped model due to the spatial distribution of the probe. Thermal coupling between the probe and the sample through the air varies as a function of the separation between them. This is especially problematic in the passive mode of operation, where the probe temperature distribution is influenced by how much of the cantilever is hovering above a heated substrate.

By understanding how researchers modelled this problem, it is possible to develop a similar framework for solving the probe temperature distribution in the Active Mode. An active mode model is particularly necessary, since the probe heat source is integrated within the cantilever, not a separate entity as the network presented in Figure 4.6, and those found throughout the literature [138], [153], [159], [170], [180], [181], [196] would suggest. Further discussion on the importance of this distinction is presented in Section 4.8.1.

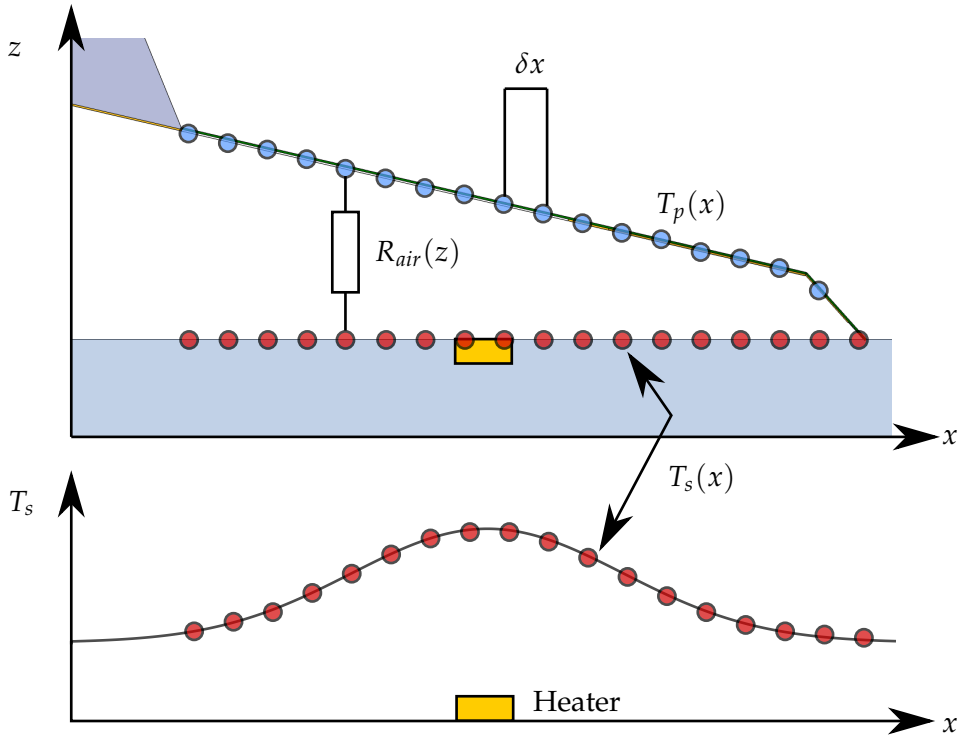

FIGURE 4.14: Illustration of the finite difference model proposed by Shi et. al [176] and adapted to the KNT probes by Ge. et al. [32], [172]. The probe, operating in passive mode, is scanned across an active sample, which is generating a temperature profile. In this case, a gold strip is generating a Gaussian temperature distribution. Both the probe and sample are split into finite elements, dx and their temperatures modelled by a series of nodes. Heat transfer occurs between the heated sample (red nodes) and the probe (blue nodes) with some efficiency dictated by the distance between them at that point ($R_{air}(z)$). The two surfaces are considered parallel plates. The resulting probe temperature is also dependent upon the geometries and thermal properties of the materials used in the probe's construction, as these effect the thermal resistance of conduction through the cantilever to the base. The governing equation for this system is presented in Equation 4.12.

4.5 Distributed models in the literature

4.5.1 Non-uniform probe-sample separation and its effect on coupling via air conduction

The issue of non-uniform sample-probe separation for air conduction was addressed previously by Shi et.al [176], who produced, to our knowledge, the first numerical model for SThM probes. Their method was later improved upon by Kim et al [140], and then further by Ge. et al [32], [172]. Figure 4.14 demonstrates the operation of the model graphically, while Figure 4.15 shows the equivalent thermal resistive

network. The governing equation is presented below;

$$\frac{d}{dx}\left[\frac{dT_p(x)}{dx}\sum_i [kA(x)]_i\right] + h(x)w(x)[T_p(x) - T_s(x)] = 0 \tag{4.12}$$

Here, T_p and T_s are the probe and sample temperatures respectively. k represents the thermal conductivity of a material, while A denotes its cross-section. The subscript i which applies to these two variables is used to indicate which of the multiple materials (SiN, Au, Pd/Pt in our case) is being considered. w is the cantilever width, and h the heat transfer coefficient of air between the heated sample and the probe. This value varies with probe-sample separation, which, in turn, varies with x. As previously discussed, h requires different treatment across different regimes of thermal transport. The full method of doing so is available in the original papers.

The solution to Equation 4.12 is found through finite difference methods, and yields a probe temperature distribution. The signal output of the probe can be estimated from the average of the temperature distribution in its sensor region, which corresponds to the final 5 µm (in the x direction) for the KNT probes.

This thermal network is a simple representation, having been reduced to a pseudo-1D problem. This means that it is far less computationally intensive than full FEA simulation. If the entire probe temperature distribution can be calculated quickly, this opens up the possibility to observe the probe's continuous response to an additional variable. In the case of Shi et. al, they solved the probe temperature distribution for multiple points on the z-axis or probe lift above the sample, and were able to reproduce the thermal-distance curves (such as in Figure 4.12) from experiment with reasonable accuracy (Figure 14 of Shi et. al, [176]).

4.5.2 Distributed models for the representation of Active Mode SThM

The above section has outlined how numerical modelling has helped to better understand the probe-sample thermal network when operating in the passive mode. Because of the low current used in this mode of operation, negligible Joule heating occurs, and q_p can safely be ignored. The same cannot be said of the active mode, in which the probe experiences significant Joule heating. Due to this, if we wish to

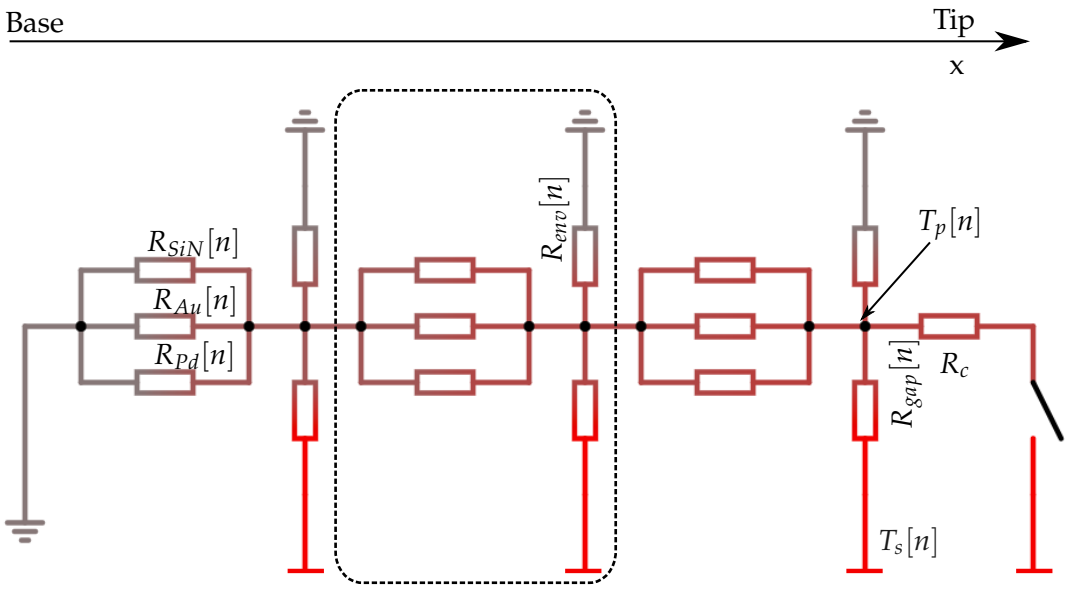

FIGURE 4.15: Thermal resistive network analogy of the layout presented in Figure 4.14. The dotted line encapsulates a single repeating unit represented of one 'node'. Each contains the nodal temperatures of the sample and probe, T_s and T_p respectively. They are connected by the horizontal resistors, which represent solid conduction through the different layers of the cantilever. Parallel representation of laminate materials was previously justified in Section 4.2.4. Heat is through the air is represented by the vertical resistors; R_{gap} for the hot sample to the probe, and R_{env} from the probe to the environment. In this example, the probe is hovering above the sample, out of contact. The sample has a uniform temperature distribution.

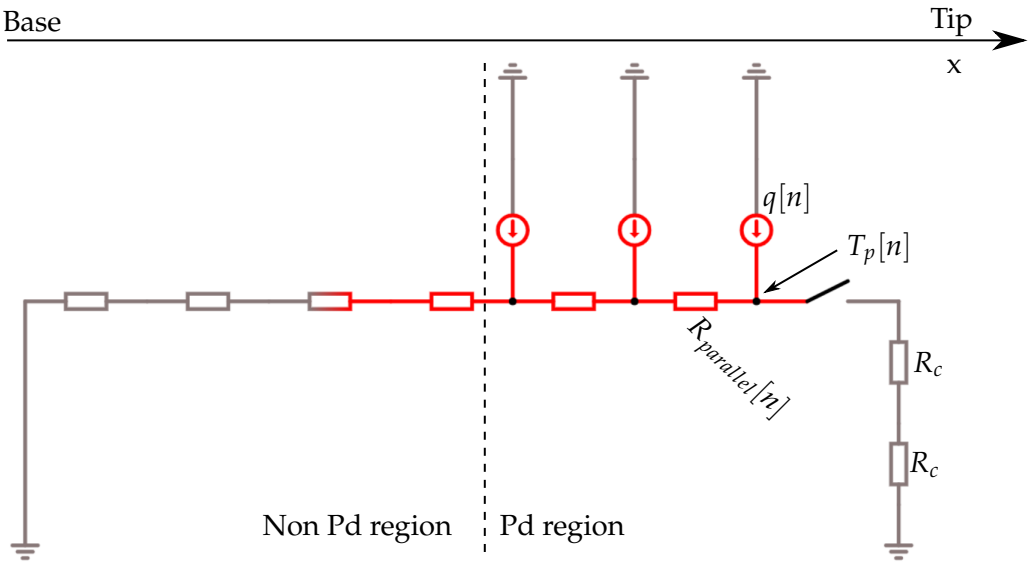

FIGURE 4.16: Reduced example of the distributed model used in this work for the calculation of active mode temperature distributions when operating in vacuum. The model used in this work considers only vacuum operation for simplicity, therefore those resistances seen in Figure 4.15 associated with heat transfer through air have been omitted. Elemental power generation has been added in the form of current sources (constant heat flux) that represent the fraction of heat contributed by each portion of the heater. On the right, a switch connects the contact (R_c) and spreading (R_s) resistances to the circuit, representing contact with a room-temperature sample. The number of elements in this figure is significantly reduced. The real model has hundreds of elements.

model the probe performance in this mode, then new models will have to be constructed.

A key aspect of the new models is the requirement for distributed heating. It is not sufficient to provide heat as a boundary condition to the tip of a distributed resistor network, as this does not accurately represent the situation. Every increment of the probe's length, dx in which the heating/sensing element is present should be represented with its own current source representing that element's fractional contribution to heating. As previously identified, the ideal current source drives a current such that the voltage is defined by the resistances of the components to which it is connected. In thermal terms, that is to say that the temperature distribution of a probe out of contact, in a vacuum, is the defined entirely by the internal heat generation and thermal resistance of the tip. In this work, it was decided to model vacuum operation, since this approach reduces the system down to only the interactions between the probe and sample, allowing for more straightforward investigation of the effects of altering probe geometry on its thermal performance. Figure 4.16 presents a simplified view of the model employed in this work, which is described in the next section.

In the active mode of operation, the probe's 'performance' may be considered its sensitivity to changes in tip-sample thermal conductance, which may be used to discriminate between samples of varying thermal conductivity. To generate the probe's response in this manner necessitates simulating a probe temperature distribution multiple times to cover the wide range of solid materials' conductivities (five orders of magnitude). Although the model presented in the following section has been developed using the commercial KNT probe as a baseline, the intention was to create a tool for informing the design of new probes with greater sensitivity. Therefore, the model was required not only to simulate a probe's response to a large range of materials, but also to compare between different designs of probes. This introduces yet another dimension of complexity, at which point it is reasonable to assert that the simulations are computationally intensive such that 3D modelling with FEA software would be prohibitively time consuming. However, the efficiency and accuracy, applicability of the 1D thermal resistive model has already been demonstrated [32],

[140], [176], making it a suitable approach for this work.

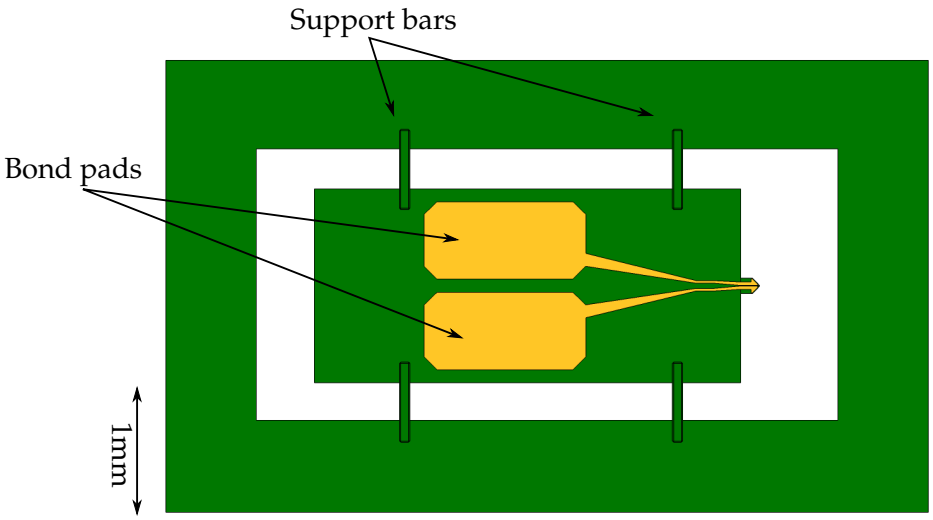

FIGURE 4.17: Scale drawing of the commercial SThM probe as it sits within its frame.

4.6 Model Implementation

4.6.1 Probe dimensions and material properties

Before discussing the development of the model, it is useful to present the dimensions and physical properties of the various materials which comprise the probe. The model is desired to predict the performance of new probes, but is first tested with the commercial KNT device as a control. It should be noted that it is our desire to minimally alter the probe's composition. While changing cantilever materials may improve performance, the uncertainty involved with developing new processes for the manipulation of unfamiliar materials was potentially prohibitively time consuming. It is therefore the goal to demonstrate that 'thermally - informed' probe design may have a drastic effect on performance without changing the materials stack or drastically altering the processing steps.

Figures 4.17 and 4.18 are scale drawings of the commercial KNT probe at low and high magnification respectively. The dimensions of the probe and cantilever are presented in Table 4.2. The thermal and electrical properties used in the model are presented in Table 4.3. For the thermal conductivity of SiN_x, we have chosen a value from the literature representative of free-standing LPCVD SiN_x layers ($3\,W\,m^{-1}\,K^{-1}$). It should be noted that the thermal conductivity of SiN_x layers can

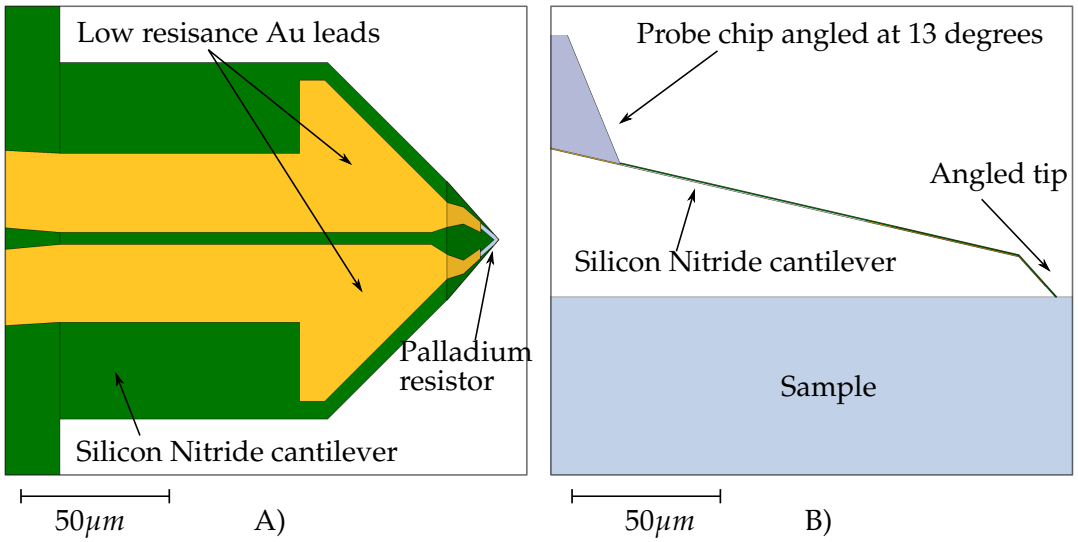

FIGURE 4.18: Scale drawing of the SThM probe cantilever, as seen from above (left), and from the side (right).

vary quite significantly depending upon the composition of the film. Unfortuantely it was not possible to measure the thermal conductivity of our films directly, therefore a value from a similar deposition method was selected from the literature.

The thermal conductivities of the metal layers have been derived from their electrical conductivity (which was measured experimentally) using the Weideman-Franz law;

$$\frac{k}{\sigma T} = L \tag{4.13}$$

In which L represents the Lorenz number $2.45 \times 10^{-8}\,\mathrm{W\,\Omega\,K^{-2}}$ [213], and T is temperature, which we held at 293 K for every result presented here. The thermal conductivity of gold calculated in this manner ($153\,\mathrm{W\,m^{-1}\,K^{-1}}$) is much lower than the bulk value used by Bodzenta et. al [181]. We propose that our value is more appropriate given the small dimensions of our gold film (t=150nm). This assertion is backed by Langer et al, who demonstrated the relationship between film thickness and thermal conductivity [214]. At 200nm, they report the thermal conductivity to be around $180\,\mathrm{W\,m^{-1}\,K^{-1}}$.

It is acknowledged that the thermal conductivity of the probe's materials can vary to a non-negligible degree within the operating temperature of these probes (order

Parameter	Value
Chip Dimensions	1500 x 3300 x 380 μm
Cantilever Material	LPCVD SiN_x 400nm
Pads and connects	Evaporated Gold 150nm
Resistive heater/Sensor	Evaporated Platinum 40nm
Cantilever Length	150μm
Cantilever Width	120μm
Rectangular Section Length	90μm
Platinum resistor width	1.5 μm
Holder loading angle	13°

TABLE 4.2: Table of Probe Geometric Properties

Material	Thermal conductivity ($W/m/K$)	Electrical conductivity ($S\,m^{-1}$)
SiN_x	10 [215], 3 [216]	Not used
Au	317 [181], 153 (W-F law), 180 at 200nm [214]	20.9×10^6 (Experiment)
Pd	30.1 (W-F law)	4.2×10^6 (Experiment)

TABLE 4.3: Physical properties of the materials from which the cantilever is composed.

of 10%). For the purposes of this model however, we have considered thermal conducitivty to be constant.

4.7 Solver Mathematics

4.7.1 Approaches to computing network solutions

Circuit analysis is a mature technique for the solution of complex electronic networks, making it an attractive candidate for the representation and solution of similar thermal network problems. Circuit simulation involves solving a representative system of equations. However, finding the solution to these equations is generally less challenging than correctly formulating the equations to represent a given circuit. Two approaches are popular when attempting to solve a circuit; Nodal Analysis and Mesh Current Analysis. Both involve the construction and solution of a system of simultaneous equations, however the former is based upon Kirchoff's current law (KCL), while the latter involves the use of Kirchoff's voltage law (KVL) [217]. In this work we opt to use a Modified Nodal Analysis (MNA) approach, since it is amenable to algorithmic operation. Further discussion on the advantages of this approach compared to the alternatives may be found in the original sources, [217]–[219]. Although MNA is capable of analysing the transient behaviours of circuits,

this functionality has not been implemented in the present model and shall therefore not be discussed. MNA is also capable of modelling transistor and amplifier behaviour through the use of current or voltage dependent voltage sources. We do not have any need for components of this type in the thermal model we wish to solve, and as such the mathematics for their treatment may be disregarded for this application.

4.7.2 Core math

The following derivation is based upon the assumption that the circuit to be analysed meets the conditions stated above (no dependent sources, no transient effects). In which case, the circuit may be represented using matrix equations of the following form;

$$\mathbf{Ax} = \mathbf{z} \tag{4.14}$$

The dimensions of the above matrices depend upon n and m, which represent the number of nodes and independent voltage sources, respectively. In this model, no voltage sources were used. Recall that in the thermal electrical model a voltage represents a temperature, and a voltage source represents a fixed temperature boundary condition. This model is intended for investigation of the active mode of operation however. In this mode, there are no fixed temperatures (other than room temperature, which is represented via ground) as the probe's Joule heat generation is represented by current sources (Sections 4.3.3 and 4.7.3).

Since no voltage sources have been used, $m = 0$ and the matrix dimensions are purely dependent on n, the number of nodes in the circuit. In the case of this model, n is related to the fracturing size, which is discussed in Section 4.7.3.

The solution of Equation 4.14 is the result of simple matrix inversion;

$$\mathbf{x} = \mathbf{A^{-1}z} \tag{4.15}$$

Description of the matrices

Matrix **x** is an $(n+m) \times 1$ vector which contains all of the system's unknowns. The top n elements represent the nodal voltages, while the following m elements represent the current through the independent voltage sources. This matrix may be considered as a stack of voltage **v**, and current **i** vectors.

Matrix **z** has dimensions $(n+m) \times 1$ and contains the values of the various sources in the system, which should be known. The upper n values contain the sum or difference of the independent current sources in the circuit, while the remaining m values represent the independent voltage sources in the circuit. As above, this matrix may be considered a stack of vectors **V**, and **I**

The final matrix, **A**, has dimensions $(n+m) \times (n+m)$ and consists entirely of known values. It best considered as the amalgam of four smaller matrices;

$$\mathbf{A} = \begin{bmatrix} \mathbf{G} & \mathbf{B} \\ \mathbf{C} & \mathbf{D} \end{bmatrix} \tag{4.16}$$

Matrix **G** is $n \times n$ in shape, and is populated by the conductances between the nodes of the circuit. **B** and **C** are both determined by the position and magnitude of the voltage sources. When only independent voltage sources are included, they are the transpose of one another. Finally, **D** is $m \times m$ and contains only zeros.

The MNA formulation may thus be expressed generally as;

$$\begin{bmatrix} G & B \\ C & D \end{bmatrix} \times \begin{bmatrix} v \\ i \end{bmatrix} = \begin{bmatrix} V \\ I \end{bmatrix} \tag{4.17}$$

It is useful to re-state the equations in terms of the thermal analogy, with the matrices in parenthesis referring to the electrical analogues;

We wish to calculate the nodal temperature distribution (**v**) as the result of the heat generated by the probe (**I**) as it flows through the sample and probe, with rate defined by the thermal admittance of the probe-sample network (**G**).

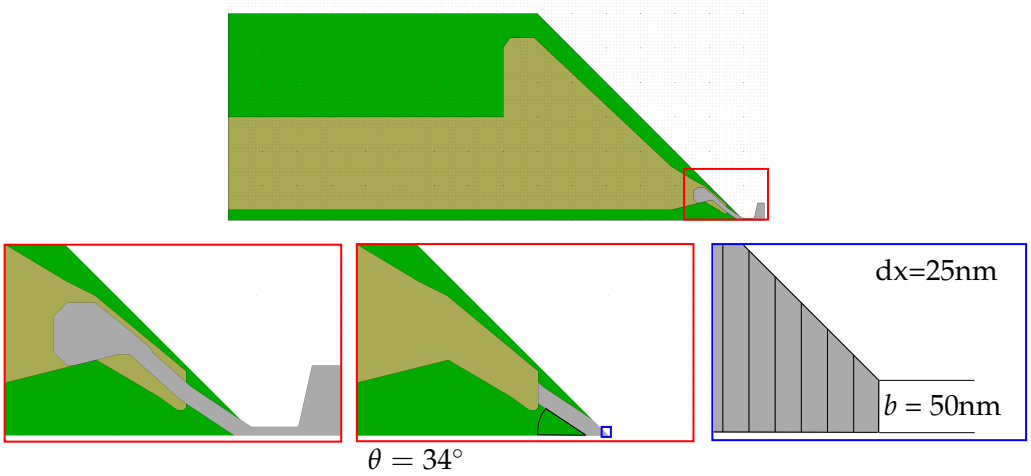

FIGURE 4.19: Probe schematics demonstrating preparation of data for the python model. In the initial design, the Pd sensor overlaps the cantilever due to the self-alignment approach. For modelling, this is removed by applying an AND operation between SiN_x and Pd. We also remove the overlap between Pd and Au, since the electrical conductance of this region is dominated by the thick Au layer (see Section 4.7.3). Fracturing of the tip is performed in python, but the output is a GDS file may still be opened for inspection. The image on the right is the result of such fracturing, and the high resolution sampling in the tip region can be seen. We also note the choice of tip truncation to be equal to a 50nm contact radius as is recommended in the literature [32]

4.7.3 Formulation of matrices from probe dimensions

The difficulty in employing an algorithm of this type comes not from the solution of the matrix equations, but the correct formulation of the matrices. In this section we outline the method employed to construct matrix equations based upon the properties of the probe. The thermal and electrical properties of the probe were previously presented (Table 4.3). The remaining unknown is the geometry of the probe's constituent material layers.

Fracturing algorithm

The two-dimensional definition of the probe's materials is taken directly from files produced in the GDSII CAD format. This approach is advantageous as it leverages the power of existing, familiar software tools for drawing probe designs. In addition, should models of a given device show positive results, the drawings required for its manufacture are already prepared, significantly reducing lead time on fabrication.

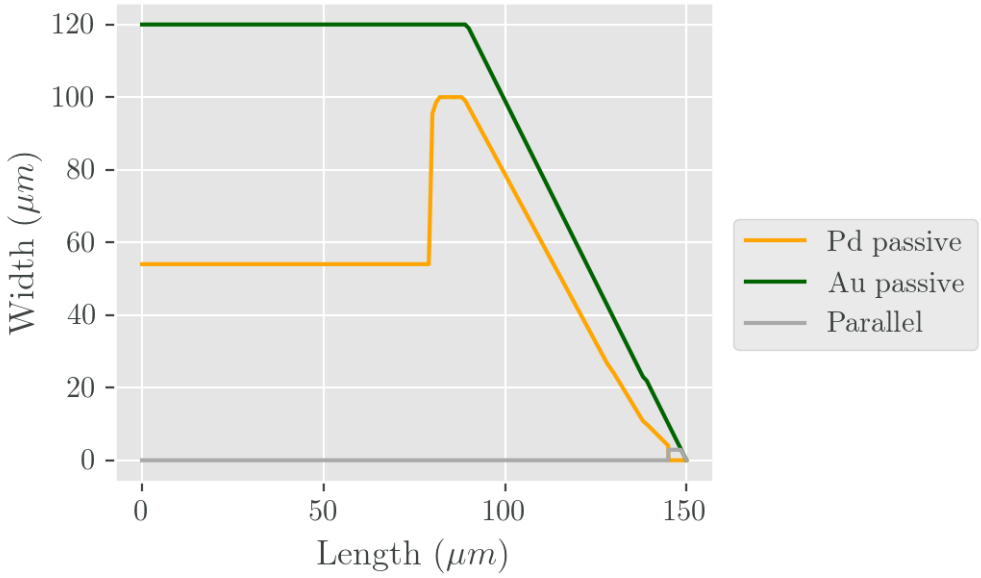

FIGURE 4.20: Elemental widths of each layer of the probe.

The conversion from a GDSII format file to the required numerical arrays is performed in Python. Much of the functionality associated with opening and manipulating these files is available through the GDSPy package[1]. Of particular use was the `.split()` function which allows for the vertical segmentation of a polygon at a defined position. Iteratively performing this operation at intervals of dx results in a multitude of narrow polygons representing the various 'elements' of the probe. It is assumed that each element has only four vertices. This condition is easy to meet if the probe design is drawn in the CAD software using a grid snap greater or equal to the desired sampling width. Division of an element's area by dx yields its elemental width, w, which is the required value for the arrays. The widths of each of the layers are presented in Figure 4.20. More detailed discussion on the implementation of this routine is reserved for the software's documentation and comments in the source code[2].

The sampling width can be defined programmatically, and does not have to be uniform throughout. In this work, we have employed a sample width of 1 µm for the majority of the cantilever, but 25nm for the final 11 µm of the tip. This setup was chosen to maximise the accuracy of the temperature profile across the very tip of the

[1]GDSpy on Github: https://github.com/heitzmann/gdspy
[2]`https://github.com/RL-AFM/SThM-Cantilever-Thermal-Model`

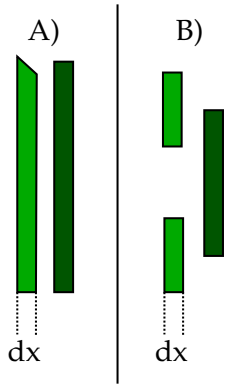

FIGURE 4.21: The width of an element or elements on a single layer is calculated from the area of the element. In this figure, example elements as they appear in an input file are given in light green, and their representative widths are shown in darker green. In A), a trapezoidal element is re-shaped into an element of constant width. In B), two elements occupying the same sample x position are summed into one representative element. This is a common occurrence in the cut-out style probes presented later in this thesis

sensor which makes contact with the sample. Later (Section 4.8.1), we will demonstrate that the majority of heat is localised in this region and the rest of the cantilever is sufficiently represented with reduced granularity.

Note that, in the lithography to used to define the cantilever, the apex is written as a triangle, thus having infinitely sharp tip. This results in an apex which is defined purely by process latitude. The probe thus has a tip with finite radius, which must be modelled as such in order for the equations to compute properly. To accommodate this in the model, the final sample is discarded, truncating the tip such that the contact area is a flat-punch style apex with 50nm contact radius, representative of the physical contact as discussed previously (Section 4.3.4)

Many polygons which comprise an 'element' of the probe are sloped, or trapezoidal segments which do not have constant width. In Figure 4.21A, we demonstrate how this is accounted for in the software. Additionally, we highlight how the program is capable of calculating the equivalent width of dx segments which are occupied by more than one polygon. This is particularly relevant to the development of the cut-out probes, in which two beams occupy the same x position (Figure 4.21B).

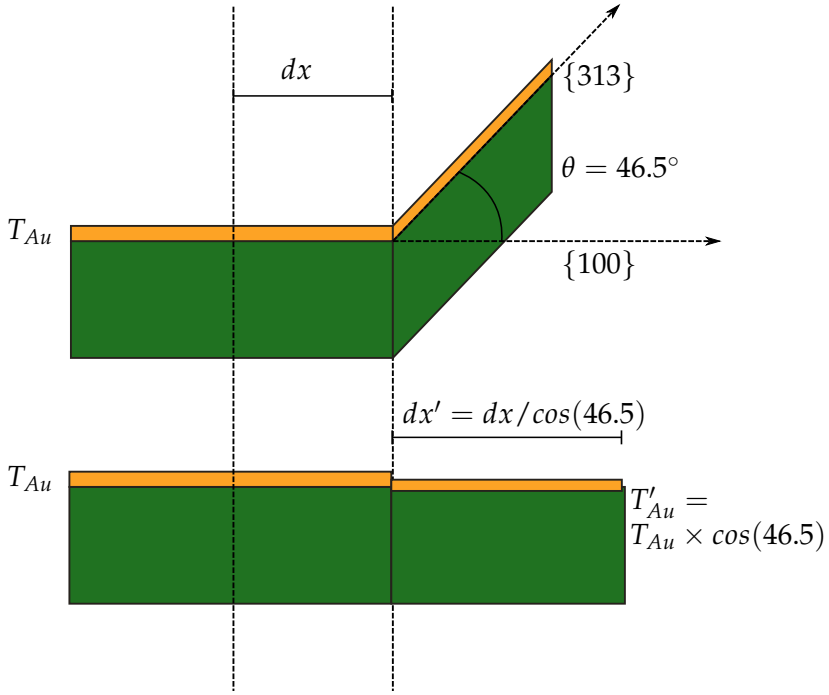

FIGURE 4.22: Two corrections should be made when converting the 3D geometry of the tip into a 1D representation. First, the length of the sampling width, dx, should be adjusted to reflect the increased distance for heat to travel introduced by the difference between the projection and fabrication planes. Secondly, the thickness of evaporated metal films should be adjusted. Metal evaporation occurs directionally and uniformly; this means that the thickness of the metal in the direction of heat flux is actually less than the nominal value.

Height

The above sections demonstrate how the 2D probe layout is used to provide an array of elemental widths. The final dimension, height, is much easier to calculate since it is simply defined by the thickness of the SiN_x cantilever and evaporated metals. While some variation is present between individual deposition runs, we have chosen to use the prescribed thickness values presented in Table 4.2

Dimensional Corrections

Two corrections have been made when considering the geometry of the materials present on the probe. Both are identified in Figure 4.22. The first concerns the difference between the writing/ lithography plane and the fabrication plane, and corrects the sampling width along the sloped 'beak' of the probe. The second correction concerns thickness variation when evaporating metals upon sloped surfaces.

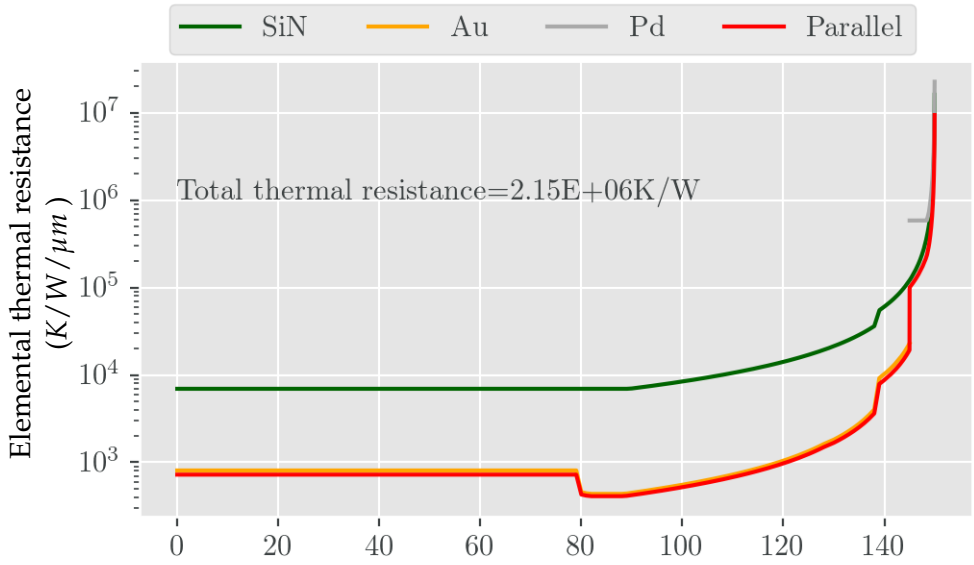

FIGURE 4.23: The elemental thermal resistance of each of the materials which comprise the cantilever. The parallel thermal resistance of each section is shown by the red line. We observe that this line mirrors the trend of the gold quite closely, which indicates that the this film has a significant effect on the thermal resistance of the cantilever. SiN_x has negligible conductance by comparison, so this trend is expected. We observe a drop in parallel resistance at 80 µm where the arrowheads 'fan out'. The figure is annotated with the total thermal resistance, which is simply the summation of all elements in the parallel thermal resistance array. Note that this calculation of thermal resistance is the result of materials and geometries alone, and does not consider temperature gradients caused by heat sources within the probe. Therefore, it should only be used as an estimate of the cantilever's thermal resistance to an external heat source that is applied to its apex. This value is one order of magnitude greater than those of Ge [32] and Assy [170], however this is to be expected, given that they report the thermal resistance of the probe to its internal heat generation. This misses out the final few microns of the probe, which, as we observe in this figure, are those with the highest thermal resistance due to their small area.

Analysis - Resistance

The treatment of the widths and thickness arrays has been presented. These values are required for the formulation of the individual values which comprise matrices **A** and **z**, which represent the thermal conductances and heat sources respectively.

The former is calculated simply using the equation governing thermal conduction in solids presented at the start of this chapter (Equation 4.5). For a given material, m:

$$R_m = \frac{L_m}{k_m A_m} = \frac{dx[n]}{k_m w_m[n] t_m[n]} \qquad \text{(4.5 re-arranged)}$$

In which length (L) is transformed to sampling width (dx), and the area (A) is represented by x-varying width (w) and thickness (t). Due to implementation in Numerical Python (NumPy)[3], efficient vectorised operations are possible, meaning the code for the above equation is able to evaluate all elements of the probe simultaneously, rather than iterating through the many elements.

The parallel thermal resistance is the one required for all further calculations. Each element is a vertical stack of between one and three materials, which is reduced to a single representative value using composite plane wall treatment, as was presented in Figure 4.4, Section 4.2.4. A simple inversion gives the values required for the conductance matrix, **G**.

Construction of the matrix G or A

The conductances between nodes of the thermal circuit must be positioned along the diagonals of matrix **A** [218]. The final entry in the matrix ([n,n]), contains the conductances of those elements which do not comprise the body of the probe. These include the contact and spreading resistances associated with touching a room- temperature sample. We have opted to use the tip-sample contact conductance reported by Ge in [32], ($R_c = 8.33 \times 10^5, G_c = 1.2 \times 10^{-6}$). The spreading resistance is calculated dynamically when considering the thermal conductivity of the material to which the probe is placed in contact. If an out of contact probe temperature profile is desired, R_s is simply set to infinity, which is functionally equivalent to opening the switch seen in Figure 4.15.

Analysis - Power

Matrix **z** contains all the sources in the system. Section 4.3.3 previously described the use of ideal current sources for the representation of constant heat generation due to the Joule effect, based upon the Joule-Lenz law and the assumption that all electrical power is converted to heat. Here, we present the determination of the magnitude of elemental ideal current sources which comprise matrix **z**.

The electrical power generated by the probe may be calculated using the following;

[3]NumPy homepage: http://www.numpy.org

$$P(x)dx = I^2R(x)dx, \quad P_m[n] = I^2 \times R_m[n] \tag{4.18}$$

On the left is the continuous form of the Joule-Lenz law, the right is the discrete method used in this work. I is the current provided to the probe, as set by the user. Since there is only one path for current flow, its value remains constant for each element of the probe. The electrical resistance of an element of a given material, m is given by R_m, whose definition is as follows;

$$R = \frac{\rho L}{A}, \quad R_m[n] = \frac{\rho_m \delta x}{w_m t_m[n]} \tag{4.19}$$

Once more, the left shows the general case, while the right presents the discrete version incorporated in this model. ρ_m is the electrical resistivity of a material, m. Values of ρ for each of the materials used in this work are presented in Table 4.3. The rest of the equation is defined by the geometry of each of the materials. A difficulty arises due to the fact that the width in the direction of current flow is not equal to the width in the y direction as provided by the fracturing mathematics. The details of how this has been handled, alongside a full derivation are presented in Appendix E.

The result of the above calculations is an array containing all the values of the independent current sources which represent Joule heating power. These data are presented in Figure 4.24, which compares the power generation per micron along the length of the cantilever, for each of the two metals. The electrical resistance of both metal films is assessed as part of this calculation. The gold contributes only $7\,\Omega$, while the palladium resistor has a value of $104\,\Omega$. This value is in accordance with the designed value of $300\,\Omega$ - the KNT probe has a $100\,\Omega$ resistor at the apex alongside two $100\,\Omega$ NiCr current limiters in the leads. Gold's low value is due to its lower resistivity, high film thickness and wide wires. The total power generated along the probe's length is calculated simply by summation across the array of elemental power generation value. We have calculated the total power dissipated by the probe at a 2mA current to be 0.37mW. Only 0.01mW of this value is contributed

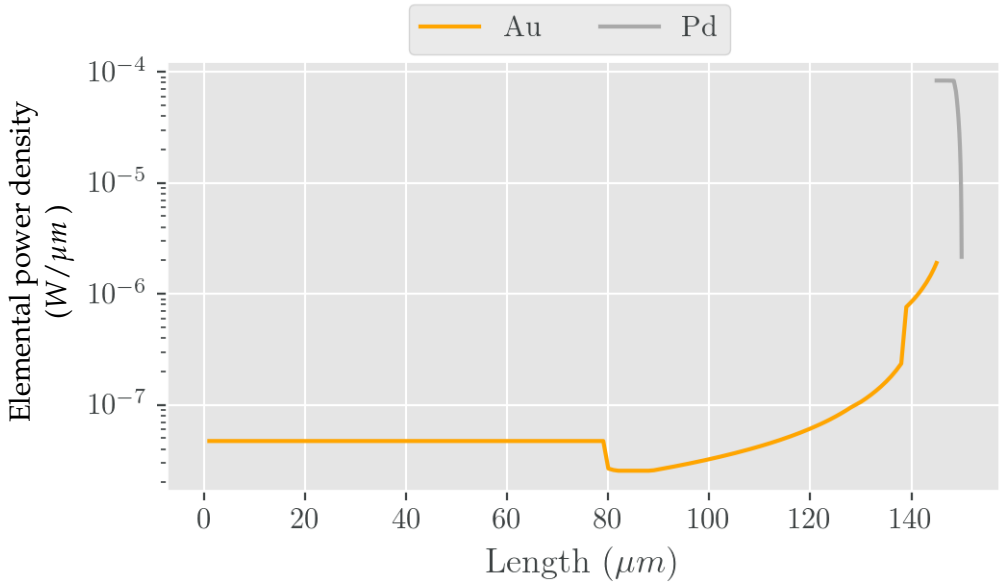

FIGURE 4.24: Power per micron as generated by the standard KNT probe when driven with a 2mA current. The gold layer (yellow) has a negligible contribution, while the palladium's (grey) power generation per micron is almost four orders of magnitude greater. The total power generated along the probe's length is 0.37mW

by the gold. Therefore, heat generation is localised to the palladium sensor region and we can consider gold's contribution to be negligible in this layout.

4.7.4 Solving for temperature

Once the conductance and power matrices have been formulated, there is enough information to solve Equation 4.15, which yields an array of nodal voltages, or temperatures in the thermal analogy. Figure 4.25 shows the temperature distribution of a standard KNT probe, whose thermal resistance was depicted in Figure 4.23 and whose power was shown in Figure 4.24. Here, the probe is shown operating out of contact with a sample, in a vacuum, and is thus the hottest it may be at this fixed current. We observe that the temperature distribution across the length of the probe is highly non-uniform, with the hottest point being found at the very apex of the probe. An approximately linear temperature distribution is observed along the body ($x < 140\mu m$) of the cantilever. Heat in this region is expected to strongly couple into the air when the probe is operated in ambient conditions, due to the cantilever's large, fin-like surface area.

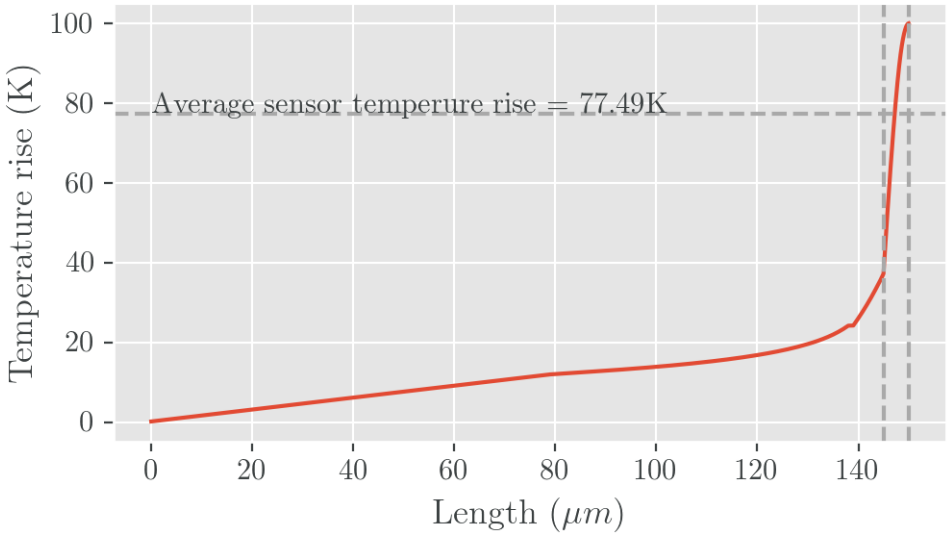

FIGURE 4.25: Temperature distribution of a standard KNT probe, out of contact, in vacuum, when driven with 1.5mA bias. The vertical dashed line indicates the extent of the palladium sensor. The horizontal dashed line indicates the average temperature across this region.

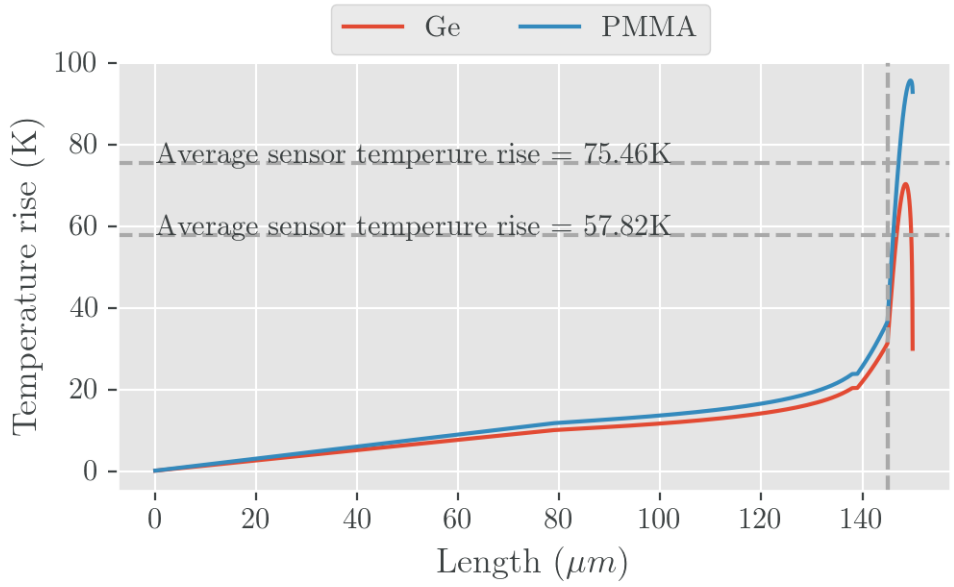

FIGURE 4.26: Simulated temperature profiles when the probe is contacted upon PMMA (k=0.187 W m^{-1} K^{-1}) and Ge (k=60 W m^{-1} K^{-1}) surfaces. $R_c = 8.33 \times 10^5$ K W^{-1},I =1.5mA.

4.8 Model Output - Probe Temperature Distribution

4.8.1 In-contact temperature profile

In Figure 4.25, we presented the simulation output for the probe out of contact, in a vacuum. In Section 4.7.3, we remarked that it is possible to model the probe-sample contact in a variety of ways by altering R_c and R_s in the thermal network as shown in Figure 4.16. A comparison of the probe's temperature profile when in contact with two materials of drastically different thermal conductivities is presented in Figure 4.26. As in the previous figure, the sensor's extent, and the average temperature across it are highlighted. We observe that for the low thermal conductivity material, PMMA (k=0.187 W m^{-1} K^{-1}), only the last few 100nm is cooled by the introduction of this material as route for thermal transport. This is very apparent in the magnified image presented in in Figure 4.37. The probe's peak temperature is located close to the sample, and the very tip of the probe is only a few degrees cooler than had it not been in contact at all (Figure 4.25). In the case of the higher-conductivity Germanium, (k=60 W m^{-1} K^{-1}) the effect of heat loss to the sample is far more pronounced and the location of the temperature maximum is close to the midpoint of the sensor. This behaviour has been identified and reported previously by groups using 3D multi-physics software [27], [173]. The form of the curves generated by our model

show good agreement with those presented in [173].

While these simulations provide a high-resolution estimation of the entire probe's temperature distribution, the data provided by experiment is far less detailed. The probe's output signal is a voltage, which is a single number that represents the spatial average of the sensor resistance [187]. This is, in turn, related to the temperature, and as such, the important figure of merit as far as predicting what the probe's output signal will be is the average temperature across the sensor region. In Figure 4.26, this is highlighted by dashed horizontal lines. It should be noted that this averaged-temperature-distribution behaviour is present regardless of the heating source, and holds true even when the probe is heated externally, such as in passive mode operation. In such cases, the probe may output the same signal despite drastically different temperature distributions [173]. Further discussion on the impact and implications of this averaging on the measurement, and probe performance, are to be found in Section 4.10.2.

4.9 Translating temperature distribution into a measure of device performance

4.9.1 What is performance?

In the passive mode of operation, the probe output is proportional to the temperature of the device under test. The 'performance' of the probe may be considered the thermal, spatial, or temporal accuracy with which the probe traces the sample temperature. While passive temperature measurements with SThM remain non-trivial to quantify, there is still a linear relationship between the output of the probe and the true device temperature, if one assumes a stable tip-sample thermal resistance.

In the active mode of operation, the 'performance' is a little more involved. In this mode of operation, the figure of merit is not the probe temperature, but rather the degree to which the heated probe is cooled by changes to its thermal environment. Typically, this mode has been employed with the aim of discriminating between solid materials of differing thermal conductivities. In this case, the performance of

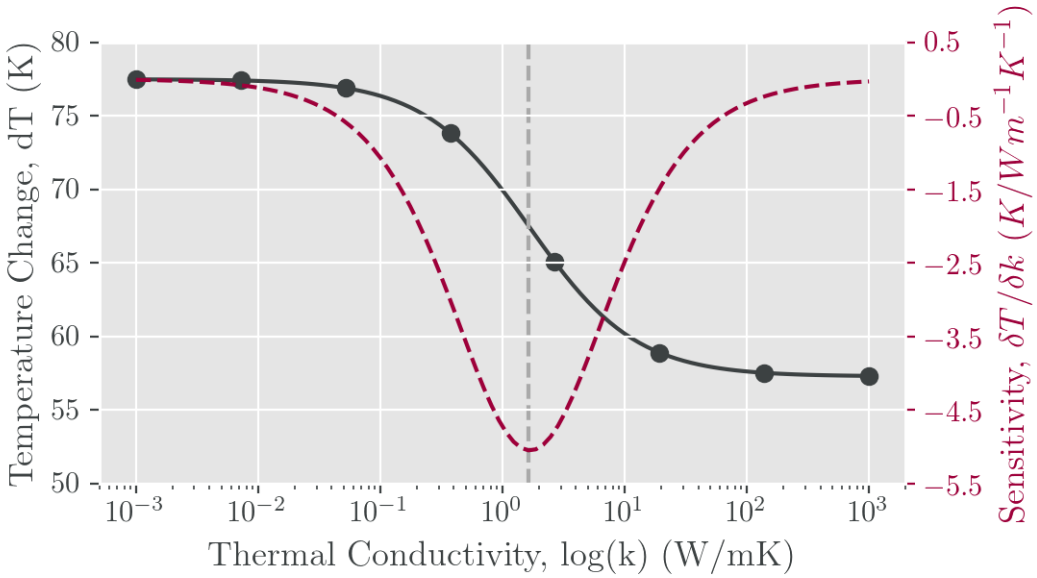

FIGURE 4.27: Average sensor temperature of the probe when placed in contact with samples across the a wide range of thermal conductivities (black). On the other axis (red) we have shown the derivative of this curve, which is a measure of the sensitivity of the probe.

the probe should be considered a measure of its sensitivity to changes in heat conduction through the tip-solid contact. In the next section, we will use the model to demonstrate how an active probe responds to the ideal case of variation in sample thermal conductivity with the assumption of a constant tip-sample contact resistance. Finally, we will present studies on how this contrast may be improved by altering the layout of the probe.

4.9.2 Modelling S-curves

Modelling of the performance of the probe in the active mode requires the simulation of the probe temperature distribution when a variety of thermal resistances are introduced to the thermal network. In the study presented in Figure 4.27, we have employed eight points, logarithmically-spaced between 1×10^{-3} and $1 \times 10^{3}\,\mathrm{K\,W^{-1}}$. This range covers from materials an order or magnitude less conductive than polymers such as PMMA, all the way to $1000\,\mathrm{W\,m^{-1}\,K^{-1}}$. This is sufficiently high to include state of the art materials for heat spreading in active devices, such as CVD polycrystalline diamond [220]. Taking the average of the sensor temperature across the sensing region gives a single temperature which is representative of the probe's output signal. These are shown in Figure 4.27 by black circles. These data are then

fitted by the solid line, whose form is a sigmoid, or S-curve which may be described by;

$$y(k) = \frac{Ak}{B+k} \tag{4.20}$$

in which k is the sample's thermal conductivity and A and B are fitting coefficients. This behaviour has been identified previously, and curves of this form have been employed throughout SThM studies [27], [166], [221], [222]. We highlight the usefulness of speed in our lightweight model here. Since the S-curve is the composite of multiple full-probe temperature distribution simulations, and we wish to compare multiple S-curves, the ability to generate these data quickly and/or parametrically is very beneficial.

The S-curve can be thought of as the response of the probe to variations in sample thermal conductivity (assuming constant Rc). However, this alone cannot be classed as the performance of the probe, which is rather the **change** in signal as a function of the change in thermal conductivity of the sample. To this end, we have added to the plot (Figure 4.27) the derivative of the S-curve with respect to conductivity axis. Henceforth we will refer to this derivative as the 'sensitivity' of the probe, having mathematical definition $\frac{\delta T}{\delta K}$ and units $K/\mathrm{W\,m^{-1}\,K^{-1}}$. We shall consider the magnitude and position of the peak of this curve as figures of merit to the performance of the probe. The sensitivity plot has Gaussian form centred around $2\,\mathrm{W\,m^{-1}\,K^{-1}}$, which suggests high sensitivity in the range of polymers and oxides, and is in excellent agreement with studies by other groups using FEA software [181] [27], further attesting to the validity of this model.

Why the S curve arises

These characteristic curves are the result of what we consider a 'thermal divider' configuration, which is analogous to a current divider in the electrical-thermal analogy. The simplest example of such a circuit is presented in Figure 4.28. Here, an ideal current source drives a circuit in which there are two branches through which

current may flow. The voltage at node V_1 varies as the ratio of resistance $R_1 : R_2$ having S curve form as seen in Figure 4.27. The form of the sigmoid is flipped because here we are plotting in R, whereas in Figure 4.27 we plotted against k, which has a 1/R relation.

When $R_2 >> R_1$, the current through this component tends to zero and the voltage at V_1 approaches the $I_{src}R_1 = 10V$. When $R_2 << R_1$, I_{R_1} tends to I_{src}, and the voltage at V_1 tends to zero. When R_2 has very low resistance, it is practically shorted, and the magnitude of V1 is dominated by the resistance of this pathway. We note that the 'centre' of the curve, the point at which the gradient is highest, occurs at $10k\Omega$, when R_1 and R_2 are impedance matched. It should be noted that, if the change in resistance of R_2 is the desired measurand, then this changes may be measured most sensitively for resistances around this value. The characteristic flattening of the S-curve at either extreme will henceforth be referred to as the saturation regimes, as the gradient of the curve in these regions is approaching zero.

In the active mode SThM measurement system, the thermal divider phenomenon arises because the heat used to probe the sample has the option of flowing through in multiple directions, as was outlined in Section 4.3. There are two branches of interest: into the sample, or not into the sample. The former would be equivalent to R_2 in Figure 4.28, while the latter is R_1. Studying this behaviour provides an idea of the limitations of SThM operation, but may also give clues as to how the performance of the probe may be improved through thermally-informed designs.

In the following sections, we discuss what defines the two saturation temperatures, and what, if anything, can be done to alter them through probe design.

Upper saturation temperature

At low thermal conductivities ($k < 10^{-2}\mathrm{W\,m^{-1}\,K^{-1}}$) the probe's temperature (and thus, the useful signal) saturates at a value equal to its out of contact temperature. It is reasonable to conclude therefore, that the summation of contact and sample spreading resistances are so large that no heat is transferred into this pathway, and is instead completely sunk through the cantilever to the base of the probe. If we assume infinite impedance into the sample branch of the network, we can conclude

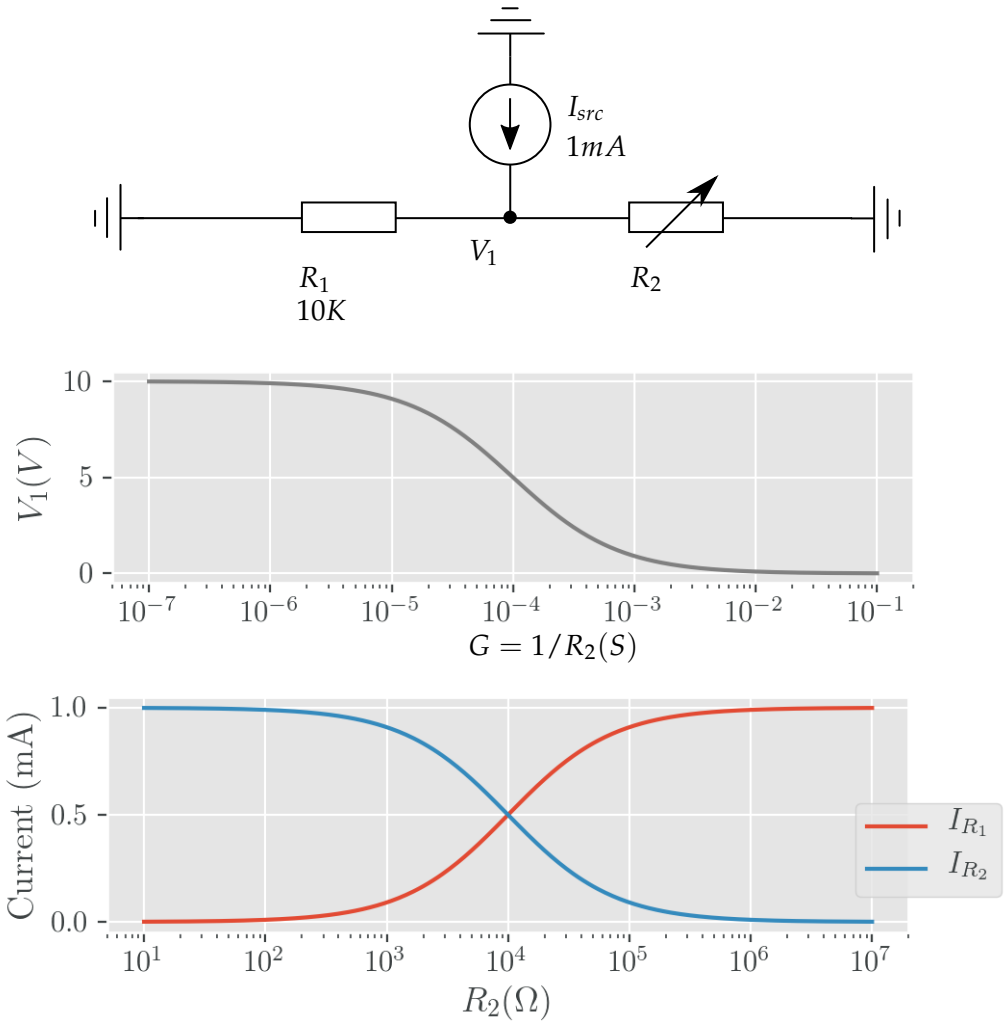

FIGURE 4.28: **Top:** Current divider circuit, which is the electrical analogue of the thermal divider behaviour demonstrated by the SThM probe. Component values are marked on the schematic. **Middle:** Nodal Voltage V1 as a function of the logarithmic sweep of the conductance of resistor R_2. **Bottom:** Current through resistors 1 and 2 and as a function of the logarithmic sweep of R2's resistance. Note that the maximum slope of the current through each resistor occurs at $10^4\Omega$, when the pair are impedance matched.

that the upper saturation temperature is the result of cantilever thermal resistance only. That is, in the case of these simulations, where vacuum has been assumed. If considering ambient operation, then the resistance of conduction to the environment would act to reduce this temperature.

Lower saturation temperature

At high thermal conductivities ($k > 100\,\mathrm{W\,m^{-1}\,K^{-1}}$), we observe a temperature floor. By this point, the probe has distributed as much heat as it can into the sample, and its temperature is not reduced despite any further increases in sample thermal conductivity. This behaviour arises because of the constant contact resistance, which is placed in series with the sample spreading resistance. Unless stated otherwise, we have used the value of $8.33 \times 10^5\,\mathrm{K\,W^{-1}}$ published by Ge et. al [32] throughout. In the lower saturation region, the low spreading resistance of the sample is dwarfed by the high contact resistance. A solid material with very high thermal conductivity such as $k = 1000\,\mathrm{W\,m^{-1}\,K^{-1}}$ would have a spreading resistance of $R_s = 5000\,\mathrm{K\,W^{-1}}$, which is two orders of magnitude smaller than contact resistance.

To demonstrate that this behaviour is indeed due to contact resistance, we present simulations in which we have varied R_c across six orders of magnitude. The results are plotted in Figure 4.29. We note that lower values of contact resistance allow for greater heat transfer into the sample and thus lead to a reduction in lower saturation temperature. Since the upper saturation temperature is not affected, the overall sensitivity of the device is improved. In this plot, we also observe a shift in the peak position, towards lower values of k (higher R_s) for higher values of R_c. This is a result of the impedance matching behaviour demonstrated in Figure 4.28.

We note that probes with larger tip radii, and thus a lower R_c, have sensitivity peaks located at higher conductivities than the nanofabricated probes which are the topic of the present work. For example, in a study by Chirtoc et. al, Wollaston wire probes were shown to have maximum sensitivity in the region of $20\,\mathrm{W\,m^{-1}\,K^{-1}}$, with an estimated tip radius of 120nm [223]. This is in contrast to the $2\,\mathrm{W\,m^{-1}\,K^{-1}}$ and 50nm radius observed for the KNT probe.

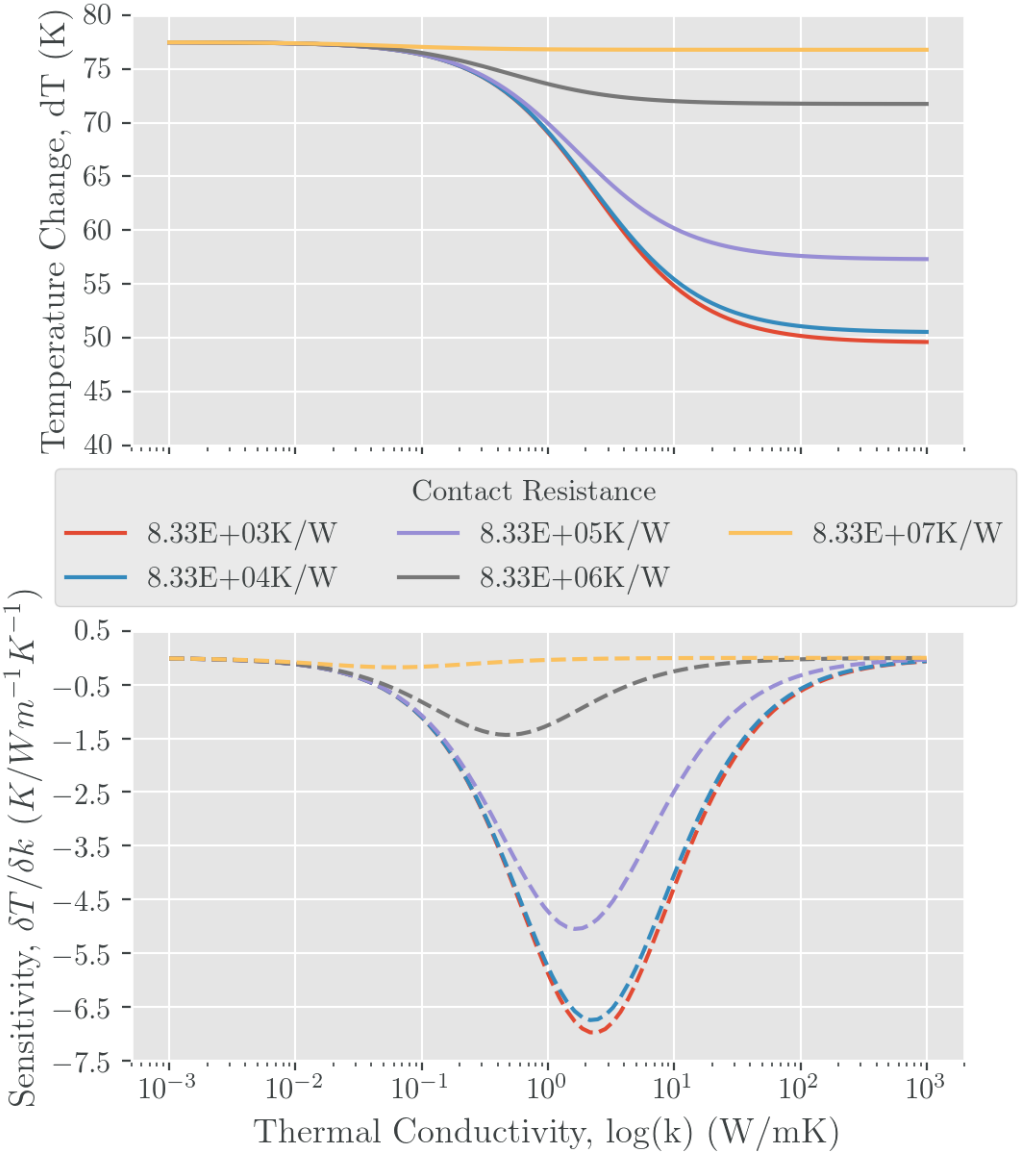

FIGURE 4.29: Tip average temperature (above) and probe sensitivity (below) plotted across the range of thermal conductivities. The various lines represent a value of contact resistance ranging from $8.33 \times 10^3\,\mathrm{K\,W^{-1}}$ to $8.33 \times 10^6\,\mathrm{K\,W^{-1}}$.

If we wish to increase the sensitivity of the thermal probe to changes in tip-sample conductance (which is required for the measurement of k), then one option would be to address the problem of contact size, which features in both contact resistance and spreading resistance, with $1/b_c^2$ and $1/b_c$ dependences respectively (Equations 4.10 and 4.11). While increasing the contact area would certainly increase the sensitivity of the devices, it would significantly diminish the spatial resolution of the technique. To achieve the high resolution measurements which make SThM an attractive alternative to diffraction-limited optical methods, one necessarily must employ a very sharp tip, through which very little heat may flow (Equation 4.10). Since resolution is one of the greatest appeals of the technique, it is desirable to find a method for increasing the sensitivity of SThM probes without resorting to a method which causes a reduction in spatial resolution.

4.10 How can performance be improved

In this section, we discuss possible methods for improving the sensitivity of active mode SThM through probe design. We address two different approaches which address the thermal and electrical properties of the probe respectively.

4.10.1 Thermal properties

An alternative approach to reducing the contact resistance is to consider the interfacial thermal resistance R_b, which is dependent upon the phonon mismatch between the bodies in contact. Wang et al [198] present evidence that the interfacial thermal resistance is minimal between two materials of similarly high Debye temperatures, and maximal between materials with dissimilar Debye temperatures. This has been employed in the context of SThM by Timofeeva et. al [165], who attached a carbon nanotube to the apex of the KNT probe. They present evidence of minimised contact resistance between the CNT-SThM and an Aluminium surface. Unfortunately however, the procedure necessary to attach and sharpen the CNT are not amenable to batch fabrication, making such probes challenging to fabricate, with low reproducibility. It is our goal in the present work to investigate if an alteration in the

fabrication of the commercial, batch-fabricated devices may make them more suitable for thermal conductance measurement. Note that it may be possible to to alter the Debye temperature ratios through an alteration in the probe materials stack, however we are limited to the materials we can use with our current fabrication capability.

Therefore, in this section, we investigate the possibility of improving sensitivity by increasing the upper saturation temperature. The first, and perhaps simplest approach, is to increase the power with which the probe is operating. While it is true that this would effectively increase the probe's sensitivity to sample thermal conductivity, there is are physical limits to the maximum power the probe can tolerate. Firstly, there is a certain current density beyond which the probe's sensing element fails due to electromigration. When considering the standard probe designs here, we use bias currents of between 1.5 to 2mA which represent the safe operating ranges for maximum self-heating (and thus sensitivity).

A second phenomenon limits the practical operating temperature of the probe, especially in vacuum environment. The bi-material bending problem that is characteristic of these thin film SThM probes [171] means that there are mechanical issues with scanning these devices at significantly elevated temperatures. The bending is caused by the thermal expansion of gold being greater than that of SiN. As such, those regions of the cantilever with a large surface area of contact between materials will experience the greatest thermal bend. If we could adjust the temperature distribution such that a larger proportion of the net heat were localised to the tip rather than the cantilever body, one might reasonably expect a reduction in the degree of thermal bend caused by self-heating.

Increasing the drive current of the probe is unfavourable due to the above reasons. However, it is possible to increase the temperature of the probe by increasing the thermal resistance of the cantilever. Doing so will additionally skew the ratio of heat flux into each side of the thermal divider, such that a larger proportion of the generated heat into the sample. The definition of thermal resistance associated with conduction through multilayer solids was previously discussed Section 4.2.4. Given the

limits imposed by the available fabrication methods, we choose to focus on geometric alterations as opposed to modifying the material stack. In the following sections we present some possible changes and investigate their effect on probe performance.

Reduction of gold volume

An insight into a simple method for increasing the probe thermal resistance can be gained from Figure 4.23, in which the thermal resistance per µm for each material was presented. We note that in the parallel summation of elemental resistances, that the profile of this line almost mirrors that of the gold pads alone. This suggests that the thermal resistance of the probe is dominated by the thick gold leads in this region. One possible approach to increasing the upper saturation temperature would be to significantly reduce the volume of gold present on the cantilever. However, there must remain sufficient coverage to allow the cantilever to maintain functionality as an optical lever. In addition, reducing the volume of the leads would increase their resistance. In the two-terminal sensor configuration found in the commercial probes, this change would reduce the sensitivity of the probe to changes in tip sample conductance, which is in opposition with our aim.

Selective removal of SiN

An alternative method of increasing the thermal resistance of the cantilever would be to introduce constriction regions through the selective removal of the SiN cantilever. These narrower areas act to restrict heat flux in this region and increase the overall thermal resistance of the cantilever. Critically however, they introduce a **local** resistance increase. Consider the design presented in Figure 4.30A, in which a portion of the base has been removed such that the cantilever is connected to the chip through two narrow beams only. This design has been featured in piezo-resistive cantilevers, since such reductions in width can concentrate stress and alter the bending mechanics of the cantilever [224]. In the context of SThM, such restrictions would indeed increase the overall thermal resistance of the cantilever, and would have a significant effect in vacuum. However, their location at the base of the probe means that, in ambient operation, a great deal of heat will be lost through fin-like surface exchange with the environment **before** reaching the base. Heat confined to the body of

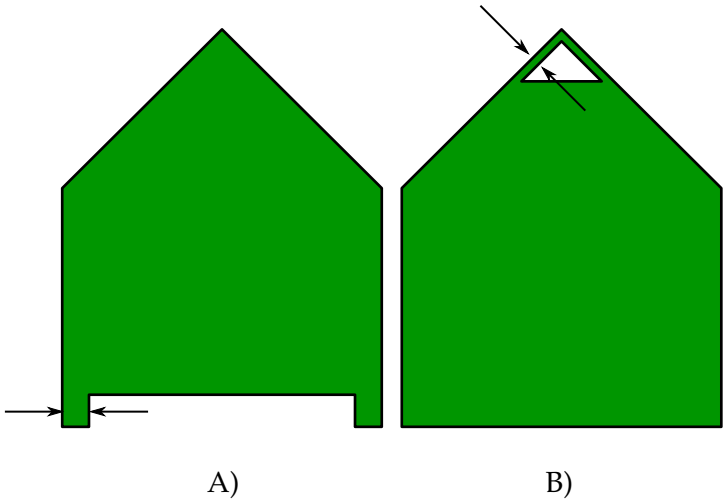

FIGURE 4.30: Schematic drawing of two approaches to increase the cantilever thermal resistance through selective SiN removal. **A:** A rectangular segment removed from the base of the cantilever. The cantilever is affixed to the chip by two beams only. **B:** A triangular segment removed from the tip such that a pair of pair or narrow beams is isolated from the rest of the cantilever.

the probe is efficiently lost to the environment, and what remains there contributes to the thermal bending.

Contrast this approach with that of Figure 4.30B: in which the cut-out region has been imposed at the tip of the cantilever. In this design, the local resistance increase is imposed between the heater and the body of the cantilever, rather than between the cantilever and the chip. Once heat is passed into the cantilever body, it is too late to contribute to probe performance. Instead, what is required is to encourage heat into the sample at precisely the location of heat generation, which may be realised through maximising the thermal resistance between the heated region and the probe body. In the following sections we use the model to investigate the impact of this approach on the cantilever's temperature distribution and overall performance.

Cut-out probe simulations

The model was used for the simulation of a variety of probes with material selectively removed from the tip. The principle of the approach is plotted in Figure 4.31. Considering the line of symmetry, the shape to be removed is a right angled triangle whose hypotenuse runs parallel to the tapering edge of the cantilever. This shape is chosen such that constant width beams are formed, upon which the sensor can

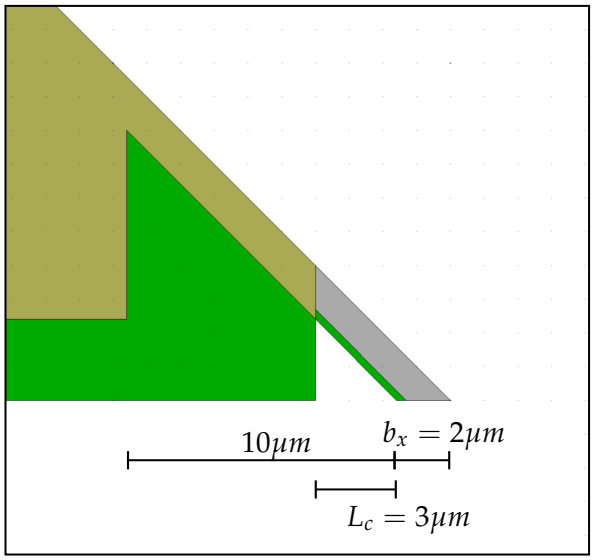

FIGURE 4.31: Schematic drawing the cut-out probe design along the axis of symmetry, with critical dimensions labelled. In the simulations, we have kept the beam width constant, ($b_x = 2$ µm) and varied L_c from 1 to 10 µm.

be fabricated. Its size and position can be described by two numbers only; cut-out length, L_c and beam width in the x direction, b_x. This shape can fully describe the situation in which the beams are equal in width to the heater which they support, which achieves the greatest possible thermal resistance attainable with this method.

In the following simulations, b_x was maintained at 2 µm, while L_c was increased from 1 to 10 µm (towards the base of the probe). The layout of the Au pads is adjusted such that the all designs feature the same electronics regardless of cut-out size. This ensures that any changes in sensor temperature are purely the result of geometric alteration. The 'wings' of the commercial probes pads have been removed to minimise the gold present on the cantilever, without significantly increasing the electrical resistance of the leads. Their layout may be seen clearly in Figure 4.32. All probe designs were drawn in L-Edit and saved to GDSII format, before being fractured and simulated using the model developed by the author [4]. Figures 4.32 compares results of the simulations for $L_c = 0$ and $L_c = 10$ µm

Note that in both cases the power generation takes the same form, and has the same overall magnitude. In the middle plot of Figure 4.32, a region of constant resistance

[4]Code repository hosted at: https://github.com/RL-AFM/SThM-Cantilever-Thermal-Model

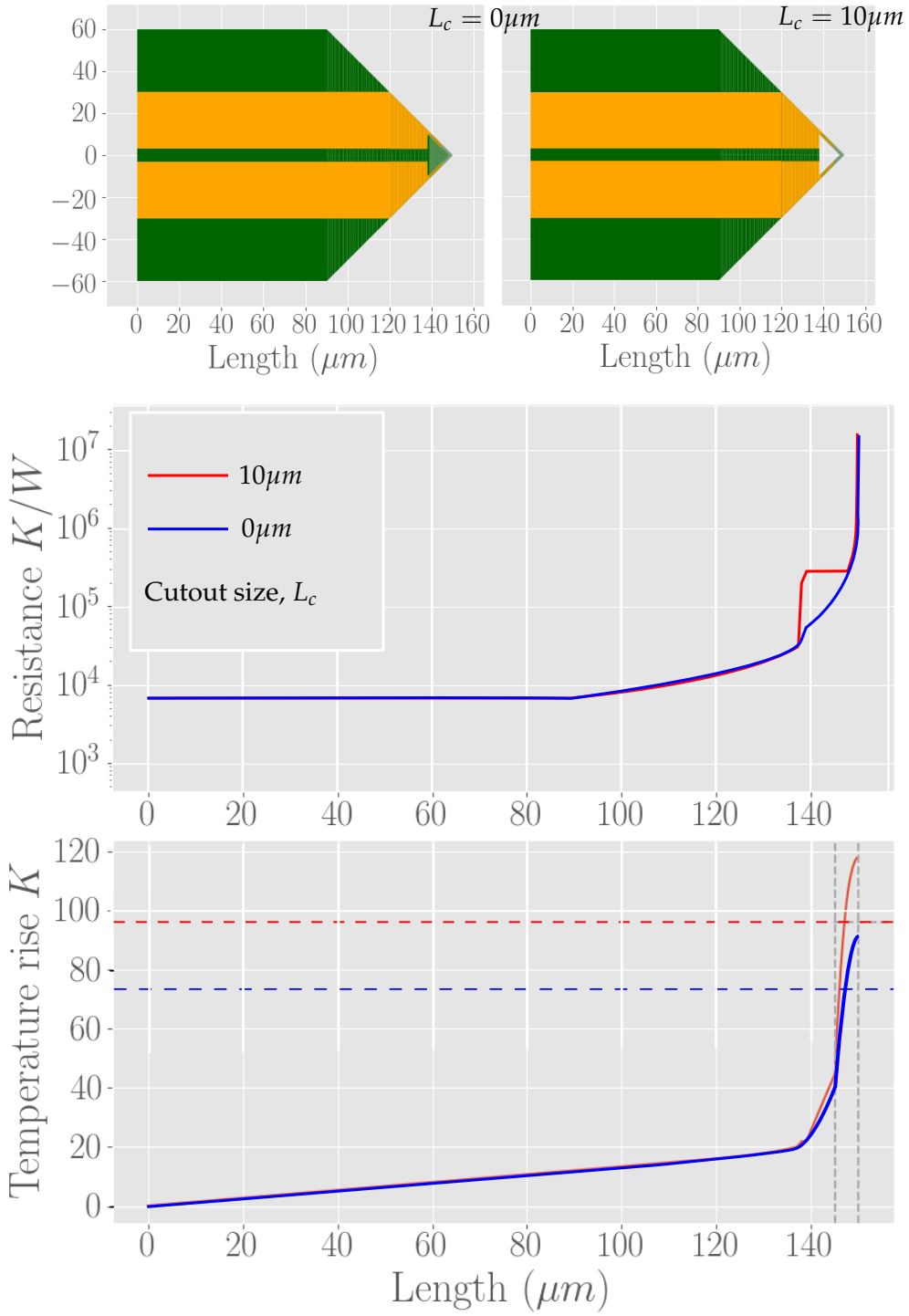

FIGURE 4.32: Comparison between simulations of a probe with and without a 10 µm cut-out. **Top:** Schematic drawings of both probes. **Middle:** Elemental thermal resistance comparison. Note in the cut-out probe (red) the region of constant thermal resistance from 138 µm to the apex. This is the result of the constant, narrow beam width. **Bottom:** Out of contact temperature profile comparison. The sensor region is highlighted by dashed vertical lines, while the average across this region is shown by dashed horizontal lines. The average temperatures for the cut-out and non cut-out are 95.88 and 73.73K respectively. The current used to drive the probe was 1.5mA (corresponding to 184 µW) in both cases.

Cut-out size (μm)	Average Sensor Temperature Rise (K)
0	73.73
1	74.76
2	79.72
3	91.58
4	91.99
6	93.11
8	94.62
10	95.88

TABLE 4.4: Size of cut-out vs. average temperature rise of the sensor, when provided 1.5mA, out of contact, in vacuum. There is a significant increase in temperature between $L_c = 2$ and 3. This is the result of the thermal resistance behaviour, which is plotted in Figure 4.33.

is observed from 138 μm onwards in the SiN layer. This is the result of implementing beams with constant width in this region.

The metric 'total thermal resistance' was previously reported as the summation of the thermal resistance of every element of the cantilever, from the tip to the base. (Figure 4.23). The total thermal resistance between the two probes presented in Figure 4.32 is increased by 8.7% due to the introduction of the cut-out region (from 2.17×10^6 to $2.36 \times 10^6\,\mathrm{K\,W^{-1}}$). Note however that the overall resistance is dominated by the constriction at the very narrow tip, whose value is nearly two orders of magnitude greater than that of the cantilever at 130 μm and below. Note that the overall resistance given by this metric is most relevant for heating the probe via solid contact to the tip, not internal generation. In the case modelled here (in vacuum, out of contact), heat is flowing towards the base of the probe only, and is thus largely unaffected by the constriction resistance caused by tapering tip. In the following section, we will identify an alternative expression of thermal resistance which factors in the temperature gradient caused by internal heat generation.

While the difference in thermal resistance appears modest, the change in temperature distribution is clearly significant. The probe with no cut-out has an average sensor temperature rise of 73.73K, while the same probe with a 10 μm cut-out has an average sensor temperature rise of 95.88K, representing a 30% increase. Table 4.4 present the full set of results for the various cut-out sizes tested.

We observe a large change in the sensor temperature rise from the 2 μm cut-out to the 3 μm one. This length (3 μm) coincides with the extent of the sensor, as can be

observed in Figure 4.31. From this we can conclude that there is significant impact to the temperature distribution when removing material up to the sensor. At which point it cannot be further isolated from the cantilever with the present fabrication procedure.

This can be understood by considering the effective thermal resistance of the cantilever. However, the term 'thermal resistance' of the cantilever is not meaningful unless the source of heat is also addressed. The thermal resistance of the cantilever to its own internal heat generation will not be the same as to external sources, even disregarding contact resistance. This was a key motivation for the development of the distributed thermal model. The Joule heating temperature is not a 'node' connected to a single lumped thermal resistance, and it is not always appropriate to treat it as such.

Here we describe the 'effective thermal resistance', which we shall define as the thermal resistance of the cantilever, in free space (no contact), in a vacuum. This figure has already been calculated experimentally by Assy et al. [170], who utilise the equation;

$$R_p = \frac{T_{apex} - T_{ambient}}{P_p} \tag{4.21}$$

In which the T_{apex} is the average sensor temperature, $T_{ambient}$ is the ambient temperature, and P_p is the power dissipated in the probe. Using this method, they were able to calculated the effective thermal resistance of the probe as $5.2 \times 10^5\,\mathrm{K\,W^{-1}}$.

It is possible to recreate this experiment in our model by simply implementing a virtual current sweep of the probe. Thanks to the lightweight nature of the model, this routine can be performed in a matter of seconds. For the commercially available probe such as the one used in their study, we reach a value of $3.32 \times 10^5\,\mathrm{K\,W^{-1}}$, which is very close to their experimentally determined value.

We were not able to verify the model through the use of a vacuum system, however we find the fact that these result to be in good quantitative agreement with the published literature to be good evidence for its accuracy. This encourages confidence in

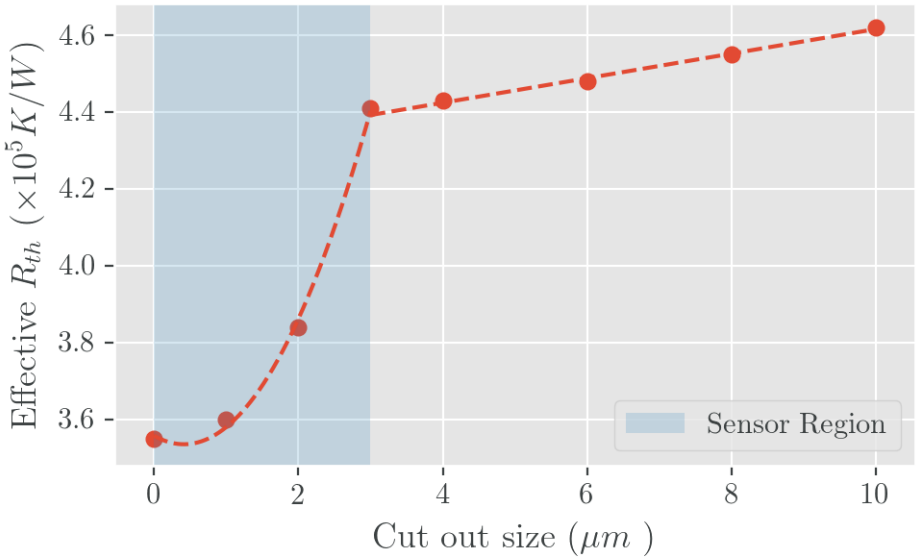

FIGURE 4.33: The effective thermal resistance of the probes as a function of the cut-out size. The length along the x-direction to which the sensor extends is shaded. Within the extent of the sensor, removal of cantilever has a strong influence on the effective thermal resistance, which has been fitted here with a 2nd order polynomial. Beyond the sensor region, removal of additional material is shown to have much less influence. In this region, a linear fit appears appropriate.

the trends reported by the model.

It is possible to employ the 'effective thermal resistance' in this study to understand the impact of removing select portions of the cantilever. As noted from Table 4.4, there is a drastic difference in the average temperature rise between the cut-outs which remove material adjacent to the sensor, and those which remove additional material. This occurs despite no change in the generated thermopower, and is therefore only dependent upon the thermal resistance. In Figure 4.33, we present the effective thermal resistance as a function of the cut-out size. We observe about 30% increase in effective thermal resistance (between no cut and 10 µm cut): this mirrors the average sensor temperature increase presented earlier.

Localisation of heat

The cut-out induces an increased thermal resistance. Because we have localised this resistance immediately adjacent to the sensor, it is reasonable to assume that, not only has the **overall** probe temperature has increased, but also that such a change would localise the generated heat to this region. To test this hypothesis, we use

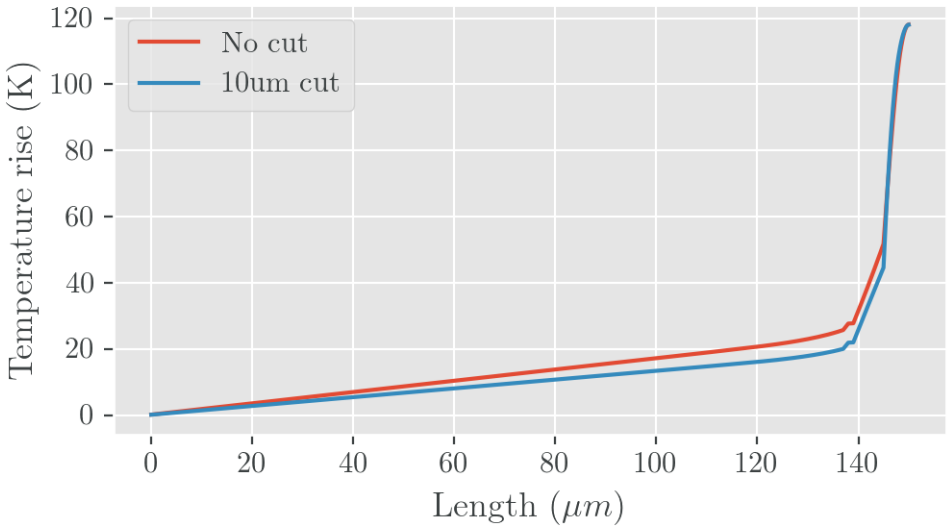

FIGURE 4.34: Comparison of temperature profiles required to read the same tip temperature in the non-cut-out and 10 µm cut-out probes. The cantilever body of the non-cut-out probe is increased compared to that of the cut-out probe when reading the same tip temperature.

the model to compare the out of contact temperature profiles of two probes. The first is the cut-out probe, size 10, run at 1.5mA, which is the typical current that has been used in all figures in this chapter (unless stated otherwise). Its total power generation is 184 µW , and its average sensor temperature is 95K above ambient. Next, we find the bias current required to achieve the same signal (average sensor temperature) from the non-cut-out probe. To achieve the same heating at the tip requires 1.7mA, 237 µW for the non-cut-out probe. The additional power serves to raise the temperature at the base of the sensor to a similar level to that of the cut-out probe. This results in the non-cut-out probe having a steeper temperature gradient. The 20 µm span between 100 and 140 µm has a temperature at least 5 degrees higher for the non-cut-out than the cut-out design.

Finally, we can use the model to predict the performance of the probes in the active mode by plotting their S-curves and sensitivity plots, as shown in Figure 4.35. As with the previous figures, we observe a large change in signal when removing cantilever material within the sensor region, followed by only modest improvements with increasing cut-out size. From these data, we can predict a 30-40% increase in sensitivity through the implementation of this change. This suggests that such

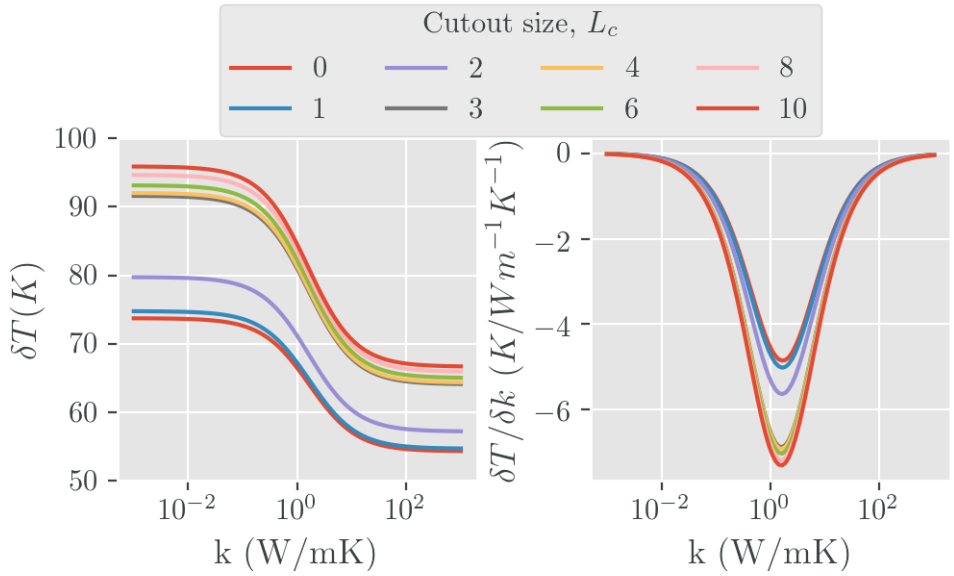

FIGURE 4.35: **Left:** Tip temperature above ambient as a function of the thermal conductivity of the sample with which it makes contact, plotted for the same variety of cut out sizes used in Figure 4.33 and Table 4.4 **Right:** Sensitivity of said probes to materials across the same range of thermal conductivities.

Cut out size, L_c (μm)	**Maximum percentage heat transfer into sample (%)**
0	26.26
1	26.78
2	28.20
3	29.96
4	30.01
6	30.13
8	30.28
10	30.41

TABLE 4.5: Percentage of generated heat transferred into the sample as a function of cut-out size

probes would be able to discriminate between more subtle differences in tip-sample thermal conduction, and that the range of materials which it can differentiate will be increased (slightly, by the wider tails of the distribution).

This change allows the probes to be operated at higher temperature without increasing the bias current. Since electro-migration is a frequent failure mechanism of these devices, this would be a valuable change.

Any increase in the resistance of the system, anywhere, will increase the temperature of the probe (node T_p in Figure 4.6). This was a contributing motivation to treat heat generation as an ideal current source. Clearly there is an increase in temperature,

which can increase sensitivity of the probes. The question arises as to how much of this increase is due to the probe's being run hotter, as opposed to the alteration of the resistance ratios of the 'thermal divider'. By taking the quotient of the lower and upper saturation temperatures, we can normalise the results for varying temperatures. Table 4.5 presents the maximum proportion of the generated heat which may be transferred to the sample for each of the various cut-out probes.

This table shows that it is not only the increased operating temperature that causes the increased sensitivity, but also the alteration of the resistance ratio in the 'thermal divider' configuration. Note also that the impact of this change is attenuated by the high contact resistance of the system; a more blunt probe would see more drastic sensitivity increases as a result of this change. As previously discussed however, the high resolution of SThM is one of its major advantages, and it is not desirable to reduce this resolution for the sake of increased thermal conductivity contrast. The high contact and spreading resistance is also why little change in the position of the peak sensitivity is observed. The increased cantilever resistance induced by this change is still small when compared to the resistance of the other side of the thermal divider.

4.10.2 Electrical properties

In the previous section, (Section 4.10.1) we identified how the sensitivity of the probe could be improved by engineering the probe's thermal performance. We have shown that one may manipulate the ratios of heat flux into the probe and sample by introducing simple changes to the probe's geometric design. However, the thermal divider phenomenon (esp. contact resistance) means there is a physical limit to the improvements one may make with this approach. There are other avenues to explore regarding the sensitivity of SThM probes however. In this section, we will analyse the electronics used to interrogate the sensor, and discuss potential routes for optimising the probe's signal.

Removal of confounding resistance contributions

The output signal of the SThM is a fractional change in resistance induced by the temperature of the probe. Ideally, only resistance changes of the probe's sensor region would be considered. Unfortunately however, there are a great many other resistances within the circuit which may add noise or attenuate the signal from the probe. A schematic of the typical resistance measurement is presented in Figure 4.36

One method for removing the influence of these resistors is to implement a Kelvin, or four terminal sensing configuration. In this set up, one pair of wires (force), provide current to the circuit under test, while another pair of wires (sense) measure the voltage drop. Assuming infinite voltmeter impedance, the resistance of its connecting wires may be ignored, since no current flows along them. In Figure 4.36, we present a possible four terminal arrangement in which the additional two terminals have been connected directly to the sensor of the probe. The requires alterations to the lithographic design of metal layers on the probe itself, and therefore represents quite a significant change. A less challenging, but less impactful four terminal measurement could also be made by bonding four wires to the two pads of the commercial probe, thus negating the contributions from the external wiring and bonding.

In Figure 4.36, additional terminals connected to the sense lines also have resistances associated with the gold leads, external wiring and bonding, however these have minimal impact upon the measurement due to the fact that no current flows through them due to the high impedance of the voltmeter. It should be noted that they still introduce Johnson noise, however. This allows some freedom in the patterning of the gold wires in this arrangement, since we no longer need to minimise the resistance of the gold layer. The force connections need to have sufficient volume such as they do not self heat. The sense connection can be arbitrarily narrow. The 'best' layout for gold is non-trivial, as it requires consideration of the thermo-mechanical properties, whilst also maintaining functionality as an optical lever.

Remove limiting NiCr resistors

The commercial probes feature two $100\,\Omega$ NiCr resistors which increase the overall probe resistance by a factor of three. In the commercial devices, this is employed to

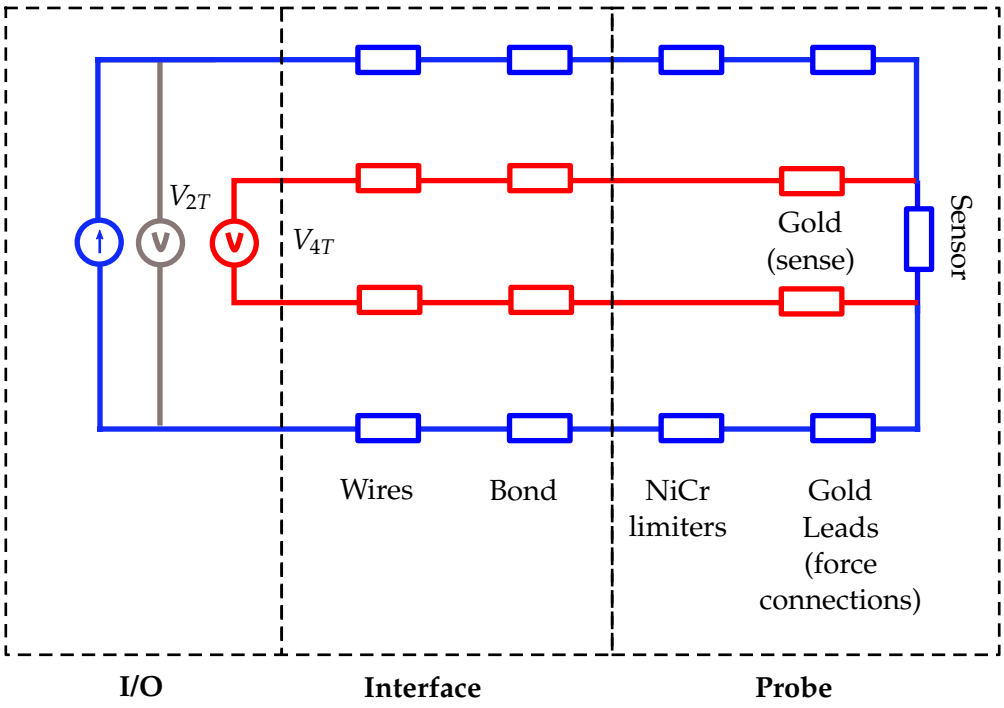

FIGURE 4.36: Circuit diagram highlighting the advantage of a four terminal setup. In a traditional two terminal setup, the resistance of the probe is calculated from it's voltage when provided constant current. The current carrying loop is highlighted in blue. Each resistor along this path contributes to the measurement. This includes the resistances of the metal on the probe, the bond to the holder, and the wires connecting the assembly to external circuitry. Only changes in the sensor resistance are desired, however. By implementing a four terminal measurement structure (red), we eliminate the contributions from all other resistances

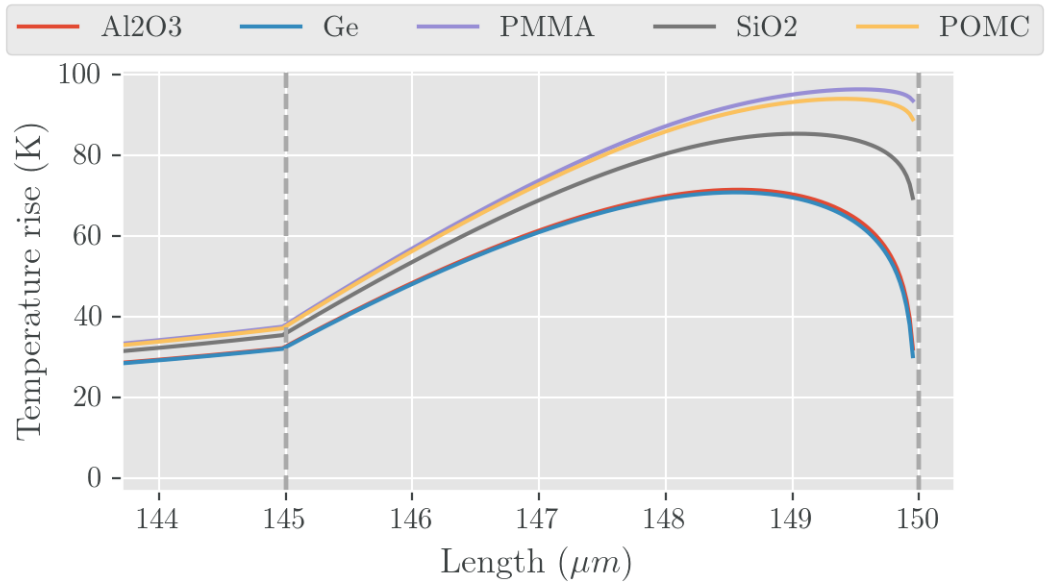

FIGURE 4.37: Simulated temperature profiles across the sensor region (outlined with dashed lines) when the probe is contacted upon materials of various thermal conductivities. The materials used are all from the Quantiheat set, whose thermal conductivities were presented in Table C.1. $R_c = 8.33 \times 10^5\,\mathrm{K\,W^{-1}}$, I =1.5mA.

trim the sensor resistance, which varies as a function of sensor width. This variance is the result of poor 'self-alignment' of sensor to the tip. While these resistors serve to keep the commercial devices within reasonable specification, they also reduce the sensitivity of the probe to changes in the resistance of the tip. For all the probes fabricated in this work, these resistors have been removed. Our custom bridge and probe driving electronics have sufficient range that these resistors are not required to permit bridge resistance balancing.

Localisation of resistance - averaging

Figure 4.37 compares the temperature profile of the commercial probe when contacted to materials with thermal conductivities spanning two orders of magnitude. The actual conductivities of each material may be found in Table C.1 in Appendix C. As was presented in Figure 4.26, the average sensor temperature between the lowest and highest thermal conductivity materials were 75.46 and 57.82K, representing a maximum difference of 17.64K. This difference is relatively small due to the averaging of the sensor temperature. We observe that the temperature profiles generated by each of the materials is very similar until the final 1.5 µm of the probe. The fact

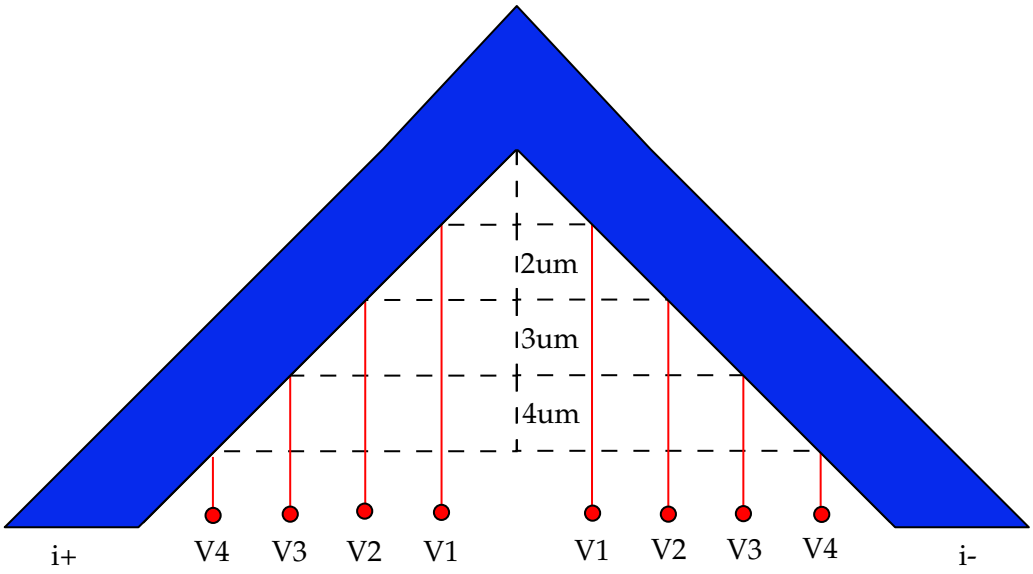

FIGURE 4.38: Adding sense terminals to the existing sensor allows to average over different regions of the heater.

that cooling appears at the very apex of the device, and that this part makes up a small area of the resistor means that the sensitivity to different materials is severely diminished. This cooling behaviour is non-controversial; having been identified by multiple groups using FEA [27], [181]. Very good qualitative agreement with Figure 6 of Bodzenta et al's study [181]. Considering only the last sample of the data, the temperature difference between PMMA and Ge is 93.7 - 30.2 = 63.5K; a drastic improvement over the initial value. But the sensor still must have some finite size, which will be limited by fabrication capability. By localising the sensor to the tip, it may be possible to recover some of the sensitivity which was previously being lost in the averaging operation.

To explore this idea further, the model was used to test the sensitivity of a commercial-style probe, whose temperature is the average of an ever smaller area approaching the tip. This may be realised physically by adding the two additional terminals required for the four terminal method outlined above, then connecting to the existing sensor with diminishing separation, as shown schematically in Figure 4.38. Analytically, it is only necessary to adjust the extent of the averaging operation. This has the advantage of keeping the thermal and electrical properties of the probe the same such the problem may be considered in isolation.

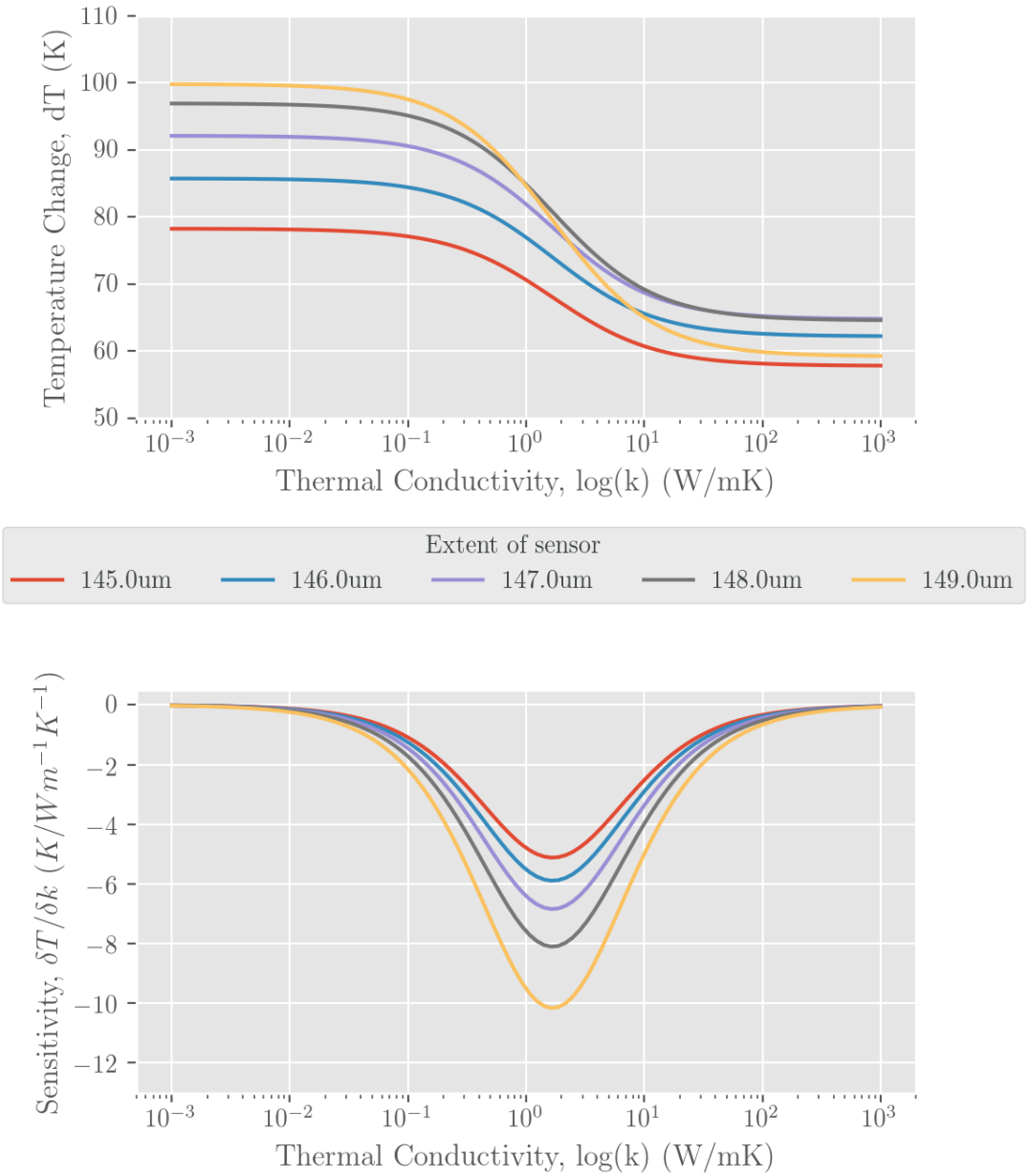

FIGURE 4.39: The sensitivity plots of probes in which iteratively smaller portions of the temperature profile are considered in the average.

The results of these simulations are presented in Figure 4.39. Together with Figure 4.37, a number of useful design rules for the optimisation of active mode SThM probes may be inferred. Examining the temperature distribution as it varies with sample thermal conductivity shows that there is a peak temperature which shifts from L=150 µm further left with increasing conduction into the sample (k). In the limit, this peak location represents the maximum length of the probe which may possibly be cooled by contact with a sample of high thermal conductivity (with this contact resistance, $8.33 \times 10^5\,\mathrm{K\,W^{-1}}$, in a vacuum). In the case of the commercial probe, under these conditions, that distance is calculated as 1.5 µm from the tip (L=148.5 µm). From this, we conclude that a sensor with extent equal to or less than this is desired. The data to the left of this location contributes far less useful data to the measurement than the data to the right, because the differences between the form of the curves is minimal in this region. Outside of the 1.5 µm extent, the sensor is influenced only by changes to the cantilever temperature and noise. Perturbances of the cantilever temperature may be caused by the laser optics, or positioning the cantilever above a heated sample region, as per Figure 4.10.

In Figure 4.39, it is observed that removing contributions from beyond the critical distance (L< 148.5 µm) raises both the upper and lower saturation temperatures, since part of the temperature distribution curve with positive gradient is cut off in each case. As the critical value is approached, the lower saturation temperature is observed to begin to fall, as the part of the temperature distribution beyond the curve's maximum starts to become more heavily weighted in the average. The increased upper, and decreased lower saturation temperatures act together to result in a sensitivity double that of the standard probe (Figure 4.39, lower plot.)

This simulation considers only the temperature differential, and not the resistance change. As the measurement is taken closer and closer to the tip, the base resistance of the probe is reduced. While this is not problematic as such, it becomes more difficult to measure changes in a small resistance at fixed current. Therefore, what is desired is the maximal resistance in the area of most drastic temperature change. We have defined the region of temperature change, but what is the limit to the resistance that we can pack into this area?

The region of maximum temperature change has been defined, the remaining challenge is how to maximise the resistance which may be imposed in this small area.

One limitation arises due to the electrical properties of the thin film sensor. These probes have been shown to fail reproducibly to electromigration damage above a certain current density. This metric can also be thought of as a maximum resistance-per-unit area. There will exist some point at which measurement with such low currents becomes impractical. While the resistance may be increased by reducing the sensor cross-section, the current will have to be reduced in turn to remain in accordance with the maximum current density. This will impose a limit on the heating that the probe can provide. A solution is that the 'sense' region does not need to comprise the entirety of the 'force' (heated) region. In a situation such as was in Figure 4.38, choosing the innermost V terminals, current is passed through the entirety of the blue 'force' region, while the sensing only occurs locally. This is one strategy that can be employed to reduce the problem of limited heating in localised heaters.

In Section 8.6.4, the optimal design for heating and sensing is discussed. Prior to that section, we consider the fabrication methods and how they will impose limitations on the structures that can be achieved. From this chapter it is concluded that;

- Only the final 1.5 µm of the tip is cooled by probe-sample contact
- The resistance measurement should consider only this region for maximum sensitivity, and the resistance of the sensor in this region should be as high as possible.
- The heating and sensing region should be de-coupled from the rest of the cantilever as much as possible. This may be achieved through implementing a sufficiently large cut-out that the sensor stands alone on isolated beams

In the next chapter we will discuss how such requirements might be realised, and the fabrication changes necessarily to facilitate these changes.

Chapter 5

Improvements to Electron Beam Lithography on Topographic Substrates

5.1 Required fabrication improvements

5.1.1 Intro

In the previous chapter, we outlined how changes in the layout of the cantilever and its electronics could improve performance of the SThM probe. The definition of both the cantilever hard-mask, and the sensor circuitry is performed using electron beam lithography. The full probe manufacturing process was presented in Chapter 3. An important conclusion of the previous chapter is that the heater/sensor region should have high resistance within the final 1.5 µm of the probe. To achieve this goal will require alignment accuracy of better than 250nm, and sensors on the order of tens to hundreds of nanometres in width.

5.1.2 Why are thin lines required?

Maximising the resistance of the RTD will be achieved through reducing its line-width. Recall that the resistance of a wire is inversely proportional to its cross sectional area. While the cross section could be reduced through reducing the thickness of the film, this method is not preferred. The present deposition is targeted for 40nm. Attempting to deposit a thinner layer runs the risk of not forming a continuous film,

or introducing defects that act as failure nucleation sites. In addition, reducing the thickness of the film to, or below the mean free path of electrons will cause the resistance to become dominated by interactions with the film boundaries, rather than temperature dependent lattice interactions [225]. Therefore, we should aim for a reduction in line-width. In Section 5.3, we will identify the challenges associated with achieving narrow line-widths on the topographic substrates used in this work.

In addition to reducing the sensor width to maximise electrical resistance, we may also wish to reduce the width of the SiN beams which form the 'cut-out' at the apex of the probe. This will increase the thermal isolation of the tip to the sample through increasing the thermal resistance of the beams. While one could locally reduce the thickness of SiN to increase its thermal resistance, this implies additional deposition and/or etch steps which would require process development and potentially reduce yield.

5.1.3 Why is alignment an issue?

The definition of a narrower resistor also highlights a previously identified limitation of the process used to manufacture these probes, which is the issue of poor alignment between the cantilever tip and the sensor EBL level. This has previously been addressed by the use of 'self-alignment', in which at least one edge of the structure to be metallised is deliberately drawn outside the extent of the cantilever, such that, upon deposition, the sensor on the substrate is the result of the logical AND operation between the two geometries [163]. This was presented in Section 3.6.2. If the order of the misalignment is on the order of the sensor width we wish to define, then the traditional self-alignment method will be unsuitable. The resistance (and therefore tolerable current) would vary wildly, and it is quite likely that parts of the sensor may not even land on the tip at all, making the device discontinuous. This poor alignment is the motivation for including the limiting resistors on commercial devices, which were discussed in Section 4.10.2

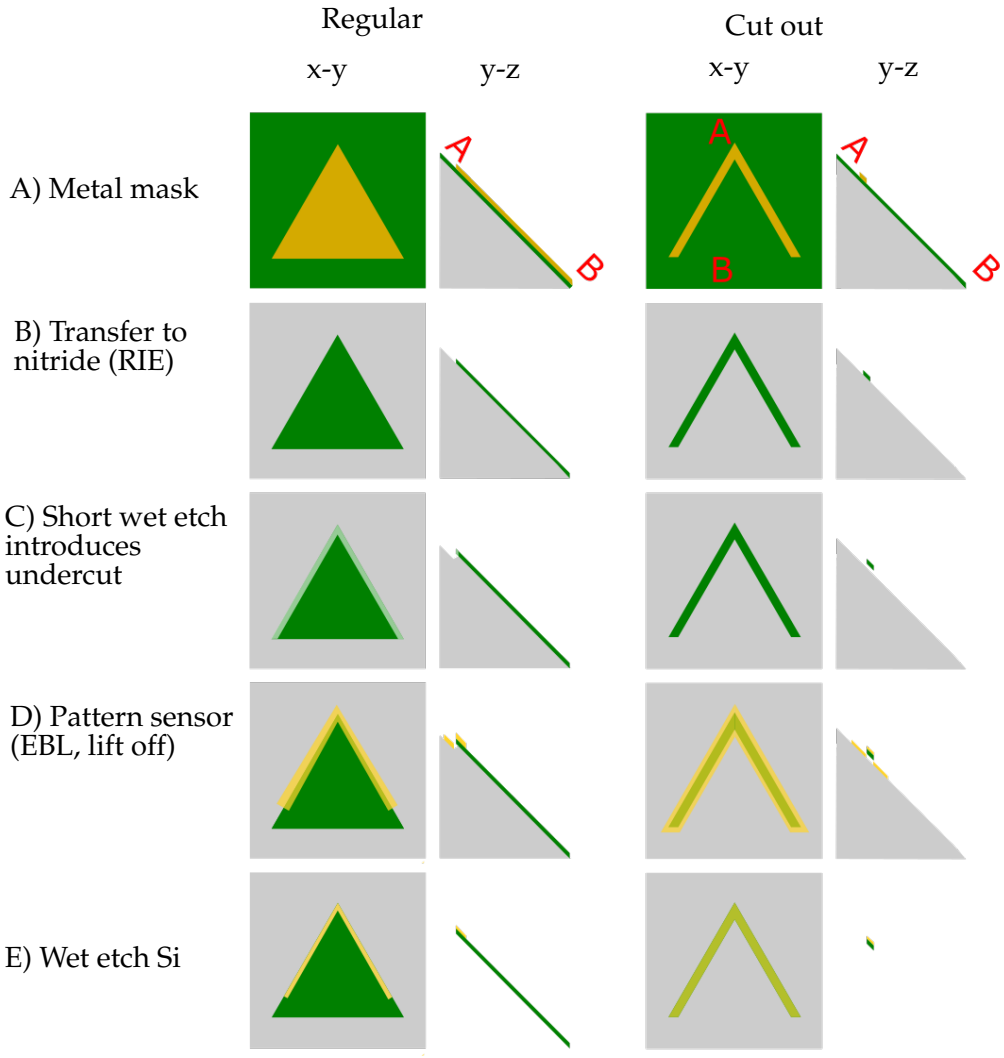

FIGURE 5.1: Comparing one and two sided self alignment strategies. The undercut etch performed in **C** may completely undercut beams which are very narrow, leaving them free-standing.

Dual self-alignment

The 'Swiss Cheese' probe fabricated by Mills [163] evidences the possibility of 'dual self alignment', which could be employed for the placement of the sensor in the cut-out probes. Figure 5.1 compares the traditional single self alignment with a possible dual alignment strategy. In the latter method, deposited metal completely overlaps both edges of the SiN beam upon which it is deposited and the resulting sensor is the logical AND operation of the two.

Figure 5.1C highlights a potential problem with this approach; with reducing line-width of the SiN beam, there is increased risk that performing the undercut etch will completely free the narrow beam. A free-standing beam of order 100nm width is at risk of being broken during subsequent processes, especially those involving rinsing or resist spinning. Such defects would be considered critical failures, and would render affected probes useless. While previous experience from the group suggested that free-standing beams should be able to withstand the subsequent processes, we had not previously attempted line-widths as narrow as those described in the upcoming Chapter.

Even if dual self alignment is to be employed, it is desirable to minimise the overlap region to reduce the risk of 'skirting'. The concern is that the overlapping regions may not fully disconnect from the metal on the cantilever. In such an event, it is important that the overlapping 'strips' are not overly wide, as this increases the risk of shorting the sensor by re-deposition of this 'scrap' metal.

If alignment were accurate enough, the sensor could be positioned atop the cantilever beams completely, with no risk of skirting. Additionally, the ability to accurately place narrow sensors, both with and without a cut-out, would allow for the quantification of the contributions brought about by either design change. Finally, improved alignment would also benefit the commercial devices, which suffer from an ambiguous tip contact due to metal flags which are the direct result of self-alignment, as shown in Figure 5.2. In fact, improving the alignment of sensor definition to AFM pyramids would be of great benefit to integrated sensor AFM in general, having been a historic challenge in the production of SNOM [160] and

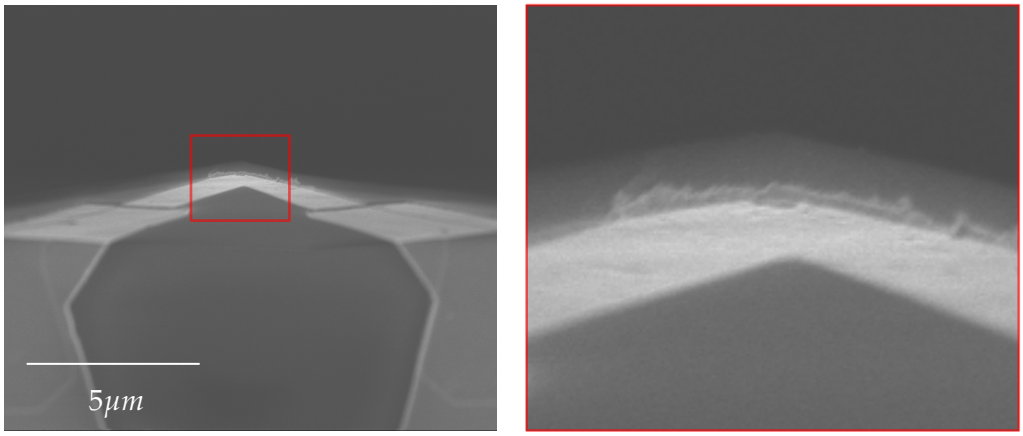

A) B)

FIGURE 5.2: SEM image showing metal flags over the probe tip. The probe is brand new and has never been scanned. Flags are caused by the tearing of the metal film during self-alignment, and result in an ambiguous tip contact that may change during scanning.

Scanning Hall Probe Microscopy [164]

5.2 Alignment

5.2.1 How is alignment performed?

An important requirement of both photo and electron beam lithography is the ability to correctly align new features to those already on the substrate. The strategy for photolithography alignment was presented in Section 2.2.2. This is an example of manual alignment, in which the tool operator manipulates the substrate such that features on both it, and the mask plate are observed to be in good alignment.

Photolithography alignment is performed between two effectively parallel planes (the wafer and the mask plate) in close proximity. No matter the alignment, all features on the mask plate are transferred to the substrate with the same size and shape. The mathematical term for the operation of moving the two objects into alignment is a rigid, or Euclidean transformation. It is termed 'rigid', since no distortions of the image occur; only x and y offsets and rotation are described by this class of transformation.

In electron beam lithography however, reduced feature size of desired patterns means

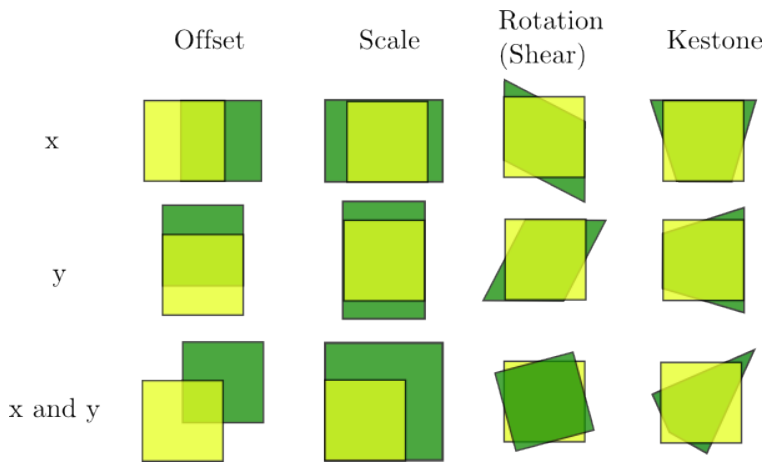

FIGURE 5.3: The possible distortions available when projecting a square onto an unknown image plane (surface). The designed shape is shown in yellow, whilst the distorted result is shown in green

that substrate tilts on the order of a few μ/mm would result in significant distortions if not properly accounted for in the image transformation. Artefacts of this type are termed 'keystone errors' due to the transformation of rectangular geometries to trapezoids, similar in appearance to the wedge-shaped 'keystone' at the apex of a masonry arch. These distortions arise from the projection of a 2D image onto an arbitrary plane in 3D space and will be familiar to anyone who has encountered a poorly set up digital projector. Appropriately, the class of transformations which cover these errors is named 'projective transformations', or homographies. Figure 5.3 highlights the different operations and types of transformations possible.

In both photolithography and EBL, the mapping of markers on the substrate to those on the pattern is the result of solving the image transform. In the former, the correct transformation is readily achieved, since the operator is able to sufficiently align the rigid bodies (mask plate, wafer) across the available three degrees of freedom (x and y offset, xy rotation). In EBL however, the machine must perform automatic image alignment through the mathematical solution of the image transform at each distinct exposure site - of which there may be thousands across a wafer.

In the following sections, we will describe how the image transform is calculated, why its performance is poor on our devices, and how we have addressed the issue.

Mathematics of pattern transformation

The solution to the image transform mapping a pattern to a sample has a different form depending on the number of degrees of freedom through which the image can be distorted. In electron beam lithography, the transformation is modelled such as to apply those distortions which were presented in Figure 5.3. The relationship between the observed position of a set of markers, i, on the wafer (X_i,Y_i), and the corresponding ideal coordinates (x_i, y_i) is given by [226];

$$\begin{aligned} x_i &= Xi + o_x + s_x X_i + r_x Y_i + k_x X_i Y_i \\ y_i &= Yi + o_y + s_y Y_i + r_y X_i + k_y X_i Y_i \end{aligned} \tag{5.1}$$

in which, o, s, r and k denote offset, scale, rotation and keystone respectively, with their subscripts indicating the directions to which they apply. These transform elements may be placed in a column vector, **T**. If the differences between observed and expected marker positions are also collated into a vector, **B**, then the relationship between the two can be calculated through the design matrix **A**, which takes the form;

$$\mathbf{A} = \begin{bmatrix} X_1 & Y_1 & X_1Y_1 & 1 & 0 & 0 & 0 & 0 \\ 0 & 0 & 0 & 0 & Y_1 & X_1 & X_1Y_1 & 1 \\ X_2 & Y_2 & X_2Y_2 & 1 & 0 & 0 & 0 & 0 \\ 0 & 0 & 0 & 0 & Y_2 & X_2 & X_2Y_2 & 1 \end{bmatrix} \tag{5.2}$$

The relationship between the differences in position and the transform coefficients is thus given by;

$$\mathbf{B = AT} \tag{5.3}$$

If the positions of both sets of markers are known, the transform coefficients may be computed by solving Equation 5.3 for **T**. With **T** known, it is possible to calculate

the displacement of a given pixel (x,y coordinate pair) within each of the coordinate transforms using the equations presented in 5.1.

It should be noted that EBL employs a two step alignment strategy;

- **Global alignment** - Four markers are placed reasonably far apart across the substrate. After the operator has aligned the tool to a central 'feature', global alignment marks are found by interrogating a large area (100's of μm) around their expected position. The image transform provided by these markers is sufficiently accurate to characterise the offset, tilt and rotation of the substrate. The search area for these markers is large, because their position was not accurately known.
- **Cell alignment** - The global alignment provides an image transform from with sufficient accuracy that these local 'cell' markers may be found using a smaller search area. This is beneficial, since the marker search routine exposes the resist in the areas in which it is performed. Cell markers are located close to the pattern writing area, therefore it is advantageous that only a small area around them be exposed.

Marker detection

Where in photolithography markers are aligned by visual inspection, EBL registration requires markers that can be 'seen' by the tool. To this end, the system includes electron detectors like those of an SEM. Finding the markers requires that they have sufficient contrast. The tool used for this work employs backscattered electron (BSE) detection for marker observation. There are two main phenomena that result in backscatter contrast [227];

- **Rutherford scattering events**, which were described in Section 2.5.3. The angle by which an incident electron is scattered is proportional to the square of the atomic number of the substrate. The greater the atomic number, the greater material's backscattering coefficient [227].
- **Contour/edge contrast**, as highlighted in Figure 5.4. Backscattered electrons have higher probability to escape the substrate with high energy at the edges of

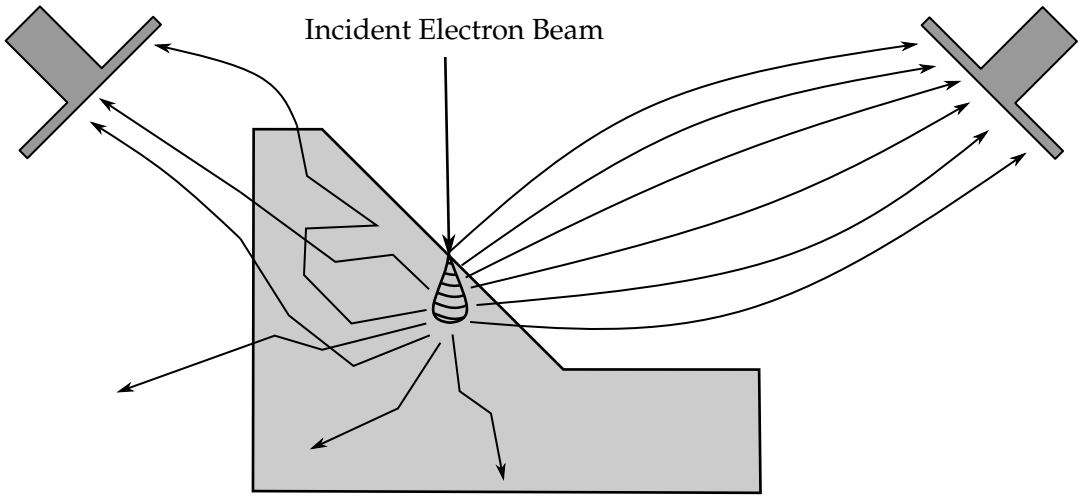

FIGURE 5.4: Mechanism by which topographic contrast arises in BSE signal. The detector on the left receives a weaker signal than that on the right. The path length to the left detector is greater, resulting in fewer electrons escaping the substrate.

topographic features. The asymmetry in path length from the sample surface to opposing detectors results in a differential in signal between them that can be used for edge detection [227].

For EBL registration, markers must be designed that take advantage of these contrast mechanisms. When employing atomic number (Z) contrast marker searches, it is recommended that the difference in atomic number between sample and marker be as high as possible (at least >30) [66]. Using a silicon substrate as an example, it would not be recommended to use titanium (Z=23) or nickel (28). Instead, tungsten (74) or gold (79) should be considered.

Of course, it may not always be practical to include such metals due to process limitations. An alternative approach is to use markers which exploit topographic contrast, using etched pits or raised mesas.

The search routine is similar regardless of the contrast mechanism employed; from an expected marker position (supplied to the tool as part of the pattern file), the beam spirals outwards until detecting a marker. Upon location of a marker, the tool performs multiple scans of each edge to improve signal to noise ratio and improve positional accuracy. More advanced details of the search routine are reported in the VB6 Operators Manual [66]

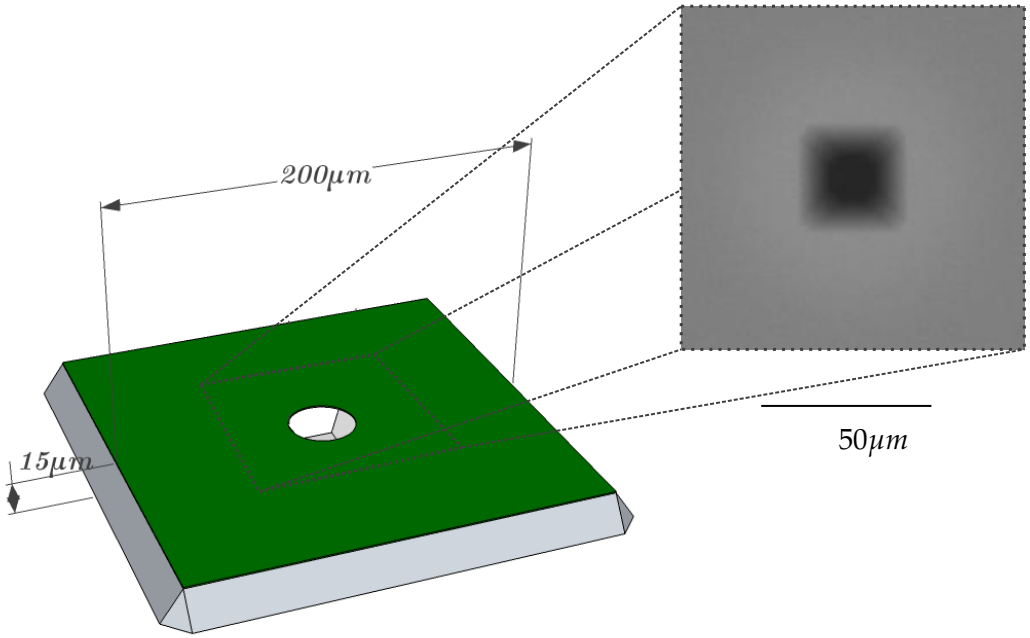

FIGURE 5.5: Schematic drawing and BSE image (inset) of the topographic markers used in this work

Our Markers

In this work, a specific type of topographic marker is used. Metal markers are not compatible with the process due to the prohibition of these materials in samples undergoing LPCVD SiN deposition. The markers are defined in the first lithography step and anisotropically etched into the sample alongside the pyramids (see Section 3.3.2 for more details). They take the form of 200μm square mesas with 32μm diameter circles in the centre, as shown in Figure 5.5. Anisotropic etching undercuts the circle opening, resulting in a {111} plane faced inverted pyramid. The inset of Figure 5.5 shows what the tool 'sees' when scanning these markers. The motivation for employing such markers is that the pit's shape is crystallographically defined, and will have similar shape regardless of any misalignment of distortion of the mask used to create it.

5.2.2 What causes poor alignment in the existing devices?

The positioning errors caused by sample loading and the environmental conditions vary between consecutive runs. By locating and aligning to the substrate markers,

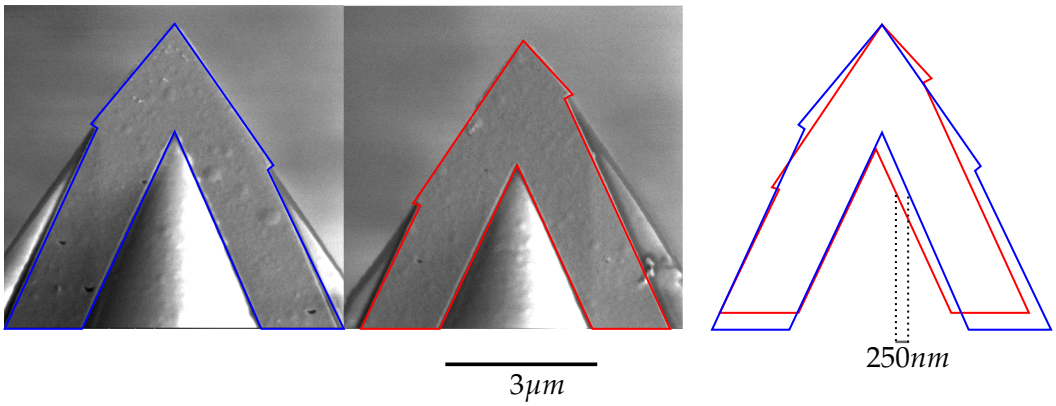

FIGURE 5.6: Comparison of the misalignment of the sensor to the tip between two probes of the same wafer. The outlines of each sensor were traced in a drawing package, and then aligned to the tip. A displacement of 250nm in the x direction is easily observable.

we are effectively finding the unique transform for the errors specific to one run. If a perfect transform could be made, then multiple runs each with distinct errors could be perfectly aligned to one another. In reality, this transform is never perfect, due to errors in the located marker positions. Often, this is caused by marker degradation due to thermal cycling or etch damage. A particular difficulty associated with this is that the damage to the markers is barely noticeable in routine wafer inspection, and the alignment problems that result are only manifest after EBL is completed.

5.2.3 How poor is the present alignment?

Within the AFM group it has been known for many years that the alignment between the sensor and the cantilever apex is poor, with common thought being that misalignment tolerances should be considered in the order of hundreds of nanometres. Previous work on substrates featuring a marker strategy similar to that used in this work suggested a misalignment of 300nm [162], [228]. In Figure 5.6, we present an example of the misalignment between the sensors fabricated in different cells of the same wafer. Although it does not demonstrate the absolute alignment between sensor and cantilever tip, it does show significant variation in placement between cells. Recall that each cell of the probe requires a new marker search and as such, entire groups of devices may have misaligned patterns if the marker search for their cell is poor. On the commercial devices, this misalignment is evidenced by the large

variations ($\pm 75\Omega$) in resistance between individual probes.

Quantification of misalignment requires the perfect image transform with which a comparison can be made. However, this perfect transform is not available, unless the marker positions are known with perfect accuracy. In reality, the most accurate transform available is limited by the errors in the marker detection system.

A direct measure of the relative misalignment between subsequent fabrication layers may be ascertained through the design and manufacture of appropriate test structures. During this project, an attempt was made to fabricate Vernier scales atop the raised pyramids such as those shown in Figure 5.9. The two parts of the scale are each written in the same resist layer, but aligned in separate operations. Unfortunately, the fabrication of these structures was unreliable and it proved challenging to parse a sensible measurement from them. One problem is that the pitch of the scales requires very narrow tick marks, since high accuracy is required and the apices of the AFM 'tip' pyramids are very small. It was during this work that we identified the problems associated with writing very fine lines atop AFM probes, as we were unable to produce reliable 50nm pitch scales

5.2.4 Improved alignment strategy

Thoms et. al. noted that the occurrence and severity of marker damage is random [226]. Because this damage introduces non-uniform errors in marker position, the authors have shown that the errors in image transform calculation can be minimised through the interrogation of a statistically large set of markers.

When more than four markers are used, the required image transform is over-determined. In such cases, the least squares method can be used to find the approximate solution which minimises the sum of the squared residuals. Those markers whose residual error is significantly large may be classed as outliers, and removed from the dataset for a further improved fit. This approach has been taken by Thoms et al [226], with the algorithm developed in the referenced paper now available on our EBL tool. The exact forms of regression analysis and outlier treatment are presented there.

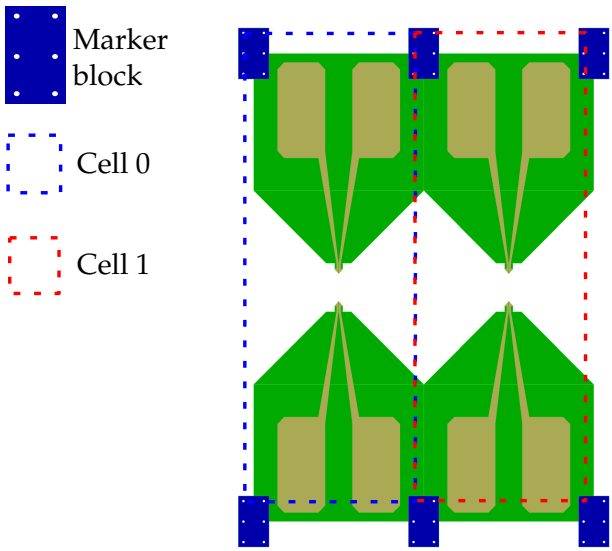

FIGURE 5.7: The probe and marker layout used in the previous commercial probes. Writing 'cells' are highlighted by a dotted line.

Re-engineering the substrate

To employ the multi-marker alignment strategy requires additional markers. The batch fabricated commercial probes feature marker blocks with six sites for alignment in each block. One 'cell' encapsulates two probes, and features four marker blocks, one in each corner, as shown in Figure 5.7.

It is advisable to always use fresh markers for every layer of EBL to be performed. Markers are exposed to the electron beam during the search routine, and therefore are subject to metallisation or etching, depending on the follow up process to be used. The marker distribution (six markers per block) employed by the commercial probe is sufficient for all four EBL exposures (cantilevers, sensors, base resistors, pads), with some redundancy in case a particular exposure fails and needs to be repeated. The ebeam 'cell' may be arbitrarily defined from any set of four markers. The minimum cell size with this layout is two probes, as shown in Figure 5.7. The choice of cell size is primarily influenced by the writing time of the pattern being registered. Beyond about 30 minutes drift compensation ceases to be sufficiently accurate and re-alignment will be required. All probes within one 'cell' will share the same align/misalignment. With exception of the pads job, the exposures are short enough such that, if desired, cells of multiple (8-16) probes could be written in

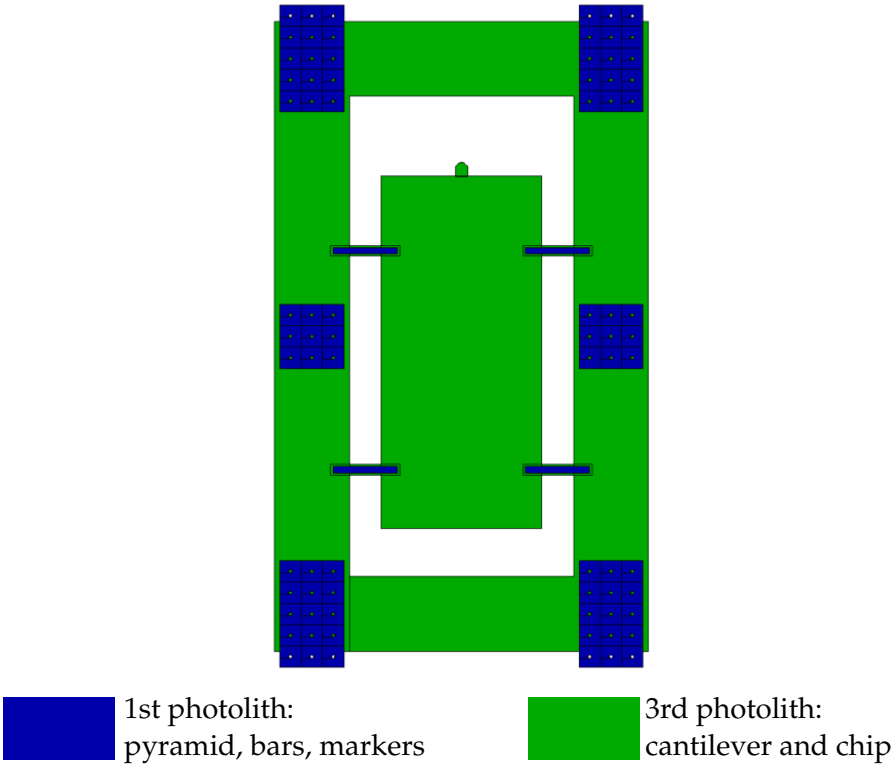

FIGURE 5.8: The updated marker distribution around a single probe. Each corner of the probe has a block of 15 markers, while the vertical midpoints have additional blocks of 9.

this time.

While the author performed the MEMs redesign of these devices into the present 'pop-out' style commercial probes, the redesign of the marker distribution was also performed [35]. Because topographic markers are used, and all subsequent patterns should be aligned to them, the changes must be implemented in the very first lithography/etching level (see Section 2.4).

Corner vs. edge

In Thoms' paper, the authors discuss the advantages and disadvantages of different types of marker distribution on the alignment quality when the positions are deliberately offset by random amounts. The two general marker strategies employed were a roughly uniform spacing around the perimeter of the writing area ('E/edge type'), and clustered around the four corners ('C/corner type'). They conclude that, in the general case, better results are achieved from markers distributed around the

edge than in the corners. However, we do not necessarily want to discount the corner approach. Due to the fact that our markers are defined by the first level of photolithography, for which a mask-plate must be produced, we have opted for a marker distribution which allows for a great deal of flexibility when defining the distribution.

Figure 5.8 presents the updated layout, in which there are 78 markers in the tile-able single probe unit. The marker dimensions and fabrication methods are the same as described previously. The choice of marker locations was influenced by the location of the supporting bars which share this lithography level. The layout also served to produce reasonably equal spacing between markers. As the probe cell is longer in y than in x, it was desired that a small set of markers be placed in the middle of the vertical support. This would allow for near equal distribution when using a cell containing probes tiled in the x direction.

Algorithm testing

Testing commenced with the hope of discovering the optimal marker distribution for our particular sample/marker/pattern combination. To test the alignment, a Vernier structure was designed to fit on the flat apex of the pyramids. This location was chosen to be suitably representative of the writing areas for most integrated sensor AFM probes, whilst not interfering with the placement of the 'side' probe. It was also a within a few microns of the device position which was most sensitive to misalignment of the sensor and tip.

To ensure the alignment was the result of maker deviations alone, and not in resist coating of other confounding parameters, both sides of the vernier scale were written in the same resist coating. To appropriately model the 'real' situation however, the wafer was unloaded and re-loaded into the EBL tool. This way its position was changed and needed to be found again.

As is the case with most new e-beam exposure jobs, this one began with dose testing. Subsequent experiments used the optimal dose found in this experiment, but severe variations in the quality of patterning between the two exposures was observed. An example is presented in Figure 5.9. By inspection of the log files, it was discovered

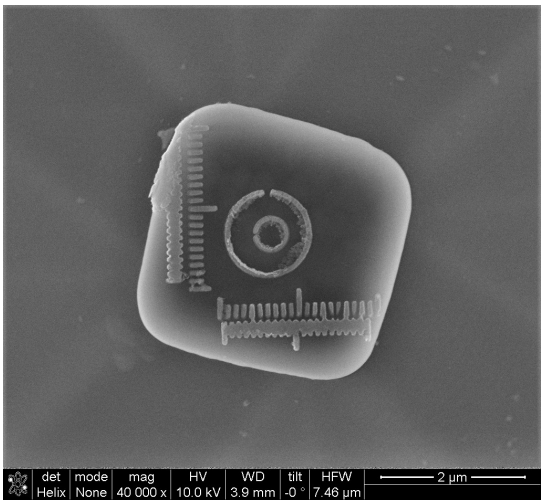

FIGURE 5.9: Vernier test structure fabricated atop AFM pyramid. Although exposed in the same resist layer and metallised in the same procedure, the two layers appear very different. While both layer appear overexposed, the outer layer looks much worse than the inner. Despite being designed at 50nm width, the resulting tick marks are between 70 and 100nm wide, which we propose is due to poor focus. This is discussed further in Section 5.3

that the problem is not actually with the dose, but with the focus of the beam. It was observed that the tool frequently fails to correctly measure the height of the raised feature, and thus does not adjust the beam focus appropriately. This conclusion sparked the body of work presented in Section 5.3, where this issue is explained in greater depth. Further characterisation of the accuracy of alignment using this approach were discontinued. While it is expected that the non-uniform coverage of resist due to spin and float coating will result in a non-uniform clearing dose distribution across the sample, the close proximity between erroneous exposures in this particular test indicated another cause. A systematic change in clearing dose would result in both features on the one pyramid to look poor, which was not the case here.

Results on live wafers

While the above test structures for quantifying the alignment improvement were unsuccessful, they did not provide any evidence that the alignment algorithm was poor - only that the strategy employed for testing it was poor. Accordingly, we proceeded to employ the multi-marker algorithm on the live wafers that would eventually make the novel cut-out probes presented in the next Chapter. Since we were

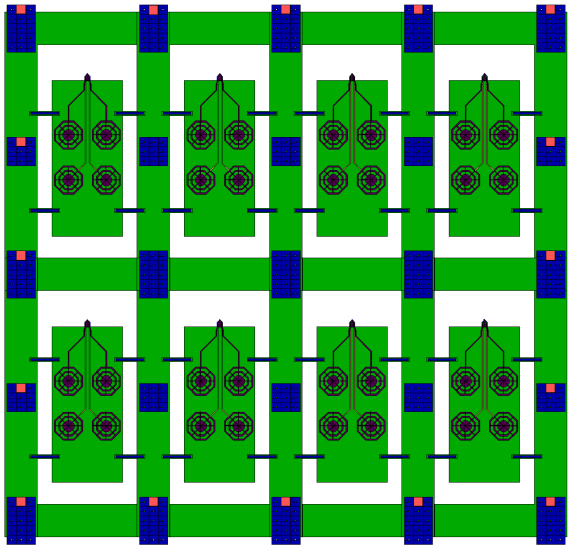

FIGURE 5.10: The basic 'cell' used for multi-marker alignment testing. An example distribution of 16 markers is highlighted in red

unable to directly measure the best marker distribution on structured wafers, we opted to use the best approach found in the literature. Thoms et. al. conclude that an edge marker distribution featuring greater than eight markers, combined with the TLS algorithm produces the best results [226]. For this reason, 16 markers around a 2x4 arrangement of probes was chosen as the base cell. Because the wafer does not fit an equal number of these units of eight probes, those cells around the edge were given some other form of edge distribution, typically using one marker from every block around their perimeter.

The lack of information on estimated alignment improvement also meant that it seemed imprudent to abandon dual self alignment. Instead, probes with and without dual self alignment were fabricated, each type having a variety of different sensor sizes. The various designs and their implementation are described in Section 8.6.4.

Since the metal of the sensors are the AND operation of the cantilever and metallisation patterns, the degree of alignment accuracy on cut-out probes cannot be qualitatively assessed from SEM imaging or resistance variation. Non cut-out (NC) probes have been placed in the same writing cell, and are therefore expected to have the same degree of misalignment, which may be investigated using these methods.

As previously discussed, no exact solution exists to the ideal transform between the wafer and the pattern on file, due to the imperfect measurement system. It is possible however to measure the difference between the locations at which patterns would have been placed had the traditional method been used, and where they have been placed when the multi-marker method has been employed. It is reasonable to assume that the multi-marker method is 'more' correct, since there is a larger set of markers from which the image transform can be estimated, and thus the influence of a single poor marker is reduced. Furthermore, it is reasonable to assert that the 'best' transformation available is that which employs multiple markers alongside outlier rejection.

The VB6 log file produces the expected, and absolute marker positions, which correspond to the stage coordinates where one would expect to find the marker, given the global alignment. Because the multi marker- outlier rejection algorithm was employed at write time, the log file reports all the data, meaning that it is possible to parse out the subsets of four markers and the full set of markers prior to outlier rejection. It is then possible to compare between the three approaches.

In each case, it is possible to calculate the transform between the expected and absolute set of markers. The log file also reports the expected pattern placement, which is the origin of the VEP file. With the transform solved, it is trivial to calculate the where the 'absolute' pattern placement. By comparison between the absolute placements of the four marker, multi marker, and multi marker - outlier alignment methods, we can present some estimation of the improvement gained by the different alignment methods.

It is hard to present a metric of overall improvement, since each cell contains multiple exposures which vary in their deviation from the four marker method. In Figure 5.12 we present the results of the average and standard deviation of the vector offsets, for each cell. In the context of this image, a high deviation means that the algorithm significantly altered the positioning. We note that all four of the 'blue' cells with high deviation do not have a red border, indicating that these cells contained outliers. It is to be expected that the biggest alterations in positioning are seen when the initial cell features outliers.

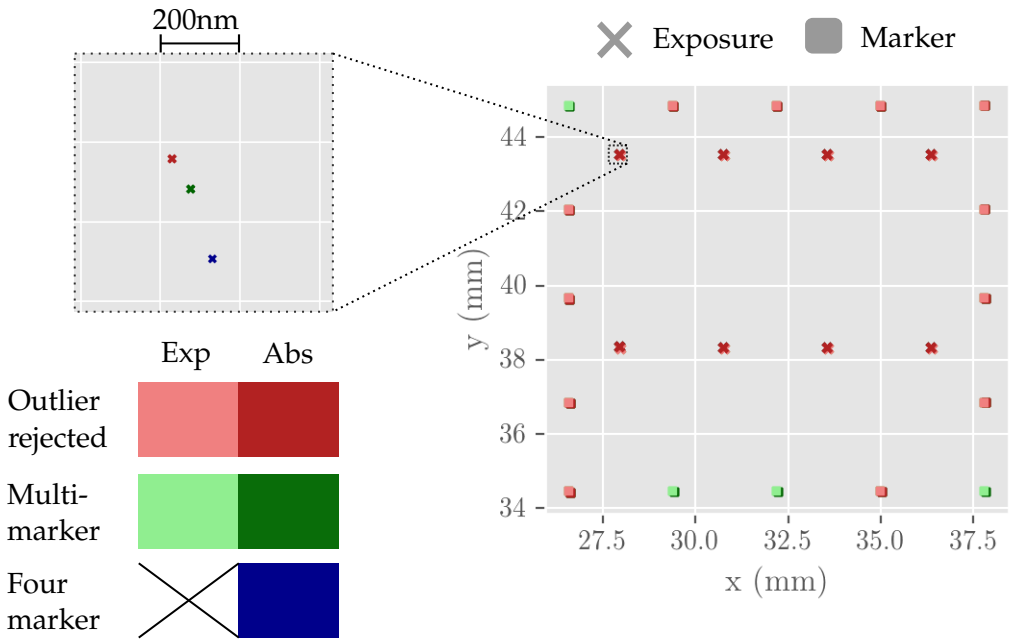

FIGURE 5.11: Marker and exposure positions for cell 0 of a wafer of probes . Inset: zoomed view of the exposure positions calculated by each of the given exposures. This cell contained 4 outliers - including outliers in 2 of the 4 corner positions

Transform Coefficients	Four markers	Multiple markers	Multi-marker with rejection
s_y	1.00	1.00	1.00
s_x	1.00	1.00	1.00
o_y	9.19×10^{-2}	8.73×10^{-2}	8.95×10^{-2}
o_x	-1.19×10^{-1}	-1.19×10^{-1}	-1.16×10^{-1}
k_y	-1.10×10^{-6}	-4.00×10^{-6}	-3.16×10^{-6}
k_x	-3.48×10^{-7}	-8.27×10^{-8}	2.05×10^{-6}
r_x	2.12×10^{-3}	2.13×10^{-3}	2.05×10^{-3}
r_y	-2.07×10^{-3}	-1.96×10^{-3}	-2.01×10^{-3}

TABLE 5.1: Image transformations between the three alignment methods on cell 0. The scale is not changed appreciably since this was already discovered by the global alignment routine.

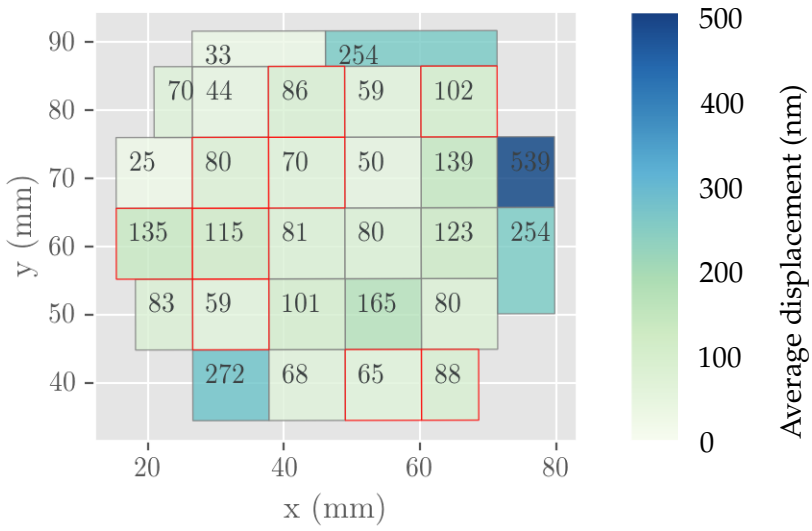

FIGURE 5.12: Colour map highlighting the magnitude of the maximum displacement between exposures using the four-marker search and multi-marker with outlier rejection search. Cells outlined in red were found to have no outliers by the algorithm. Each cell contains 8 exposures. Here we have annotated and coloured the figure by the exposure with largest deviation from the four marker method.

As an aid to understanding; cell 0 in the bottom left of 5.12 is annotated with 272nm of displacement. Figure 5.11 shows the marker positions and exposure locations of this particular cell, and the inset image shows the exposure locations using the three methods. The 272nm figure is the displacement between the four marker (blue) and outlier rejected multi-marker algorithm (red) in Figure 5.11

Closing remarks

There is no reason not to use the improved marker search method. However, its degree of improvement is still not quantified. Further experiments utilising various marker distributions should be employed. AFM wafers are already challenging substrates on which to perform EBL. The fact that micro-machined markers are prone to subtle errors in positioning makes good alignment even more difficult. An alternative approach would be to employ Penrose markers, which are more fault tolerant and have a higher degree of positional accuracy (greater autocorrelation peak) [229]. It has not been possible to fabricate these out of metal however. This is due to process constraints, specifically the requirement of no metal in the SiN deposition.

As it stands, the algorithm routinely adjusts the position of exposures by around 100nm, which indicates that four-marker misalignment was at least this value, and possibly higher. A misalignment of 100nm is enough to have significant impact on a 300nm wide sensor fabricated at the tip of the probe, which is something that was attempted in the next Chapter.

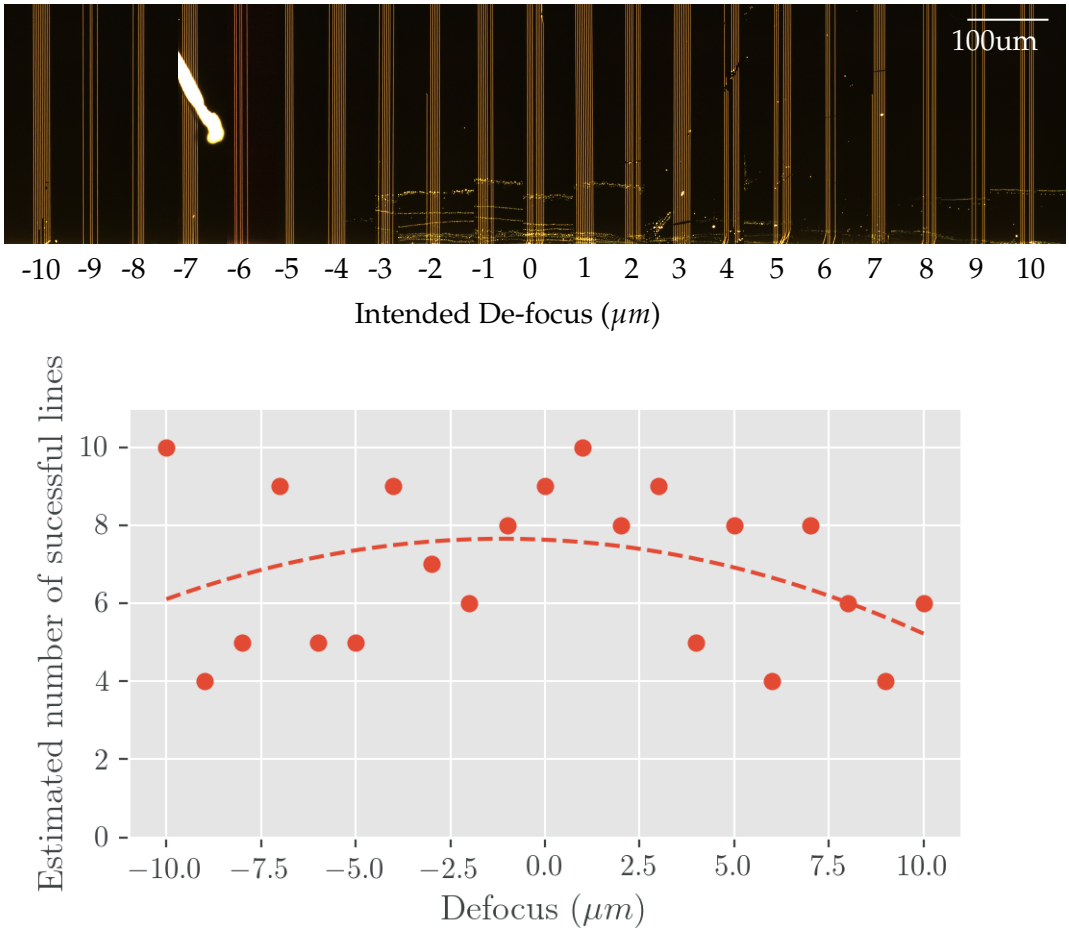

FIGURE 5.13: 500nm wide lines exposed into a PMMA bilayer at various levels of deliberate defocus. The beam parameters we chosen to be the same as that of the cantilever definition: 2nA (6nm), 8VRU, $2100\mu C/cm^2$. The pattern was transferred into 5nm NiCr 50nm Au using metal evaporation and lift off. **Above:** Darkfield optical images. **Below:** Defocus vs. estimated successful number of lines transferred. We observe a weak, but present correlation between focus and successful patterning

5.3 Line-width

5.3.1 Motivation

In the previous section we discussed the difficulties encountered in patterning 50nm line-width isolated features atop AFM pyramids. Through log file analysis, it was observed that the laser height sensors (whose operation was discussed in Section 2.5.2), frequently failed to record a sensible measurement in the location of exposure. In such cases, the nearest successful height measurement will be used, which for these samples is commonly 1 device length away (2.8mm). Given that typical substrate tilts for 3" wafers loaded into this system are on the order of microns per

millimetre, it is clear that selecting such a distant focal point is not an ideal solution.

Through the study of many log files, it was discovered that this issue was not unique to the test samples run in the previous section, but rather common to all topographically structured AFM wafers. This was verified by inspecting a number of log files recording the exposures of commercial SThM probe wafers, kindly provided by Kelvin Nanotechnology. A Python script to parse the order and location of exposures was created to assist with visualising the issue. Figures 5.14 and 5.15 are the results of running this script on a micromachined AFM wafer with roughly 200 exposures, and on another 3 inch, previously un-patterned wafer with thousands of exposures. Note that the same materials stack is employed in both cases.

In Figure 5.15, less than 6% of exposure locations suffered a failed height measurement. Interestingly, on these substrates, failures are localised in the three positions which correspond to the clamp locations of the 3" holder. Because the pattern density is high, and the wafer tilt is minimal, none of the failed height measurements resulted in noticeable patterning errors. In contrast, Figure 5.14, highlights that nearly 50% of measurement locations on this sample have a failed height measurement. It is clear from the inset figure marked 'plane fit', that there is significant variation in the measured values, which are not characteristic of the real surface. From consideration of the measurement apparatus, it is reasonable to assume that the height measurements fail due to a specular reflection of the incident laser from the substrate. The sloped side-walls of the etched features will scatter the light, reducing the summed signal into the photodetector.

There are two nominally flat planes on the AFM substrates on which patterns are written; the surface which was masked during the pyramid etch (Appendix A Step 12 - includes marker blocks, support bars and pyramids) and everywhere else that was unmasked, which is $14 \pm 2\mu m$ lower. The latter of these two surfaces comprises the majority of the total area. In the sensor deposition step, the beam's focal point is adjusted in software to account for the fact that we are attempting to write on the upper surface, where high resolution is required. The supposition is that we always measure the lower surface, however. The features comprising the raised surface all

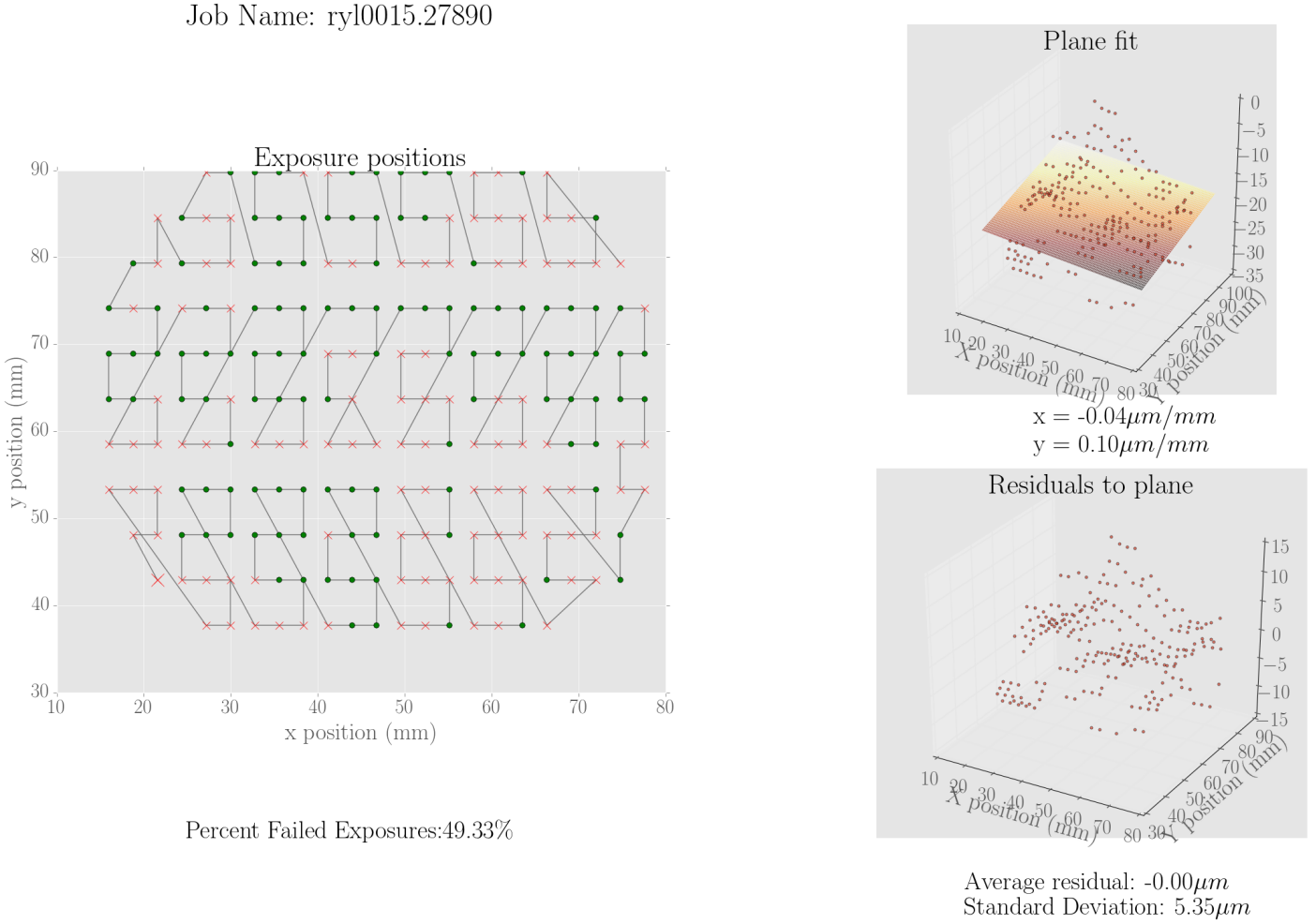

FIGURE 5.14: Log file analysis of a sensor deposition ebeam job on a micromachined AFM wafer. The larger plot shows the exposure success by location. The grey line indicates the order of exposures. The inset figure (top) shows the points as measured by the tool (excludes failed measurements), alongside the best fit plane (wafer tilt). The lower inset figure presents the same point cloud normalised to remove the wafer tilt calculated in the upper figure.

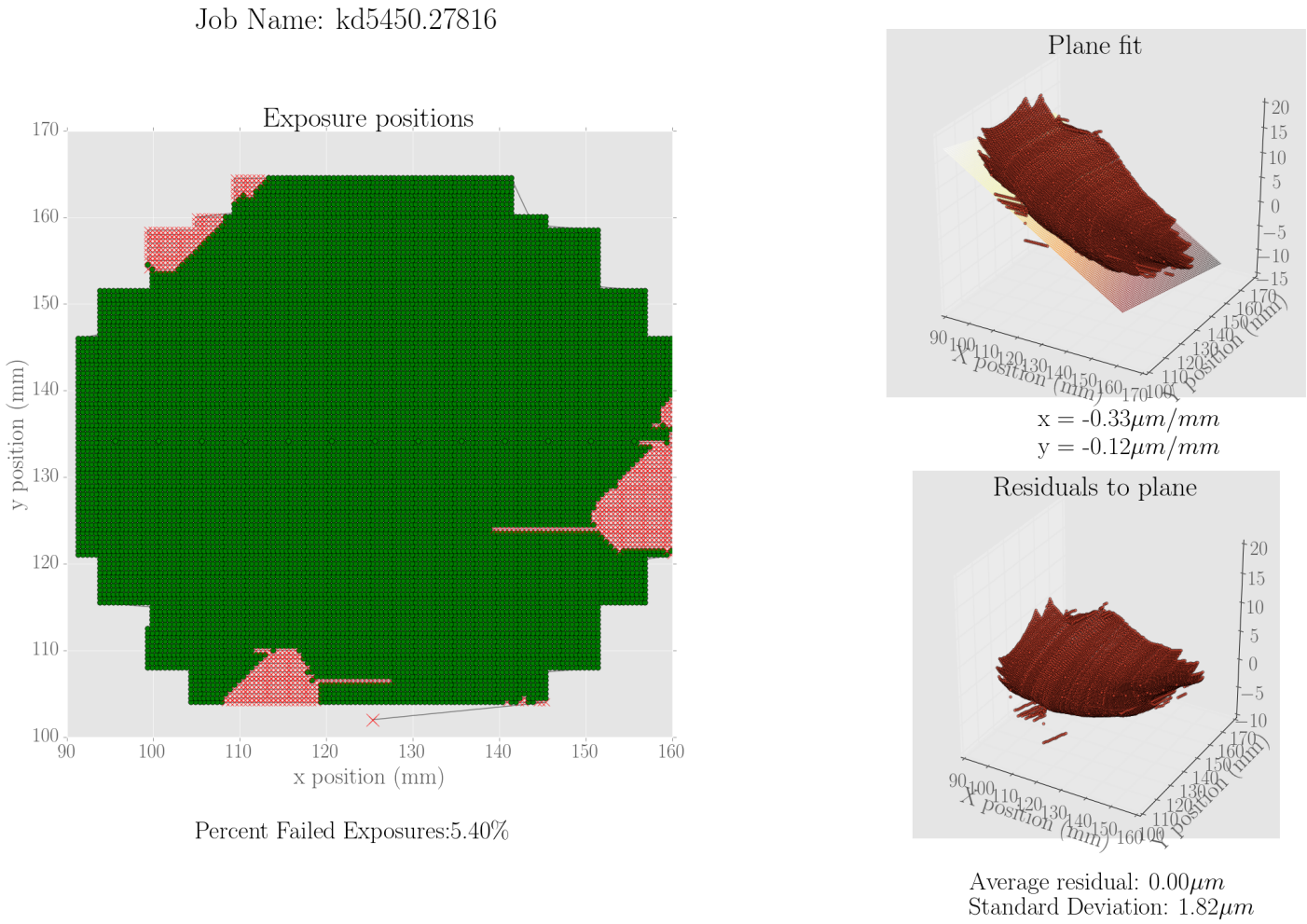

FIGURE 5.15: Log file analysis of a sensor deposition ebeam job on a un-patterned wafer. The larger plot shows the exposure success by location. The grey line indicates the order of exposures. The inset figure (top) shows the points as measured by the tool (excludes failed measurements), alongside the best fit plane (wafer tilt). The lower inset figure presents the same point cloud normalised to remove the wafer tilt calculated in the upper figure. A second order wafer bow is evident from the residuals to the plane fit.

have area smaller than the spot of the laser beam, so this is a reasonable assumption. However, there are some occasions where a measurement more characteristic of the upper surface is returned. This would not be problematic if it were reproducible, however it appeared to be random in all the log files examined An example distribution of measurements is seen in the inset of Figure 5.14.

5.3.2 Method

In addition to measuring exposure heights in real time, the VB6 offers an alternative 'height-mapped' mode. In this mode of operation, the height at a given exposure location is interpolated from a previously calibrated height map. The manufacturers remark that 'height readings can be taken at defined positions on patterned substrates where the height meter readings are not disturbed by the patterning' [66]. This approach would appear very useful for our application, however the pattern density of our substrates was such that no tileable location for successive correct height measurements could be found. Therefore, modifications had to be made to this approach. Rather than providing a simple 'height map' to the tool for interpolation, software was developed measure and calculate the best fit 'n-th' order surface for the wafer. With the surface equation known, the tool can query the software for the required height at the supplied exposure position. The surface equation is calculated from an array of measured points which are collected prior to write-time. Since nothing has changed in the measurement system or sample surface, we still observe a large number of laser height sensor failures or uncharacteristic reports of height. The novelty in this approach lies in the outlier rejection. All points for which an LHS error was returned are removed from the dataset before a preliminary fit is made. Similarly, all those measurements which are uncharacteristic of the system are removed prior to the first fit. For this work, uncharacteristic measurements are those whose residual error to a tilt correction are greater than 10um. This has the added advantage of filtering out any measurements from the top plane (marker blocks etc.), removing any ambiguity and allowing us to offset from the known, lower surface as required.

With all the bad points removed, we apply a least squares regression to minimise

the sum of the squared residuals. The equation used to model the surface takes the form;

$$z_i = B_0 + B_1 x_i + B_2 y_i + B_3 x_i^2 + B_4 y_i^2 + B_5 x_i y_i \tag{5.4}$$

Where z_i represents the surface height at position 'i', and B_n represents the coefficients which describe the various x, y components. Note that this equation is for a 2D second order surface, which is able to account for both tilt and bow. While higher order distortions were implemented, we found that introducing greater degrees of freedom reduced the quality of the fit. It is not expected that significant 3rd order (or above) deformations should occur, therefore these should not be accounted for in the fit.

Equation 5.4 may also be expressed in matrix form;

$$\mathbf{Z} = \mathbf{DB} + \epsilon \tag{5.5}$$

Where $\mathbf{Z}$ is an $n \times 1$ column matrix of measured heights at 'n' unique x, y coordinate pairs. $\mathbf{D}$ is a design matrix which contains k independent variables for n points. The required number of terms, k, is related to the desired order of the fit, containing x and y locations raised to the nth power and the associated cross terms. $\mathbf{B}$ is a $k \times 1$ column matrix containing the fitting coefficients and ϵ is an $n \times 1$ column matrix of the residual errors.

An example for matrix $\mathbf{D}$ for a 2nd order fit is presented below;

$$\begin{bmatrix} 1 & x & y_1 & x_1^2 & y_1^2 & x_1 y_1 \\ 1 & x & y_2 & x_2^2 & y_2^2 & x_2 y_2 \\ 1 & x & y_3 & x_3^2 & y_3^2 & x_3 y_3 \\ \dots & \dots & \dots & \dots & \dots & \dots \\ 1 & x & y_n & x_n^2 & y_n^2 & x_n y_n \end{bmatrix} \tag{5.6}$$

Solving Equation 5.5 for **B** yields the coefficients of the surface equation which best fits the cloud of xyz points provided.

The vector of residual errors may then be analysed for significant outliers. In this work, we have considered outliers to be any points falling outside 2.5 standard deviations of the residual error. Such points are removed from the point cloud (xyz), and the surface equation is recalculated. This operation may be repeated a number of times until the solution 'converges' and no further outliers are removed.

The surface equation resulting from these fit and regression operations is made available to the VB6 during write time. The tool queries the equation at the intended exposure location and adjusts the focus according to the height returned. At the time of writing, we have continued to allow the tool to perform in-situ laser height measurements alongside this height-mapped mode. Both the measured and calculated values are reported in the log files, allowing for comparison between the two methods. In addition, the full height map is saved.

The height map is defined by adding the following command to the Belle file;

$$\text{miniheightmap } x_0, y_0, \Delta x, \Delta y, nx, ny \tag{5.7}$$

where x_0 and y_0 are the coordinates for the bottom left corner of the mapped area, Δx and Δy are the repeat distances for x and y respectively, and nx and ny are the number of repeats in each direction.

5.3.3 Results

Coated vs. uncoated, positional errors

With the height mapping deployed on the VB6, an experiment was performed to examine the impact of the measuring the height at different locations across the sample. One advantage of the height mapped method is that it is possible to take measurements some distance away from the exposure location. Another benefit is that one may perform a height map of arbitrary resolution regardless of the exposure frequency. This was exploited during the following experiment, during which

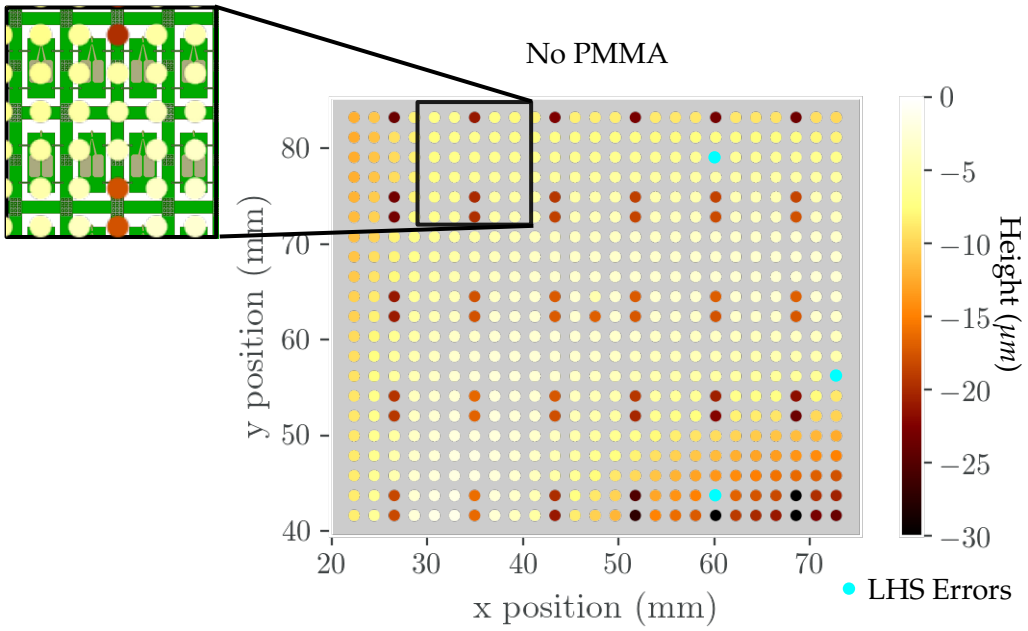

FIGURE 5.16: Height measurements on a topographic AFM wafer without resist coating. Points which returned laser height sensor errors are highlighted cyan.

one blank exposure was defined at the centre of the wafer. The unit cell containing a single probe tiles with period 2800 µm in x and 5200 µm in y. The frequency of measurement points was chosen such as to be higher than the tiling of the unit cell, but still tiles to hit the normal exposure location every few probes. Its period was chosen to be 2100 µm by 2080 µm, in x and y, corresponding to 75% and 40% of the period of the probe cell. Thus, the exposure location was measured every 4 probes in x and every 5 in y, as can be observed in the inset figure of Figure 5.17

Because no pattern transfer was required, the wafer was able to be submitted without any resist coating. The colour of the dots on the plot denotes the residual error to a 2D plane fit.

There are periodic outlier height measurements which are roughly 15 µm higher (negative is less separation between lens and substrate) then the rest of the measured points. These correspond to measurement locations which are immediately north and south of the central ebeam marker block, which is a large raised region. This is evident in the inset image of Figure 5.16.

Only three locations actually failed to record a measurement, which we considered unusual given how frequently these defects tend to occur on production wafers. The

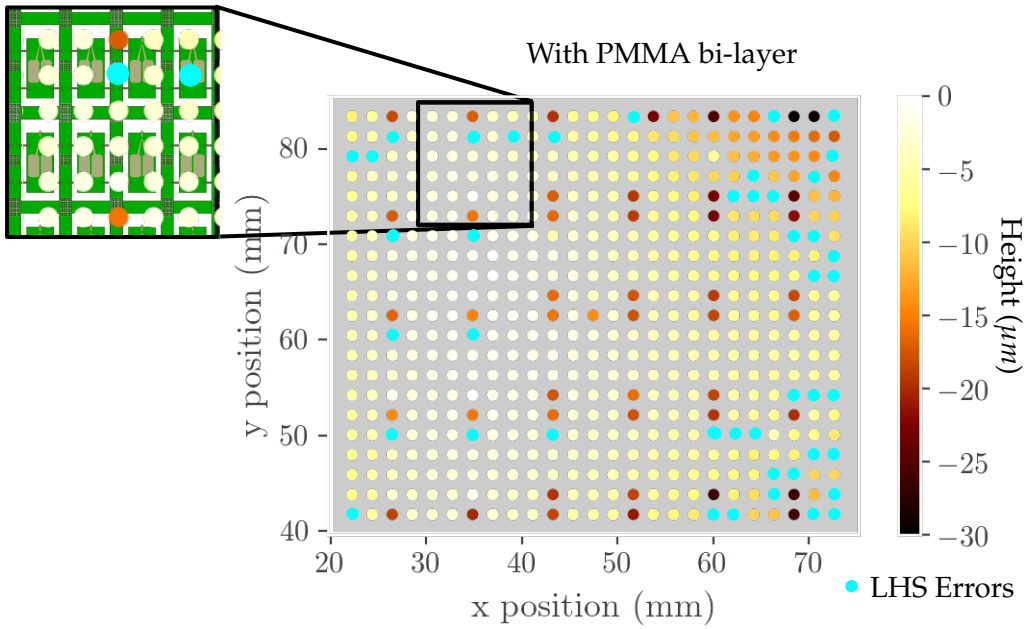

FIGURE 5.17: Height measurements on a topographic AFM wafer with a bi-layer of PMMA. Points which returned laser height sensor errors are highlighted cyan. Many more such errors are present in this map than that of the same wafer uncoated.

most obvious difference was that this substrate was not coated with resist. Therefore, the experiment was repeated on the same wafer, simply coated with the PMMA bilayer as given in step 26 of Appendix A.

Figure 5.17 shows the result of this height-mapping operation. This time, far more failed measurements occurred. Interestingly, periodic failures appear in those locations which measured erroneously in the previous experiment. This is reasonable, since the slopes of these features cause non-specular reflection, and their height is undefined. In the ideal case, the height of the raised surface is measured, but one may safely assume they report lower signal, since the feature's area is less than that of the laser spot. From these experiments it may be concluded that the height mapping fails due to a combination of both topography and resist coating. It is speculated that the resist introduces some degree of thin film interference which lowers the intensity of the reflected laser beam used for height measurement.

Stitch Experiment

An experiment was developed to assess the performance of the height fitting algorithm, using the standard measurement as a benchmark. In the first instance, the

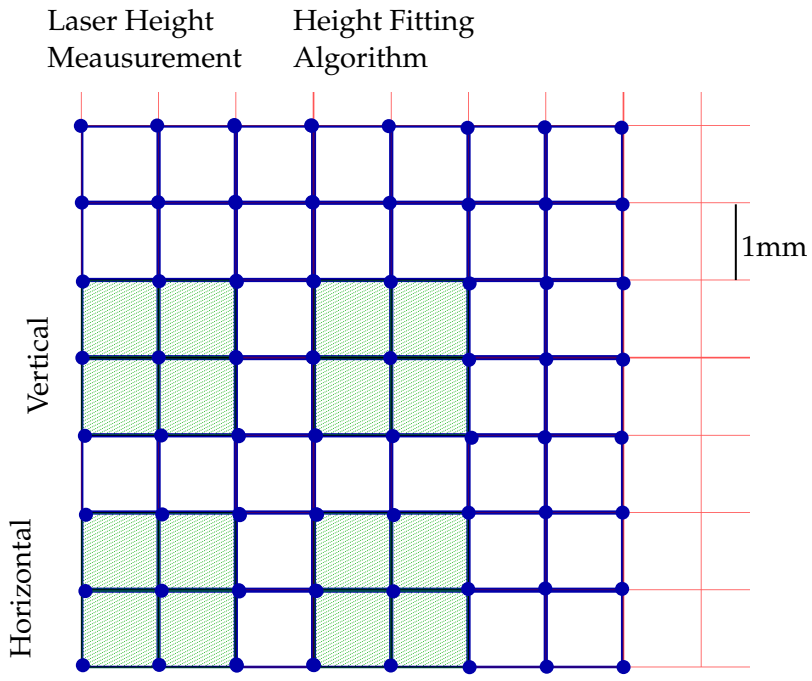

FIGURE 5.18: Schematic drawing of the stitch test pattern. The main field grid is shown in red. Filled green squares denote a grating pattern which encompasses the entire field. The 2x2 arrangement of fields gives the maximum number of field boundaries for the minimum writing time. Units on the left are written using the traditional LHS method, while units on the right are written using the custom algorithm. Intersections of lines on the blue grid indicate height measurement points for the mapping routine. Measurements are thus half a field away from the exposure location, whereas in - situ height measurements are performed at the centre of the pattern. The exposed patterns will thus only be identical if the height fitting algorithm is able to faithfully calculate the height at the centre of the field.

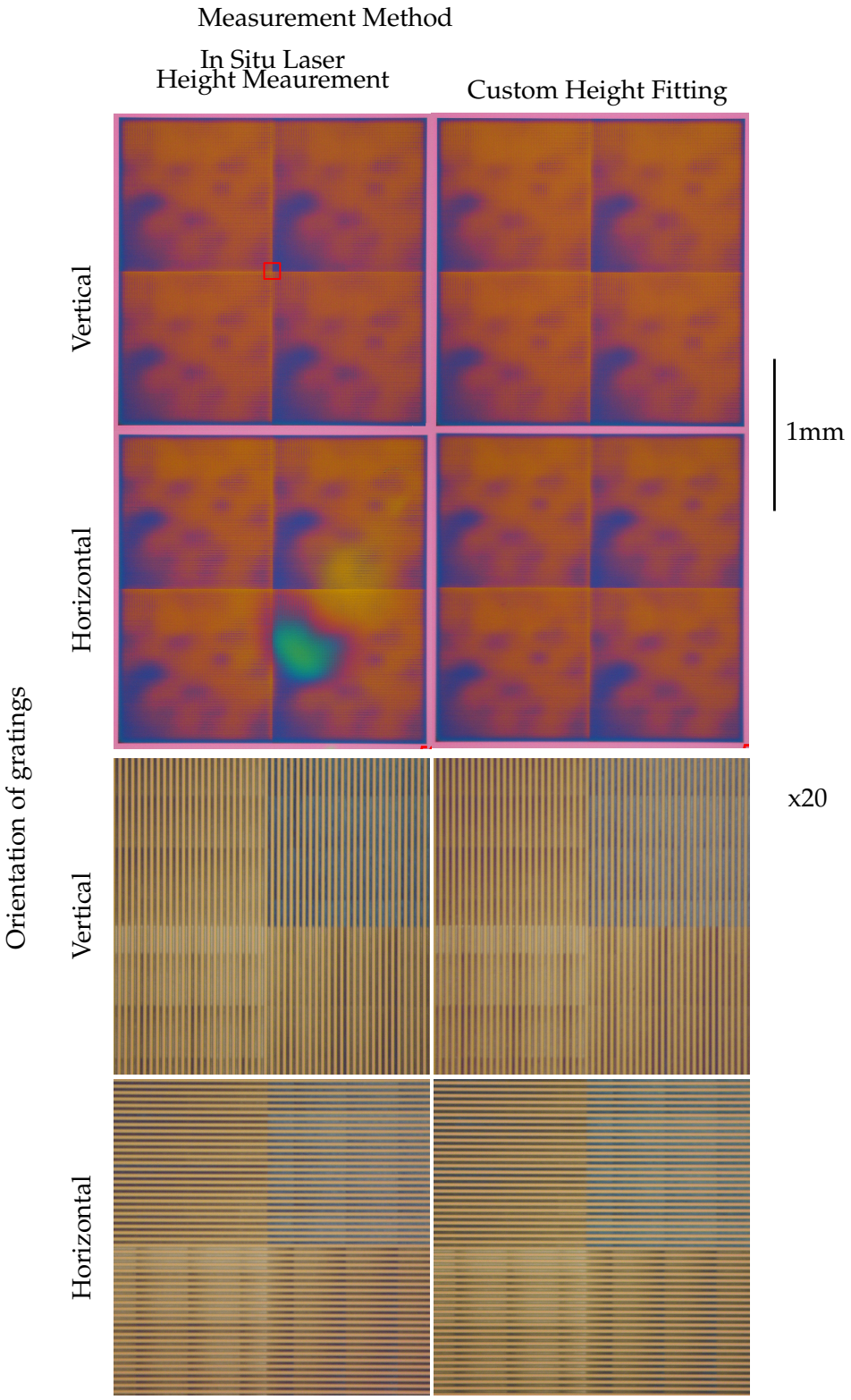

FIGURE 5.19: Optical micrographs comparing the gratings written on a new, flat wafer with in situ height measurement and the novel height mapping algorithm. The gratings written using the height fitting method are identical to those written with the traditional method, demonstrating its suitability. Negligible stitch errors are observed in either exposure.

two methods are compared by writing identical patterns on an ideal wafer (i.e, a new, flat, polished wafer with a spin coated PMMA bilayer.) A test pattern was developed which would highlight stitch errors, which were previously described (Section 2.5.2 and Figure 2.12). It has been shown that stitch errors can be an accurate proxy for the measure of focal point inaccuracy [67], [230]. Figure 2.12 highlights how erroneous height measurements can cause bloating of features and alter the periodicity of gratings. At field boundaries, any misalignment and aperiodicity will be most obvious. Analysing stitch errors by the exposed resist is preferred over lift-off for experiment, since lift-off pattern transfer introduces another process variable.

Figure 5.18 shows the layout of the pattern schematically, whilst Figure 5.19 highlights the results of this experiment after exposure and development. Excellent similarity between both methods is observed, demonstrating the validity of the new algorithm. Consulting the log file of this job reveals that the LHS method measured all sites successfully, therefore the new method is considered optimal. While in the height-mapping mode, our software requests the tool to take a height measurement prior to exposure, even though this value is ignored in favour of the calculated height. This allows for a comparison between the calculated value and the in-situ measurement. For this sample, the two agreed to an accuracy of +/-10nm, which we consider to be a very promising result.

Vernier quality

The primary application driving the development of this work was the poor lithography observed on the Vernier test structures for quantifying the performance of the improved alignment algorithm discussed in Section 5.2. The test structures, and the result of initial attempts to pattern them atop AFM pyramids were presented in Section 5.2.3 and Figure 5.9. In the present experiment, the same test structures are written using both the in-situ laser height measurement method, and the height-mapped mode developed here. Due to the design of the height-mapping software, it was possible to compare both approaches on the same wafer, simply by defining discrete regions which should use height mapping or not. Performing both exposures on the same wafer ensures the same type of resist stack, metal deposition and

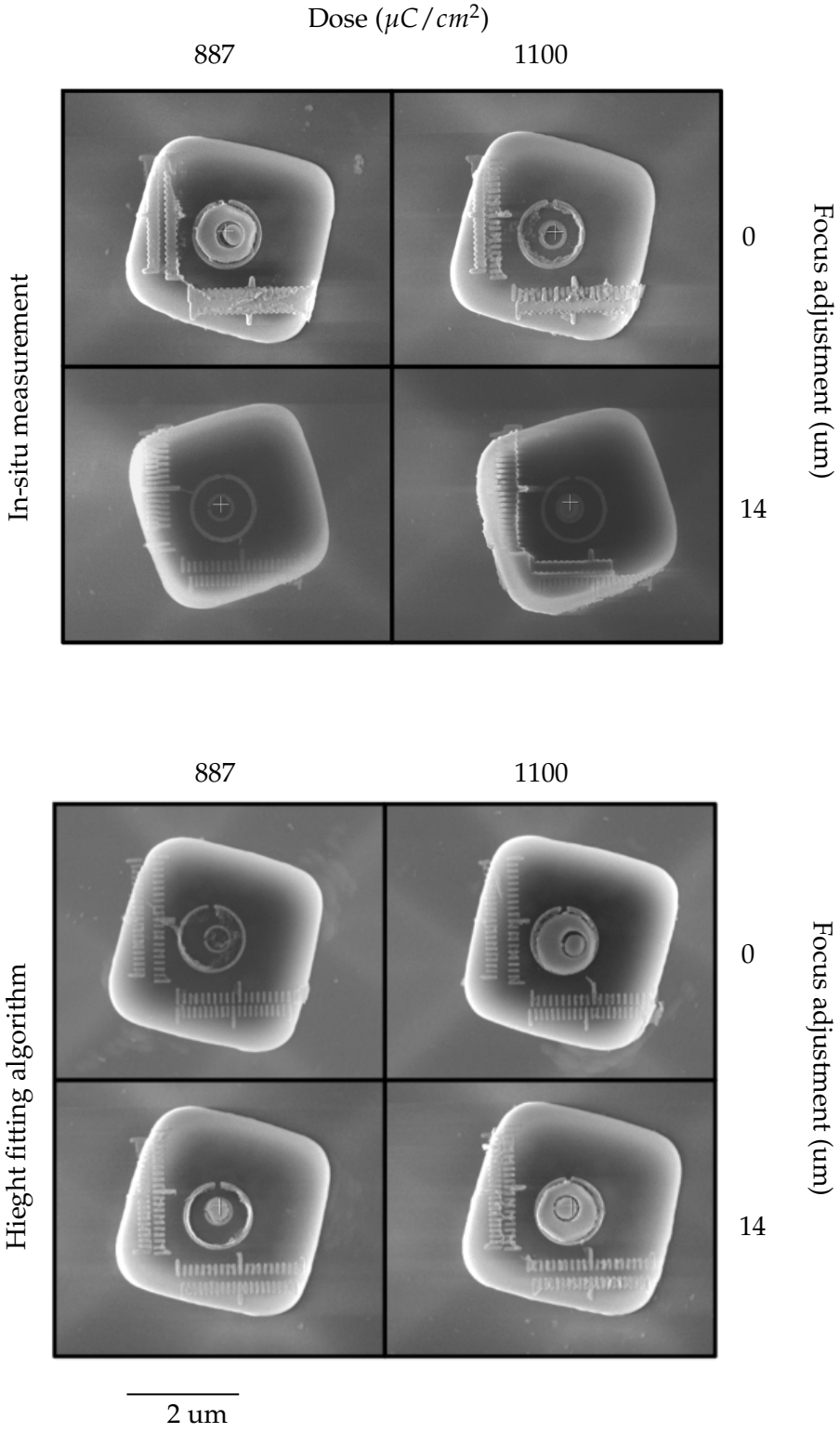

FIGURE 5.20: Comparison of writing quality of Vernier alignment test structures when exposed using the focal points suggested by in situ vs. height mapped measurement methods. For each approach, two doses and two focal points have been presented. The focal point is expected to be roughly 14um above the measured value, since this represents the height of the pyramid relative to the bottom surface of the wafer. Those features written using the height mapped measurement have better defined, more isolated lines in all cases, and demonstrate less variation between the four images presented. This suggests increased process latitude, which is crucial for the development of novel devices.

development conditions.

Figure 5.20 compares SEM images of the Vernier test structures patterned using both methods.

5.3.4 Discussion

While it was not possible to fabricate the test structure perfectly onto topographic wafers using the developed algorithm, we observe positive results in Figure 5.20. Feature bloat is reduced, and the improved accuracy of the pattern transfer is evident. In Figure 5.19, it was observed that this approach was certainly no worse than the in-situ measurement. While it would be preferable to consider testing the novel e-beam techniques described in this chapter further, our aim was to fabricate functional SThM probes, and no further effort could be expended on this topic. However, following the positive results exhibited throughout this chapter, these modifications were introduced on **all** e-beam lithography levels of the new SThM probes described in the following Chapter. Throughout that chapter, we will highlight those areas in which the modifications made here have had a significant impact on the yield, functionality and sensitivity of the new device.

Chapter 6

Novel SThM probe design and manufacture

6.1 Feasibility study

6.1.1 Design and motivation

The studies performed using the thermal model presented in Chapter 4 suggested two alterations to the probe design and manufacture; the introduction of a cut-out for increased thermal isolation of the sensor from the cantilever, and the re-design of the sensor electronics. This section is concerned with the implementation of the first change - the cantilever cut-out.

While preliminary modelling results had shown increased thermal resistance with increasing cut-out size, it was not clear whether or not probes with a sizeable portion of the apex material removed would be mechanically feasible and if they would be fit for purpose as contact mode AFM probes. It was also unclear as to whether or not such probes would be possible to fabricate. Some difficulties were envisioned, particularly the e-beam definition of the beams, and the etching of these beams to form the required undercut for dual self-alignment. For these reasons, it was decided to fabricate a small batch of cut-out probes early on in the project. Doing so allowed for the supplementation of early modelling results with practical fabrication experience which could be used to assess the feasibility and practicality of the proposed designs.

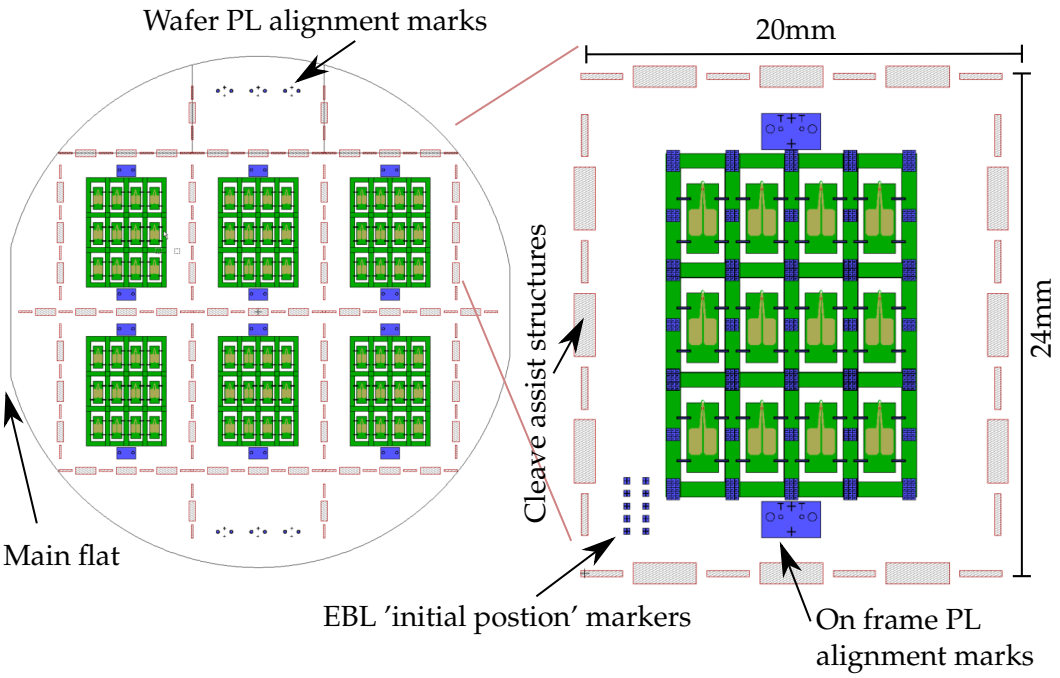

FIGURE 6.1: Schematic of the 'frames' wafers developed for rapid prototyping of novel SThM probes. **A:** shows the entire wafer featuring six frames, while **B:** shows a magnified view of a single frame.

As part of the author's work on the Quantiheat project, a rapid prototyping platform for novel AFM probes was developed, known as a 'frames' wafer. These wafers feature 6 units of a 4x3 array of probes, which are batch fabricated together throughout the chip definition and bulk micromachining steps. The wafer may then be cleaved into individual 'frames', which each contain the registration features required to align with both photo and electron beam lithography. Frames may then proceed with custom cantilevers or sensor layouts. The layout of the frames wafer is presented in Figure 6.1. This approach to probe manufacture is particularly suited to experimentation with those changes which cannot be changed in pattern design, i.e. testing different etch depths, or trying out different metal deposition conditions.

In the standard process (Appendix A, steps 25 through 45) the cantilevers are defined in a two part process. First, the outline of the cantilever is drawn with EBL using a small spot to ensure a high resolution tip. The interior of the cantilever is then filled in using photolithography. The traditional design is shown in Figure 6.2A. For frames substrates, the cantilever definition mask plate was updated to use the pattern shown in Figure 6.2B to allow for a variety of cut-out designs to be designed

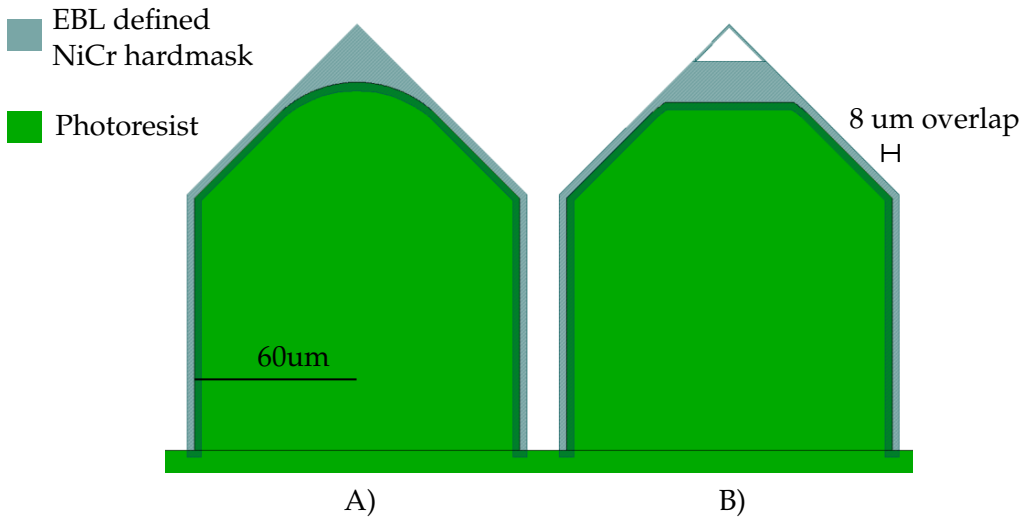

FIGURE 6.2: Schematic outlining the strategy for cantilever definition. The outer layer is defined using ebeam lithography (blue) first, then filled in using photolithography (green). **A)** shows the traditional design, while **B)** shows the updated design which can accommodate a variety of cut-out shapes.

and fabricated. EBL patterns are defined in software and do not require a physical mask, therefore it was important to design a photolithography pattern which was compatible with a wide range of potential EBL designs.

There are two main considerations in the design of the cut-out probes. The first is the width of the beams upon which the sensor will be patterned, b_x (see Figure 6.3). Subject to the limitations on this width imposed by fabrication capability, the design will be determined by the desired width of the sensor. For this reason, this value will be discussed as part of Section 8.6.4, alongside the electronics design. The second consideration is the extent to which the cut-out away from the tip, L_c, as was defined in Figure 4.31 of Section 4.10.1.

For this experiment, cut-out sizes (L_c) were iterated from 2 µm to 24 µm at 2 µm intervals. The size of b_x was kept constant at 1 µm, resulting in a sensor width of 700nm. This is narrower than the sensor of the commercial probes, but not sufficiently narrow as to challenge the resolution of the lithography. This range of cut-out sizes was chosen for the following reasons;

- To discover and if possible, quantify any relationships between L_c and mechanical performance; namely deflection sensitivity)

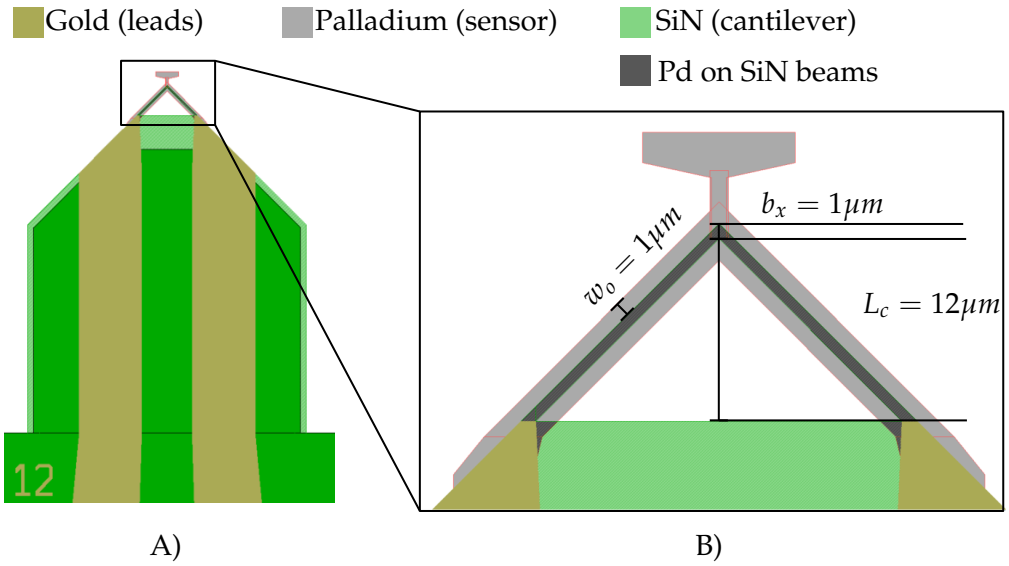

FIGURE 6.3: Schematic drawing of one of the designs for the first iteration of cut-out probes. **B** Is a magnified view of the sensor beams. The cantilever beams upon which the sensor is deposited was presented in Figure 6.2B. w_o denotes the width to which the sensor layer extends beyond the SiN beam on each side, chosen to be 1 µm. The large shape at the top of the image is a lift-off enhancement structure which is patterned over the apex of the pyramid. This can be seen in Figure 6.7

- To compare the mechanical properties of probes with a cut-out entirely confined to the sloped 'beak' of the probe, vs. those in which the cut-out extends onto the flat region.
- To identify if it is possible to perform lift-off of all the desired cut-out sizes with good yield.

6.1.2 Fabrication

Cantilever Definition Ebeam

A gallery of images logging the fabrication of the new cut-out cantilevers is presented across Figures 6.4 and 6.5. The e-beam job which defined the cantilever outline was written with the smallest spot, however it still required careful dose testing and proximity effect correction to achieve the results presented in Figure 6.4A. The narrow beams in close proximity to a 'block' triangle is a structure that suffers from proximity effect distortions.

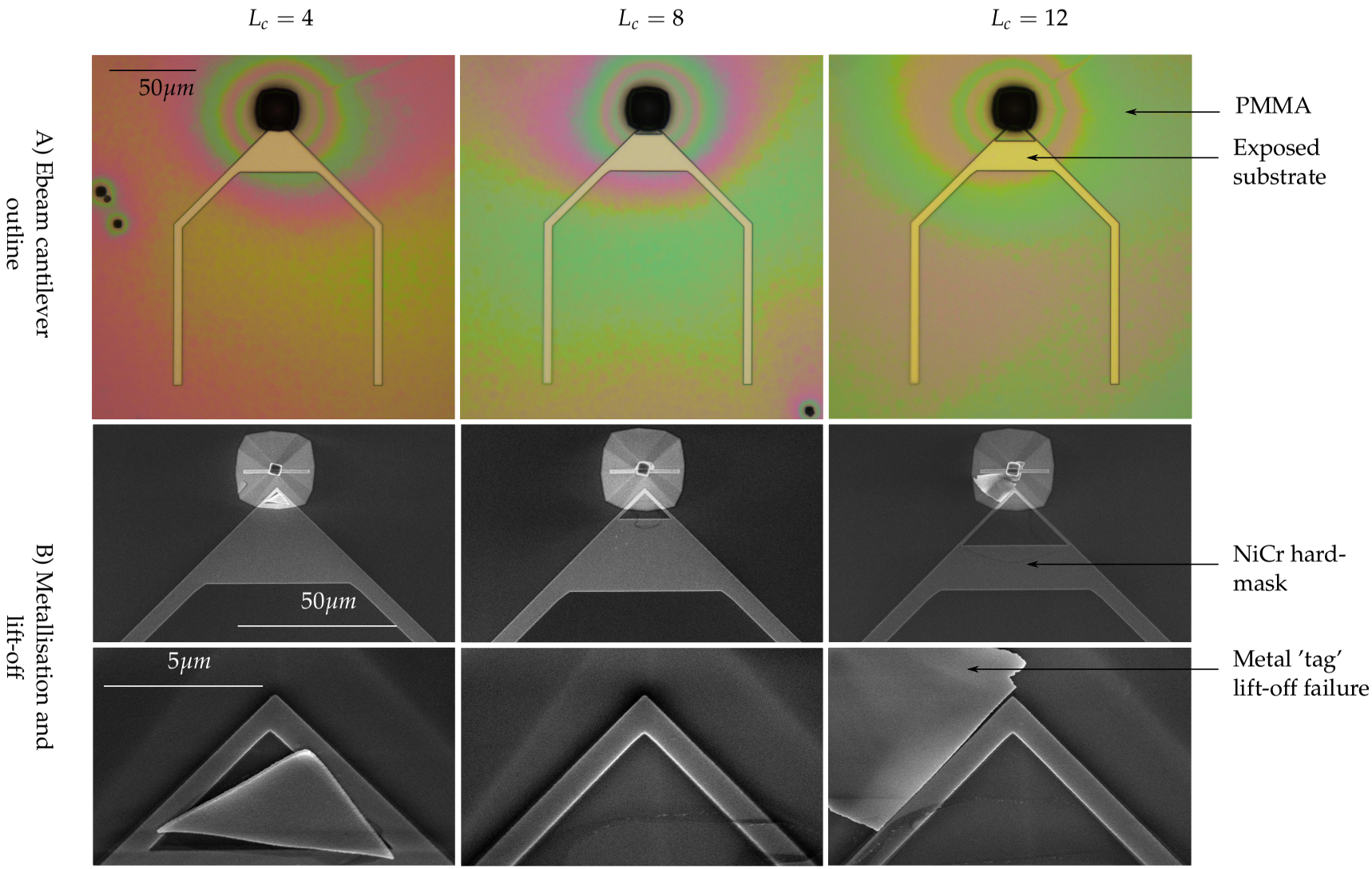

FIGURE 6.4: Fabrication gallery for feasibility study cut out probes - cantilever hard mask EBL. **A:** EBL pattern after exposure and development. Note the resist non-uniformity which is observable in the form of concentric rings of optical interference. The angles of the pyramid's walls are too high to be captured in optical microscopy, and thus appear black. **B:** SEM images of the same pattern after metallisation of 75nm NiCr and lift-off. $L_c = 4$ has failed to lift-off properly due to its small area. $L_c = 12$ has a metal 'flag' at the tip which is also an indicator of poor lift-off.

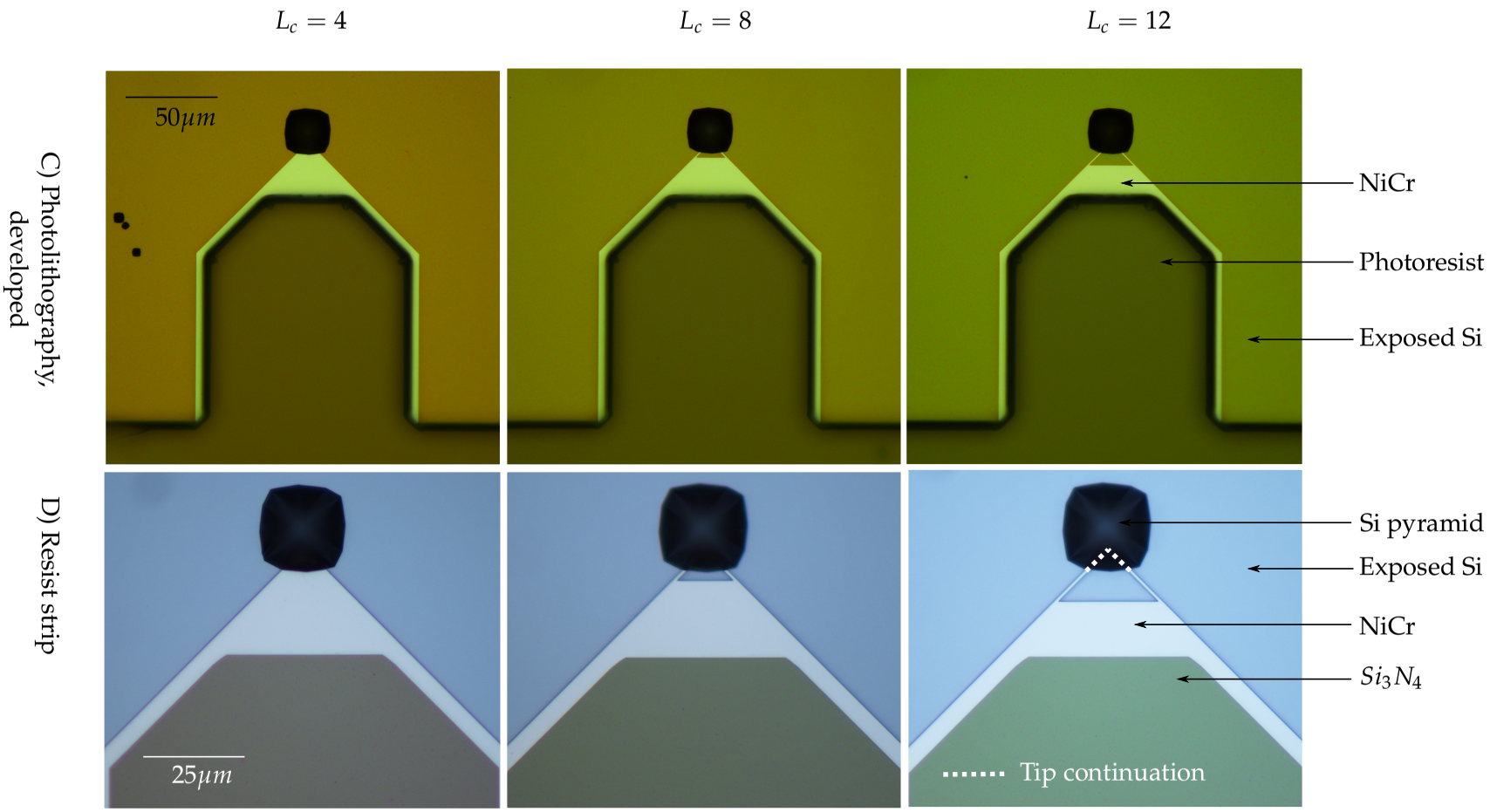

FIGURE 6.5: Continuation of Figure 6.4 - cantilever hard mask photolithography and dry-etch. **C:** Photolithography defines the inner portion of the cantilever. These images are after exposure and development. **D:** The same probes after dry etching through the SiN film and removing residual photoresist, but before removing the NiCr hard mask.

A particular concern in the fabrication of these designs was the lift-off of the triangle shape which comprises the 'cut-out'. It is completely surrounded by the cantilever mask, which is intended to remain on the wafer. Lift off processes are often facilitated through 'tearing' or 'peeling' of the metal film as the resist underneath it is dissolved away, starting at narrow, linear features.

When a region of metal intended for lift-off is completely bounded, it is more difficult to find an edge from which to begin the 'peeling' processes which facilitates good lift-off. Agitation of the solvent can help, but it is most effective when there is a partially released 'edge' of the feature which the forces can act upon to assist with peeling. This is rarely the case with bounded shapes.

In Figure 6.4B, we can observe that the smallest ($L_c = 4$) design has failed to lift-off properly. This was also true of $Lc = 2$, which may indicate that there is difficulty lifting off the feature when it is entirely placed on the sloped surface of the pyramid wall. However, the most likely cause is the small area - the difficulty of lifting-off bounded features was previously discussed - this challenge is increased when the feature is particularly small. A short dip in an ultrasonic bath was employed to resolve the issue, but did not solve the problem. Sonication is recommended for lift-off, however prolonged ultrasonic agitation is dangerous to these substrates once the back etch has been performed, as this removes a significant portion of the substrate. The probes sit in a thin membrane of Si that is easily broken during ultrasonic agitation; during the course of this work, two wafers have been destroyed due to propagation of cracks induced by sonication.

Metal regions which are not properly lifted off will mask the subsequent dry etch process, and their outlines will be transferred into the SiN cantilever. A key motivation for this sample was the investigation of lift-off success as a function of cut-out size. From this experiment we may reasonably conclude that smaller cut-outs are more challenging to fabricate. Throughout the rest of this section, one can observe the effect of the failed lift-off as this defect propagates throughout the fabrication process.

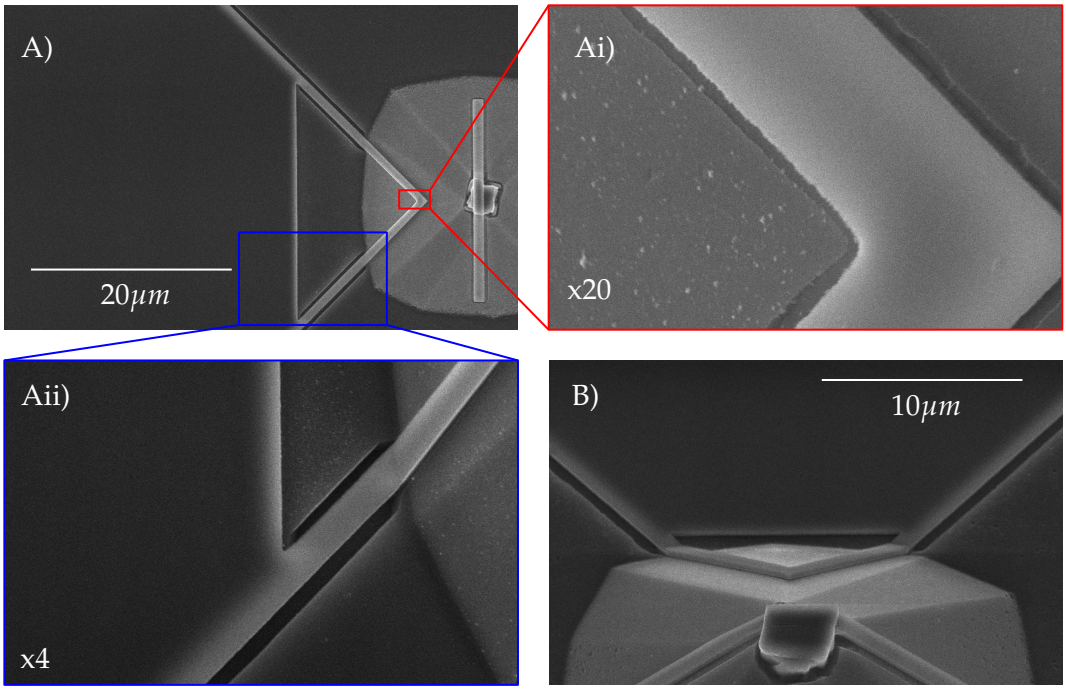

FIGURE 6.6: Gallery of SEM images showing the undercut which results from a 2 min KOH etch. The probe is shown at two separate angles, **A)** and **B)**. Images **Ai)** and **Aii)** are magnified views of image **A**. Undercut SiN is evidenced by the increased brightness compared to SiN directly laminating Si surface. In **Aii)** the etch has completely undercut the part of the beam which is on the flat plane, however this does not appear to be the case for the part of the beam on the slope, as seen in **Ai)**. This is to be expected since the planes which comprise the pyramid {313} etch slower than the {100} planes of the surface. **B)** shows the same device as **A)** viewed from a different angle. The cantilever beam is clearly taller than the Si, but the undercut is less pronounced on the slope.

Sensor deposition - Undercut

For dual self alignment to be successful, a short wet etch is employed to introduce the required step profile. However, completely undercutting the beam is undesirable, as was discussed in Section 5.1.3. The commercial devices are subject to a 7 minute wet etch. The cut-out probes were given only two minutes in the first instance, then inspected in the SEM to assess if further etching was required. Figure 6.6 shows the results. This degree of undercut was certainly sufficient on the flat plane, and appeared reasonable on the pyramid from Figure 6.6B. For this reason, fabrication proceeded without further etching.

Sensor Deposition - Deposition

Ebeam lithography to define the sensors was then performed. There were some concerns that spinning and/or float coating resist on the free-standing beams would cause damage or poor coverage. The latter is not an immediate concern when performing dual self alignment because we desire the entire beam to be metallised regardless. However, performing traditionally aligned lithography on free-standing beams would require sensible coverage to ensure masking in the unexposed regions.

The layout of the sensor was presented in Figure 6.3. The developed pattern is shown in Figure 6.7E, with the metallised result in row F. Upon SEM inspection it was discovered that the metallisation was discontinuous between the beam and the Si substrate, which evidenced that dual self-alignment was viable with this layout.

Release Etch

After sensor deposition, fabrication proceeded as usual with the deposition of the gold pads and wires. The final step is the release etch. It was unknown whether or not such narrow beams would withstand the etch process, particularly being raised and lowered into various aqueous solutions. Surface tension has been observed to bend and break delicate cantilevers. This can be mitigated by orienting the wafer such that surface tension acts perpendicular to the bending axis of the cantilever beams.

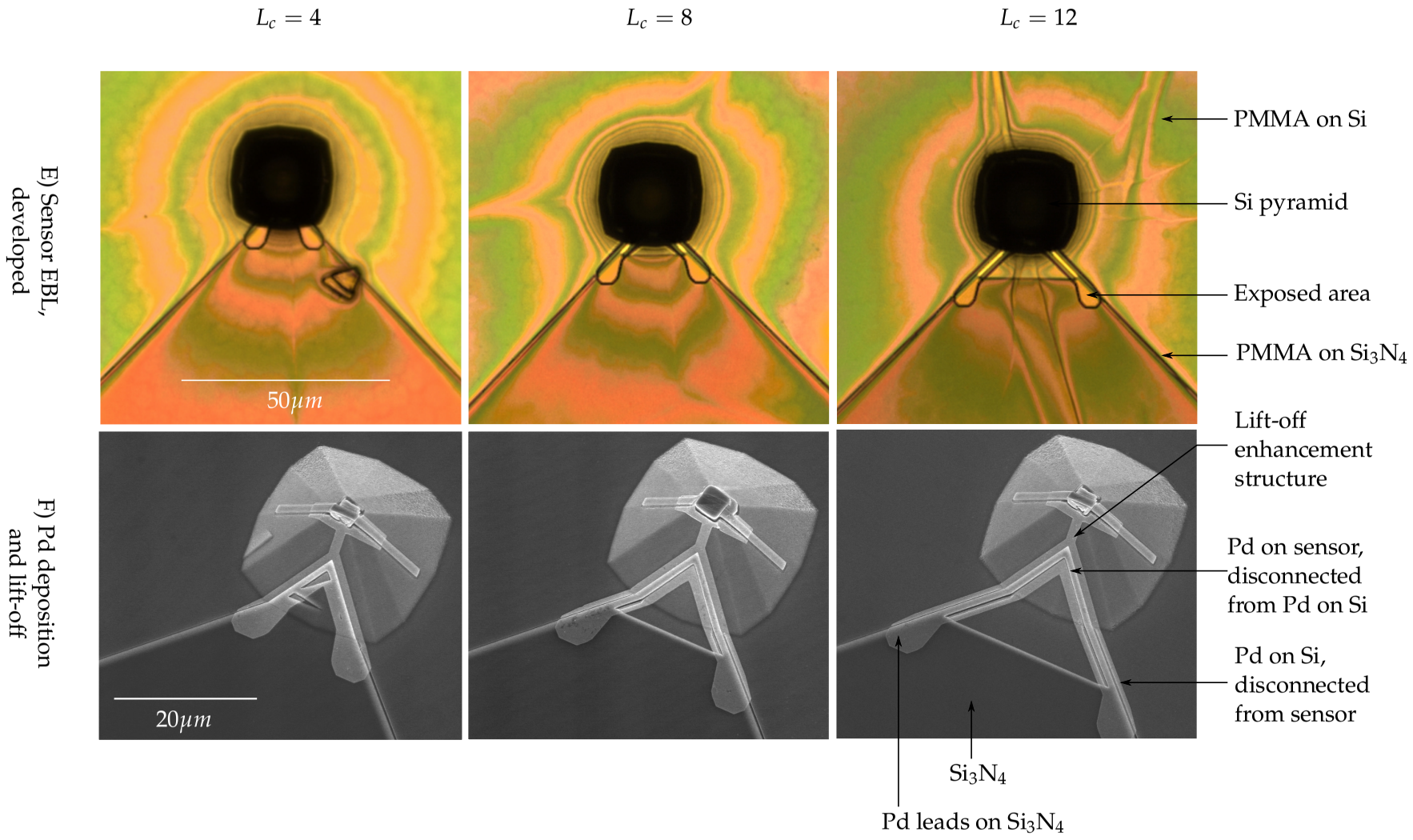

FIGURE 6.7: Image gallery showing the processing of early cut out probes: sensor ebeam and lift-off. In the optical images, the non-uniformity of the resist can be clearly observed by the interference fringes. In the $L_c = 12$ probe, wrinkles in the float coating resist may also be observed. In the SEM images, one can compare the deposited metal to the cantilever beams. The deposited metal overlaps the beams as per Figure 6.3. All the Palladium not deposited on the SiN will be removed upon release.

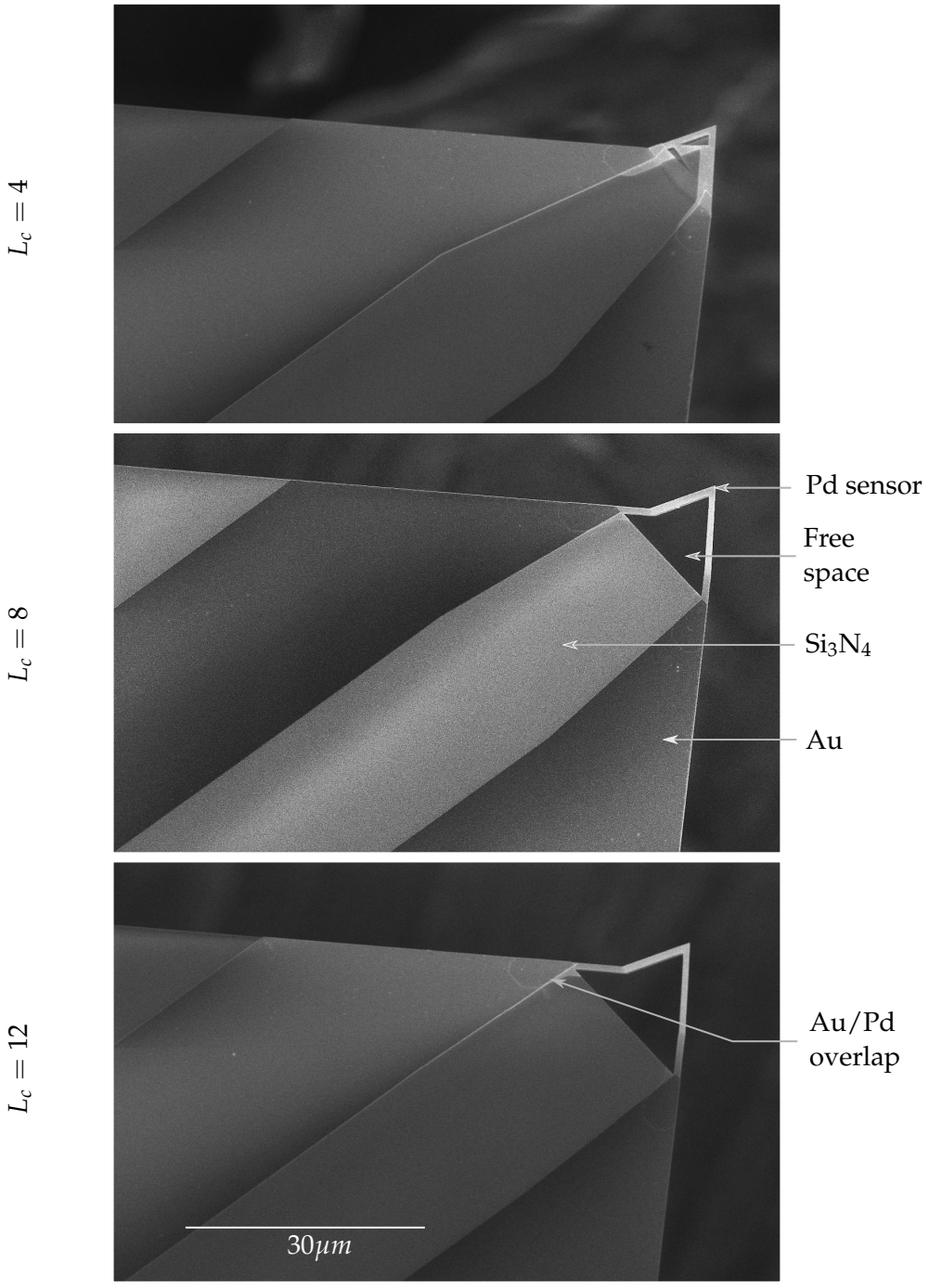

FIGURE 6.8: SEM gallery of early cut-out probes after release. Note that the Si_3N_4 structure defined in Figure 6.4 has transferred faithfully into the sensor, including any defects.

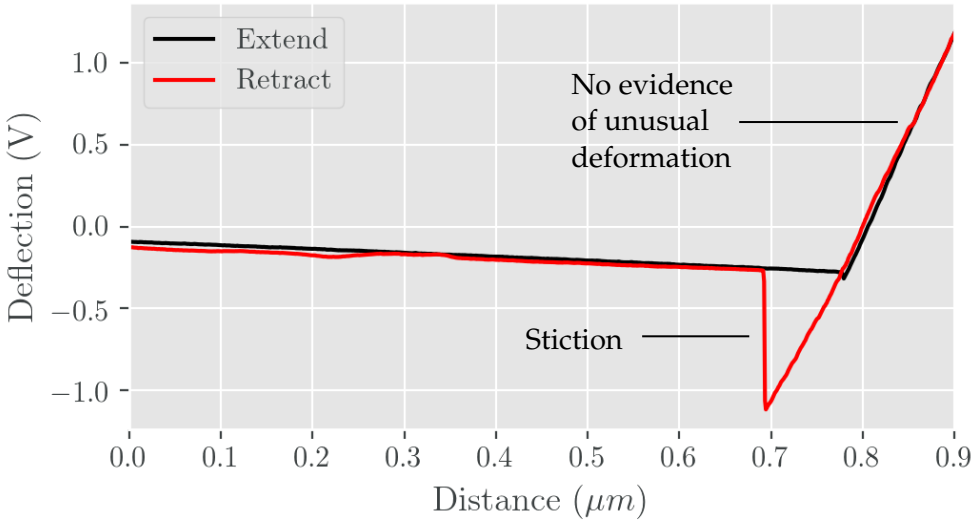

FIGURE 6.9: Force distance curve for initial cut-out size 12 probe. Assuming a spring constant of 0.3 N/m, which is typical for these probes, the maximal force applied in this curve would correspond to 60nN

The probes were successfully released using the standard release etch (Step 58, Appendix A). Gentle rinsing and N2 blow drying from methanol, which has lower surface energy and more readily evaporates than water. This enables the probes to be cleaned and dried without causing damage to the cantilevers or their narrow beams.

Figure 6.8 presents a gallery of these probes after release. We observe that the lift-off issue in the probe in which $L_c = 4$ has propagated all the way through to release, resulting in a cantilever without a proper cut-out. Because the layout of the sensor is defined by the cut-out, failures of this kind will result in a sensor with reduced resistance due to the unintentionally increased width. While they may be functional, their performance will not be improved with respect to the commercial devices, and may in fact be lowered by the reduced sensor resistance, non uniform current density and asymmetric thermal conduction.

6.1.3 Mechanical Testing

Deflection sensitivity

Released probes were loaded in to the AFM to ensure reasonable performance as standard contact AFM probes. The laser signal was observed and compared with

that of standard commercial devices. The laser 'sum' is a measure of the total light entering the photodiode through reflection from the cantilever. These cut-out probes yielded the equal or greater sum than their commercial counterparts, despite reduced gold area, indicating their suitability as optical levers.

Tests were performed to measure the sensitivity of the probes during force-distance probing to ensure that their behaviour is not drastically altered by the changes implemented to the cantilever. Namely, there was some concern that the narrow beams might bend or buckle under load, rather than deflecting the cantilever appropriately. Figure 6.9 presents a single force-distance curve of the same type that was collected in this experiment, in which no evidence of unusual deformation was observed.

The 'sensitivity' of the probes is the gradient of the force-distance curve when the probe is in contact with the sample surface. It quantifies the relationship between the photodiode voltage and the distance travelled by the piezo, and was deemed a suitable measure of whether or not these proof-of-concept cut-out probes were comparable with standard devices, and if there was any dependence on deflection sensitivity with cut-out size, L_c. The force experienced between the probe and the sample can be estimated from the distance travelled beyond the contact point, and the probe's spring constant, which we assume to be the typical 0.3N/m for this estimation. As such, it is reasonable to assume forces of the order of 100nN, which is on par with (or slightly greater than) typical contact SThM forces.

A statistical analysis of the sensitivity was performed for all 12 sizes of probe. Multiple F-D curves were collected at the same location for each probe. Gwyddion was used to find the first order fit ($a + bx$) to the contact regime of the probe, and the sensitivity coefficient b was averaged for the many contacts. The results are presented in Figure 6.10, where we observe a weak correlation between cut-out size and sensitivity. The trend is reducing sensitivity for increased cut-out size, meaning that less bending of the cantilever occurs for the same applied force, which might suggest the beams were bending rather than the 'body' of the cantilever. It should be appreciated however, that the laser spot cannot be positioned reproducibly between individual probes. Additionally, with increased cut-out length, the laser must be positioned closer to the base of the chip, which is the fixed position from which the

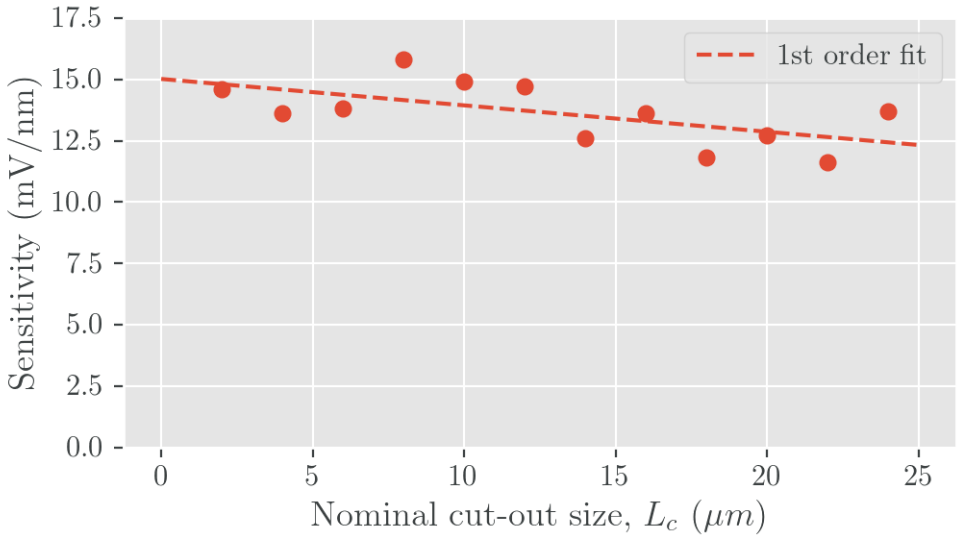

FIGURE 6.10: Comparison of the deflection sensitivity between all 12 varieties of the initial cut-out probes.

lever is deflected. Therefore, the deflection sensitivity will be reduced by positioning the laser in this region.

From this, it is possible to conclude that implementing a cut-out region, even one which is quite large, does not have significant impact on the mechanical functionality of the SThM probe.

Contact scanning

A probe with reasonably large cut-out $L_c = 12$ was selected for contact scanning on a sample with significant relief. The results are presented in Figure 6.11. The probe is clearly suitable for contact mode scanning despite the significant change to the cantilever layout. The scan shows no obvious signs of mechanically induced scanning artefacts.

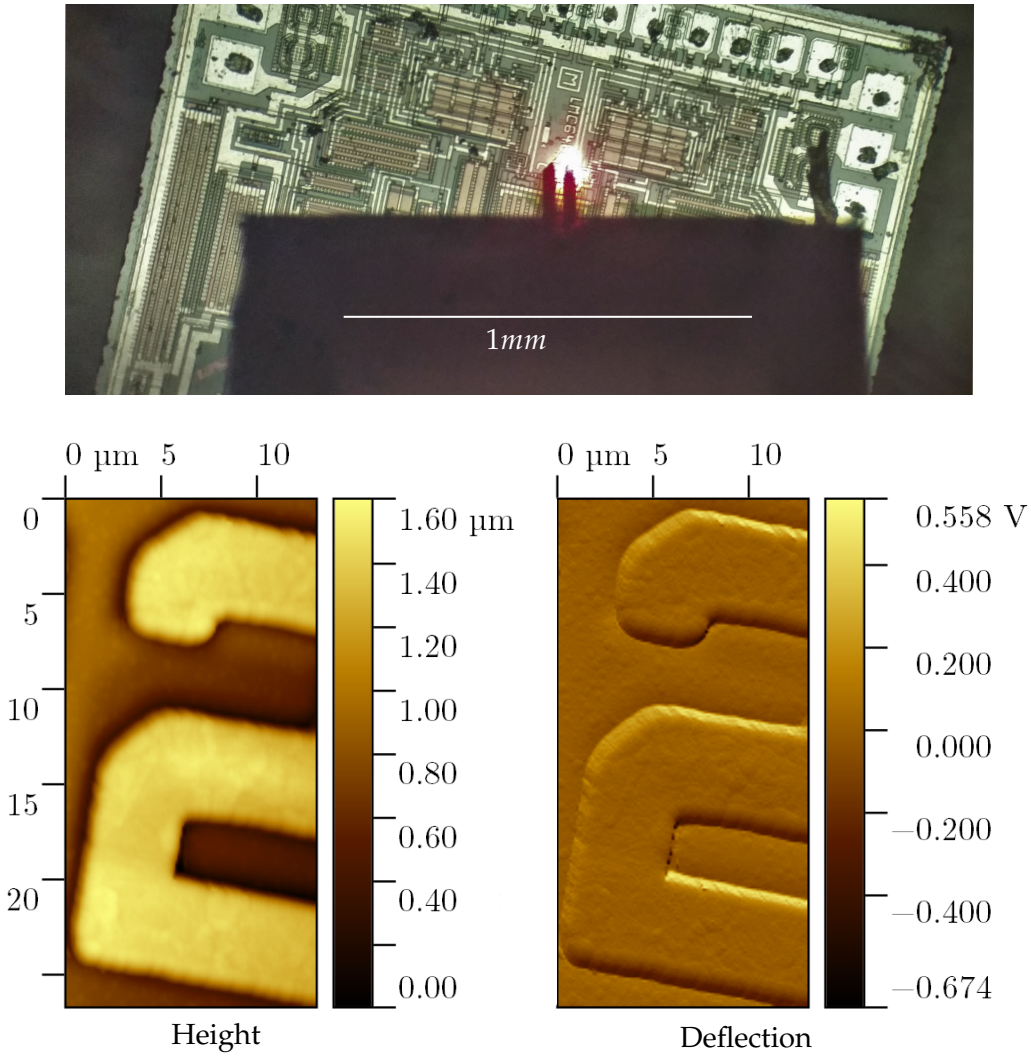

FIGURE 6.11: Scan result for an early cut-out probe.
[Scan result for an early cut-out probe, in which $L_c = 12$. **Top:** The sample over which the probe was scanned, which is an LMC6202 IC. The part number of the IC is etched into the device, and the probe is scanned over the number '2'. **Left:** Height channel AFM data, **Right:** Deflection channel AFM data.]

6.2 Four terminal cut-out probes

6.2.1 Motivation

The results of the previous section demonstrated that 'cut-out' SThM probes were feasible to fabricate, and were mechanically suitable for contact scanning. In this section, we combine the insights from the previous fabrication run with the insights gained from simulations performed with the thermal model. These inform the design of the advanced probes, which are enabled by the technologies developed throughout this thesis (height fitting, improved alignment).

The wafers developed feature arrays of eight probes, the designs of which are presented across Figures 6.13 and Figure 6.15. Four sensor/cut-out sizes were chosen to challenge the limits of the improved fabrication methods, and to identify the relationships between the changes and the resulting performance. In addition, all four sensor layouts were deployed on cantilevers without a cut-out structure, with the intention of distinguishing the performance benefit introduced by each of the two key changes (cut-out, and sensor).

Section 6.2.2 describes the motivation behind the designs of the 8 probes chosen, while Section 6.2.3 outlines the process behind their fabrication.

6.2.2 Design

Pads layout

The re-design of the sensor also necessitated a re-design of the gold leads to which it is connected, and the pads on the chip.

On the cantilever

With four terminal probes, the bridge circuitry compensates for the resistance of the wires, therefore they may be arbitrarily narrow. The design presented in Figure 6.12 features gold leads of width 1.16 µm and thickness 145nm. The self heating of gold features was already shown to be insignificant (Figure 4.24, Section 4.7.3), and has not been significantly altered by the reduction in wire width in this design.

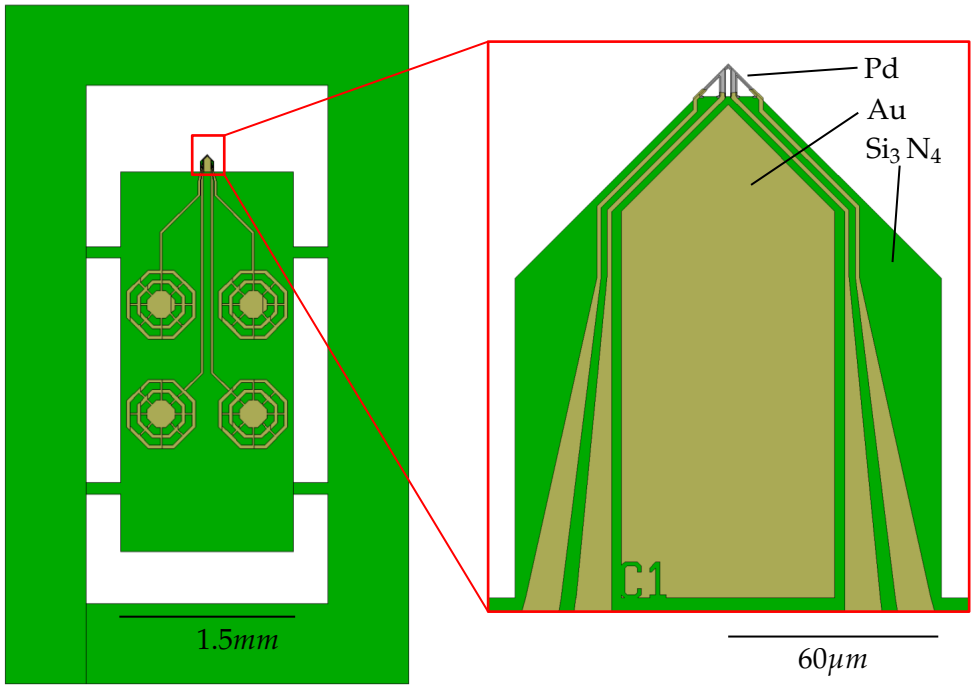

FIGURE 6.12: Schematic drawing showing the revised pads layout for four terminal probes. The two upper pads correspond to the two outer leads, while the two lower pads connect to the two inner leads. The probe's designation is subtracted from the bottom left of the reflector for easy identification when performing optical/SEM inspections. The pads have reduced area to minimise exposure time during electron beam lithography

The large central reflector region was chosen to eliminate the optically transparent region down the probe's centre, which was the result of using the gold leads as a reflector. The intention was to reduce heating of the sample from the laser. This large gold region extends along the entire length of the cantilever, the intention being to improve the thermal coupling between the cantilever body and the chip, allowing for better sinking of external cantilever heating, such as that which is the result of the laser deflection system. While it is true that reducing the gold volume on the probe increases the probe's thermal resistance, we posit that once heat has entered the body of the cantilever, there is little benefit to increased thermal resistance in this region. The pad and interconnect design shown in Figure 6.12 was designed such that the same layout could be shared across all probe designs, with only the tip electronics being re-drawn in each case.

On the chip

The pads layer is written in a single stage of electron beam lithography, using the 128nA spot, which is the largest available. However, the required exposure area for four filled-in pads is greater than 1.5 mm^2, which requires a significant amount of beam time. In this design, the total area is reduced to 0.7 mm^2, which allows for more probes to be written in the same time. The updated pads layout is presented in Figure 6.12. The interior octagons are 240 µm in diameter, which is large enough to approach with probe station needles or a wire bonding tool. The outer rings of octagons extend to 600 µm diameter, allowing for reasonable accuracy when working with the probes by hand, such as silver painting, or measuring their resistance using regular probes. Outer rings are connected by multiple lines to ensure electrical continuity even if one line is broken. Any failure to lift off between the concentric rings -a lithographic fault - is actually beneficial as it provides more area with which to bond, without having to expose said region using the electron beam.

Cut-out size

The cut-out probes developed in the previous section exhibited poor lift-off of the NiCr hard-mask with diminishing cut-out sizes $L_c < 6$µm. This was the primary failure mechanism experienced during fabrication. It was observed that bounded

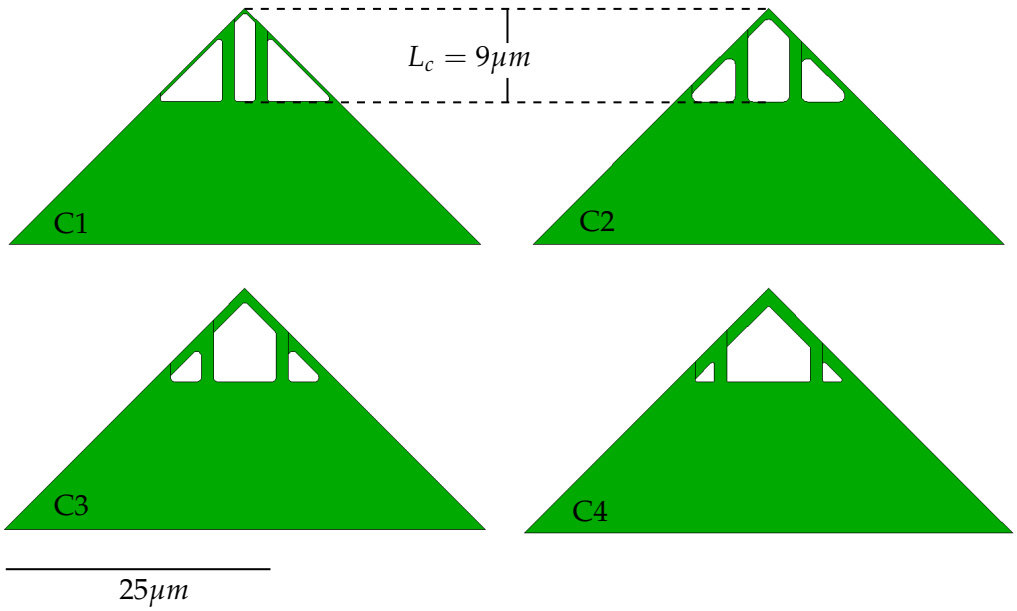

FIGURE 6.13: Schematic drawing of the designs of the four cut-out tip designs to be transferred into SiN. These tips feature four beams, each supporting a connection to the tip. extent of the cut-out is 9 µm. The annotations of C1 through 4 represent the name of the probe. The naming convention is presented in Figure 6.14. Probes with a lower number have narrower outer beams, and are expected to have the greatest localisation of heat, but will tolerate the least current and be hardest to fabricate. Those with larger beams are not expected to have the same performance increase, but instead offer improved reliability and uniformity. Outer and inner beams have different widths, which allows for some choice between which pair are chosen as the drive/sense leads. The rationale behind this design choice is given in the body of the text.

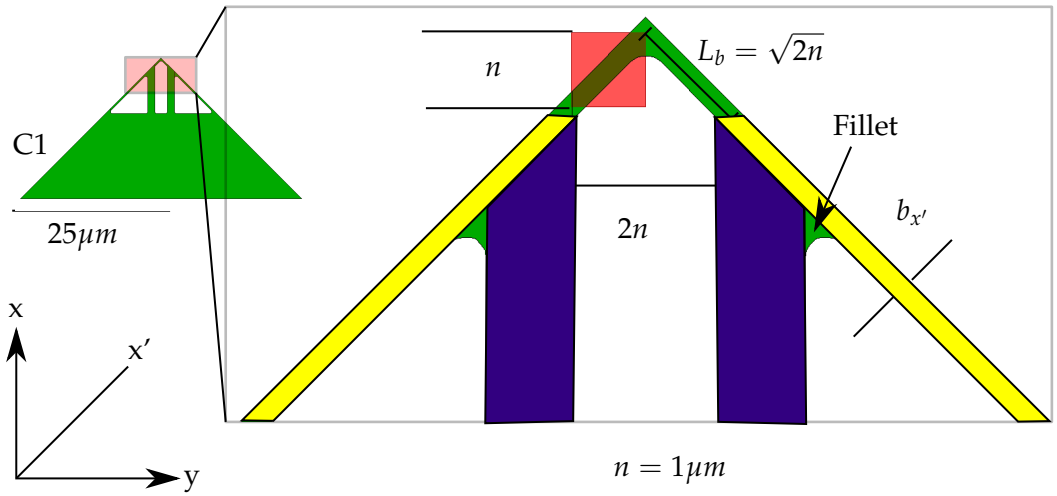

FIGURE 6.14: Schematic drawing highlighting the dimensions of a C1 type probe. The naming convention is defined by the side of square n, which describes the scaling of the sensor. The width of the sensor and outer beams in the x' direction is the result of scaling such that the sensor resistance is always 110 Ω.

features positioned wholly on the pyramid side-wall were difficult to lift off. No significant degradation in mechanical performance was observed for cut-out sizes up to 24 µm, however results from the model (Figure 4.33, Section 4.10.1) showed that there were diminishing returns in terms of thermal performance from extending the cut-out beyond the sensor region. Although only a weak correlation between deflection sensitivity and cut-out size was observed experimentally (Figure 6.10), it was decided not to implement such a large cut-out. An extent of 9 µm was chosen for all the cut-out designs. This was expected to achieve a reasonable balance of mechanical stability, ease of lift-off, and increased thermal resistance.

Also noteworthy in Figure 6.13 is the filleting of all the internal vertices of the design. This change is introduced with the aim of improving lift-off of NiCr in these challenging regions by encouraging the propagation of an existing tear [231], [232]. The difficulty in lifting off this triangular internal structure was previously presented in Figure 6.4. The filleting may be seen more clearly in the magnified view of Figure 6.14

Sensor Size, n (um)	Width, x' direction, $b_{x'}$ (nm)	Maximum Current (mA)
1	291	0.67
2	583	1.35
3	874	2.02
4	1166	2.69

TABLE 6.1: Sensor width and maximum current for the four probe designs chosen.

Beam width (electronics design)

The thermal model presented in Chapter 4 suggested that the averaging of the temperature along the sensor length was a limiting factor in the sensitivity of the SThM probe, since only the final few 100's of nm was appreciably cooled by the introduction of a solid contact. Therefore, the sensor should be scaled down for increased performance. However, the resistance should not be appreciably reduced, otherwise it will not be possible to accurately measure changes in resistance at a given current.

Reduction of the length of the sensor would be associated with reduced resistance. Compensation by making the resistor narrow is an obvious solution, but this would be limited by the reduction of yield for narrow wires and electrical fragility. This trade-off is investigated experimentally by the iteration of sensor size and four terminal separation as shown in Figure 6.13.

A four terminal measurement was employed on these devices, with an individual beam dedicated to each connection.

The resistance of the commercial probes' sensor was calculated as 110 Ω based upon its dimensions and material properties. This calculation is expected to be accurate, given that the they have measured resistances of $350 \pm 50\ \Omega$, which includes the two 100 Ω NiCr limiters. The sensor of the new probes presented here targets this 110 Ω value, and is achieved through scaling the sensor using the dimensions highlighted in Figure 6.14. The different sensor sizes are tabulated in Table 6.1.

In the cut-out probes, the width of sensors is defined by the width of the beams upon which they are fabricated as the result of dual self-alignment. It is desirable to fabricate non cut-out probes with comparable sensors to investigate the thermal isolation

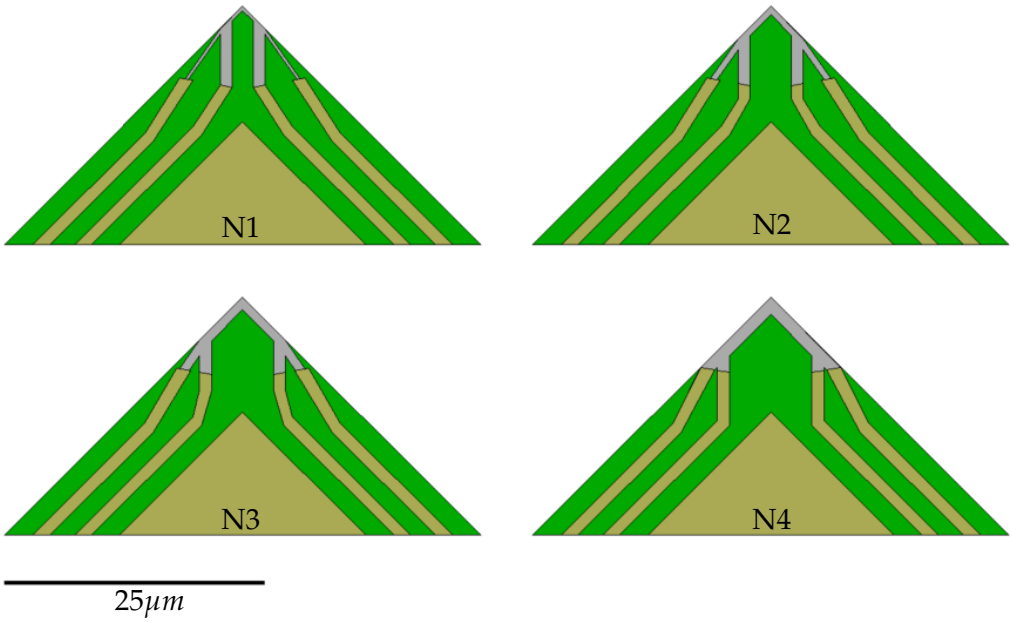

FIGURE 6.15: Schematic drawing of the four non cut-out sensor designs. The outer terminal's width and the inner terminal's position mimics that of the cut-out probes of the same size.

introduced by the cut-out. Therefore, an attempt was mas made to write sensors with width equal to that of the beams of the cut-out probes. The design of the non cut-out sensors to facilitate this comparison is presented in Figure 6.15. As with the cut-out probes, the width of the outer leads is modulated in conjunction with the position of the inner terminals to result in a sensor of fixed total resistance. In the final run of these designs, the sensor was positioned flush to the edge of the cantilever apex. This also served as a test in practical terms of the improved alignment algorithm. Size 1 sensors of width 291nm (C1, N1 type probes) will require very high placement accuracy to result in a sensor of the desired width (and therefore, resistance). This resistance variation therefore serves as an accurate and convenient proxy for positional accuracy of the lithographic exposure.

Dual mode operation

The maximum current of the sensor/heater was calculated from the maximum current density tolerable by the commercial probes. This figure was evaluated from long term stability and failure experiments previously performed by the group [172].

Since all areas of the pattern are the same thickness, the maximum current is limited only by the width. The sensor width is the narrowest point and thus defines the maximum current, but operating at low currents will minimise the degree of heat generated. For this reason, it was decided to have beams of asymmetrical width. This would allow for operation in a couple of different 'modes', depending on the configuration of the connections to the probe;

- **Current through outer beams.** The long extent of the narrow outer beams allows for maximum heat generation at the designated tolerable current. These outer beams have high resistance and elevated temperature, but the measurement is only performed between the two **other** terminals, meaning **only the portion of the sensor which is being actively cooled is being measured**
- **Current through wider inner beams.** If current is driven through these beams, there is reduced self-heating. The high resistance of the narrow outer beams is inconsequential, since they are disregarded in a four terminal measurement. Less Joule heating occurs in this mode, but the sensor extent and resistance is the same. This mode is well suited for 'safe' operation, and for temperature measurement. It should be noted that the probe could still be used in a two-terminal configuration using only these terminals, since the majority of the resistance is still at the narrow sensor.

6.2.3 Manufacture

Dose Testing

The results of initial dose testing are presented in Figure 6.16. A pattern was developed featuring all four cut-out probe tip designs, placed in close proximity. The processing steps for this sample match that of the cantilever definition in the commercial devices, including resist profile, development and metallisation.

A second dose test was attempted, this time using the height fitting algorithm and the over-size under-dose algorithms in BEAMER PEC software (Section 2.5.3). The results of this dose test are presented in Figure 6.17. We observe much crisper pattern transfer, including sharp narrow beams, minimised line-edge roughness and

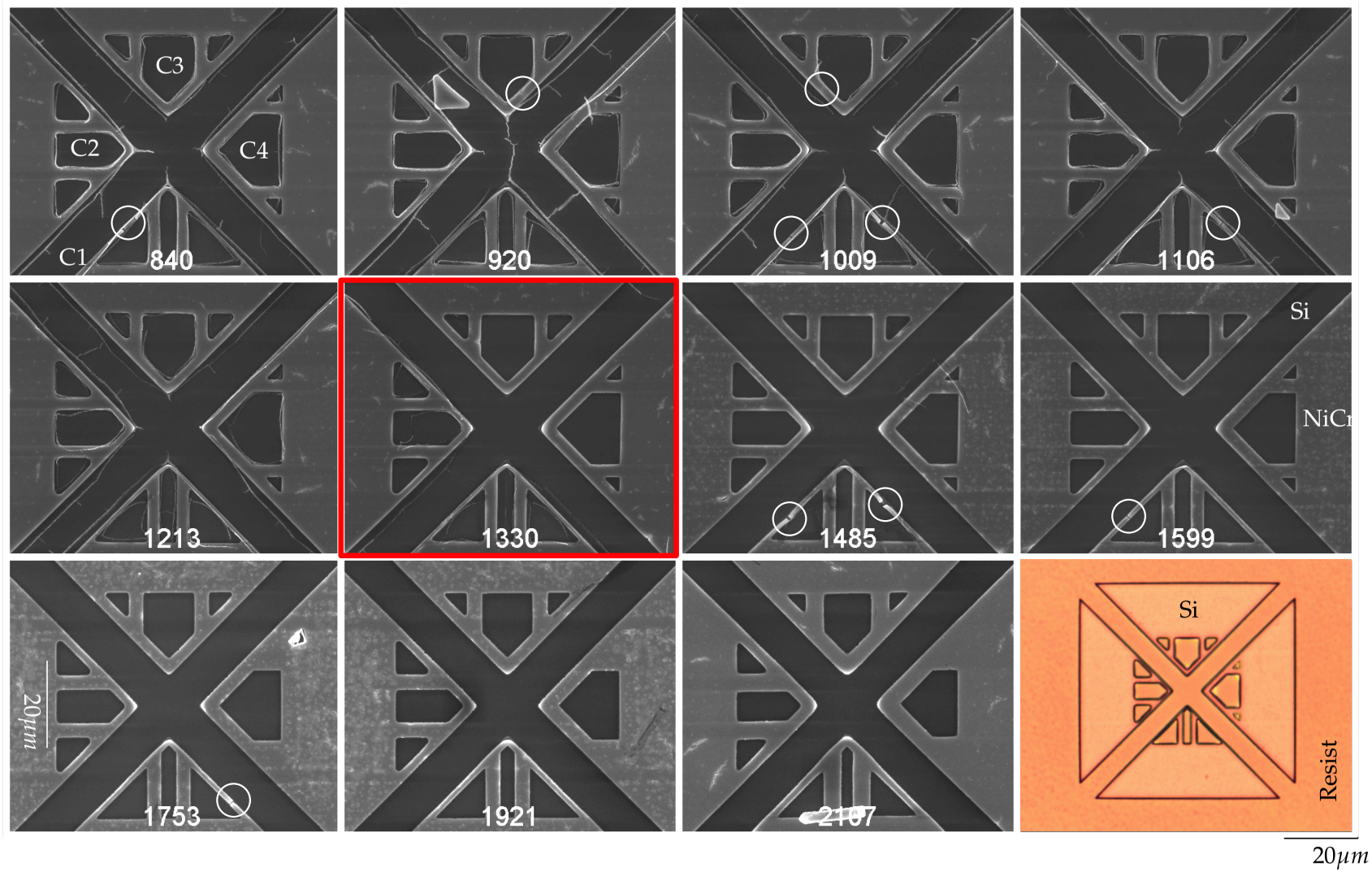

FIGURE 6.16: Results of initial dose testing of four terminal cut-out cantilever tips. 11 doses were incremented, from 840 to 2107 (annotated). The pattern was exposed using electron beam lithography, metallised and lifted-off. The image in colour is an optical micrograph of the highlighted pattern before metal deposition. Stitch errors are highlighted by white circles.

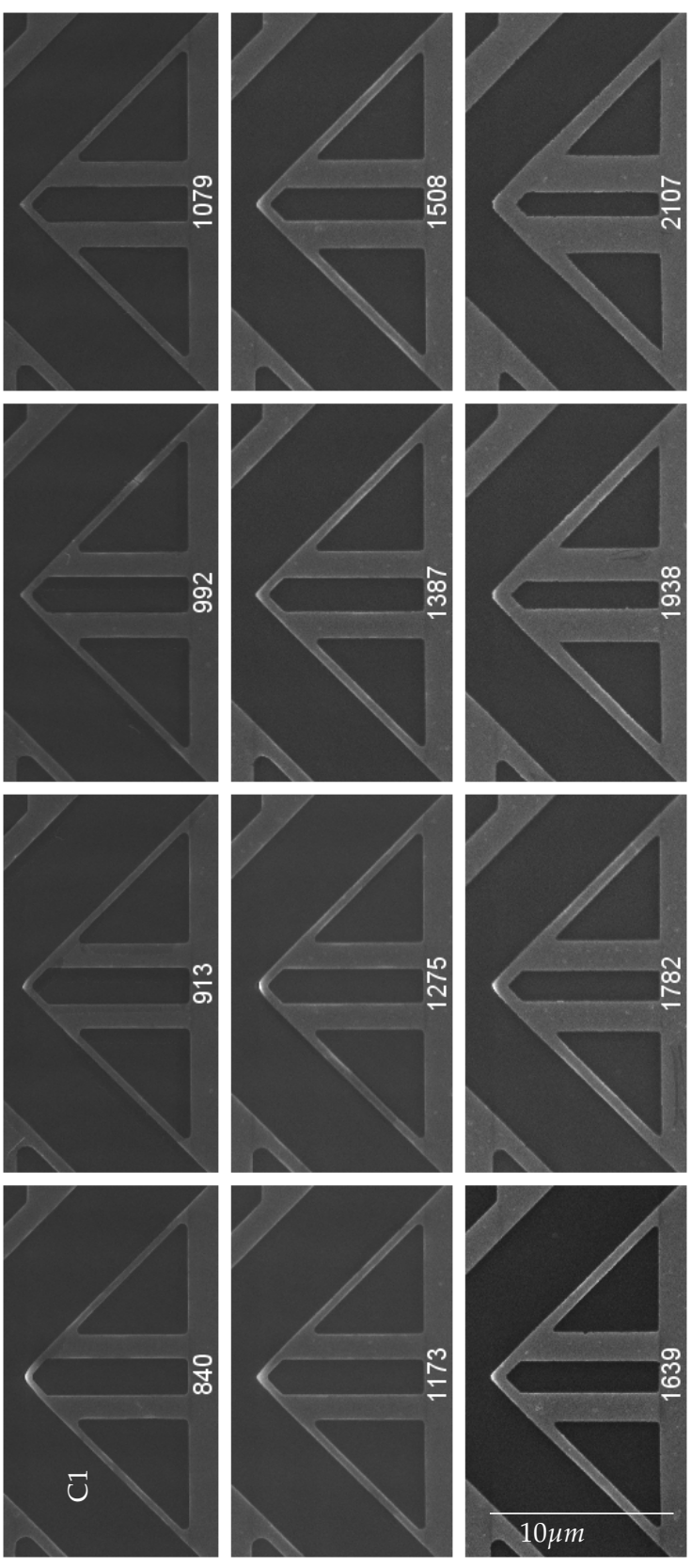

FIGURE 6.17: Second dose test of four terminal probes tips, using advanced ebeam methods. The height fitting algorithm and oversize/under-dose were used. Unlike Figure 6.16, no stitch errors are observed in this exposure.

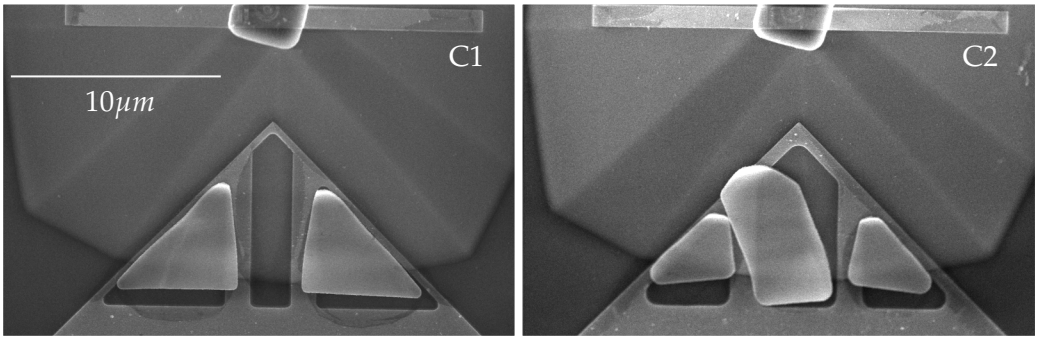

FIGURE 6.18: SEM images highlighting the lift-off failures encountered in early four terminal cut-outs

the complete disappearance of sub-field stitch errors, which were annotated in Figure 6.16. From this work, an optimal dose of 1200 µC cm^{-2} was selected because of its balance between minimal line-width and pattern quality.

Lift-off failures

As was seen in Figure 6.16 and through the previous section on the early cut-out probes, a key challenge in the fabrication of these devices was the lift-off of small features. This problem persisted in the fabrication of the four terminal cut-outs, as can be seen in Figure 6.18. This wafer of devices was given the same treatment as the initial cut-out probes when performing lift-off. Short soak in warm acetone, vigorous pipetting, no ultrasonic agitation. Evidence from the previous section (Section 6.1) shows that poorly lifted off features are not removed during subsequent processing, and these issues are transferred all the way to the eventual device. Given the poor yield of this step on this wafer, it was decided to re-visit sonication.

Ultrasonic Damage

The wafer presented in Figure 6.19 was subject to around 15s of sustained ultrasonic agitation before being removed due to damage being observed. In certain locations, a probe has been completely released from its membrane. In others, parts of the Si membrane have broken off. In the largest of the defects, cracks have propagated across multiple sites, and would likely continue to propagate during subsequent processing.

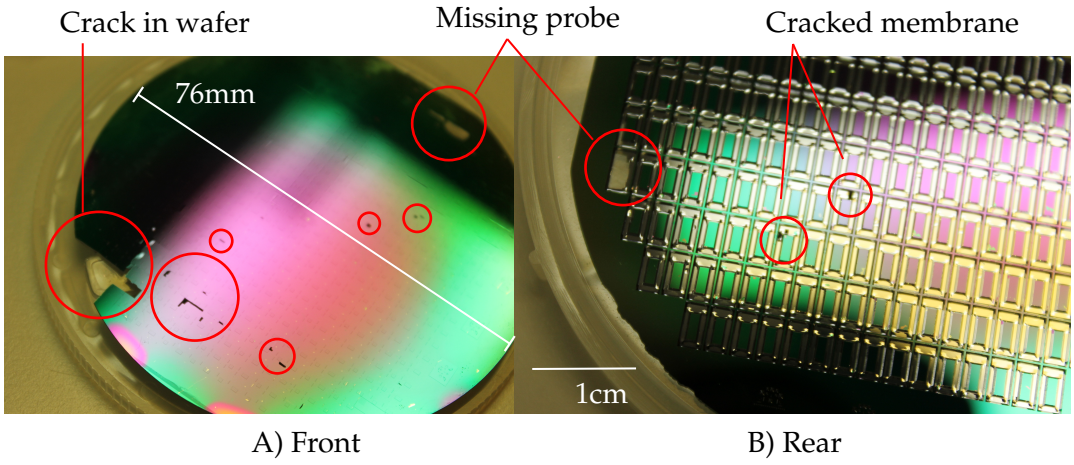

FIGURE 6.19: Photographs highlighting the damage caused by ultrasonic agitation. Damaged regions are highlighted in red

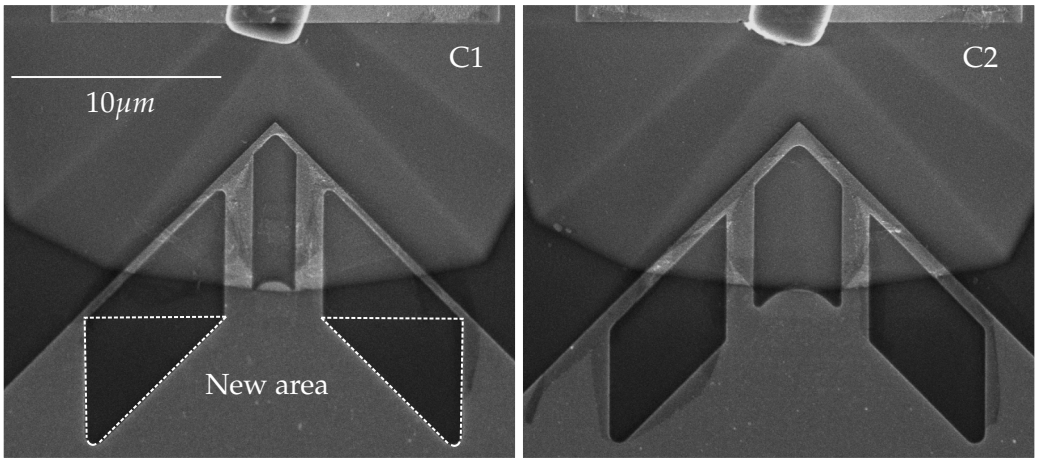

FIGURE 6.20: SEM images showing successful lift-off of the cut-out probes after altering the design and processing. The scale is equal to that of Figure 6.18

This unfortunate result confirmed suspicions that sonication could cause damage to probes which have undergone the deep back etch. Given that the back etch has high variability, and perhaps those wafer which are slightly under-etched may better withstand prolonged ultrasonic agitation. This wafer was discontinued due to its fragility.

Rework - Larger cut-out lobes

The first iteration of cut-out probes demonstrated a relationship between the size of a bounded feature and its success in being lifted off. They also highlighted the fact

that mechanical performance was not degraded by increasing cut-out sizes across the range of sizes fabricated ($2 < L_c < 24$). Given this information, and the failures of the designs presented in Figure 6.13, it was decided to increase the size of the cut-out. Specifically, the 'lobes' were doubled in area, and the filleting radius was significantly increased. These changes are evident in the comparison between Figures 6.18 and 6.20

Processing change - overnight soak, 5s ultrasonic

In addition to the above pattern changes, the lift-off process was reviewed. Firstly, the wafer was allowed to sit in warm solvent for much longer; overnight (at least) as opposed to the two or three hours employed previously. In addition, a sonication of 5 seconds **maximum** duration was introduced to aid in removing any metal flags. Lift-off success was greatly improved by these two changes. Figure 6.20 presents two tips similar to those in Figure 6.18. Successful lift-off and excellent pattern transfer is observed in these devices, and there was no evidence of gross damage to the substrate.

Undercut Etch

After successful transfer of the cantilever pattern from the NiCr hard-mask to SiN, an undercut etch is performed. The preliminary fabrication run indicated that two minutes of KOH etching was sufficient. Therefore, the same etch was repeated in this case. The results of this etch are presented in Figure 6.21. Regions of the cantilever which are undercut by this etch are evidenced by their lighter tone in the SEM image. SEM inspection indicated that the etch depth was sufficient to create the required step for dual self alignment.

Sensor deposition

Electron beam lithography was performed to pattern the sensors on the end of the probes. These exposures made use of both the height mapping and improved alignment algorithms which were presented in Chapter 5. Multiple probes were inspected after lithography, metallisation and lift-off. Figure 6.22 presents a set of adjacent N type probes, which are all written in the same cell, and thus are expected

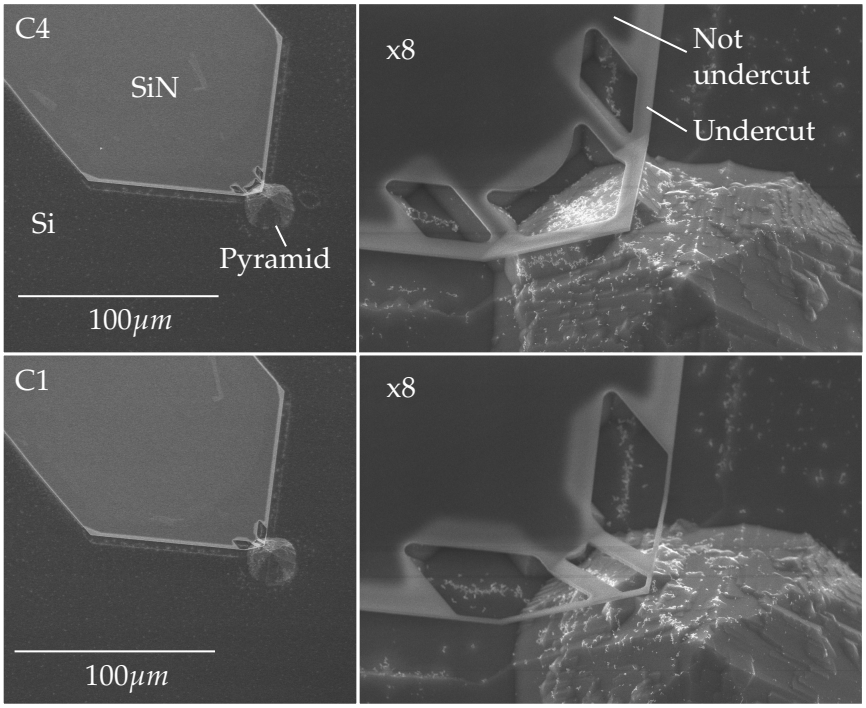

FIGURE 6.21: SEM images showing the undercut etch of cut-out probes.

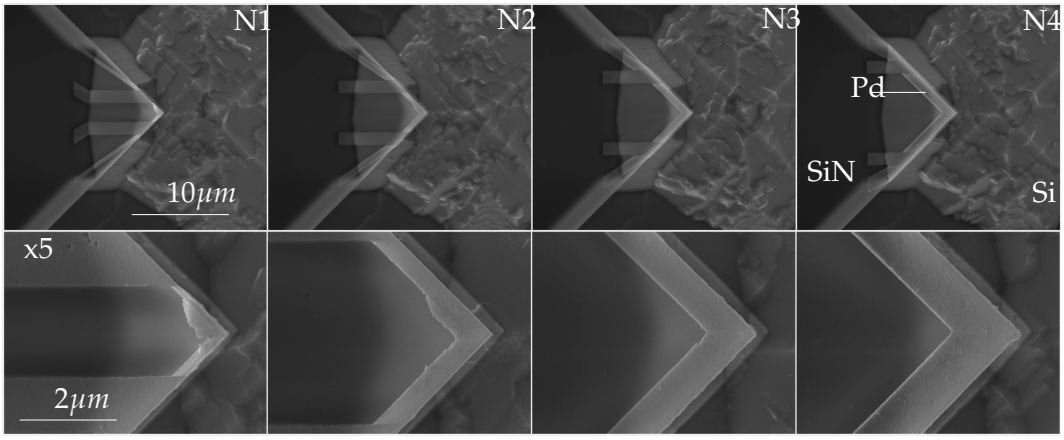

FIGURE 6.22: SEM gallery showing alignment of the sensor to the non-cut-out probes.

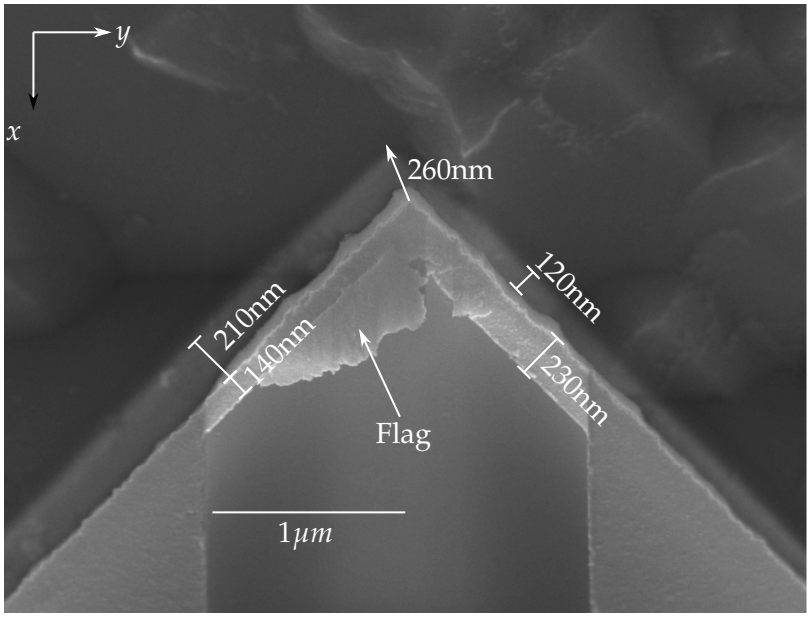

FIGURE 6.23: Annotated SEM image highlighting the misalignment of the sensor on an N1 type probe. The flag is an additional, but unrelated lift-off.

to share the same degree of misalignment. Figure 6.23 presents a larger view of the N1 type probe of Figure 6.22, annotated to show the degree of misalignment. Although the lithography is significantly improved we still observe some errors in line-width and positioning. The sensor width is too large (350 as opposed to 290nm), and the alignment error is evident. An observed vector error of 260nm in positioning between sensor and cantilever tip indicates that sensors this narrow are likely to have large variation in their positioning and resistance. Consider that the probe shown has a misalignment in both y and x. A misalignment in x reduces the total sensor width across the whole length, but a misalignment in y gives asymmetrical width. In the example presented in Figure 6.23, the sensor width on the left is significantly less than on the right (140:230nm), and almost half the designed width. This probe is unlikely to withstand the maximum current calculated for its designed width. The minimum sensor width cannot be assessed without individual SEM inspection. This variability in sensor shape severely limits the utility of such probes as mass-produced metrological consumables.

The sensor design for the cut-out probes was calculated as the 'grow' operation of the SiN layer as drawn in L-Edit, given a target growth of 300nm. This resulted in a shape for the metallisation which was extends beyond the beams 300nm on

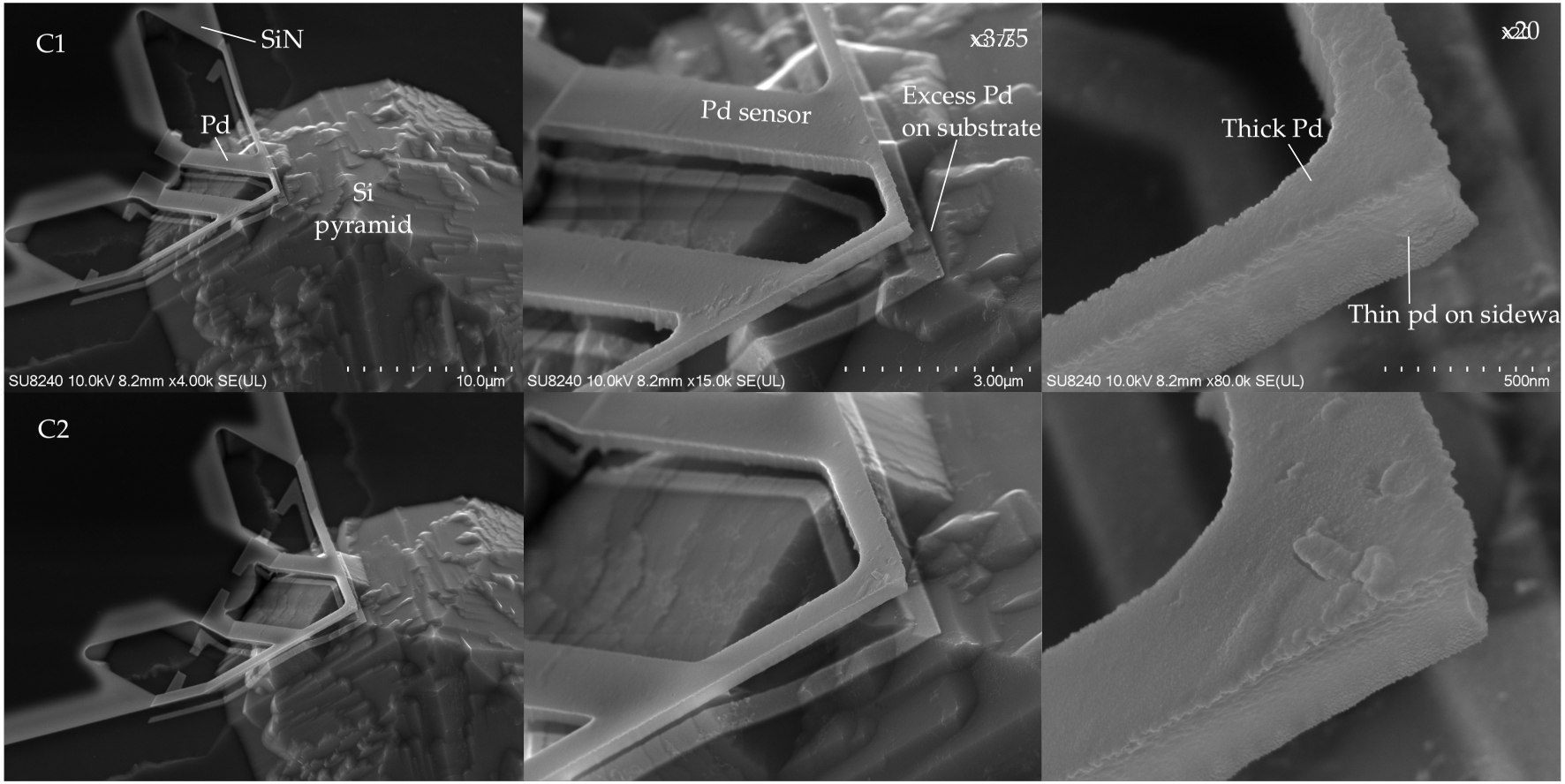

FIGURE 6.24: SEM gallery showing a C1 and C2 type probe after sensor deposition. The undercut and the discontinuity of metal between the SiN and Si surface is evident.

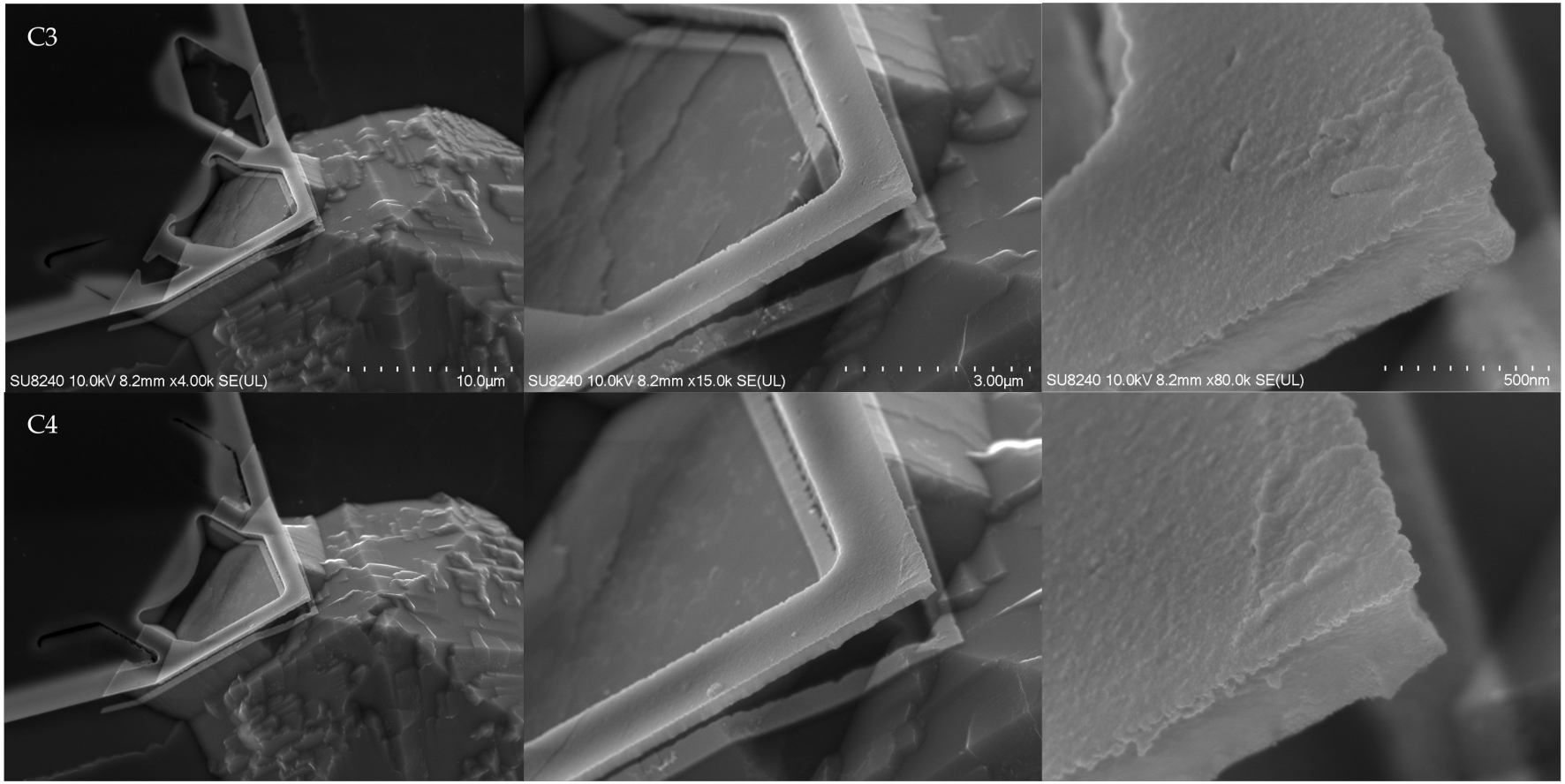

FIGURE 6.25: SEM gallery showing a C3 and C4 type probe after sensor deposition. The undercut and the discontinuity of metal between the SiN and Si surface is evident.

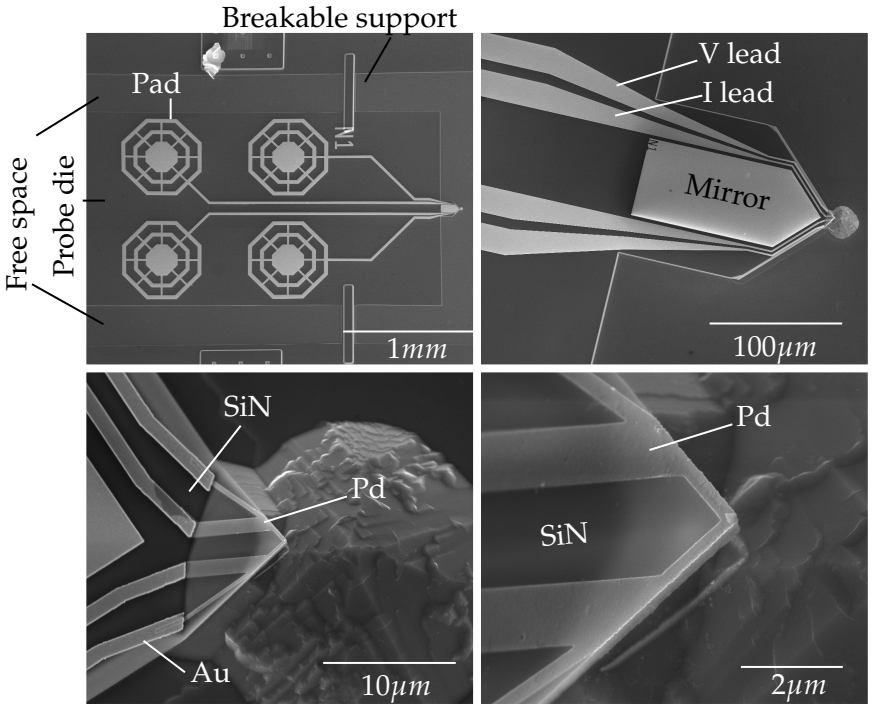

FIGURE 6.26: Gallery of SEM images showing the metallisation of the pads layer - N1 type probe

each side. This is large such that beams are still completely covered despite any lithographic misalignment. Dual self-alignment results in a sensor which extends equal length to the beams. Figures 6.24 and 6.25 show the result after patterning on these devices. The undercut is clearly visible, as is the discontinuity between the metal on the SiN cantilever and Si substrate.

Pads metallisation

The layout for the reflector, pads, and gold leads was discussed in Section 6.2.2. The fabrication procedure is identical to that of the commercial probes (steps 54-56 of Appendix A). Figures 6.26 and 6.27 present SEM images of the updated design realised on N1 and C1 type probes respectively. In the latter, we observe self alignment of the gold layer to the narrow outer beam.

Release etching

Release etching was performed according to the standard recipe (Step 58, Appendix A). No probes were lost during the etch or subsequent cleaning processes. As with

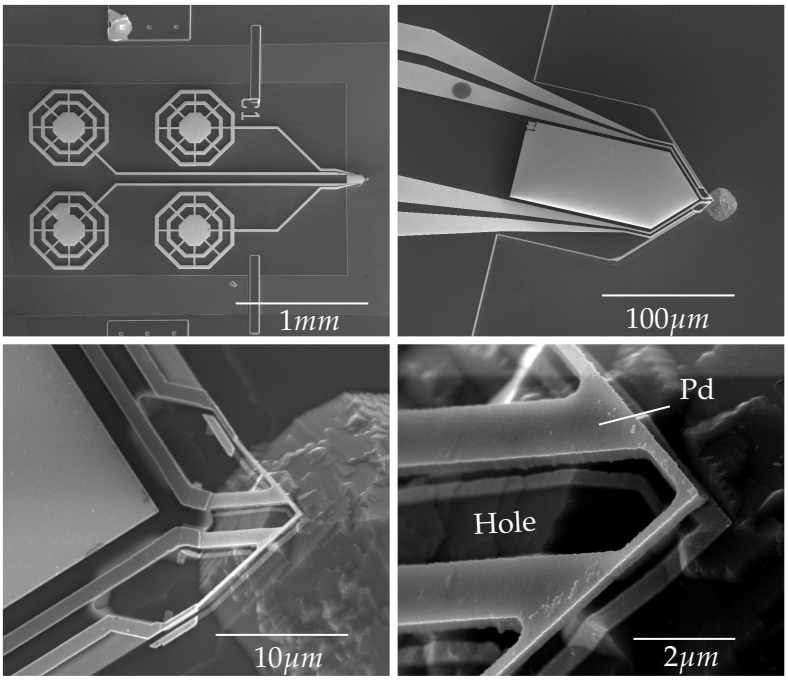

FIGURE 6.27: Gallery of SEM images showing the metallisation of the pads layer - C1 type probe

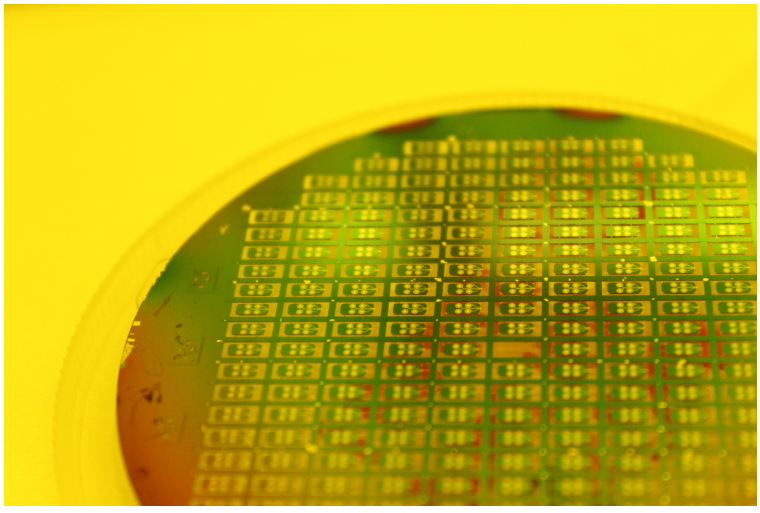

FIGURE 6.28: Photograph showing the wafer of four-terminal probes after release. No probes were lost during the release etch and subsequent cleaning steps. The missing central probe is designed to float away during the etch as an indicator of the etch rate.

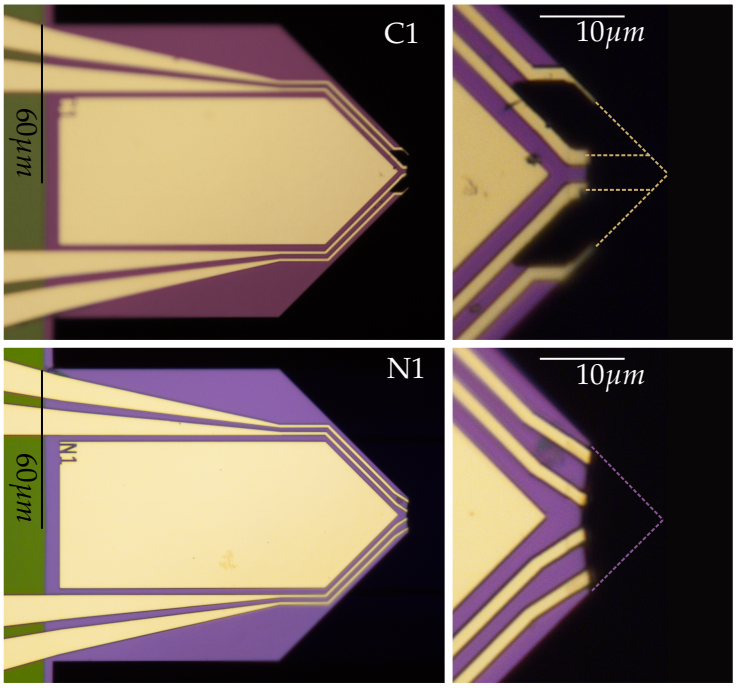

FIGURE 6.29: Optical micrographs showing released cantilevers. The angled 'beak' of the probe cannot be viewed in bright-field mode, therefore dotted line annotations have been added to demonstrate where the tip would be.

the previous cut-out probes, attention was paid to the orientation of probes as they were transferred into or out of aqueous solutions to avoid surface tension induced damage. Similarly, nitrogen drying was performed extremely gently in order to avoid damage . The drying angle was selected such as not to apply significant force to the bending axis of the cantilevers. A photograph of the released probes in the wafer is presented in Figure 6.28. Figure 6.29 presents a size 1 probe of both 'C' and 'N' type. In both cases, the probes are reasonably clean given how conservative the cleaning processes were.

Released devices

Probes were left in the wafer after release and carefully loaded into the SEM for inspection. Images were captured of each probe, and any defects noted. After a full row of probes was inspected (which took roughly 1hr per row), they were popped out of the wafer and transferred into boxes based upon the probe type. Finally, released probes had their resistance measured by hand, using a non auto-ranging

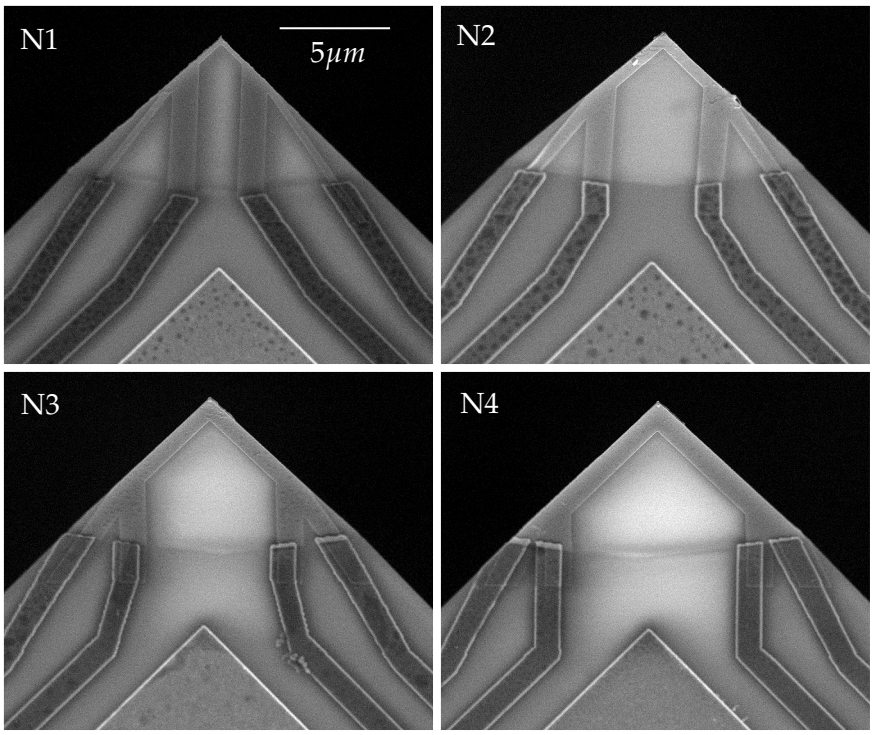

FIGURE 6.30: SEM gallery showing defect free released 'N' type probes.

Probe Type	**C1**	**C2**	**C3**	**C4**	**N1**	**N2**	**N3**	**N4**
Probes inspected	15	16	9	8	11	10	5	5
Probes passed	8	7	8	7	2	4	5	3
% Yield	53%	44%	89%	88%	18%	40%	100%	60%

TABLE 6.2: Yield analysis of probes by type (top half of one wafer)

bench ohmmeter to ensure they were not biased by too great a current.

The yield of the various designs is presented in Table 6.2. Probe are deemed successful if they exhibit no obvious defects upon inspection, have electrical continuity, and reasonable resistance (between 100 and 400 ohms). The procedure for calculating resistance of these four terminal probes is presented in Appendix D.

Figure 6.33 presents the plot of resistance as a function of probe type. We note high scatter in the measurements of N1 and N2 type probes. This is predominantly the result of misalignment of the sensor to the cantilever. The fact that the narrowest N type probes have the highest resistance variation indicates that these devices suffer from misalignment between the sensor and the cantilever edge. Given that the next smallest N type probes do not suffer such bad scatter suggests that the magnitude of the misalignment is on the order of half the width of the N1 sensor, i.e (290nm /

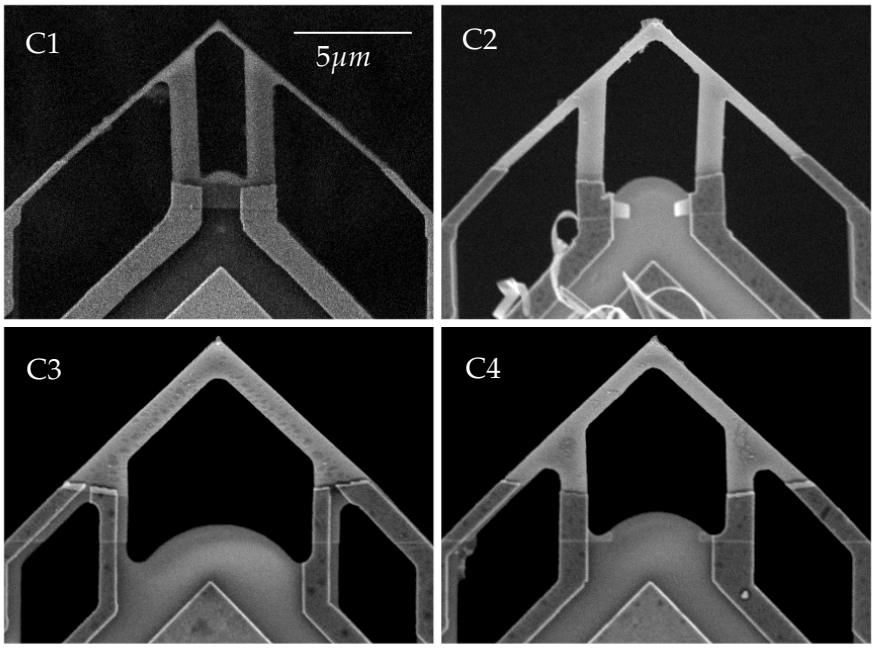

FIGURE 6.31: SEM gallery showing mostly defect free released 'C' type probes.

2 = 145nm). This is in agreement with previous estimates of alignment tolerance as discussed in Section 5.2.

The fact that C1 and C2 type probes do not exhibit this degree of resistance variation demonstrates the utility of dual self alignment as a method for defining the width of metal sensors.

6.2.4 Failure mechanisms

This section presents a gallery of images presenting the defects which were observed during SEM inspection of these probes. Figures 6.34 and 6.35 are collections of SEM images showing the defects. Appendix F features tables which describe the defects and their implications in greater detail.

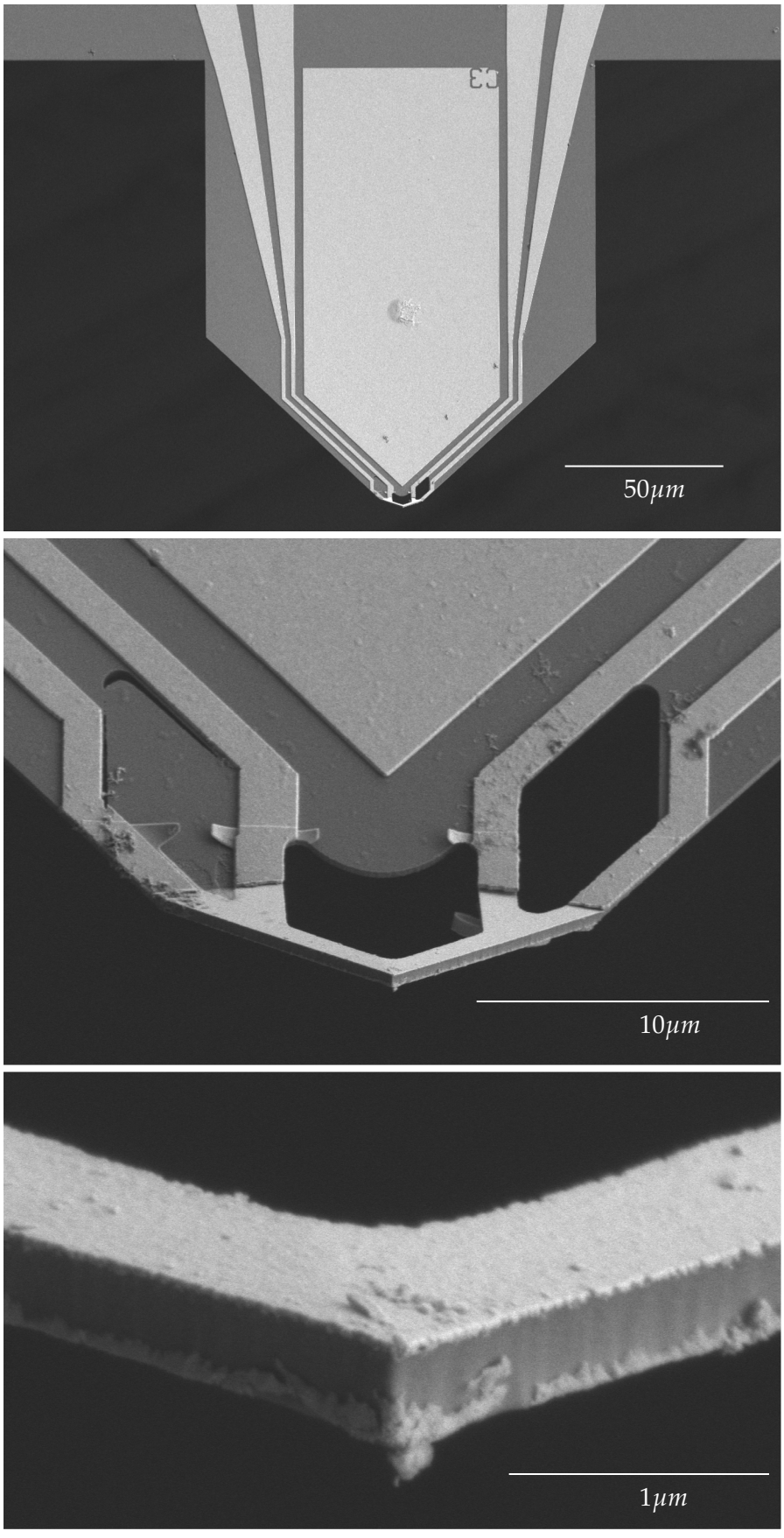

FIGURE 6.32: Set of SEM images showing a released C3 type probe. The cut-out region on the left failed to lift-off properly at the NiCr cantilever definition hard-mask, and thus this region remains in SiN. In this particular case, the electrical performance of the probe is unlikely to be affected.

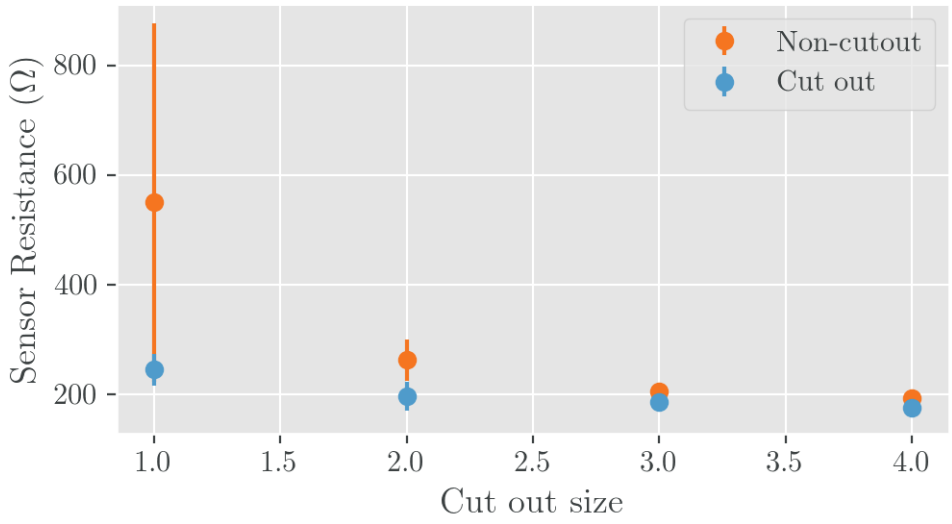

FIGURE 6.33: Post release measured resistance as a function of probe type. The points and error bars represent the average and standard deviation of the resistance respectively.

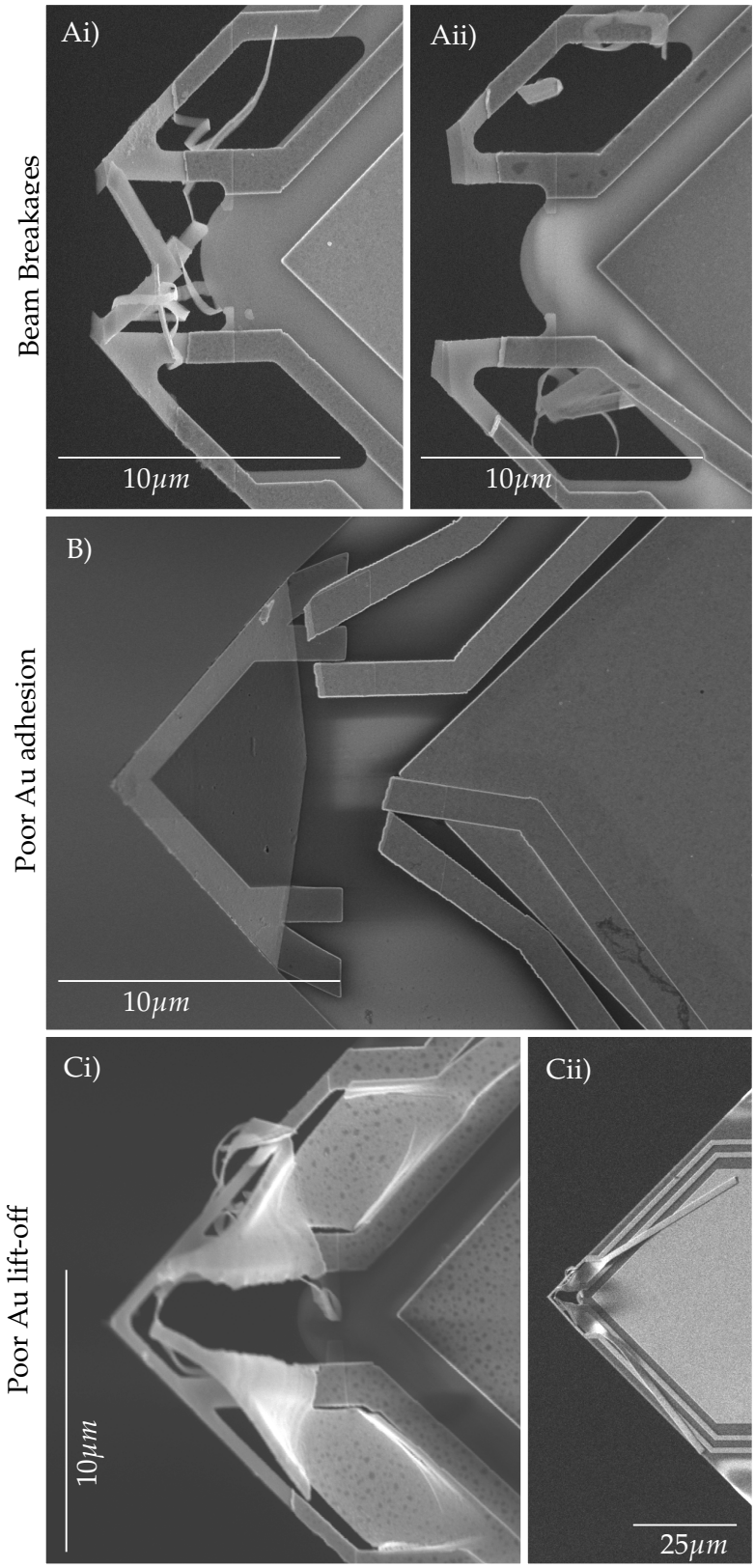

FIGURE 6.34: Gallery of probe failure mechanisms 1: A) Broken beams of C type probes. B) Poor adhesion of gold leads, especially at the Pd/Au interface. C) Poor gold lift off.

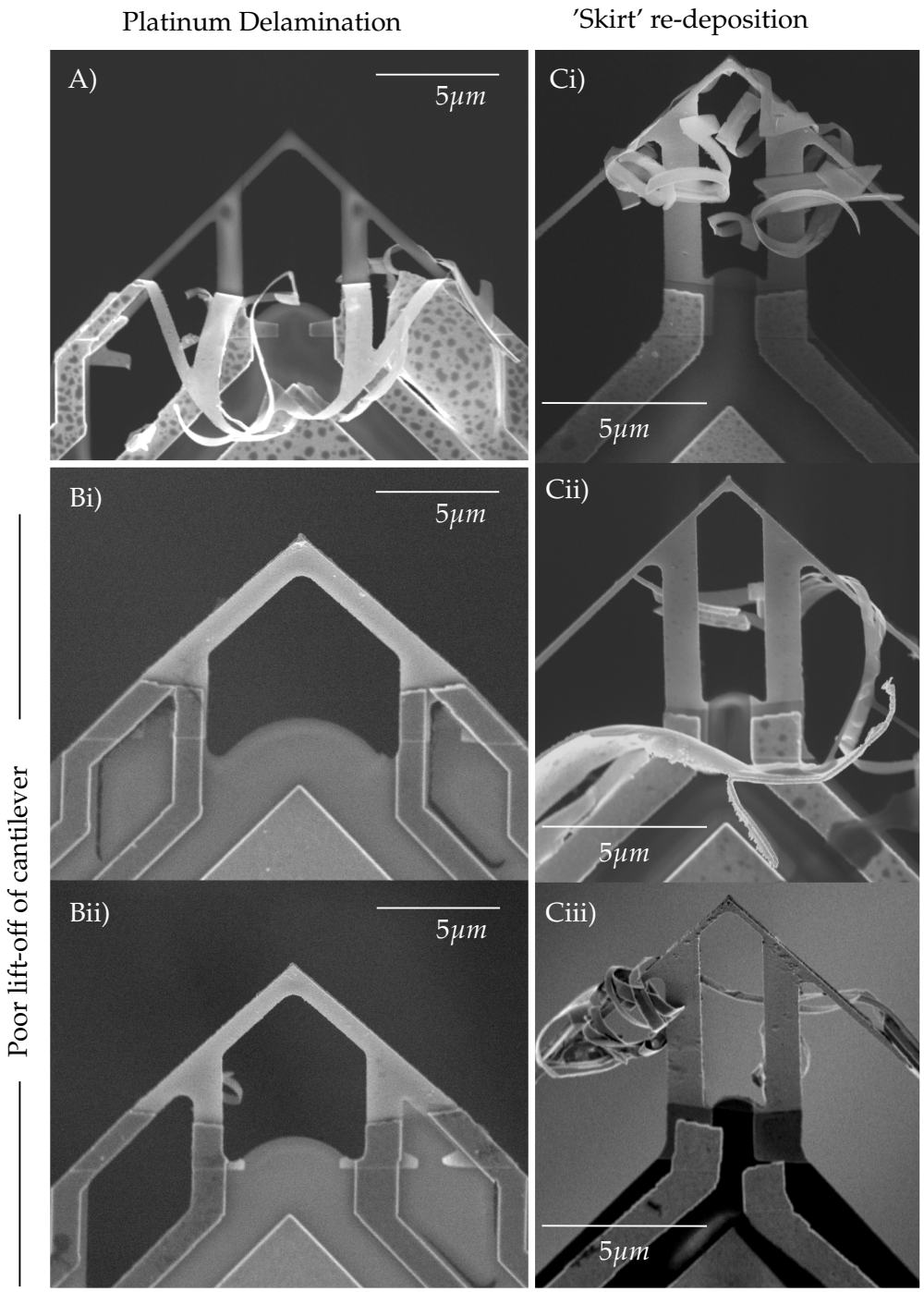

FIGURE 6.35: Gallery of probe failure mechanisms 2: A) Delamination of Pd sensor B) Poor NiCr lift-off during cantilever definition, resulting in cut-out regions not being etched out of the SiN C) Re-deposition of the metal 'skirts' that overhang the SiN beam as a result of dual self alignment. Thin strands of Pd/Au release from the Si substrate, but have coiled around the narrow beams during release.

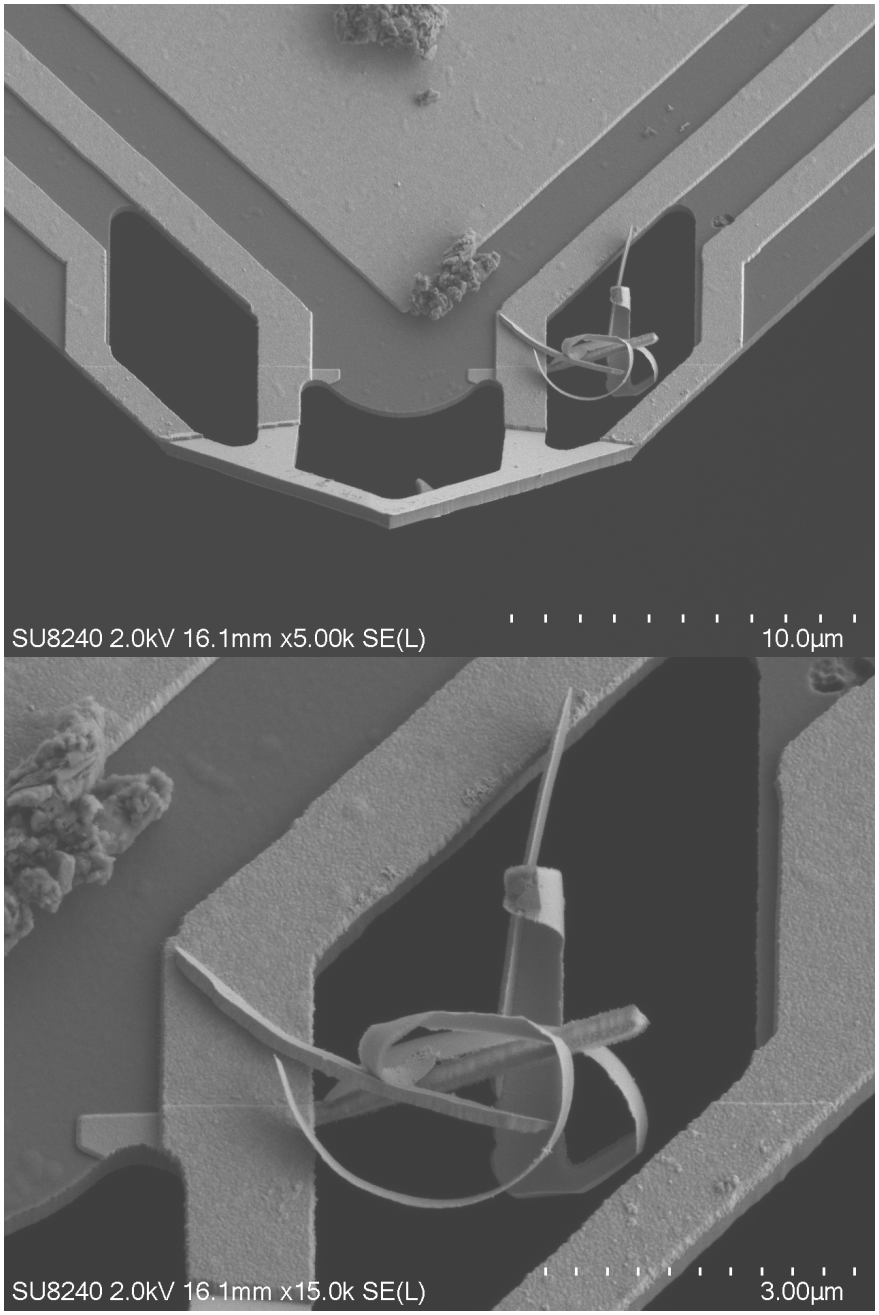

FIGURE 6.36: SEM images showing a C3 type probe with a metal redeposition defect, as shown in Figure 6.35C. The point of attachment is not clear. This particular defect does not appear to be shorting any leads, so likely has a negligible effect on probe operation. Additionally, some contamination can be seen on the gold reflector.

Chapter 7

Results

7.1 Self Heating Coefficient

7.1.1 Method and motivation

Probes are characterised electrically first, since this is a low-risk test requiring minimal interaction with the devices. Since they are very fragile, it is sensible to minimise handling of the probes. Similarly, it is sensible to only perform contact AFM measurements with the probe after it has been characterised electrically, since there is some risk of destroying the probe during contact scanning.

The first test is resistance testing, which was discussed in the previous chapter. Probes which passed visual inspection and exhibited reasonable resistance ($200 \pm 100\ \Omega$) were glued to AFM holders and silver painted by hand to the four terminals of the probe. An example of such a bonded four terminal probe is shown in Figure 7.1. Probes were resistance tested again after bonding at the end of the wires to compensate for any change in resistance brought about by the wires and silver paint. The method for calculating the sensor resistance of a four terminal probe from the various permutations of 2-terminal measurements is presented in Appendix D.

The process for choosing appropriate resistors to drive the devices was presented in Section 3.7.2 (Chapter 3). The 'SThMpackage' software [1] accounts for the probe type (C or N, size 1-4) in its calculation of the maximum current. The resistors suggested by the program yield only half the maximum calculated tolerable current for a given

[1] Hosted at `https://github.com/RL-AFM/SThMpackage`

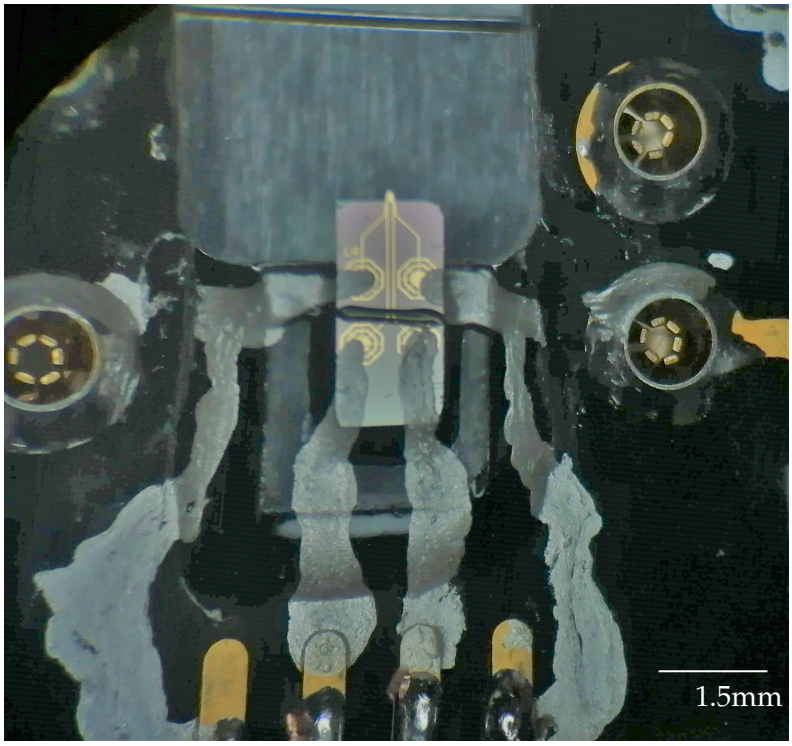

FIGURE 7.1: Photograph showing a bonded and silver painted four terminal SThM probe.

probe type to account for any variations in wire width from designed values, such as those exhibited by narrow N type probes (Figure 6.23)

I-V sweep

After the probe is bonded and a bridge has been made, I-V tests are performed. This serves two purposes simultaneously; assessment of the bridge balance, and characterisation of the thermo-electrical properties of the probe. Careful inspection of the bridge output shows that the IV curve is well-fitted by a third order polynomial of the form[2];

$$V_{out} = A_v(aI^3 + bI + c) \tag{7.1}$$

In which;

- I denotes bias current
- A_v is the gain of the instrumentation amplifier, which is -101 in this work

[2]Interactive version available at `https://www.desmos.com/calculator/mnoezl4wtv`

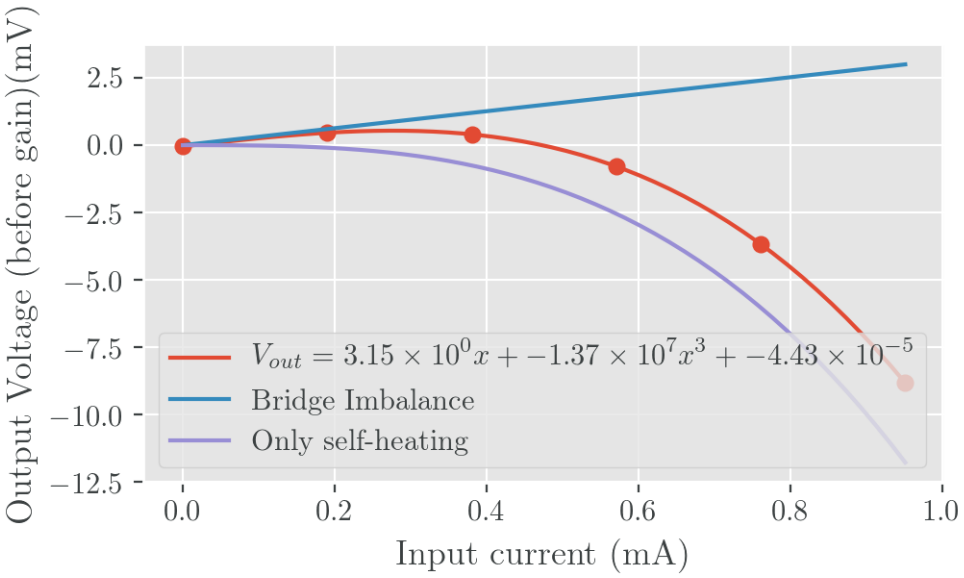

FIGURE 7.2: Decomposition of bridge output (red) into probe response (purple) and bridge imbalance (blue). The equation to which the data points are fit is annotated on the figure. The equation suggests that the bridge is imbalanced by 3.15 Ω, the probe has a self heating coefficient of 1.37×10^{7}, and the circuit has a DC offset of −44.3 µV, which in this case is negligible. This bridge imbalance can easily be addressed by changing the balance resistor R_b

- c represents an amplifier offset voltage which is in the order of µV and may be ignored for all but the most sensitive of probes.
- b is the DC term brought about by bridge imbalance
- a is a coefficient which scales the third order self-heating response

It should be noted that the functional form of Equation 7.1 is the expected result from the theory of operation of a Joule heated resistor in a Wheatstone bridge, not simply an empirical fit. Fitting the experimental data points to this function allow for the computation of the listed coefficients. The curve may then be decomposed into its component parts; the bridge imbalance (linear), and the self-heating response of the probe as it would appear with a perfectly balanced bridge. This is presented in Figure 7.2. Since the values of all components in the circuit are known, the coefficients may be directly stated in terms of the output of the Wheatstone bridge (before the gain stage), as a function of bias current. In such cases, b is a direct measure of the bridge imbalance, in Ohms.

The coefficient a has I^3 dependence. This arises since the voltage of the probe is

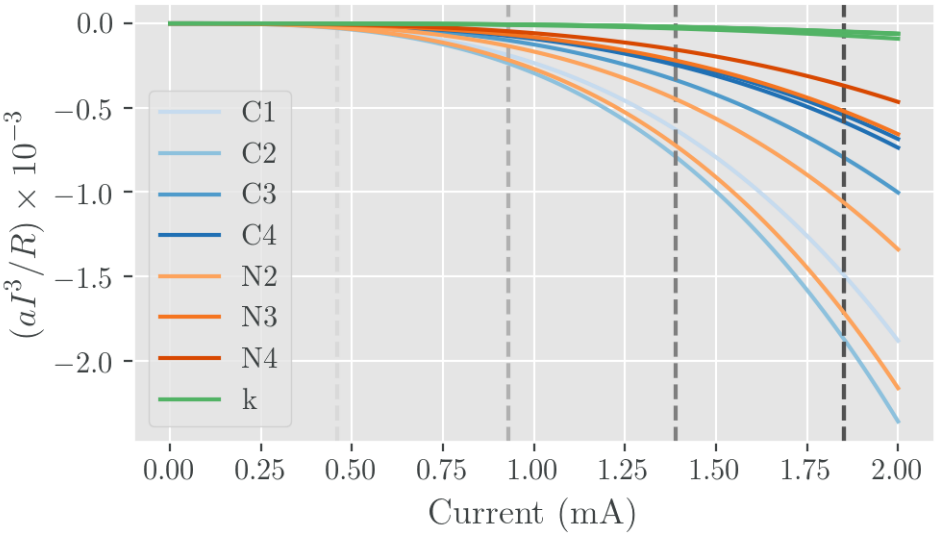

FIGURE 7.3: Normalised self heating response for all the probes used in this Chapter. This figure compares the self-heating sensitivity of many probe types. By plotting the cubic term alone, we remove the influence of bridge imbalance. Dividing through by the electrical resistance of the probe R normalises the Joule heating output of the individual probes. Note that there are multiples of some probe types (such as N2's) and omissions of others (N1) depending on which devices were available and survived testing. The figure is annotated with dashed vertical lines indicating the maximum current for the four sensor types. The larger, type 4 sensors (dark grey) are capable of withstanding around 1.8mA current, whereas the small C1 type (light grey) should not be used above $450\mu A$

given by IR, but R varies as a function of the Joule heating power, which has relation $P = I^2R$. Therefore, $a \propto I(I^2R)$.

7.1.2 Results

The probe's output voltage is the result of the thermal network discussed in Section 4.3. In these experiments, there is no interaction with any sample, and it is assumed that the total heating of the thermal network is the result of the probe's own Joule heating. Since there is no sample interaction, heat losses result purely from cantilever conduction and losses to the environment. In such cases, the self heating response of the probe may only depend on;

- The magnitude of the generated Joule heat (Electrical resistance dependent)
- The thermal resistance of heat abstraction down the cantilever and to the environment (cantilever mechanical design dependent)

Style	Self heating coefficient, a
C1E21	-4.68E+07
C2E6	-5.10E+07
C3C19	-2.13E+07
C4A8	-1.46E+07
C4C4	-1.37E+07
N2B10	-6.68E+07
N2D10	-3.41E+07
N3B3	-1.61E+07
N4B8	-9.91E+06
k1	-4.97E+06
k2	-3.33E+06
k3	-3.32E+06
k4	-3.15E+06

TABLE 7.1: Table of self heating coefficients for a variety of novel and standard probes. The naming convention is as follows; a 'C1' type probe is a cut out probe with a size 1 (smallest) sensor, N4 is a non cut out probe with a size 4 sensor. 'k' probes are nominally identical commercial probes as manufactured by KNT

- The accuracy with which these temperatures are reported via the probe's RTD (Cantilever electronic design dependent)

To this end, Figure 7.3 presents the comparison of the probes' normalised self heating response - aI^3/R. The fits performed in Figure 7.2 allow for the decomposition of the bridge outputs, which enables the isolation of the cubic self heating behaviour, aI^3. This was then divided by the electrical resistance of the probes, R, to normalise the generated Joule heat. The determination of a from experimental data used at least five points for each curve, and the resulting fits to these data exhibited at least 0.98 coefficient of determination (R^2) values.

All probes that were bonded and prepared for use in this Chapter are included in Figure 7.3. This includes four commercial devices (green), and all but one (N1) of the novel designs. The full list of probes tested, and their I^3 coefficients, are presented in Table 7.1.

From Figure 7.3, it is possible to conclude that;

- All of the newly designed four terminal probes have greater self-heating sensitivity than the commercial probes.

  - The non cut-out probes are not expected to have drastically different thermal performance from the commercial devices, since they lack a cut-out or any other change to the thermal resistance of the cantilever. However, the four - terminal layout means that changes to the tip temperature are more accurately monitored, since a larger proportion of the electrical signal is defined by the temperature of the tip region.

  - For cut-out probes, an increase in the thermal resistance of the cantilever is expected. The isolation of the heater/sensor from the body of the cantilever is intended to localise the heat to this region. Therefore it is believed that for this type of device, the actual temperature of the tip is higher than that of a comparable N type probe that is generating identical Joule heat. Thermal resistance to the environment also plays a second part, however, since increasing thermal resistance into the cantilever body will reduce the fraction of heat available for dissipation into the environment through the fin-like body of the probe.

- One might expect a smaller sensor to have higher resistance, however recall that these devices are designed to have equal resistance, and that in Figure 7.3, the response has been normalised for variations in electrical resistance.

  - In the non-cut out probes, this is again the result of more accurate electronics. More and more of the electrical signal is defined by the hot tip at smaller sensor sizes.

  - In cut-out probes, in addition to the above, the smaller the sensor, the greater the thermal isolation between the heated region and the body of the cantilever.

  - While the smaller sensors increase the self-heating response of the probes, it should be remembered that the maximum allowable current for these devices is reduced compared to that of the commercial probes. This has been annotated on the figure with dashed vertical lines. However, even when running the novel devices far below their maximum allowable currents they show far better sensitivity than the commercial devices, even

when the latter are biased at their maximum continuous current rating of 2mA

- The cut-out probes are expected to exhibit better sensitivity than their equivalent N type counterparts. There is some evidence to support this when comparing the responses of the C3 and two C4 type probes with the N3 and N4 type probes. However, the dataset compares only one or two of each probe, and can therefore not be considered statistically rigorous. The variation between the pair of N2 type probes suggests that there exists significant scatter within the families of probes, presumably caused by fabrication variances.

The characterisation method presented here would serve well as a standardised acceptance test for all new probes. It is convenient since the bridge balance must in any event be assessed before experimentation, and the self-heating behaviour of the probe should be verified. The software for performing such measurements has been made available. As further work is done using these probes, a more complete data set will become available, at which point it will be possible to better characterise their performance.

7.2 Active Mode Experiments

7.2.1 Bulk samples

Method and motivation

The probe's response to contact with materials of various thermal conductivities was presented in Section 4.9.2 as the result of simulations using our thermal model. An experimental evaluation of the probe's Active Mode sensitivity therefore requires a set of samples with dissimilar, known thermal conductivities. Given a reasonable selection of samples, the curve may be reconstructed through the fitting of experimental data. The Quantiheat project, of which this work is part, provided such a set of materials with conductivities spanning four orders of magnitude (0.1 to 100 $\mathrm{W\,m^{-1}\,K^{-1}}$). The materials used, and the methods employed to measure their thermal conductivities are outlined in Appendix C.

In the model, perfect mechanical contact between the probe tip and the substrate was assumed. This cannot be realised experimentally, since nanoscale roughness is present on all surfaces. However, this issue was identified by the consortium, and steps were taken to mitigate the effects of local roughness variations. All samples in the Quantiheat set have been highly polished, resulting in Ra values on the order of 10s of nanometres or better. In addition, all point measurements presented in this section have been repeated at least five times across five distinct locations, totalling 25 unique contact events.

The model also assumed vacuum environment, which represents the ideal environment for quantifying changes to the thermal resistance of SThM probe cantilevers. Vacuum removes confounding effects introduced by ambient operation and makes it easier to draw relationships between design changes and observed results. However, this was not available to us during this body of work, and therefore ambient measurements had to be employed. This is not necessarily detrimental, since a great number of SThM studies are performed under ambient conditions. While characterisation of the probes in this environment is more challenging, any improvements under such operating conditions would be of significant practical importance.

Ambient operation is harder to characterise because of the heat transfer between probe and sample that occurs through the environment. This is true not only of a standard laboratory setting, but also of aqueous SThM and any other techniques in which non-negligible heat transfer (radiation) may occur through the medium. As such, each approach/retract curve has a complex, piecewise form as was presented in Figure 4.12. It is not readily apparent which aspects of this curve are of most interest when attempting to correlate probe heat abstraction to sample thermal conductivity. There are two main schools of thought however;

- The contact to the sample is the most important part of the signal change. Isolating the jump to contact allows one to see the contribution to heat abstraction made by the introduction of the tip-sample contact.
- The over-all signal change, far (mm's away) to in-contact is the most important metric. This figure encompasses heat losses through **all** pathways, but does not distinguish between the proportion of heat lost via each route.

In this experiment, the full thermal-distance curves were collected and both of the above metrics were extracted from the data. The measurements were performed using the 3ω method, meaning the probes are driven with AC and their signals detected using a lock-in-amplifier. The theory of 3ω operation is presented in Appendix B. Phase sensitive detection ensures that only signals of the correct frequency are considered, making the measurement insensitive to temperature variations which may result from changes in environmental conditions.

The bridge electronics and software were set up to deliver maximum tolerable currents at 5V DC, for commercial probes. However, bridges for the new four terminal probes were provided with limiting resistors such that 5V DC delivers half of each design's maximum current. In this experiment, all probes were driven at 2.83V AC, which equates to 4V peak. The high signal to noise of the lock-in detection system meant that signals from even lightly biased probes were easily detectable.

The frequency chosen to drive the probes was 135Hz. Evidence in the literature suggests that probes of this type act as a thermal low pass filter with -3dB point in the kHz range [181], therefore lower values than this should be used for minimum

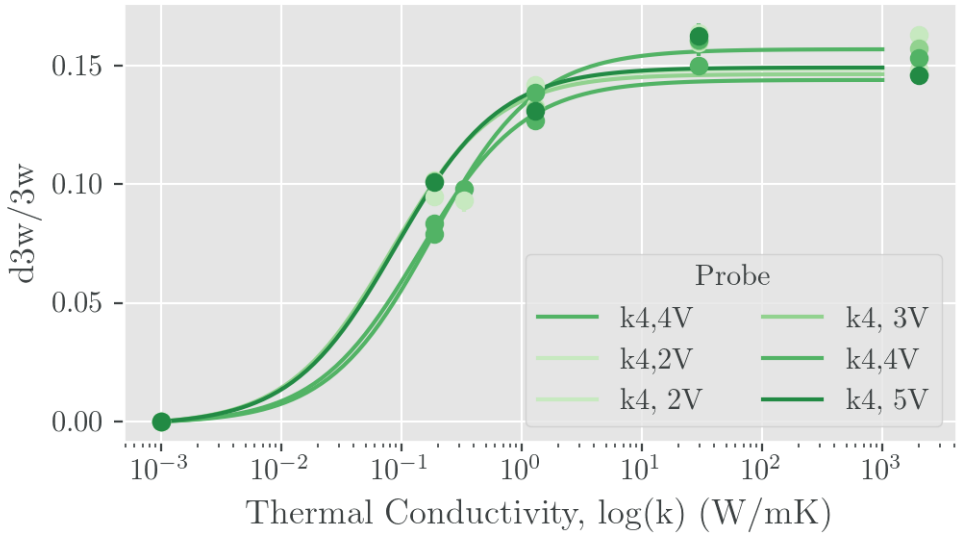

FIGURE 7.4: S-curves from the same probe operating at a variety of voltages

signal attenuation. This behaviour has also been measured as part of this work, is presented in Section 7.2.2. 135Hz is a reasonable number since this avoids any harmonics associated with UK mains power (50Hz, 100Hz etc.), and those from any harmonics of 60Hz generated by test equipment and/or displays.

Bias dependence

The metric used to compare the probes in this section is '$\Delta 3\omega/3\omega$'. This is the fractional change in the third harmonic of probe temperature upon making contact with the sample. It is common in SThM studies to present results in the form of a change in signal rather than an absolute temperature [166], [221], whether that be a change in voltage, power or resistance. Because this is a ratiometric figure, it is assumed that results between different probes are comparable, despite their operating at different temperatures due to maximum current limitations. This assertion was tested experimentally by biasing a commercial probe at a variety of voltages, between 1V and 5V peak. Figure 7.4 presents the results of this test, which does not indicate any correlation between the bias of the probe and the sensitivity of the 3ω signal to sample thermal conductivity variation.

Data fitting

The Quantiheat sample set was designed to calibrate probes over a range of conductivities. In this work however, we desire to compare new probes with each other and to the standard commercial design. To this end, it is not necessary to use all the samples. This is fortunate, since the whole QH set would prove prohibitively time consuming to test with the many different probes manufactured. A reduced set was defined which contained only enough samples to reasonably reconstruct the contrast curve. A discussion on fitting to these data was previously presented, Section 4.9.2 and the equation given in Equation 4.20. The same equation was used for the fitting of the data here. In this implementation however, we employ a weighted fit to give more confidence to those data which had less scatter; i.e those measurements giving similar results between multiple contacts and multiple locations. This is achieved by providing the fit routine with the average and standard deviations of the data gathered from contacting each material.

The samples chosen were PMMA and POM-C for the determination of low thermal conductivity performance. Al_2O_3 was chosen, and expected to lie within the upper saturation regime. SiO_2 was selected as a midpoint to assess the curvature between the saturation regions. In addition to these Quantiheat samples, an additional sample of single crystal diamond was used. While the thermal conductivity of this sample was not as well characterised as the others, it was quoted by the manufacturer as k=2000 $W\,m^{-1}\,K^{-1}$, which is certainly high enough to lie well within the upper saturation temperature, which was the purpose of this sample.

Data collection

The probe's signal was split between the 'Signal Access Module' and an oscilloscope. Connection to the latter allows for real-time data to be captured even when the probe is not engaged. For this experiment, the probe's output is recorded on the scope starting from many millimetres away as the sample/ is located and focused upon. The out of contact signal is observed to be very stable, with low noise. Oscilloscope data capture is started in conjunction with the engage operation on the AFM. The signal is recorded as it makes it's approach up until the solid contact is established. The probe is allowed to scan for a few seconds in each direction, meaning it comes into contact with a large number of unique contact positions. This means that the

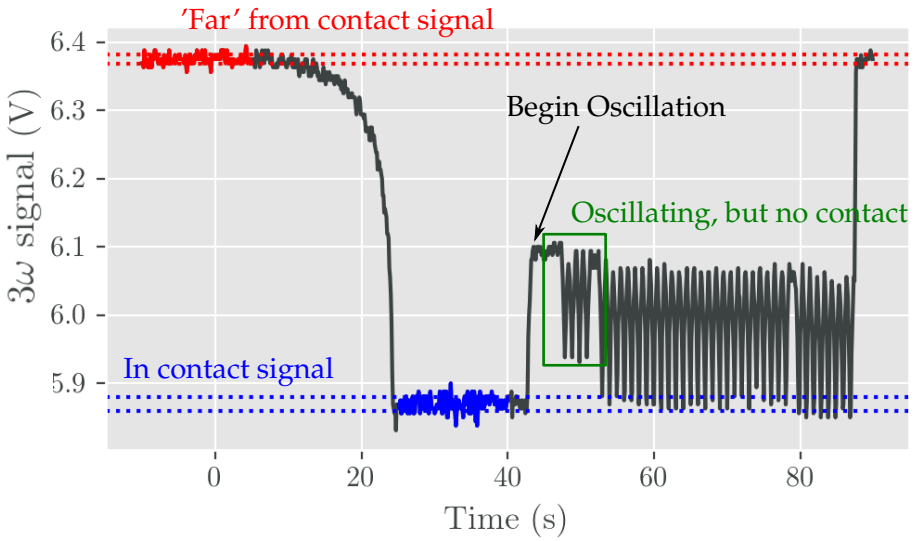

FIGURE 7.5: Annotated oscilloscope trace of an SThM probe approaching, contacting and then oscillating above a PMMA sample. In the green box, the probe is freely oscillating a few (<2) microns above sample surface. The centre of its oscillation point is then reduced until contact with the sample is made. The average and standard deviation in out of contact and in contact temperatures are calculated and compared to produce the difference (+ error) in temperature between no interaction with the sample at all, and when a solid contact is established.

average and standard deviation of the 'in contact' signal can be calculated, giving a more rigorous data set than a single contact. The probe is then switched into the force distance mode and begins to oscillate. The probe's height above the sample is then modulated until it is observed to be making repeated contacts with the sample. This is easily verified by the monitoring the AFM's Force Distance (F-D) software, where the approach and retract signals show obvious signs of contact being made (see the thermal-distance curve presented in Figure 4.12). Once the probe is verified to be in contact with the sample, multiple F-D curves are captured by the AFM before disengaging the probe. The whole process is captured on the oscilloscope, with an example of this being presented in Figure 7.5. The data from the oscilloscope is analysed to define 'in contact' and 'far from contact' signals, and the difference between the two is calculated. This difference is compared between the various samples, and is then used to construct a weighted S-curve, as described in Section 7.2.1. The experiment is repeated for multiple probes, and their S-curves plotted together for comparison.

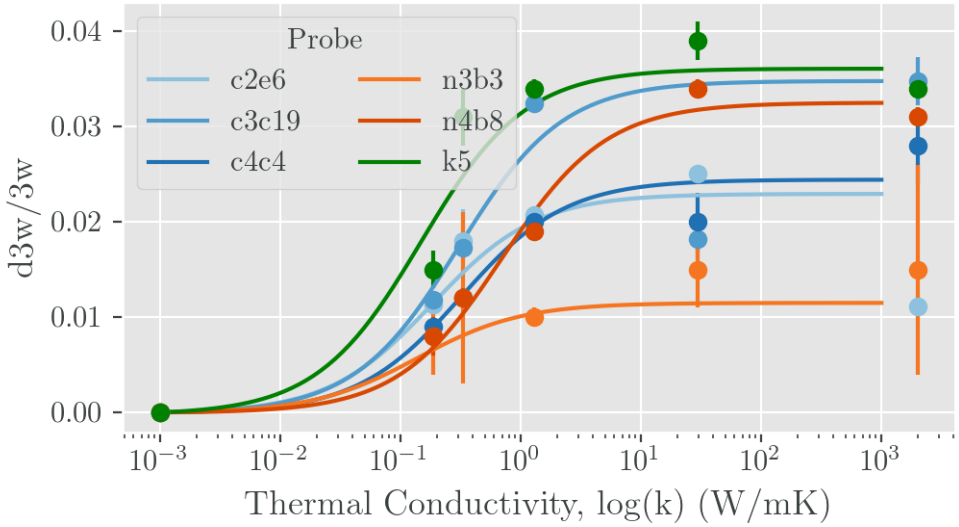

FIGURE 7.6: S-curve comparison of the 'jump to contact' for a number of the novel probes. Probes N2 and C1 did not survive this test, and no suitable N1 probes could be found from those probes which were removed from the wafer. The first two characters indicates the probe type, while the latter characters are the specific probe IDs defined by their position on the wafer. The average signal change is presented as points, while the standard deviation within the set is denoted by vertical error bars. The fit to Equation 4.20 is poor in all cases, and there is large standard deviation, particularly evident for high thermal conductivity materials.

A similar procedure occurs for the 'jump only' data. This information is parsed from the AFM force/thermal-distance curves which are generated in conjunction with the oscilloscope signal. Multiple files are generated, one for each contact of the probe. Software was developed to read folders of these files, all of which pertained to a single material. In each file, the jump is located using the maximum of the signal's derivative, before applying second and first order fits to the out-of and in-contact regimes respectively. Given a jump location 'x', we subtract the fitted signals; out of contact[x] - in contact[x]. It is reasonable to assume that this method offers increased accuracy when compared to estimation by eye, since the use of a fit averages out oscillations and noise in the vicinity of the jump. The results from a single sample are averaged, and their standard deviation passed to the weighted fit function. The normalised results $(\delta 3\omega/3\omega)$ of the jump only magnitude are presented in Figure 7.6.

This figure presents some interesting data. The commercial probe appears to have a better defined S-curve, with greater magnitude between it's lower and upper saturation regimes. The novel probes have high scatter, and comparatively poor fits. The standard deviation for individual contacts within a set of measurements on the same material is quite high. While one may infer something about the probes from this experiment, it may also lead to questioning the purpose of such a measurement. These probes have been designed for greater sensitivity, with heat better localised to the tip, and the signal being more dependent on the temperature of the tip alone. One might expect them to outperform the commercial devices when looking at the efficiency of heat abstraction upon contacting a various materials. Looking at the jump only might be valid for vacuum operation, where there is a clear 'binary' distinction between in and out of contact. In ambient, its not clear what exactly the jump represents. From Figure 7.5, we observe that there is some distance dependence, and that the probe is exchanging heat with the sample many microns (100s) from contact. It is not apparent whether or not the probe loses comparable proportions of its heat across this distance for different materials. In such cases, comparing the jump to contact temperature change is not like-for-like and comparison cannot be justified.

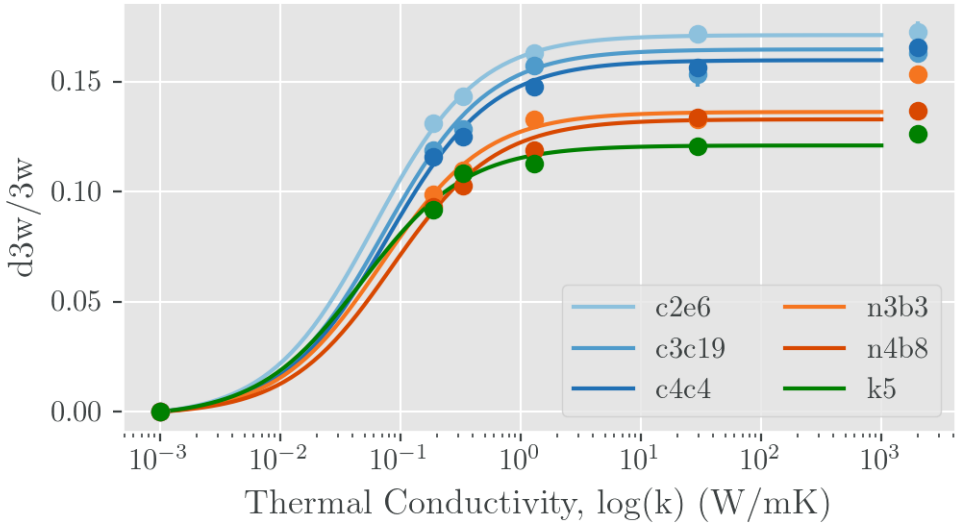

FIGURE 7.7: S-curve comparison between 'far' and 'in' contact for a number of the novel probes. Probes N2 and C1 did not survive this test, and no suitable N1 probes could be found from those probes we removed from the wafer.

If the probe's design has had the intended effects, one of which is to more accurately measure heat flux into/ out of the tip, then it is reasonable to suppose that these probes should have a lot of scatter between different locations on a sample. Since solid-solid conduction depends on contact area, any increase in the proportion of heat resulting from the solid-solid signal measurement is likely to better track changes in tip-sample conductance, not sample thermal conductivity. One would expect to see a more faithful representation of tip-sample conductance as a function of position on the sample, which is likely to have appearance similar to the topography channel.

Figure 7.7 compares the 'far' to 'in-contact' data gathered during the same experiment. Here, the scatter is significantly reduced, and the commercial probe is observed to have the poorest sensitivity. Both N type probes demonstrate a minor improvement over the commercial probe, while those with a cut-out show even better sensitivity. In both N and C type probes, those with smaller, more localised sensors demonstrate better results.

What has happened here? By not trying to parse out the solid contribution only we have a simpler measurement that makes no assumptions about what proportion of

heat is lost to the air vs. the sample, only considering the **overall** change induced by a sample. It may be that this is a more suitable measurement for sample k dependence characterisation. The N type probes are expected to outperform the KNT probes simply through the improved accuracy which results from the use of a four terminal design. The cut-out probes are expected to have higher cantilever thermal resistance, which will act to localise more heat to the tip. By considering the lumped thermal model presented in Figure 4.6, we can see that an increase in R_p will 'push' heat through the other branches of the network. The cut-out doesn't just increase the overall resistance of R_p, it does so by localising heat to the tip, which will reduce the influence of losses to the environment from the heated cantilever body. This heat transfer pathway is efficient because of its large surface area. Then, if R_p and R_{env} are increased, the most attractive route for heat transfer between tip and sample is through the air R_{air}. Note that **any** increase to resistance in the network will increase the system temperature, but if the heat can be lost via an alternative pathway, it will do so. In this case, heat that was being lost down the cantilever (and contributing nothing to the measurement) is instead being transferred to the sample through the air and through the solid contact, and doing so with some degree of dependence on the thermal conductivity of the sample. We speculate that the results of Figure 7.7 arise due to an increase in the local temperature of the air immediately surrounding the tip. This is advantageous, since spatially localised measurements are the fundamental motivation for employing a microscope. Comparing the signal change across the full range vs. the solid-solid contact alone it may be noted that this jump comprises between only 10 and 30% of the overall signal change.

The combination of Figures 7.6 and 7.7 may suggest that lift-mode/aqueous operation may be an attractive avenue for further SThM studies. While we have presented some evidence here that a highly localised sensor increases sensitivity to sample thermal conductivity variation, making the probe more 'sensitive' acts to improve its measurement of nanoscale tip-sample conductance measurement. Scanning the probes just out of contact removes the variation in signal associated with ever-changing solid-solid contact, replacing with a highly localised region of heated

fluid. In such cases, a local, small hot spot is ideal; maximising the coupling between probe and sample through the fluid, while minimising heat dissipation into the environment.

Tovee et. al. have already observed thermal conductivity contrast with reduced topographic artefact coupling when operating SThM probes in the liquid environment [233]. Their signal to noise, and spatial resolution, appear reduced for the measurements performed under liquid, but they still exhibit obvious materials contrast, demonstrating the feasibility of the technique. They remark the 'immersion SThM' (iSThM) technique requires dedicated probe optimisation for the layout of the heater for improved resolution and performance. It is our assertion that the probes designed in this work would be of great benefit in this regard. They have also confirmed that the dominant heat transfer mechanism in this environment is through the liquid rather than the tip sample-contact, and that this may help to reduce or eliminate the impact of topographically coupled imaging artefacts. The probes developed in this work exhibit improved sensitivity, and greater localisation of heat to the tip; improvements which would, respectively, improve the signal to noise ratio and resolution of iSThM measurements.

Increasing the resistance of any component in the network will increase the upper saturation temperature to some degree. Unfortunately however, in ambient operation, it would appear that the primary result of increasing the cantilever thermal resistance is increased thermal coupling between sample and tip through the environment. Figure 7.7 suggests an improvement in the sensitivity of the probe to changes in sample k, however it is likely this could be improved further by consideration of the lower saturation temperature also. Externally heating/cooling the sample can increase the temperature differential between the probe and sample, as has been demonstrated by Kazmierczak et al. [234]. Employing this technique, alongside the probes presented here is likely to produce images with very high thermal conductivity contrast. While in the referenced study promising results were presented using a cooler (low current) probe and a heated sample, the probes developed in this work have been specifically designed to localise heat to the tip. Therefore, a sample cooled below ambient would maximise the temperature differential, and exhibit the

greatest contrast. One consideration for this method is that it is the temperature difference between the 'boundary condition temperatures', drawn as grounds in Figure 4.6. These are the base of the cantilever, where it joins with the chip (assumed to be a heat sink), and at the sample. Kazmierczak et al. remark that the thermal image contrast is influenced by the temperature difference between these two points.

Due to the strong dependence of contact resistance on physical interaction area, images gathered with such probes are unlikely to produce any data which can be used in the determination of local sample thermal conductivity. The better probe for thermal conductance measurement might be a blunt probe in which the contact resistance is lower and sample k has a more predominant role, but the requirement for high spatial resolution (which is the quintessential characteristic of a microscopy technique), will be a significant competing aim.

7.2.2 Frequency domain measurements

Method and motivation

In the previous section we have asserted that the observed improvements in k sensitivity are due to the changes implemented in the probe design. These novel probes were designed to localise heat to the sensor region by increasing the thermal resistance to the cantilever. Their sensors were designed with the intention of more accurately reporting the temperature of the tip region of the probe only, minimising or negating the influence of the rest of the cantilever. The experiments on bulk samples were intended to verify these claims, however the variation in tip-sample contact conductance makes it challenging to assert an un-ambiguous 'improvement' in measurement. These probes appear to give a better measure of tip-sample conduction, rather than sample thermal conductivity, a result that is unsurprising considering the physics of the measurement technique.

Therefore, an additional experiment was required to corroborate the above claims as to the origin of the improvements seen in Figure 7.7. To this end, non-contact frequency domain measurements have been employed on the same probes. In the following sections we will demonstrate how the transient response of the probe can inform us about how the changes to its design have affected its thermal performance.

These experiments are performed using 3ω, as before. The lock-in amplifier (LIA) used has a frequency sweep feature, which has been used to ramp the input voltage, ω. The 3ω magnitude is output from the LIA into an oscilloscope for monitoring and capture. The data is gathered and converted into decibels, taking the low frequency (<10Hz) 3ω as zero dB and plotting the subsequent high frequency attenuation as negative dB losses. This is a typical way of presenting frequency domain data, commonly seen in filter design. As can be seen from Figure 7.8, which plots the magnitude-frequency response of a variety of probes, SThM probes act as a thermal low - pass filter.

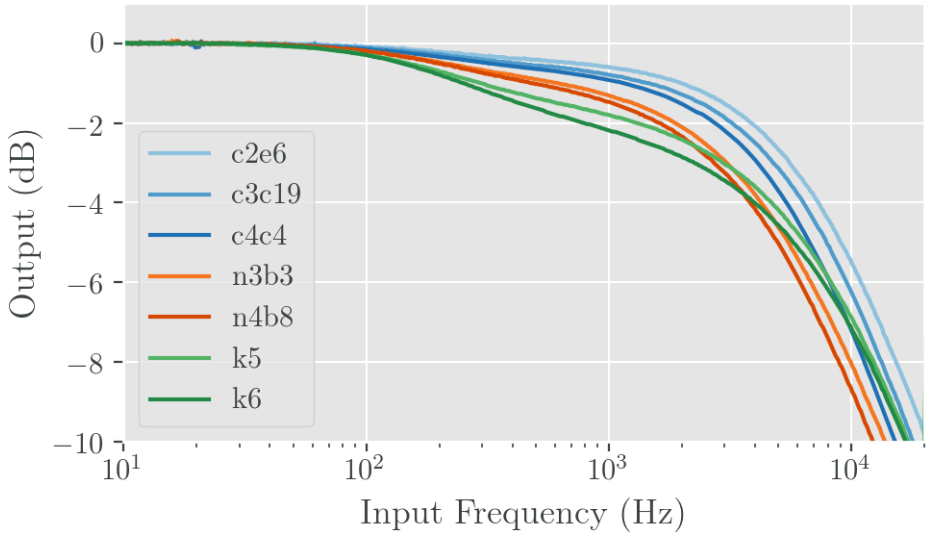

FIGURE 7.8: Frequency response curves comparing the commercial device against a selection of novel probes

Results and discussion

Figure 7.8 compares the frequency response of all probes that comprised the set used in Figures 7.6 and 7.7, and an additional commercial probe, k6. Previous frequency domain experiments in the literature have shown very similar behaviour to the pair of commercial devices shown here [187], [235]. Particular attention should be paid to the response of the commercial probes between 10^2 and 10^3Hz. A 'scalloping' profile may be observed at the knee of the curve - a behaviour which is impossible to describe with a first order filter. This behaviour was also observed by Puyoo et al [187], who had initially developed a model of the probe upon a first-order system. They proposed that this deviation was the result of the NiCr limiting resistors, and added a second first order low pass to their model to accommodate. This explanation is not compelling however, as the NiCr resistors have minimal TCR and therefore cannot significantly contribute anything to the thermal behaviour of the system. Note that this behaviour was not seen on either the Wollaston wire [149], or thin-wire thermocouple probes [236]. Bodzenta et al. agree that the NiCr limiters cannot be the explanation, and argue that the probe's complex architecture means that it cannot be described by a simple first order system [235]. This would also explain why this behaviour was not observed on the simpler, wire based SThM probes.

It is possible to add transient analysis to the model proposed in Chapter 4, however this would require significant effort in its implementation. In addition, it would greatly increase the complexity of the model, at which point, the problem might be better suited to analysis using commercial FEA software. Bodzenta et al identified that a suitable model can be created using a reduced number of poles, achieved by lumping together the portions of the probe whose temperature is most affected by certain modes (regimes) of thermal transport. They distinguish between three regions; contact, active and coupling zones.

The contact zone comprises the immediate contact region, having characteristic length L_c on the order of 100nm. This length is smaller than the diffusion length of heat (μ_{th}) in solids at typical SThM operating frequencies ($10^1 - 10^4$Hz), which is calculated using;

$$\mu_{th} = \sqrt{D/\pi 2f} \tag{7.2}$$

Where D denotes diffusivity and f indicates frequency. To this end, the heat capacity of this region may be omitted and the network reduces to the series combination of R_c, R_s and R_{pC}. R_c and R_s have the same definitions as in Figure 4.6. R_{pC} is used to denote probe thermal resistance in the contact zone.

They define the active zone (A) as the area comprising the heated region, with characteristic length circa 10 µm. As with Figure 4.6 it employs an ideal current source to model the probe's Joule heating. However, it also includes thermal resistances to ambient, and the heat capacity of the cantilever and air in this region. If the probe is in contact with a sample, its heat capacity in this region must also be considered.

The coupling zone comprises the remainder of the cantilever, and has characteristic length scale roughly 100 µm. Bodzenta et al remark that this region has complex geometry, and could be modelled using a 'transmission line'-esque chain of resistors and capacitances. This is identical to the approach taken in our model, described in Chapter 4, simply adjusted for the transient regime.

The equivalent circuit, with each of the zones highlighted, is presented in Figure

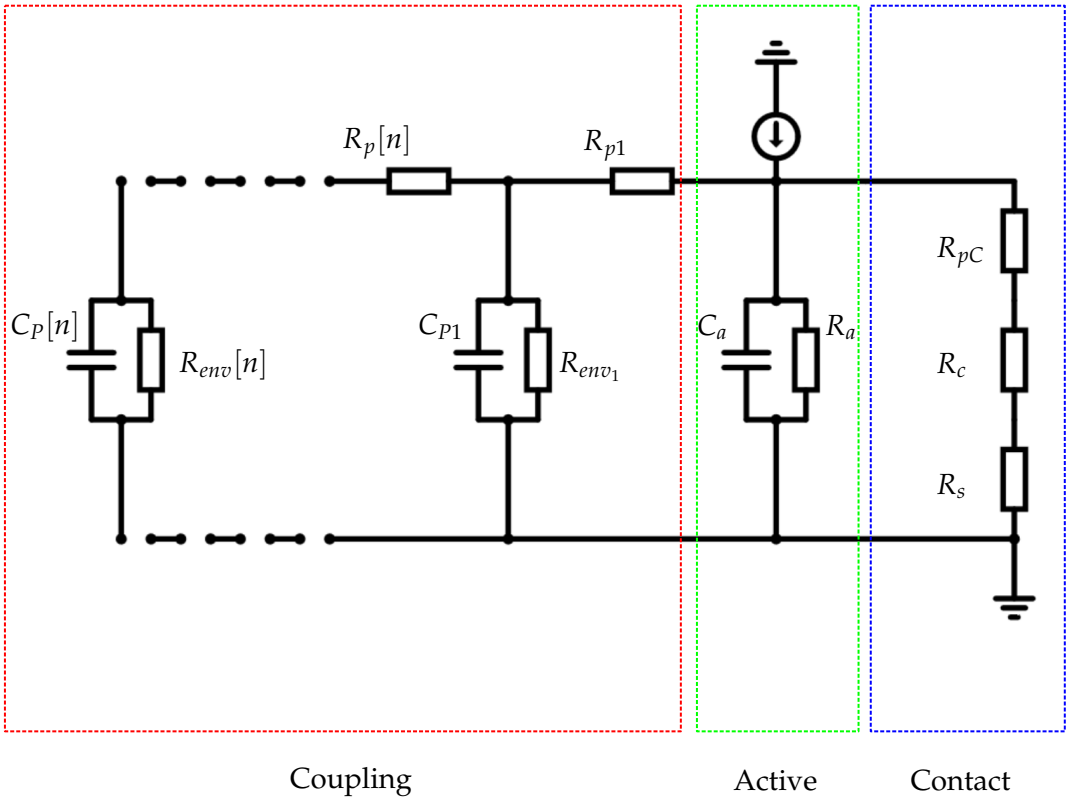

FIGURE 7.9: The transient equivalent thermal - electric network of an AC driven SThM probe as proposed by Bodzenta et al [235]. The contact zone is composed of contact and spreading resistances, R_c and R_s respectively. The final resistance in this zone, R_{pC}, relates to the thermal resistance of the cantilever in the contact zone (<100nm). The active zone features a single RC unit which is the combination of the thermal resistance of losses to ambient, R_a, and the heat capacity of the cantilever in the Active region. The coupling zone is composed of 'n' repeating units of RC cells, interconnected by Rp resistances. The RC unit reflects the environmental losses and heat capacities of the probe along some element of its length, while the Rp resistances denote the resistance to thermal conduction along the cantilever itself.

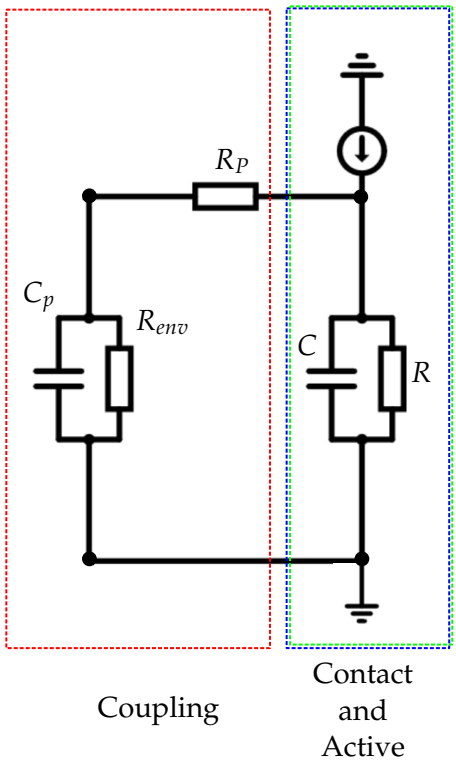

FIGURE 7.10: 2 pole reduction of the model presented in Figure 7.9. The Active and Contact zones have been merged together. The derivation of the equivalent elements is outlined in [235].

7.9. Although this model is compatible with the use of 'n' elements, Bodzenta et al identified the three regimes of thermal transport phenomena, and demonstrated that they have different timescales. As such, they propose to use a minimised model of three quadripoles (two port networks) only. Using such a model, they were able to provide a fit to their experimental data with excellent accuracy (Figure 6, [235]). The same data, fitted with a Single Cell Lumped Approximation (SCLA), did not provide enough freedom to accurately account for the 'scallop' at the knee of the curve, which is clearly a real feature of frequency plots using the thin film SThM probes regarded here. This assertion is evidenced by its observation by multiple groups [149], [235] and here.

Bodzenta et. al. also opt to further minimise the model into two poles only, by joining together the contact and active zones. This is presented in Figure 7.10. They found this approximation to be in excellent agreement with their experimental data and three pole model, suggesting that the nanofabricated SThM probe can be effectively modelled with only two time constants.

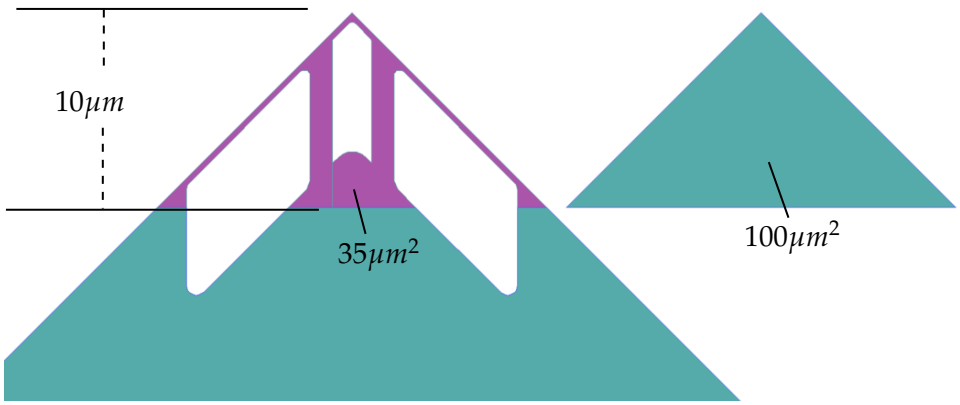

FIGURE 7.11: Schematic drawing highlighting the difference in area between the C1 and regular type probe. The final 10 microns of the C1 type probe (highlighted) have only 35% of the area of the solid triangular tip

In air, contact zone time constant was calculated as 103 µs, with cut-off frequency occurring at 1.54kHz. By contrast, the coupling zone's transient data are as follows; $\tau = 930$ µs, f_c = 170Hz. The composite of the two transient behaviours is the reason for the unusual frequency sweep profile for these probes. From these properties, we can conclude that the 'scallop' is the result of the body of the cantilever, whereas the more aggressive filtering is the result of transient behaviour of the contact/active zone.

Considering Figure 7.8, what can be said of the changes to the probe design? The progressive reduction of the contribution from the pole with lower f_c demonstrates the diminishing influence of the cantilever body on the probe's response as a function of the changes to probe design. In the case of the N type probes, improvements are likely to be primarily the result of the four terminal measurement. Using this technique, the probe response more accurately follows the sensor temperature, being independent to the resistance of the rest of the electronics, including those which are located on the cantilever.

The cut-out probes are expected to have modified the thermal behaviour of the probes by providing isolation between the sensor and the cantilever body. The removal of cantilever material near the apex will both increase the thermal resistance

into the body of the probe, R_P, and reduce the heat capacity of the probe in the active/coupling region. A quick estimation of the difference in heat capacity can be made by considering the change in area along the final 10 µm of the cantilever; since the material in question has not changed, and neither has its thickness, then the heat capacity of the probe scales linearly with area. From Figure 7.11, one can observe that the final 10 µm of the C1 type probe has roughly a third of the heat capacity of the standard design.

The combined influence of increased resistance and reduced heat capacity manifests as a faster probe, with higher cut-off frequency, as verified experimentally in Figure 7.8. Qualitatively, we observe in this figure almost a complete elimination of any cantilever influence. The form of the data looks closer to that of the SCLA, meaning that the 'second' pole brought about by cantilever effects has been almost completely eliminated. We find this to be compelling evidence that the design changes implemented resulted in a real and observable increase in the thermal resistance of the cantilever, in such a way as to reduce its influence on the measurement.

Note that their model was re-produced as part of this work. Unfortunately, attempts to fit our experimental data to their model were unreliable; five unknowns proves too many for a reasonable fit without 'teaching' the model what to expect. It is our expectation that if one or more of the parameters could be reliably estimated either with experiment or calculation, then the two pole model would prove useful for the determination of probe resistance/ heat capacities.

7.3 Passive mode measurements

7.3.1 Motivation

In the previous section we concluded that the changes to the design of the cantilever result in a reduction in the influence which the cantilever body has on the measurements being performed. The active mode measurements on bulk samples showed some evidence of an increase in sensitivity, but this was confounded by the difficulty in discerning contact-area based effects from the rest of the data. The frequency plots showed quite compelling evidence that the cantilever influence was significantly reduced, even if said improvements were not manifest in a manner which could easily be observed in the bulk sample S-curve method. To strengthen this assertion, it was decided to perform passive mode scans over a heated sample. The asymmetry caused by sample - air - cantilever conduction is well documented [32], [237], and has been described previously in this thesis (Section 4.3.6). The experiment described in this section was designed to examine whether or not the cut-out probe would demonstrate lower asymmetry thanks to;

- Reduced SiN volume in the beak (close proximity to sample)
- Rejection of the cantilever contribution due to four terminal design.

7.3.2 Method

The sample chosen is a substrate of single crystal diamond, patterned with a 6 $\times$ 6 µm NiCr heater and tapering Au contact pads. The layout of the pattern may be surmised from Figures 7.12 and 7.16, which consist of a low magnification photo of the sample, and an SThM scan over the heated area respectively. This sample, which was previously designed and fabricated by Dr Y. Zhang, was identified as a suitable sample which did not require additional development.

The high thermal conductivity of the substrate allows heat to spread far through the substrate, giving a large hotspot from a small heated area. This is advantageous for the investigation of image asymmetry brought about by sample-probe heat conduction through the air. The ideal sample might have hotspots of the order of the

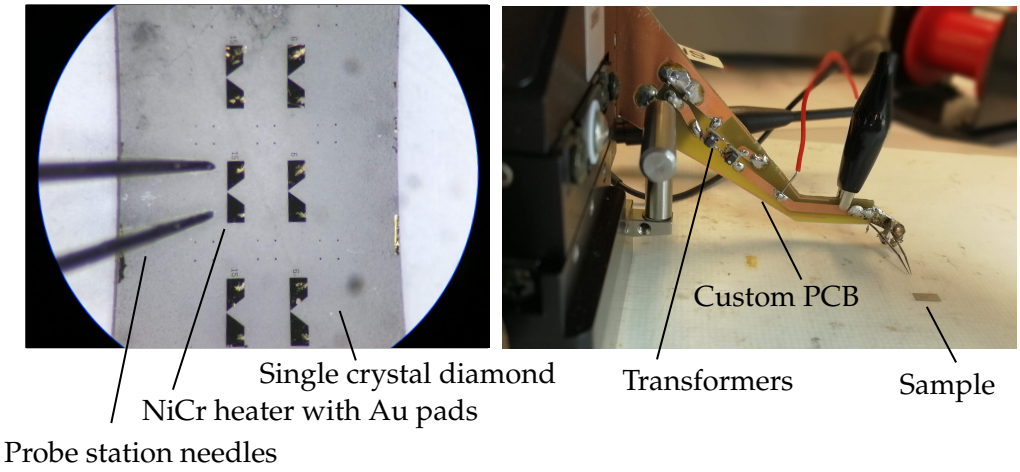

FIGURE 7.12: Photographs of the active sample experimental setup. Left: Micrograph of the sample. Right: Photograph of the micromanipulator and custom PCB used to make electrical contact to the sample.

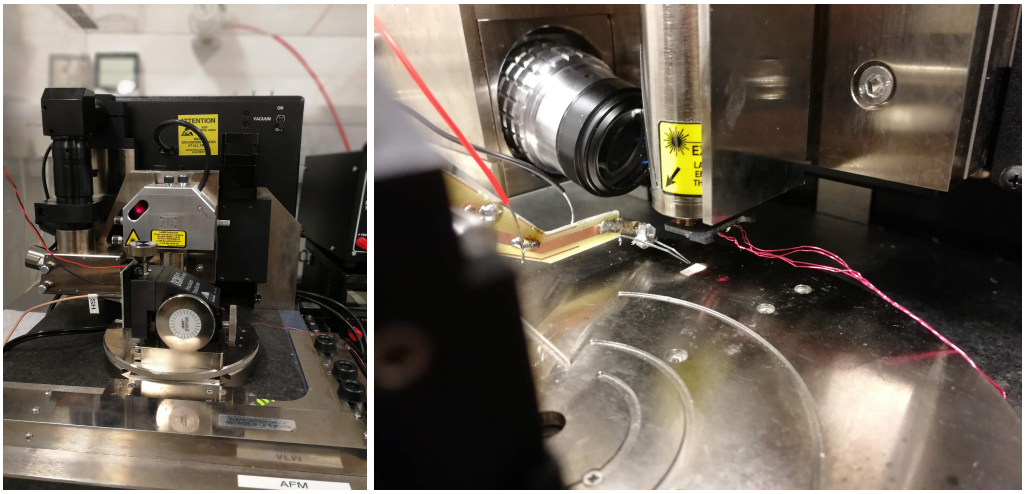

FIGURE 7.13: Photographs of the experimental setup loaded on the AFM stage.

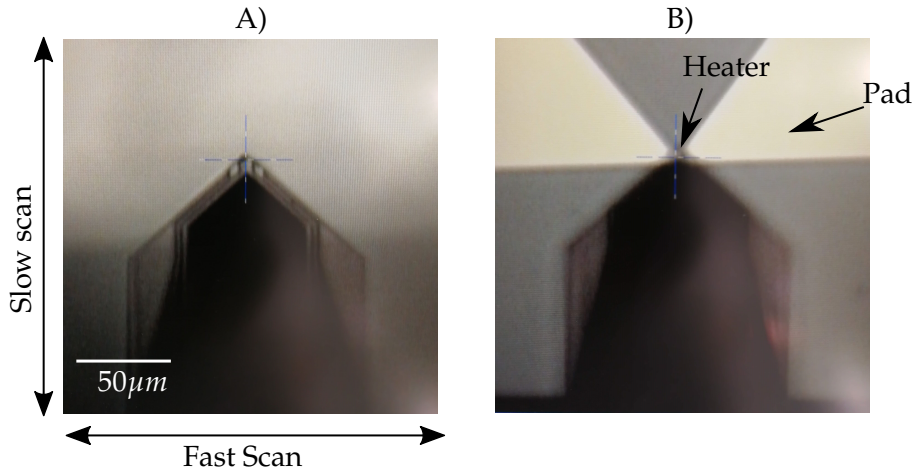

FIGURE 7.14: Image captures of the C2 type probe prior to (A), and after (B) contacting upon with the diamond/NiCr active sample. The arrows denote the fast and slow scan directions

cantilever width (100 µm), however such a sample was not available at the time this work was to be performed.

The substrate contains multiple heater devices, as may be seen from Figure 7.12. Rather than bonding to each site, connections to individual heaters are made using probe station needles attached to a micro positioner. The needles are attached to a custom PCB which is shaped such as to fit underneath the head of the Dimension AFM and allow the needles to contact the sample without interfering with the operation of the probe. The layout of the experiment is presented in Figure 7.13A and B from the front, and side views respectively.

On the PCB there resides a transformer isolation circuit, which is used to float the probe to the sample's potential. This is required due to the lack of a passivation layer on the active device. The transformers are highlighted in Figure 7.12.

Two probes were selected for this experiment; one C3 type probe, and a commercial type probe used as a control. The sample was biased to the same voltage during both scans. Each probe was scanned over a 25 μm^2 area using identical scanning parameters. The probes are necessarily biased with AC to allow for transformer isolation, and their 3ω output is measured.

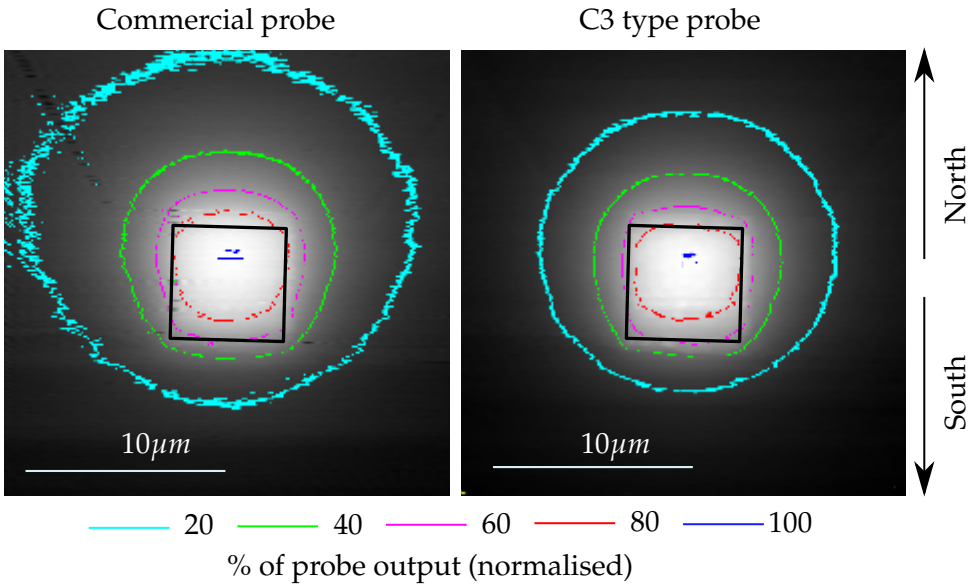

FIGURE 7.15: 3ω thermal image comparing the temperature distribution of the same heater, as measured by a commercial and C3 type cut-out probe. Rings highlight temperature contours occurring at 20% intervals of the normalised response. The C3 type demonstrates reduced asymmetry, and more faithfully reproduces the temperature profile of the device. Note also the more squared shape of the 80 and 60 percent contours in the C3 type probe. The heater outline is highlighted with a black square.

7.3.3 Results and discussion

Figure 7.15 presents the SThM images gathered by scanning both of the probes over the region previously described. The data have been processed in Gwyddion to normalise the 3ω signals, and to colourise them for easier data visualisation. The colour scale is from hot white to dark black, however the highlighted contours represent isotherms at 20% increments of the total temperature. The same data are presented in an alternative manner in Figure 7.16A and B, in which the extent of the heater and pads have been annotated with dashed lines. Figure 7.16C has the two sets of contours overlaid, while D) presents the topographic image. Note that these images share are of the same orientation as the photographs presented in Figure 7.14, and thus share the same fast and slow scan directions. From these results the asymmetry is apparent; the contours of the commercial probe are elliptical, not circular, with the pointed end of the ellipse located on the north side of the image. This corresponds to the situation in which the body of the cantilever is positioned directly above the heated region. As the probe approaches the heated feature, from south to north, the

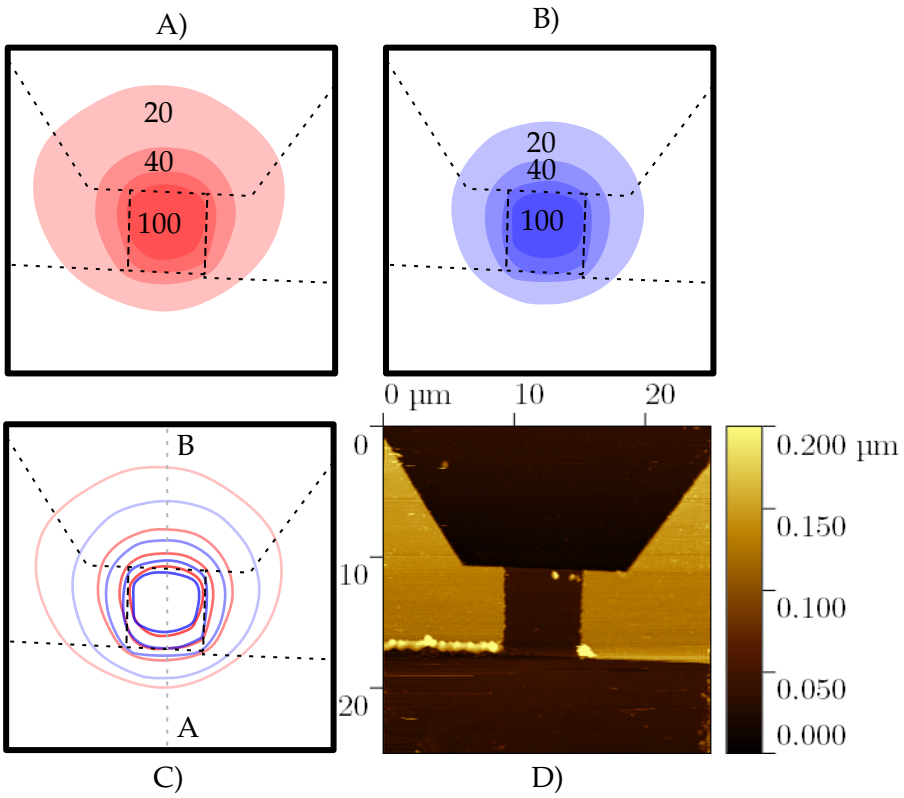

FIGURE 7.16: Comparison of the temperature contours that result from scanning the active sample with a commercial and a C3 type probe. A) and B) are the commercial and C3 probes' temperature contours overlaid on the outline of the heater. C) compares the two sets of temperature contours. D) Shows the height data which was collected simultaneously with A).

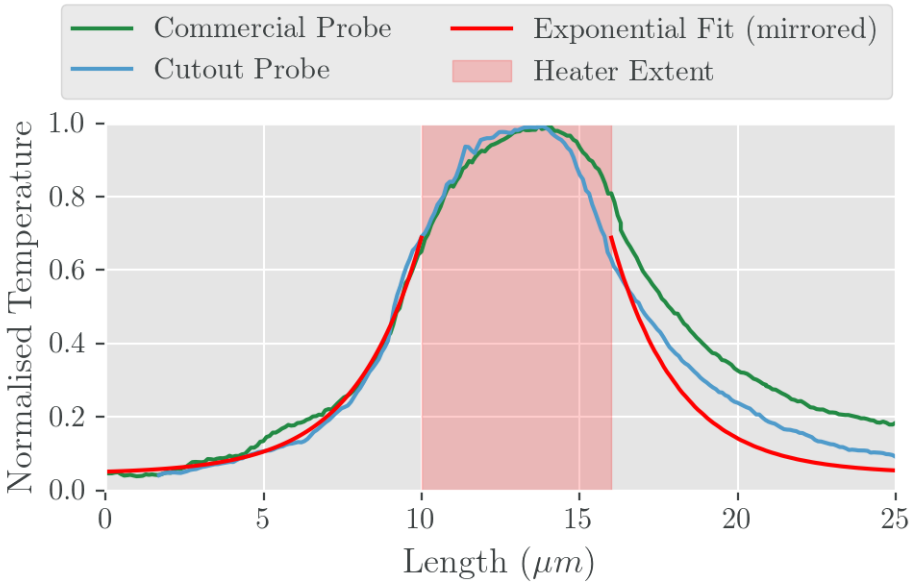

FIGURE 7.17: Comparison of the normalised temperature traces gathered by the commercial (green) and cut-out (blue) probes as they scan over the same thermal feature. The measured temperature on the south of the heater (L<10um) is nearly identical for both probes. A best fit exponential has been calculated for this region and plotted in red. The best fit solution has been mirrored on the north side of the sample, however we note that both probes experience some asymmetry. However, the temperature asymmetry in the commercial probe is almost twice that of the new, cut-out, four terminal probe.

initial temperature readings are expected to be more accurate, since only the sensor region is in close proximity to the heater.

From Figures 7.15 and 7.16, one can easily observe the reduction in asymmetry resulting from the use of the C3 type probe. The overall temperature distribution is less skewed, with more circular shape, and the contours closest to the heater exhibit a squarer shape which is more representative of the true temperature profile.

To further elucidate the differences between the two temperature profiles, it was decided to compare thermal traces across the cross section marked 'A-B' in Figure 7.16C. The result is presented in Figure 7.17. The 'length' axis begins in the south at 0 µm and extends to the north of the image. It is clear from these traces that the temperature profiles measured by both probes are practically identical while approaching the heated region. However, the traces diverge as the probe travels onto and beyond this region. For the sake of comparison, we have calculated a fit for the

temperature response on the approach part of the curve, and have flipped and mirrored this on the north side for a reference estimate of what a device with no asymmetry might look like. The commercial probe suffers from strong thermal coupling between the heater and the cantilever body, manifesting as an obvious temperature asymmetry. While the cut-out probe also exhibits some degree of asymmetry, its response is much more similar to the 'ideal' red trace. While qualitative in nature, we consider this compelling evidence that the cut-out type probes developed in this work can considerable reduce the temperature-asymmetry artefact that is common in passive mode ambient SThM. In conjunction with the results of previous experiments presented in this chapter, it is fair to conclude that we have been successful in fabricating a probe which is more sensitive to the temperature of its sensor, and whose signal is more independent of its cantilever temperature.

Chapter 8

Conclusions and Future Work

8.1 Introduction

Scanning thermal microscopy continues to be at the forefront of developing thermal metrologies, in part due to its excellent spatial resolution. As the technology has matured, the capabilities of thermal probes have extended beyond temperature measurement and other thermal metrology applications have emerged, with particular interest being shown in materials characterisation.

Of the multitude of thermal probes available, a small number have emerged as popular due to their commercial availability. As such, many studies have been performed regarding their operation. However, comparatively few studies have been performed with the explicit aim of optimising the probe for a given application. While the KNT probe has become popular for both thermometry and thermal conductance measurements, the probe has not been optimised for either.

In this work, tools and techniques have been developed to aid in the development of the next generation of commercially viable, mass-producible SThM probes. We take this opportunity to emphasise our belief that batch fabrication should be a prerequisite for consumable metrology devices for high reproducibility. In addition to designing, fabricating and testing novel probes, it has been a key goal of this work to contribute to the understanding of thermal probe design, and to identify which parameters should be adjusted to optimise for different kinds of operation.

The following sections summarise the conclusions from each aspect of this work,

and, where applicable, presents the recommendations of the author in regards to the direction of future work in these areas.

8.2 A thermal model for probe development

One dimensional thermal electrical analogues have been applied in SThM studies throughout the literature, and have been particularly useful in characterising the commercial device. In some cases, the probe is approximated into a chain of connected lumped elements, with each lump representing an area of the probe which is governed by particular thermal phenomena. This is a sensible and computationally efficient approach which has been demonstrated to accurately characterise the operation of the probe. However, such models do not yield a temperature distribution of sufficient resolution to inform the design of **future** probes. This is a pre-requisite for probe design, because the output signal is entirely dependent on the averaged sensor temperature. In both modes of operation of the probe, a high temperature gradient is observed along the few microns close to the sample contact, caused by the high thermal resistance of the probe in this region.

The model developed in this work allows for a high-resolution temperature profile of the thermal probe, operating in the active mode, in a vacuum. Employing the same mathematics as SPICE circuit simulation models allows for a computationally efficient solution to the temperature distribution of the probe, as the result of its elemental power generation and thermal resistance. Attaching contact and spreading resistances to the end of the network allows for simulation of the probe temperature distribution while contacting a material. Due to the lightweight nature of the model, it is possible to parametrically alter aspects of the model and compare multiple temperature distributions. This was used to compare the temperature distribution of the same probe when touching various materials and characterise its active mode performance. It has also been used to compare the out of contact temperature profiles of probes with differing designs. This was performed to assess the thermal isolation of the sensor from the cantilever by calculating the maximum temperature achieved for the same input power. Such numerical experiments would have been prohibitively time consuming with FEA. A great strength of this model is the automatic fracturing

of GDSII files into a set of elements for use in the simulation. The GDSII file format is a standard CAD file for the microfabrication industry, and allowing their importation means that designs can be used for both simulation and production. Much of the challenge in creating 1D numerical models is the fracturing of designs into usable elements. There is no reason why this module could not be employed for other numerical models of other micro-fabricated devices.

The key insights that were concluded from numerical experiments performed with the model are as follows;

- **Heater isolation.** In the active mode, generated heat preferentially flows down the cantilever to the base of the probe. Since it is this Joule heat which is being used to probe the thermal properties of the sample under test, heat lost via any other pathway may be considered parasitic, and will diminish the probe's ability to discriminate between materials of similar thermal conductivity. Simulations in which material was selectively removed from the cantilever were shown to increase the effective cantilever thermal resistance (Figure 4.33), localise heat to the heater/ sensor beams and increase sensitivity (Figure 4.35).

- **Sensor localisation.** The probe's output is proportional to the average of the temperature along its length. With this high resolution thermal model, it was possible to model the temperature distribution in this region as a function of a variety of probe geometries and sample conditions. One particularly illuminating experiment was that presented in (Figure 4.37), in which a probe's temperature distribution was calculated as the result of contacting upon materials of various thermal conductivities. It was observed that the peak temperature not only diminished, but the position of the peak temperature also shifted further from the apex of the probe (contact point) with increasing thermal conductivity. There is a limit to the thermal conductivity of solid materials, and therefore a limit to the heat abstraction that can be expected (for a given contact radius). Therefore, active probes should be designed such that the sensor lies entirely within the region of cooling. In all operating regimes, the sensor should have minimal area, and be located as close to the tip as possible such as to minimise the loss of signal resolution through resistance averaging.

- **Sensor electrical isolation.** Compounding the above point, the probe's signal should be dependent on the resistance of the sensor, not on the leads, current limiters or external circuitry. A four terminal approach in which the sensor is measured independently from the current carrying loop was identified as a practical solution. If one wishes to generate significant Joule heating, a large heater is an attractive option, but the sensor should be localised to the apex. It is possible to decouple the heating from the sensing by implementing the novel layout presented in Figure 4.38.

The above design principles apply not only to the thin film style of SThM probes described in this work, but are expected to be applicable to other varieties of thermal probe.

While the work reported here has focussed on simulations in the active mode, and in vacuum, there is nothing preventing the model from being extended to account for ambient operation, or a variety of other phenomena. For example, passive mode measurements may be realised by reducing the current to the probe such that self-heating is negligible, then applying a fixed temperature (voltage source) to the tip of the probe. Similarly, coupling between the probe and sample through the air as described by Ge et al could be employed by adding a z dependent thermal resistance of air conduction.

It is interesting to consider the possibility of simulating transient mode operation with a model of this type. Transient systems are well approximated with the SPICE-type algorithm employed in this work, and could be realised by adding elemental heat capacities to the body of the probe. This is, in essence, the same method as presented by Bodzenta et. al and discussed in Section 7.2.2. While they found that the probe's response could be reasonably approximated with only two time constants, a full elemental model would allow for simulation of the temperature distribution across the entire cantilever. This would then allow for predictive simulations of probes' transient mode performance before fabrication. This information would benefit a variety of studies, for example that of nanoscale thermal diffusivity. Beyond transient studies themselves, a probe's transient performance is a good indication of its thermalisation time, which can pose a limitation to its measurement

speed. This information would be very beneficial in the development of intermittent contact mode SThM. Due to the increased friction and time in contact with the sample, contact mode operation has been observed to degrade the tip, causing undue damage, and resulting in an ambiguous contact radius/ contact material. Presently, intermittent contact SThM is prohibitively time consuming as an imaging technique due to the dwell time required for the probe and sample to thermalise. Probes with a lower heat capacity could reach thermal equilibrium with the sample faster, allowing for increasing oscillation frequencies to be employed.

Other areas of interest which could be investigated with this model include the influence of the laser on the probe's temperature response. If the spot size and power of the laser are known, it is possible to represent its distributed irradiance upon the probe in the model. By consideration of the optical properties of the probe, one may append appropriate fixed temperature sources to the probe to represent the laser heat generation. Investigations regarding the influence of laser positioning on probe output may then be performed. This approach could be used to design and model probes which are minimally impacted by laser illumination.

This model may also be extended beyond thermal properties alone. The transformation from 2D probe design into a collection of elements with material properties is useful for any distributed calculation. Much like the probe has been represented as a series of thermal resistances in this work, it may also be expressed as a series of springs, simply by considering the stiffness and modulus of elasticity of the materials rather than the thermal conductivity. Within our group, there has been significant progress on modelling the bi-material bending experienced by the probe through the extension of the model developed during this work. By considering the mechanical and thermal properties of the probe simultaneously, it will be possible to characterise the deflection of the probe, the angle of the laser, and the force exerted between the probe and sample in various loading configurations. It follows that this work will be able to suggest a probe which in which bi-material bending is less-prevalent, and for which the deflection behaviour is well characterised.

Finally, there is no reason that any of the improvements suggested here should stand alone. It is reasonable to envision a model in which coupling through the air between

a heated sample and the probe introduces a bi-material bend.

8.3 Fabrication developments

8.3.1 Alignment accuracy

In Chapter 5, an implementation of a statistical alignment algorithm was presented. The novel probes developed in this work employed this algorithm during all their electron beam lithography exposures, and the magnitude of the improvement was calculated through comparison between the exposure positions written with the algorithm, and the exposure locations which would have resulted from only using the four markers at the corners of the cell. Displacements between the two were routinely observed to be over 100nm. Critically however, corner cases such as cells with non-rectangular marker distributions, had their exposure positions altered by values on the order of hundreds of nanometres. Improvements were further evidenced by the device-to-device resistance variation of the N type probes, since resistance variation is a suitable proxy for misalignment in this case. Particular attention is drawn to the N2 variety, in which 580nm width sensors are positioned in alignment with the probe apex. Minimal resistance variation of $250 \pm 20\Omega$ (8%) was observed, suggesting that any misalignment was negligible for these devices. This is contrasted with the $110 \pm 50\Omega$ (45%) resistance value routinely observed in the commercial probes (discounting the 200Ω fixed resistance introduced by the NiCr limiting resistors).

Future development in this area should be concerned with optimising the number, and distribution of markers around the writing cell. In the longer term, a shift to a different marker type, such as a Penrose pattern should be employed. A change to metal markers would also offer increased contrast, but depositing metal in the first lithography step would require a significant re-design of the current, mature process. Finally, the sensor could be intentionally recessed from the apex by a small amount (e.g. 50nm). This would ensure no 'flags' of metal from the sensor make contact, and remove any ambiguity as to which material is contacting the tip. Ensuring no metal makes sample contact would also allow for these probes to investigate electrically active devices directly, without the requirement for insulation or transformer

isolation.

8.3.2 Height measurement

The height measurement algorithm developed in this work was shown to be equally as effective as the in situ measurement for flat samples with a uniform bilayer resist coverage. Importantly however, the map of wafer heights allowed for an estimation of the wafer height even in those areas of the wafer in which no sensible measurement could be achieved.

This algorithm, when employed on topographic substrates, allowed for the proper definition and lift-off of narrow (<300nm) cantilever beams on the side of the AFM pyramid for the first time. Experiments writing 50nm line-width verniers on raised pyramid tops was shown to have improved writing quality and process latitude. It is not expected that many further improvements to the writing quality can be attained without addressing the resist non-uniformity which results from our unusual application methods (spin + float coating).

From the comparison between the height measurements performed on the topographic wafer with and without resist, it may be concluded that the accuracy of measurement depends not only upon the presence of sloped features, but also upon the thin film structure. Perhaps a spin-coated bottom anti-reflective layer coating could be applied to the substrate to prevent destructive interference of the laser beam.

8.3.3 Alternative resist technologies

Optimising the focus of the beam provided some increase in process latitude when working with topographic AFM wafers. Unfortunately however, there will always be some variation in clearing dose due to the non-uniform thickness of the resist film. Float coating introduces wrinkles and tears in the deposited resist film, while spin coated resist pools at the base of raised features and thins significantly towards the top edge. An alternative approach is to employ spray coating, which is used routinely in MEMS manufacture for the coating of high aspect ratio features. Because the resist is sprayed on, top-down, it achieves more uniform coverage of topographic

features than spin coating. Typically however, spray coating is used for photoresists, not electron beam lithography resists.

The idea of formulating an electron beam lithography spray resist was identified mid-way through this project, and a body of process development work was performed. While significant progress was achieved, the process was not mature enough to be implemented on SThM probes, and thus was not included in the body of this text. However, a full report is provided in Appendix G

8.4 Novel probe manufacture

The frames substrate developed as part of this work will allow for the rapid prototyping of devices that use the generic probes technology platform. The first batch of cut-out probes were realised on this platform. They indicated that probes with extensive beams could be fabricated, released and scanned without significant mechanical penalty. They also indicated that dual self-alignment could be successfully achieved on such probes. The fact that these probes did not feature the skirting artefact seen on later cut-out probes may indicate that a metallisation pattern with wider overlap is better, as there is more metal to adhere to the sacrificial Si substrate.

The second batch of cut-outs featured eight different probe designs. The yield and resistance accuracy of each was characterised. Of particular interest was the resistance variation of the probes with the smallest sensor sizes (C1, N1 = 291nm width sensor), presented in Figure 6.33. The size 1 sensors without a cut-out had 550 ± 300 ohms resistance, while the cut-out probes of the same size demonstrated negligible resistance variation. This demonstrates that the dual self-alignment approach is suitable for the definition of narrow sensors whose width is completely dependent upon the width of the underlying cantilever.

The yield breakdown for the different types of probes in this batch was presented in 6.2. For a first attempt with so many deviations from the mature process, we consider this an excellent yield. Further work will be required to improve the yield to commercially acceptable levels however. Of the numerous probe types, there were multiple failure mechanisms, making a full breakdown inappropriate for this

section. However, Appendix F contains a gallery of images of the failed probes, alongside a description of the mechanism, suspected causes, and suggested course of action should such probes be attempted in the future.

8.4.1 Methodology for characterising novel probes

Promising experimental results were presented within Chapter 7, however it is important to highlight another aspect of this work which we believe to be quite impactful. In this work, we have presented a methodology for the characterisation of novel SThM probes. To our knowledge, there is no present literature which outlines how this should be achieved, especially for the less-mature 'active' mode of operation. While calibration with a set of bulk samples with known thermal conductivity has been proposed, it has been demonstrated unsuitable for probes with sub-micron tip radii. Because the nanoscale contact area introduces such massive contact resistance, small fluctuations in this contact area, such as those introduced by surface roughness, introduce significant changes in tip-sample conductance. Without a method for quantifying the tip-sample contact area, these changes are purely confounding, and can be very misleading when attempting to compare different probe designs. A probe with ostensibly improved sensitivity to variations in tip-sample conduction may not demonstrate better sample thermal conductivity contrast if it has contact radius smaller than the probe to which it is compared. Tip radii sizes may vary due to fabrication variability, or due to mechanical wear that occurs during interactions with sample surface. Additionally, in ambient operation, unquantified thermal coupling between probe and sample through air precludes like-for-like measurement between samples. Therefore, it is advantageous to characterise probes using methods which do not rely on sample contact.

In this work we have presented non-contact metrics to characterise the probe's sensitivity to changes in its sensor temperature. The first, the 'self-heating coefficient', is taken as the third order component from the probe's I-V curve divided by the electrical resistance of the probe. Assuming fixed ambient temperature and no interactions with a sample, sensor temperature is the result of Joule heating and thermal conduction through the cantilever and heat dissipation to ambient. As such, the self heating

coefficient can be used to compare probe designs which aim to localise heat to the sensor region and minimise losses down the cantilever or into the environment. A second non-contact method for the characterisation of novel SThM probes was presented in this work, in Section 7.2.2. It is proposed that performing out-of-contact frequency sweeps of novel probes can be a useful tool in the analysis of new designs. Of particular interest is the observation of diminishing cantilever contributions, verified by the reduced influence of a pole with low cut-off frequency. In Figure 7.8, we observed this minimisation for both N, and C type probes, indicating that both changes in the sensor design and geometric layout can improve performance.

8.5 Scanning results from novel probes

8.5.1 Self heating coefficient

Initial characterisation of the probes involved performing I-V sweeps to measure their electrical resistance. The sensitive, thermally-isolated probes developed in this work were observed to begin self-heating at reduced current than the commercial probes, making bridge balancing challenging. However, an alternative approach was developed that allowed for better characterisation of the probe and bridge. Fitting the bridge output to a curve of the form $aI^3 + bI + c$ (in which I is current) allows for simultaneous acquisition of the magnitude of bridge imbalance, and the self-heating coefficient of the probe (a)

This value has been identified as a useful metric for comparing the self-heating efficiency of different probes. It contains information about the electrical resistance of the probe, from $V = iR$, but also varies with the temperature of the probe - which is the result of the Joule heating $P = i^2R$ and the efficiency of heat dissipation from the probe, which, all other resistances being equal, is a measure of the thermal resistance of the cantilever.

All the novel probes developed in this work were shown to have higher self-heating coefficient. In both the C and N type probes this is due to better localisation of the sensor to the cantilever tip; more change in signal was observed for the same

change in temperature. The cut-out probes demonstrated a further increase in self-heating coefficient compared with their N type counterparts, which is the result of better localisation of the heat to the tip. Although the Joule heat generation has not increased, the isolation of the heater from the cantilever means the sensor reaches higher temperature.

It is believed that the self-heating coefficient is a useful metric for describing the performance of heat delivering thermal probes, and is suitable for adoption in other works.

8.5.2 Bulk sample S curves

Experiments performed in which probes of each type were contacted upon materials of various thermal conductivity produced interesting results. Thermal conductivity imaging has typically been qualitative in nature, so there is great interest in calibrating probes with curves of this type. However, it was not clear as to where the probes' out of contact reference temperature should be taken when performing such experiments in air. As such, the data was presented here in two forms; one considering the signal change to be the magnitude of the 'jump' in thermal signal immediately upon making contact (Figure 7.7), and the other considering the temperature change from many microns away from the surface (Figure 7.7 to the point that no distance dependence was observed). In the former measurement, the scatter was high for all probe types and sample thermal conductivities, and the fit to the expected 'S-curve' was poor. The new probes were not observed to perform any better than the commercial probe. However, when considering the signal from far to in contact, the scatter for all measurement points was negligible and the fit to the S curve was excellent. When presented in this format, there is a strong correlation between sensitivity and sensor design. While the N type probes are expected to perform better than the commercial probes because of sensor design alone, it is proposed that the cut-out probes exhibit better sensitivity when measured in this way due to increased cantilever resistance; the heat which would have previously travelled along the solid cantilever has instead heated the air around the tip, allowing for improved coupling between the probe and sample through the air. Conduction through air is expected to be much

more stable than conduction through the tip sample contact, which is pressure and roughness dependent, strongly influenced by contact area. The implications of this, especially as they pertain to SThM operation in other environments (liquid) were provided in the body of the text (Section 7.2).

8.5.3 Frequency domain analysis

An investigation into the transient properties of the newly developed probes was presented. Bode plots of the novel probes were compared with those of commercial probes, and those published in the literature. The shape of the curves generated by the new probes lacked the characteristic 'scalloping' of the commercial probes which has been observed at around 170Hz, and has been shown to be due to the time constant of the cantilever body. By reducing the heat capacity of the tip region, and increasing the thermal resistance from the tip to the cantilever, it was possible to minimise the influence of the cantilever's transient thermal properties. Additionally, the change in profile of the 'N' type probes' curves (which have not received geometric alterations) indicates that the sensor re-design alone has resulted in an electrical signal which is more independent of the cantilever temperature. In the case of the cut-out probe with the smallest sensor tested, a cut-off frequency of 8Khz was achieved, compared with around 2kHz for the commercial devices.

These increases in probe speed will have immediate benefits in acquisition time due to faster thermalisation, but optimised probes of this kind could also open the door to other transient regime measurements, such as thermal diffusivity.

8.5.4 Passive mode scans

A common artefact of passive mode SThM is a temperature 'asymmetry' which is observed between the probe's signal when approaching a heated feature vs. when scanning the region beyond the heated region such that the cantilever body is directly above it. Thermal loading through the air causes the probe to overestimate the substrate temperature in such cases.

A promising reduction in this artefact, shown in Figures 7.15 and Figure 7.17, was observed with a C3 type probe. It is expected that should this experiment be repeated with a smaller sensor and larger cut-out, such as the C1 type probe, that the artefact would be further diminished. In the longer term, this result suggests that a probe whose cantilever area is minimised, and whose sensor is as local to the contact point as possible would be the best choice for optimising SThM probes for thermometry.

8.6 Further Experiments and Technology Transfer

In this work we have realised probes with improved sensitivity in the active mode, and greater insensitivity to a common artefact in the passive mode. There are many further experiments which should be performed and disseminated via journal publication.

8.6.1 Vacuum mode scanning

The performance of the fabricated probes was characterised over four experiments throughout Chapter 7. Unfortunately however, we were unable to access a vacuum AFM system during this time. While ambient operation is an important aspect of SThM which accounts for a great deal of the experiments performed with the technique, vacuum operation can offer complimentary insights which should also be considered. Not least, vacuum operation significantly simplifies the thermal network of the system by eliminating losses to air, coupling between the probe and sample through the air, and conduction through the liquid meniscus at the tip. The heat transfer network is thus reduced into the 'thermal divider' configuration presented in Section 4.9.2. The model developed in this work considered only vacuum operation, and probe design was therefore concerned with optimising the solution to the thermal divider problem. It is expected that the sensitivity of the developed probes to changes in tip-sample thermal conduction is drastically improved in vacuum compared to the commercial devices. With the ability to perform experiments that are characteristic of the modelled situation, it would be possible to verify the model's accuracy further, and to improve its predictive capability. This may also

enable the calculation of unknown values that are had to extract from experiment, in an approach such as that taken by Ge et al, who were able to calculate contact resistance by fitting the value to the model output. [32]

In addition, it would be interesting to repeat the probe characterisation routines presented in Section 8.4.1. In fact, let it be noted that these characterisations could be employed for each environment in which the probe is intended to operate. The self-heating coefficient will be drastically increased without losses to air. One would also expect a noticeable difference in the frequency response of the probe, since the environment offers zero heat capacity and practically infinite thermal resistance. One can imagine that there are interesting insights to be found about how a given probe design dissipates heat to the environment by repeating these experiments in both air and vacuum, or at a variety of ambient pressures.

8.6.2 In fluid/hover mode scanning

In this work, we observed high scatter in the jump-to-contact temperature drop when performing thermal-distance scans on bulk samples in ambient conditions. However, when considering the change in temperature from far to in contact with the device, the new probes demonstrated increased sensitivity, and a strong fit to the modelled S-curve. It is proposed that the reason for the high scatter in the jump-to-contact is because the probe-sample contact area is unknown for each contact event and is not considered. One method for eliminating this high uncertainty is to avoid contact with the sample altogether, and instead have the probe hover some fixed distance from the sample surface. Coupling between the probe and sample could be improved by introducing a fluid environment with higher thermal conductivity than air. Immersion SThM has already been the subject of significant interest due to its applications for biological samples, however a major detractor from its development has been the increased heat dissipation due to the more conductive environment [233]. While this issue will still plague the novel cut-out probes presented in this work, they have a key advantage which makes them well suited to this application. By isolating the heater to narrow beams and increasing the thermal resistance to the cantilever body, we have localised heat to the tip. This is particularly important in

this environment, where any heat in the fin-like cantilever body will be readily and efficiently dissipated into the environment. It is expected that these probes generate a local temperature field of heated liquid in close proximity to the sample surface that can be used to probe the sample thermal properties.

8.6.3 Passive mode performance

The probes presented in this work were developed with the active mode of operation in mind, however in Section 7.3 we identified a significant reduction in the asymmetry artefact which occurs when driving the cantilever body over a heated sample region. There remains more work that could be performed to quantify the accuracy and repeatability of these probes for temperature measurement. Obviously, the problem of contract resistance will still introduce an offset between the absolute and measured temperature, but it is expected that these probes with more local, four terminal sensors should be more insensitive to external temperature perturbations. Experiments might include scanning over micro-hotplates with known temperature fields, or modulation of the laser position on the probe body to ascertain whether or not the new design is more tolerant to laser heating.

Further alterations could also be made to the probe to optimise its stability in the passive mode. For example, it stands to reason that a probe with an even larger cut-out would be more insensitive to the cantilever coupling artefact. In Section 6.1 we demonstrated that significant portions of the cantilever could be removed without compromising mechanical feasibility of the probe.

8.6.4 Addressable heaters

These probes were designed such that the 'force' and 'sense' terminals could be swapped depending on the desired use case. This was discussed previously in Section . In this work, the probes were only operated using current through the outer beams, since this configuration gives the greatest degree of self-heating. It would be interesting to characterise these probes using the methods outlined earlier in this Chapter. It is reasonable to assume that they will demonstrate a lower self-heating coefficient, since current will flow through the wider beams which have

lower impedance and generate less Joule heat. While this is not advantageous for the active mode scans performed in this work, it is useful for passive mode measurements in which Joule heating is a confounding heat source.

8.6.5 More topographic sample

It should be acknowledged that only a limited number of samples were fully 'imaged' with the probes presented in this work. We experienced no issues with hard contact scanning, and saw no evidence that the probes would not be fit for purpose when performing deflection calibration and force distance curves (Section 6.1). That being said, probes with such drastic changes in layout might be expected to have buckling/torsional stresses with tracking over samples with significant topographic variation. It is the author's belief that most such issues can be avoided by careful selection of positional feedback parameters and consideration of the orientation of the probe relative to the topographic features. That is to say, the scan should be oriented such that the probe 'beak' encounters large edges side on, rather than headfirst.

In the longer term, SThM should move away from hard contact scanning, and towards the gentler intermittent contact modes. These ostensibly more fragile probes necessarily have a reduced heat capacity due to the removal of cantilever material. They feature a natural trade-off between mechanical stability and thermalisation time. A significant hurdle preventing adoption of intermittent contact SThM is the dwell time that would be required for the probe and sample to reach thermal equilibrium. Removing this limitation through faster probes would be a significant step forward for the technique. This was discussed previously in Section 8.2

8.6.6 Technology Transfer

Throughout this section we have highlighted some important experiments which should be performed with the probes developed in this work, or the next iteration of probes which are developed based upon this work. Once those results have been disseminated through journal publication, it is intended that said probes are transferred to Kelvin Nanotechnology and made available commercially. The probes presented in this work are actually no more involved or expensive to produce than the ones

available currently, since the changes are only in the layout and writing of layers written with electron beam lithography. No additional processing steps have been added in this work. It is our expectation that a probe such as the 'C2' design could be adopted for commercial manufacture with little further development. The first demonstration of these probes had a reasonable high yield, with the main detractor being the 'skirting' artefact that resulted from writing too large an overlap in the sensor region. Fixing this is anticipated to be a simple pattern change only.

Perhaps before moving to commercial manufacture however, it would be advantageous to distribute these probes throughout Quantiheat partners, or the wider scanning community. As end users of the probes, they will have valuable input into what they would consider to be a significant improvement to the present commercial probe. As the field increases in popularity, more and more research groups are adopting the technique, but for slightly different applications. While there are advantages to having the majority of end-users congregate around a single probe design (as is the case presently), there are also advantages to having bespoke probes manufactured for a specific measurement type. In this work, we have paid particular attention to the active mode performance of the probe, and found that there have been some improvements in the passive mode as a fortunate by-product.

As thermally informed probe design matures, it is envisioned that product lines of probes each best suited for a given application will emerge. It is our hope that the fabrication improvements, modelling methods and experimental methodologies presented in this work will provide a useful reference for the development of the next generation of probes, regardless of which direction the field moves in.

Appendix A

Process sheet for standard SThM probes

- **Orange** - Photolithography exposures
- **Blue** - EBL exposures
- **Grey** - Plasma processes
- **Green** - Optical/SEM inspection steps

#		Process Steps
1	Pyramid Level Photolithography	Clean 3" dsp 380um Si/SiO2(40nm)/SiN(60nm) wafer using dipper. Acetone, Methanol, 5mins each ultrasonic. Water rinse. N_2 blow dry.
2		Spin S1828 - Back Side - 3krpm - 30s. Bake 90°C oven - 30min.
3		Ash - Front Side - 100W - 5min
4		Spin S1818 - Front Side - 4krpm - 30s. Bake 90°C oven 30min.
5		MA6 - Mask RYL0010 - 5 seconds. *Align e-beam markers to flat* *Booking Details:*
6		Develop - 1:1 microposit:water - 75s. RO water rinse.
7		Optical Inspection - *Ensure all pyramids are present*
8		Postbake - 120C Oven - 20 minutes
9	Nitride Dry Etch	BP80 - C2F6 - 5min - 20sccm - 23mT - 100W to etch SiO2/SiN. *Booking Details:*
10		Strip Resist - Acetone - 5 mins ultrasonic - IPA rinse.
11		RIE80+ Ash - O2 - 5mins - 100W - 50mT - 50sccm *Booking Details:*

#		Process Steps
12	1st Wet Etch	HF Dip - 20:1 RO:HF - 3mins to de-oxidise wafer. Wet etch - 618.9g KOH + 1.5L H2O, take 1.6L and + 400ml IPA stirred @ 55°C, etch 1hr then calibrate. Sulphuric rinse ~5:1 H2O:Sulphiric Acid - 1min - H2O rinse.
13		Optical Inspection - Look at surface, pyramid top, base, etch depth. *Record results:*
14	Send	Slilcon Nitride Etch - 5:1 RO:HF - 50min. Rinse in H2O. Package up & send to Chalmers for 400nm LPCVD low stress SiN.
15	Back-Side Photolithography	H2O rinse. Spin - Front Side (Pyramids) - AZ4562 - 3krpm - 30s - to protect this side. Bake - 90°C - 30min.
16		Spin - Back Side - S1818 - 4krpm - 30s. Bake - 90°C - 30min.
17		MA6 - Using BSA, align circle markers on back etch mask RYL0012 to etched circles on pyramid side of substrate, expose 5s.
18		Development - 1:1 microposit:RO - 75s. RO rinse. Inspect.
19		Optical Inspection - *Record results:*
20		Post bake - 20min - 120°C Oven

#		Process Steps
21	Back- Side SiN Etch	BP80 - C2F6 - 20 sccm - 100W - 23mT - 27min to etch through SiN. *Booking details:*
22		Strip resist in acetone 5min ultrasonic, IPA rinse.
23		Ash - Gala - 80W - 5min.
24	BS wet	HF Dip - 20:1 H2O:48% HF 3min. Wet etch - 618.9g KOH + 1.5L H2O - 105°C, etch 75min (320um). Neutralise - 4:1 H2O:Sulphuric rinse 1min, H2O rinse. Inspect, measure depth. Optical Inspection - Measure the etch
25	E-beam cantilever definition	Ash - Gala - 80W - 2min.
26		Spin - 8% 2010 - 2500rpm - 30s. Oven bake - 180°C - 15min. Spin - 4% 2041 - 2500rpm - 30s. Oven bake - 180°C - 15min. Float coat 1.5% 2041. Oven bake - 180°C - 30min.
27		Cantilever Definition ebeam job (RYL0114)
28		Development - 2.5:1 - 23°C - 1min. IPA rinse. Inspect.
29		Ash - 30s - 80W. Evaporate 75nm NiCr in Plassys II. Lift-off. No ultrasonic.
30		SEM inspection - make sure tips are not tagged.

#		Process Steps
31	Photolith Cantilevers	Ash - 100W - 5mins
32		Dehydration Bake - Oven 180 - 30 mins / hotplate 180 - 5mins
33		Spin AZ4562 - Allow to cool for a few minutes before spinning. Apply 80/20 and wait 20s. Spin @ 3k, 30s. Wait a further 20s. Apply AZ4562 - same spin parameters
34		Solvent Loss Time - Wait 30 mins.
35		Hotplate Bake - 15mins - 102C
36		Second AZ Spin - Same parameters as before. Repeat the same solvent loss and hotplate bake.
37		Delay rehydration - 60mins - after 2nd softbake
38		MA6 - Align and expose. 6x (10s exposure, 60s wait)
39		Development 1:4 AZ400K developer:H20 for 4mins, changing to fresh developer after 2mins. Water Rinse - 5 mins. N2 Dry.
40		Hardbake - 120C oven 20 minutes
41		Optical Inspection/Dektak: Make sure the resist is properly covering the bars, and has been developed away appropriately.

#		Process Steps
42	Etch Cantilevers	RIE80+ Interferometer Etch CHF3/O2, 50/5sccm - 55mT -150W. After level out give 150% over etch (approx 24min). Inspect to ensure etched through at tip.
43		Resist Strip - Warm acetone 15min - IPA rinse. Ash - 7min - 120W. Inspect to ensure resist is fully removed. No ultrasonic.
44		Chrome Etch - Warm - 10min. H2O rinse. Inspect.
45		Short Wet Etch - Etch in 7m KOH (61.9g KOH in 150ml H2O) 9min - fresh solution, use hot. Thorough RO rinse. Inspect - undercut should be visible. Nanostrip - 15min. Thorough rinse H2O. Ash - full power - 10min.
46	Base Resistors	Spin 8% 2010 - 2500rpm - 30s. Clean back. Oven bake 180°C - 15min. Spin 4% 2041 - 2500rpm - 30s. Clean back. Oven bake 180°C - 15min. Float coat 1.5% 2041 Oven bake 180°C -
47		Base resistors e-beam job (RYL0015)
48		Develop - 1:1 - 23°C - 30s. IPA rinse. Inspect.
49		Ash 30s 80W. Evaporate 33nm NiCr 5nm Pd in Plassys IV. Lift-off. No ultrasonic. SEM inspection.

#		Process Steps
50	Tip Resistors	Clean, ash, Spin 8% 2010 - 2500rpm - 30s. Clean back. Oven bake 180°C - 15min. Spin 4% 2041 - 2500rpm - 30s. Clean back. Oven bake 180°C - 15min.
51		Tip Resistors e-beam job (RKR0131)
52		Develop 1:1 - 23°C - 30s. IPA rinse. Inspect.
53		Ash - 30s - 80W. Evaporate 5nm NiCr - 40nm Pd - Plassys IV. Lift-off. No ultrasonic. SEM inspection.
54	Pads	Clean, ash, Spin 8% 2010 - 2500rpm - 30s. Clean back. Oven bake 180°C - 15min. Spin 4% 2041 - 2500rpm - 30s. Clean back. Oven bake 180°C - 15min.
55		Pads ebeam job
56		Develop 1:1 - 23°C - 30s. IPA rinse. Inspect.
57		Ash - 30s - 80W. Evaporate - 5nm NiCr - 145nm Au - Plassys II. Lift-off. No ultrasonic. SEM inspection. Test a few electrically. Should be approx. 310-380Ω. Barrel ash 10min 80W before release.
58	Release	Wet Etch - Kit 2- 1.4L TMAH + 350ml IPA 80°C etch through until centre probe floats away (60-90mins) then etch for further 50-100%. Total time around Remove wafer carefully, and rinse well carefully. Blow dry
59		Inspect & measure probes electrically. Resistivity should have increased slightly ~20Ω. Cleave wafer into individual probes.

Appendix B

3ω Theory

B.1 Derivation

The probe is driven with AC current of the form;

$$I(t) = I_0 cos(\omega t) \tag{B.1}$$

For purely resistive materials (no reactance), all of the electrical power is dissipated as heat.

$$P = Q = I^2 R_0 \tag{B.2}$$

where R_0 denotes the electrical resistance of the probe at room temperature.

Solving Equation B.2 demonstrates that the heat flux created through Joule heating has a 2ω dependence;

$$Q(t) = R_0 \cdot \frac{I_0^2}{2} \left(1 + \cos\left(2\omega t\right)\right) \tag{B.3}$$

The probe temperature as a function of time can be described by the sum of steady state and transient components;

$$T_p(t) = T_{ss}(t) + T_{2\omega}cos(2\omega t + \sigma) \tag{B.4}$$

where $T_p(t)$ is the probe temperature, $T_{ss}(t)$ is the steady state component of probe temperature and $T_{2\omega}$ is the 2nd harmonic temperature amplitude. We introduce σ to account for any phase difference between electrical and thermal signals. T_{ss} accounts for any DC bias, and the contributions from ambient temperature drift - both of which may vary over the duration of a scan.

The probe signal is then the product of the input current and its time-varying resistance. Recall that under self-heating conditions, the resistance of the probe is dependent upon its temperature. Therefore;

$$V_p\left(t\right) = I\left(t\right) R\left(T\left(t\right)\right) \tag{B.5}$$

$$V_p = R_0\left(1 + \alpha T_{SS}\right) I_0 cos\left(\omega t\right) + \frac{R_0 \alpha I_0 T_{2\omega}}{2} cos\left(\omega t + \sigma\right) + \frac{R_0 \alpha I_0 T_{2\omega}}{2} cos\left(3\omega t + \sigma\right) \tag{B.6}$$

Of the three terms of this sum, two depend upon ω, whilst the final depends on 3ω. Note the presence of the steady state temperature component, T_{SS}, in the first term. Therefore, the 1ω signal includes both electrical and thermal components. Conversely, the third harmonic of this voltage contains solely information on the thermal signal.

In 3ω Active mode SThM, we use a lock-in amplifier to measure the amplitude of this third harmonic in the voltage signal. By doing so, we monitor changes in the amplitude of the Joule-heated temperature only. This isolates the measurement from any thermal or electrical drift, since only abstraction of heat at the source frequency ω is accounted for.

Appendix C

Thermal Conductivity of samples in the Quantiheat set

The thermal conductivity of the materials provided was measured by LNE, the 'Laboratoire National de Métrologie et d'Essais', a French National Metrology Institute (NMI). The measurement is an indirect one, based upon three distinct measurements of thermal diffusivity, specific heat, and density. The thermal conductivity is then given by;

$$k = ac_p\rho \tag{C.1}$$

where

- a is the thermal diffusivity as measured using the laser flash method [238]
- c_p is the specific heat, as measured with a differential scanning calorimeter [239]
- ρ is the density, as measured with the Archimedean immersion method.

The uncertainty of the calculated thermal conductivity measurement was reported as 5%.

The following table presents the materials which comprised the Quantiheat active calibration set, alongside their thermal conductivities.

Material	**Thermal conductivity (**$\mathrm{W\,m^{-1}\,K^{-1}}$**)**
PMMA	0.187
POMC	0.329
SiO_2	1.28
Al_2O_3	29.8
$Si\,n^{++}$	71.2
$Si\,p^{++}$	93.4
Ge	60
Ge Sb	60
TiO_2	12.52
CaF_2	9.17
ZrO_2	3
Glass	1.14

TABLE C.1: Thermal conductivities of the Quantiheat sample set

Appendix D

Calculating the resistance of the sensor in four terminal probes, using measurements across all combinations of terminals

Four terminal resistance measurements are typically performed using a four terminal probe - station. In this configuration, two probes are used to supply current to the probe, while the other two measure voltage drop between them, Note that no current flows through the voltage terminals, since they present extremely high impedance. In the case that a four terminal measurement system is not available, it is still possible to calculate the resistance across the sensor using only a two terminal standard ohmmeter. In Figure D.1 we present a simplified representation of the probe's resistive network.

There are six unique pairs of connections between the four probes. The resistance measured between them is the series sum of whichever resistors R_1 through R_S comprise the connection between terminals.

For example, the resistance measured between terminals 1 and 4 is given by;

$$1 \rightarrow 4 = R_1 + R_S + R_4 \tag{D.1}$$

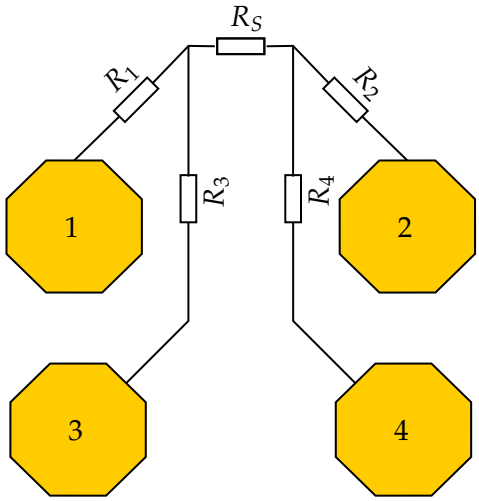

FIGURE D.1: Circuit diagram denoting the four pads and leads which connect to the probe's sensing resistor.

The full set of measurement results for all terminal combinations may be solved as a system of simultaneous equations. In matrix form;

$$\mathbf{Ax} = \mathbf{b} \tag{D.2}$$

Where **A** is a design matrix of binary values indicating which resistances comprise a given pair of terminals, x is a vector representing each of the individual resistors and b is a vector representing each of the possible terminal combinations;

$$\begin{bmatrix} 1 & 1 & 0 & 0 & 1 \\ 1 & 0 & 1 & 0 & 0 \\ 1 & 0 & 0 & 1 & 1 \\ 0 & 1 & 1 & 0 & 1 \\ 0 & 1 & 0 & 1 & 0 \\ 0 & 0 & 1 & 1 & 1 \end{bmatrix} \begin{bmatrix} R_1 \\ R_2 \\ R_3 \\ R_4 \\ R_S \end{bmatrix} = \begin{bmatrix} 1 \rightarrow 2 \\ 1 \rightarrow 3 \\ 1 \rightarrow 4 \\ 2 \rightarrow 3 \\ 2 \rightarrow 4 \\ 3 \rightarrow 4 \end{bmatrix} \tag{D.3}$$

Solving for **x** yields an array of resistances representing the four leads and the sensor. Note that the solution requires calculating the pseudo-inverse of **A** , since it is not square.

The fact that the lead resistances are also reported is useful, as it may give an idea of the degree of accuracy with which the sensor was aligned to the cantilever. For example, if $R_1 < R_2$, it might indicate that the resistor is narrower on lead 2 and that there was a misalignment in the $+x$ direction. This conclusion is reasonably valid when probes in the same writing cell are experience resistance imbalances of the same kind, since they are all written using the same alignment operation. If an individual probe experiences such an imbalance, other causes such as contamination or poor adhesion should be considered first.

Note that an auto-ranging ohmmeter should not be used for measuring probe resistances as it is highly likely that they will provide a probe which exceeds the maximum of the probe.

Appendix E

Joule Heating Calculation for Cantilever Modelling Program

E.1 Theory

As current travels through the metal layers of the probe, Joule heating occurs. When considering purely resistive materials (no reactance), it is reasonable to assume 100% of the generated electrical power is dissipated as heat. For a simple estimate of the probe power, $P = I^2R$ may be used, however this is not appropriate for the distributed model. Instead, we require an array of elemental heat generation magnitudes which can be used with our thermal resistance matrix to calculate the temperature distribution.

E.2 Derivation

Starting from the Joule-Lenz law;

$$Q(x) = P(x) = I^2R(x) \tag{E.1}$$

The above can also be stated in terms of the current density and metal resistivity;

$$Q(x) = P(x) = j(x)^2\rho \tag{E.2}$$

Where j denotes the current density, and is the quotient of current and conductor cross-section in the direction of current flow, A. ρ denotes the electrical resistivity of the metal, and is related to its resistance through the equation;

$$R(x) = \frac{\rho L(x)}{A(x)} \tag{E.3}$$

For much of the probe, the current flow occurs parallel to the x direction. In such cases, we begin by calculating the resistance of the element using Equation E.3;

$$R(x) = \frac{\rho dx(x)}{w(x)t(x)} \tag{E.4}$$

In which L is replaced by $dx(x)$ - the sampling length, and the cross section of an element is given by its x-dependent width and thickness. Although metal layers are deposited uniformly, we must still consider the case in which the metal is deposited on the pyramid slope. Here, the thickness of the metal in the direction of current flow is reduced when compared with its nominal thickness as the following;

$$t_{slope} = t\cos(46.5^\circ) \tag{E.5}$$

Where 46.5° is the angle between the {313} planes of the pyramid and a (100) surface plane.

The sample width, $dx(x)$ contains an x dependence, which arises due to differences between the writing plane and the projection plane when defining features on an angled surface. This situation occurs on the pyramid sidewalls, whose position is fixed at $139\mu m$, so a simple trigonometric correction can be applied to all samples in which $dx \times [n] >= 139\mu m$.

E.2.1 Correcting for off-axis current angle

The tip of the probe features a Palladium resistive element which follows the outer edge of the taper. As such, it lies off the x-axis. The widths of all materials in this model considers the vertical (y) extent. This value differs from the 'width' of the Pd

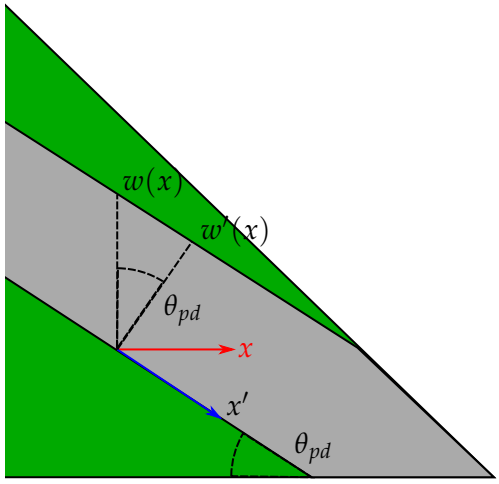

FIGURE E.1: Schematic demonstrating the difference between the width of the Pd sensor in the relative to the x axis and relative to the x' axis, which is the direction of current flow

wire in the direction of current flow. A correction must be performed to correctly handle those regions for which this is the case:

$$w'(x) = w(x)sin(\theta_{Pd}) \tag{E.6}$$

In which w' is the width in the direction of current flow (normal to x' axis), w is the initial, vertical width provided by the model's fracturing routine. θ_{Pd} denotes the angle between the x and x' dimensions. It is 34° degrees (as shown in Figure 4.19) for the commercial KNT probe, and 45° for the novel probes described in this work. In the source code, this operation is handled by the function `transform_heater()`

There is an additional problem when considering that the resistor 'turns a corner' at the very tip. This problem is particularly evident given that we consider only one half of the probe due to the axis of symmetry along its length. Correct treatment of this problem is non-trivial. If naively handled, the reduction in sensor width that occurs in the final microns of the probe would result in an increased power generation, which is clearly unphysical. There is no restriction in current in this region, it is simply turning the corner which is not present because we have only simulated one half of the symmetrical probe.

As such, we have adopted a strategy in which we calculate the volumetric power

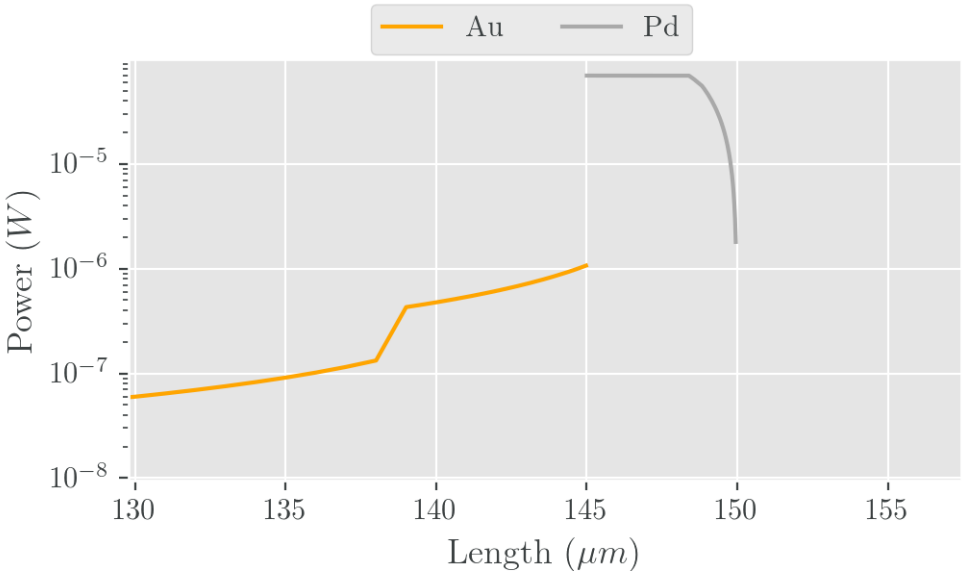

FIGURE E.2: The elemental power generation of the Gold and Palladium layers as a function of position for the final 11 µm of the cantilever (the tilted 'beak' section). Note the reduction in power generation at the end of the probe due to the reduction in Pd area.

generation and scale to element area. This assumes uniform power generation across the entire sensor, which we believe to be a more appropriate treatment. With the scaling strategy applied, the power generation per unit area is independent of this tapering. In fact, the reduction in area towards the apex yields a reduction in power generation that mimics what would occur at a bend in a conductive wire due to current crowding [240]. This may be seen in Figure E.2, which is a magnification of the general power plot presented in Figure 4.24, Section 4.7.3. Note that the increased current at that would occur at the concave edge has not been implemented in this model.

The power density scaling method requires that a fixed width sensor be used in the design. This requirement is fulfilled by the commercial probe, and has been fulfilled in all the novel probes presented in this work. This fixed width (in the x' direction) is found automatically by the mode of the w' array. We use γ to represent the fixed width which is used throughout the following equations. The method is most easily understood by starting from volumetric power density. For clarity, we will omit elemental notation and trigonometric corrections.

$$Q = j^2\rho \tag{E.7}$$

$$j = \frac{I}{\gamma t} \tag{E.8}$$

$$R = \frac{\rho L}{A}, \quad \rho = \frac{RA}{L} = \frac{R\gamma t}{dx} \tag{E.9}$$

Substituting in ρ to Equation E.7 and reducing;

$$Q = \frac{I^2 R}{\gamma t dx} \tag{E.10}$$

Which is clearly power per meter cubed. Multiplying through by the dimensions of the element, $(t \times w(x) \times dx)$, gives the power per element which is our desired value;

$$Q(x) = I^2 R(x) \frac{w(x)}{\gamma} \tag{E.11}$$

We arrive back to $Q = I^2 R$, but with a scaling factor of $\frac{w'(x)}{\gamma}$. Note that $w(x)$ will only ever equal, or be less than γ, resulting in power reduction at the apex rather than a power increase due to reduced width. An additional benefit of this calculation is that it yields the electrical resistance of the sensor through the summation of the $R(x)$ array. This is a useful number to know when designing new probes, giving an idea of the sensitivity of circuitry that would be required to interface with such a probe.

Appendix F

Failure mechanisms of four terminal cutout probes

F.1 Beam breaks

Name	Beam breakages
Figure reference	6.34A
Description	The beams at the cantilever apex are either broken, buckled, or have snapped off completely
Suspected Cause	Unclear. Must be something that occurs during/after release. Perhaps surface tension related. Perhaps N2 gun, or stress within the metal?
Probes affected	Cut-outs only
Severity	High. Probe cannot be used
Frequency	Low. 5 out of a half wafer
Avoidance	Needs investigation into the cause. Gentle wafer handling and care when submerging/removing wafer from liquids

F.2 Au adhesion

Name	**Poor gold adhesion**
Figure reference	6.34B
Description	The Gold has failed to adhere to the substrate in the region connecting the leads to the sensor. Au wires appear to have 'slid' to one side or another, causing an open circuit.
Suspected Cause	Cantilever contamination prior to gold deposition. Perhaps also because the Gold wires run partially up the 'beak' of the cantilever but not very far.
Probes affected	Both, but more frequently observed on non-cut-outs
Severity	High. If electrical continuity is broken, the probe cannot be used to perform thermal measurements.
Frequency	Low/medium 7 in a half wafer
Avoidance	High power ashing before resist coating, review the de-scum ash that is performed immediately prior to Gold deposition.

F.3 Au lift-off

Name	Poor Gold lift-off
Figure reference	6.34C
Description	The Gold film in-between the pairs of leads leading to the tip has failed to lift-off properly and appears to be connected to the edge of the cut-out. Appears to be related to the platinum de-lamination defect discussed below
Suspected Cause	Unclear. Perhaps the undercut etch was not deep enough in these regions. The Au inside the cutout should be deposited on the Si substrate, but that region is covered in resist.
Probes affected	Cut-outs only
Severity	High.
Frequency	Low. Two instances in all probes inspected.
Avoidance	Perhaps exposing resist in this region so this chunk of gold can be deposited on Si would be beneficial.

F.4 Platinum delamination

Name	**Platinum Delamination**
Figure reference	6.35A
Description	Platinum peeling off the SiN tip. May be related to the Au lift-off defect outlined above
Suspected Cause	As in Table F.3
Probes affected	As in Table F.3
Severity	As in Table F.3
Frequency	As in Table F.3
Avoidance	As in Table F.3

F.5 Lift-off failure cantilever

Name	**Lift-off failure of cantilever hard-mask**
Figure reference	6.35B
Description	The rhombuses which should be free space in the cut-out designs are instead occupied by SiN. Poor lift-off in cantilever definition has transferred all the way through the process
Suspected Cause	Insufficient soaking/agitation in the lift-off process of defining the cantilever hard-mask .Can be observed early on in the process. Cantilevers may be easily re-defined if the frequency of this defect is too high.
Probes affected	Cut-outs only. Typically size 3 and 4 where the side lobes are smaller.
Severity	Medium. This defect was not observed in the central region which defines the width of the sensor. See Figure 6.32 for an example of a non-critical failure of this type
Frequency	Low. 4 in a half wafer
Avoidance	A re-assessment of the cut-out shape may help. More agitation may help, but there are risks associated with this which were outlined in Section 6.2.3.

F.6 Skirt re-deposition

Name	**Lift-off failure of cantilever hard-mask**
Figure reference	6.35C
Description	Metal strands (curls, shavings) are deposited on the cantilever apex. On the cut-out probes, metal strands wrap around the released beams. The strands are the metal 'skirts'/overlaps which were employed for self alignment.
Suspected Cause	This defect was not observed on the initial cut-outs design. May be caused due to narrower overlap ($300nm$ vs $1\mu m$) lowering the probability that the strips will properly adhere to the Si substrate. May be caused by the lack of the lift-off enhancing structure (which can be seen in Figure 6.7), which was on oversight in this design. It may also be undercut etch depth related. If the metal film is not completely discontinuous then the skirt will be unlikely to float away.
Probes affected	Cut-outs predominantly. Looks worst on C1 type probes with the long, narrow beams. Small curls have also been observed on N type probes, but with reduced frequency.
Severity	Variable/ unclear. It depends on the location of the re-deposition. Metal shavings may short between terminals, which would be a critical failure. They may protrude and cause an incorrect contact. Others appear to be purely cosmetic however; see Figure 6.36
Frequency	Medium. 10 - 15 per half wafer.
Avoidance	It may be that a large Pd region outwith the cantilever region would give the metal strands something to curl around other than the beams of the cutout probes. A deeper undercut etch may also help ensure the film is discontinuous between Si substrate and SiN beam.

Appendix G

Spray Coating

G.1 Present Resist Technologies

A key technology in our group is the ability to pattern metal features onto AFM tips using EBL, which has allowed for the creation of many novel functionalised AFM probes. Such patterning is not possible using the typical resist application of spin coating due to the significant topography of the substrate. Fluid dynamics and surface tension dictate the profile of the film, which was previously presented in Figure 3.9. Resist build-up at the foot of raised features will require greater dosing or development to clear out written features, which imposes a limit on the minimum line-width attainable in these locations. Thinning at raised edges means that if these substrates were to be metallised, the exposed pyramid apices would be 'capped' with metal - a critical failure.

We overcome the problem of discontinuous coverage by employing the float coating technique [160] (described in the main text in Section 3.6, Figure 3.10). We supplement traditional spin-on deposition with this method, using it to drape an additional thin film over any raised features.

G.2 Issues with float coating

Although capable of mitigating some of the issues with spin-on deposition, float coated resist films typically features defects such as wrinkling an tearing, as highlighted in Figure A.3. Tearing occurs infrequently enough to be tolerable, whereas

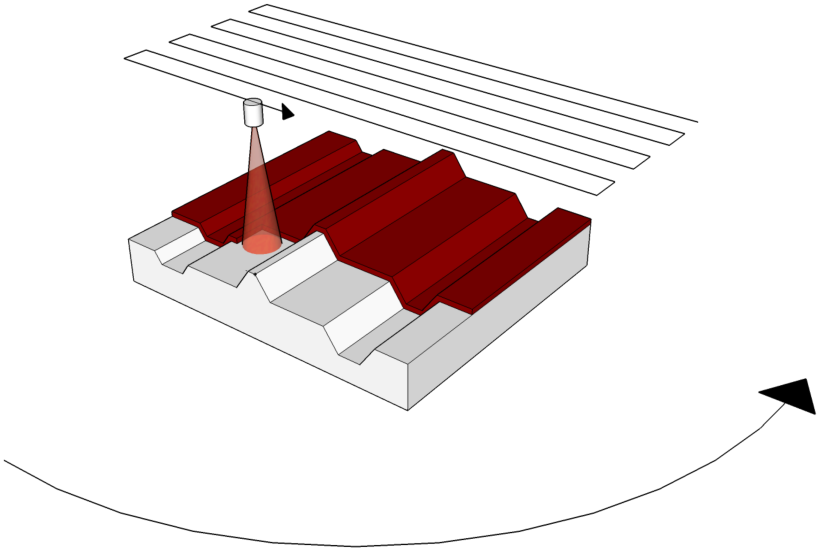

FIGURE G.1: Schematic of a spray coating operation. The sample is loaded onto the stage and held in place by vacuum. A motorized sled raster scans the nozzle across the sample surface whilst spraying the resist-solvent mixture. The extent of the scan is greater than that of the wafer to ensure good coverage of the edges. A single pass will likely result in periodic thickness variation, so the wafer can be raised and rotated before starting a subsequent pass. The stage incorporates a programmable heater to adjust the rate of local re-flow.

wrinkling poses a more serious limitation. Local thickness variations of three times the nominal value require significant overdosing to ensure feature clearance. As above, this condition restricts minimum attainable line-width.

G.3 Introducing Spray Coating

Spray coating offers an alternative method of resist deposition. The fundamentals of this process are highlighted in Figure G.1. Since the resist is applied from above, this technique can offer better coverage of topographic features. The nozzle ejects an aerosol consisting of Nitrogen gas, resist polymer and solvents. The correct selection of solvents is important, and should include both a high and low volatility solvent[130]. The former is required to reduce the viscosity of the resist and allow for atomisation. Most of this is evaporated before reaching the sample surface. The latter is required to facilitate local re-flow of the resist on the substrate and prevent simply 'powder-coating' the sample.

Historically, spray coating has only been used for photoresists, however we identify

TABLE G.1: Spray Coated E-beam Resist Recipe

Material	Category	Boiling Point	Volume Ratio
12% 50K PMMA	Resist	N/A	1.00
Acetone	High Volatility Solvent	56C	18.48
Anisole	Low Volatility Solvent	154C	14.56

TABLE G.2: Spray Coater Parameters

Parameter	Description	Units	Notes
N2 Flow	Nitrogen flow rate	l/min	40 l/min maximum
Resist Solution Flow	High Volatility Solvent	l/min	
Stage Temperature	Low Volatility Solvent	C	20C to 80C
Slew Rate	Speed of sled travel	mm/s	
Pitch	Pitch of the raster scan	mm	Minimum 0.1mm
Passes	Number of repetitions of the raster	N/A	90 degree rotation between passes

it as a potential alternative to float coating if a suitable recipe for e-beam resist can be found. This has not been widely attempted, evidenced by the presence of just one paper in the literature[241].

G.4 Challenges

The machine manufacturers do not support e-beam resist coating, and there are no appropriate resists on the market for purchase. Therefore, we have developed a recipe of our own. We were unable to acquire the exact chemicals used in Linden et. al[241], however their work has been invaluable in informing the correct ratios of solvents. Our recipe is presented in Table G.1.

In addition to developing the resist dilution, considerable effort has been invested in finding the optimal parameters for the machine's numerous deposition options. These are summarised in Table G.2.

Preliminary testing on resist dilution and coater parameters will not be reported here. Many early results could be judged by eye alone. Beyond this point, stylus profilometry and optical microscopy were used.

For stylus profilometry, we introduce a scratch in the resist with a soft tool to ensure no damage to the substrate. Scanning the profiler tip over this scratch gives a flat plane with which to perform tilt correction, and gives a measure of the step height (resist thickness). The scratch prevails after baking, allowing comparison between

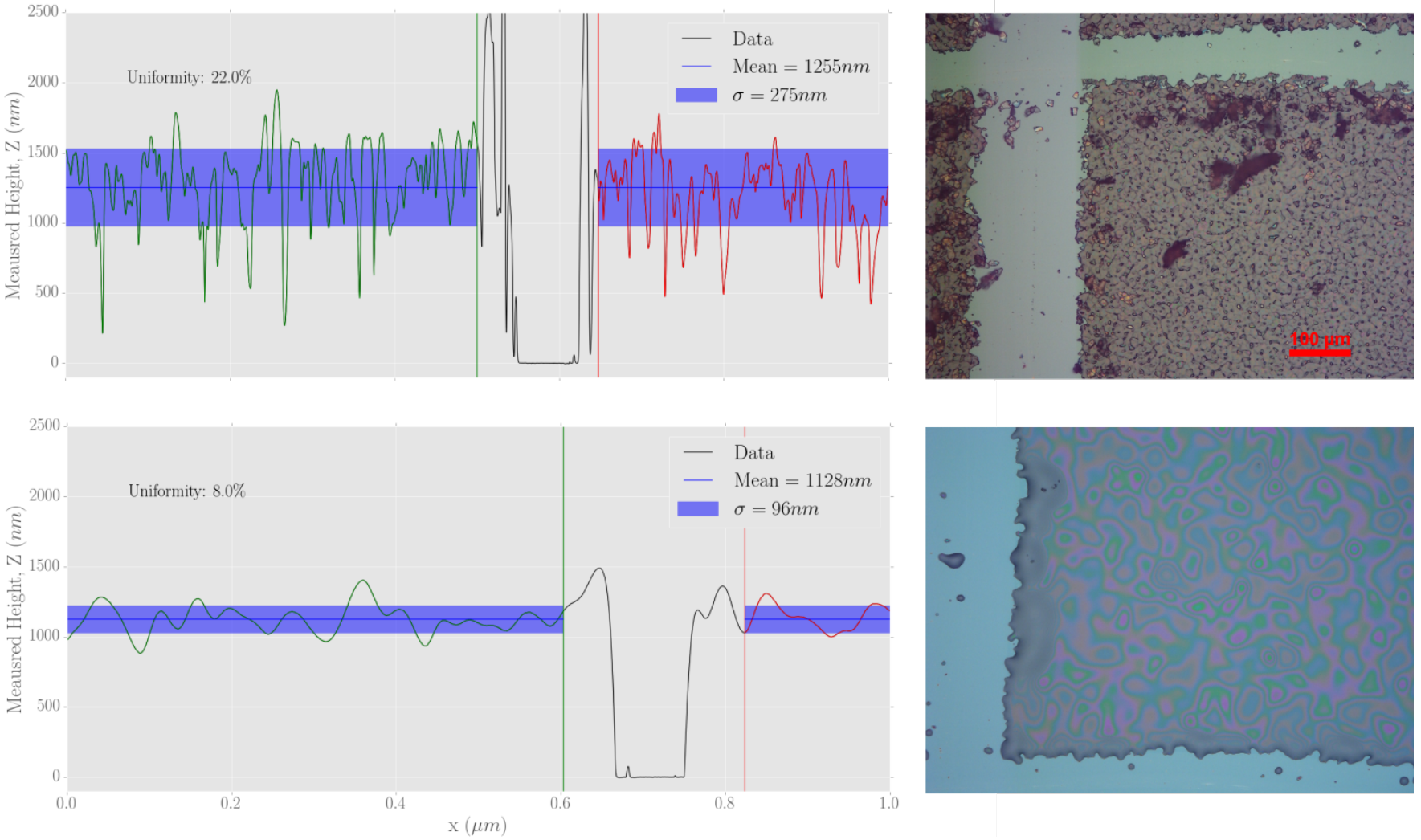

FIGURE G.2: Comparison of a spray coated wafer before and after baking. The as deposited film (above) is highly porous and non-uniform After 30 minutes of baking in a 180C oven, homogeneity is increased (below). The stylus traces are analysed with a custom program. The red and green marker lines can be manually moved to exclude the location of the scratch from the calculation. Note that either side of the scratch there is typically some resist build up, so it is not sufficient to average any non-zero heights. The average and standard deviation is used to report the uniformity, in which 0% represents perfect uniformity. Although the baked film is smooth and continuous, it is double the required thickness.

baked and as-deposited films. An example result is presented in Figure G.2. This particular example has thickness of around 1um, about double the desired amount. When working with films of more appropriate thickness, we observe some porosity, even after baking. The stylus profilometer reports only a line trace, so occasionally misses such defects, especially if they are low density. Additionally, the 2.5um tip radius may prove too large to accurately image small holes.

On such samples, we employ image analysis using ImageJ. Pixel thresholding is used to identify areas of the image in which the substrate is exposed. The sum of these pixels can be reported as a figure of percentage coverage. Alternatively, the thresholded image can be processed using the cell counting algorithm to count pores of a particular size or shape. This processing is used in the production of Figures G.3.

G.5 Results

Preliminary experiments identified two figures of merit. We introduce first - the volume coefficient, and demonstrate the linear dependence between this and the deposited film thickness (Figure G.4 (right), Equation G.1);

$$\text{Volume coefficient} = \frac{\text{Resist Flow Rate} \times \text{Number of Passes}}{\text{Pitch} \times \text{Slew Rate}} \tag{G.1}$$

The linear dependence of average thickness upon volume coefficient holds true regardless of any individual parameters. However, it gives no information on the roughness or coverage of the film. Although this is dependent on many different parameters, we focus on one of particular interest, which we have named the flow ratio. This is the ratio between gaseous and aqueous material from the nozzle, which is a measure of the pressure of the system. It has been noted that this will effect the particle size of droplets in the aerosol [129].

Figure G.3 demonstrates the effect of increased Nitrogen flow on wafer coverage and porosity. These data are used to derive a power law dependence of wafer coverage and flow ratio (Figure G.4, left). This fit highlights that complete coverage of the wafer is highly unlikely, even at the machine's maximum flow ratio of 420. However,

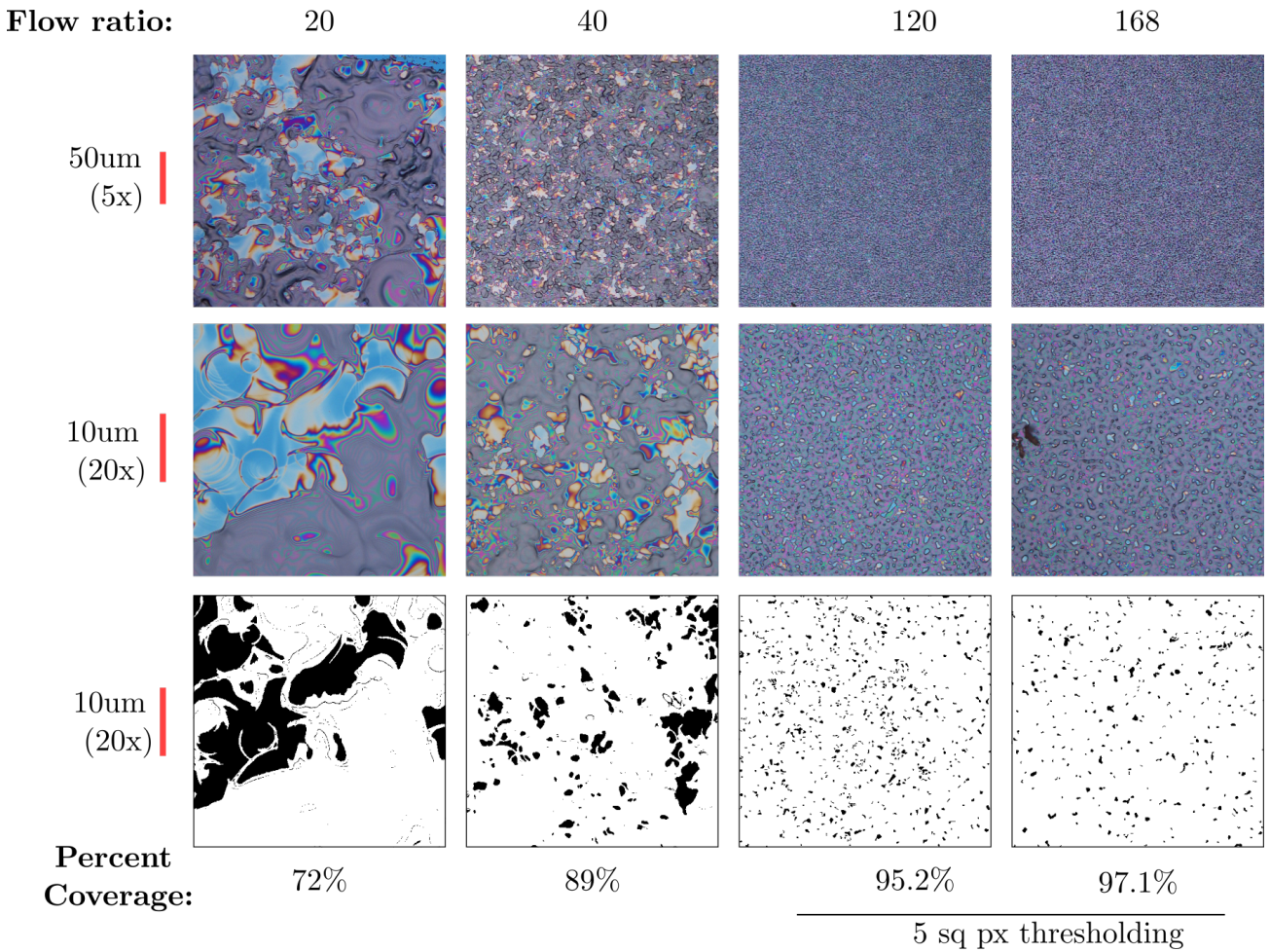

FIGURE G.3: Pore analysis of a number of as-deposited films. Each column represents a film deposited with a different flow ratio. The higher the flow ratio of Nitrogen to resist, the better the coverage. This is calculated with ImageJ thresholding, and a mask is produced for easier comparison.

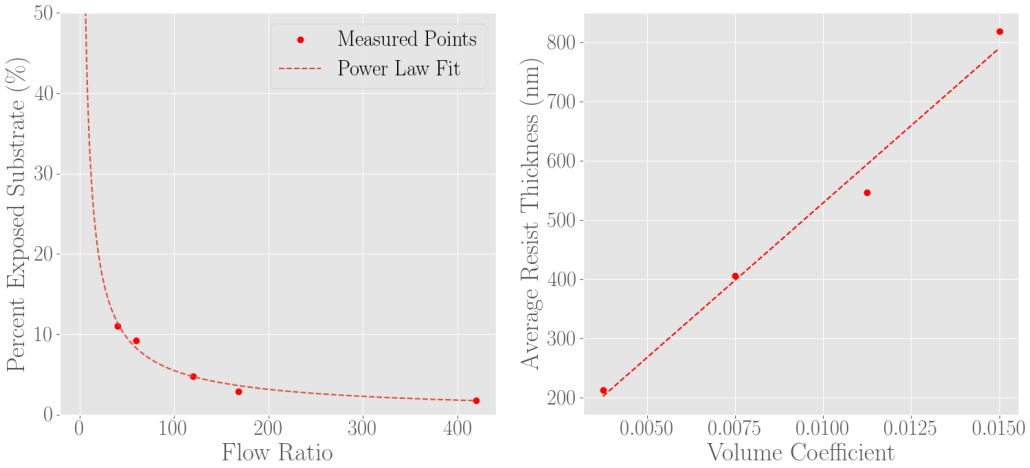

FIGURE G.4: Left: Increasing the 'flow ratio' of Nitrogen to resist improves wafer coverage. Right: Average resist thickness as a function of Volume Coefficient.

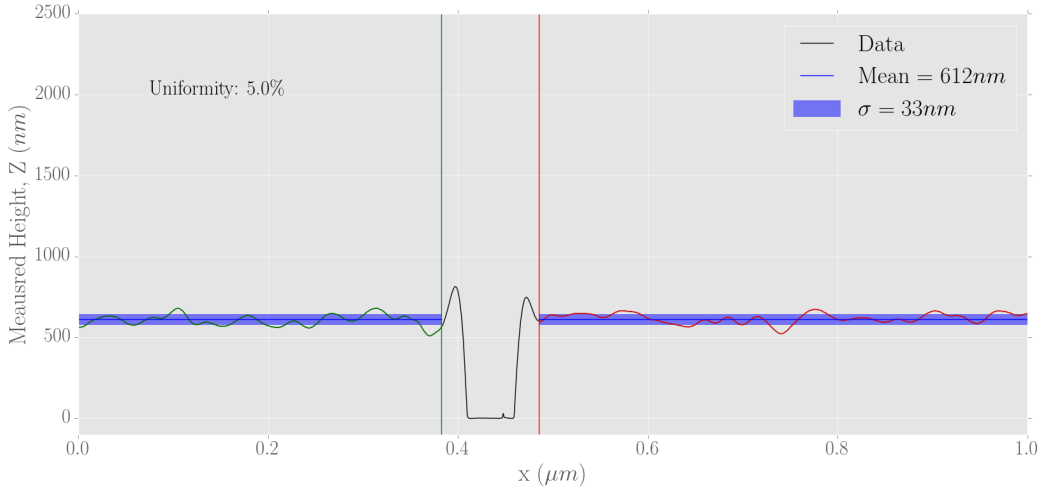

FIGURE G.5: Stylus profilometer trace across a scratch in a spray coated resist film

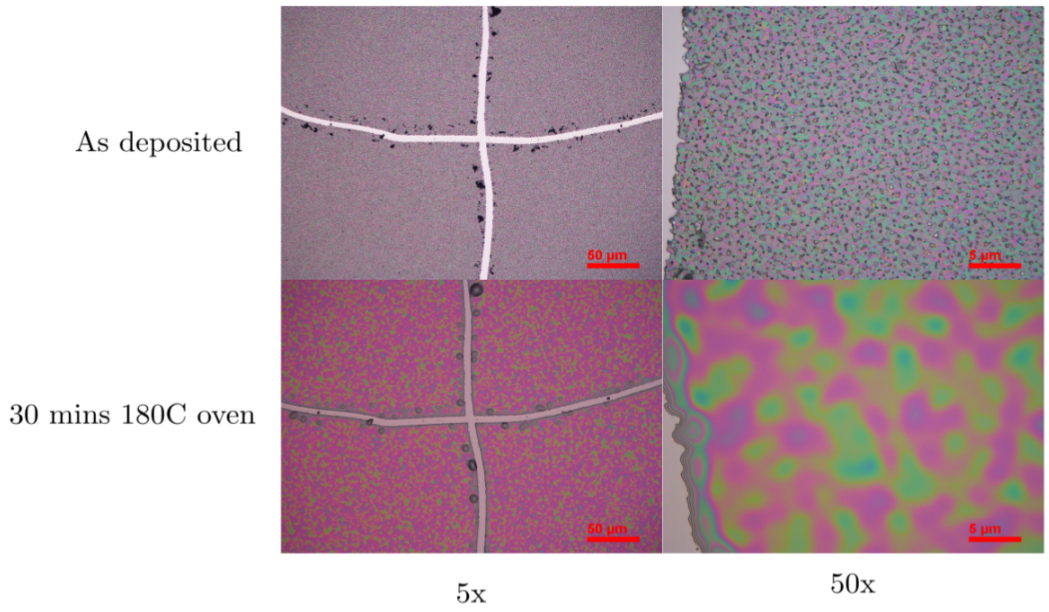

FIGURE G.6: Image gallery comparing a thin, nearly continuous PMMA film before and after baking. The resist has been scraped off in the x and y directions to expose the surface and allow for measuring the film thickness and levelling of the profilometer data. Before baking, there are some 'pores' present in the resist which appear to have re-flowed away after 30 minutes of high temperature baking.

poor coverage at this stage can be mitigated by soft-baking, which partially re-flows the resist and drives off any residual solvent in the mixture.

Optimising the volume coefficient and flow ratio, combined with a 30 minute, 180C soft-bake produced the results presented in Figures G.5 and G.6. The substrate was flat, un-processed Si wafer. We achieved a thickness of 612 ± 33nm, representing a uniformity of 5%. Note that the best published result is 15%[241].

G.5.1 Topographic Wafers

Following promising results on flat wafers, we progressed to topographic samples. Gratings of $50\mu m$ and $10\mu m$ pitch were written across raised bars of $14\mu m$ height, at a range of doses. Metal lift-off was performed to selectively remove metal in the un-exposed areas, before inspection via SEM. The results of this experiment are presented in G.7. Although we observe sharp features and excellent definition at low magnification (Figure G.7a), we identify a critical failure at higher magnifications (Figures G.7c and G.7d). Metal has adhered to the substrate along the edge of the

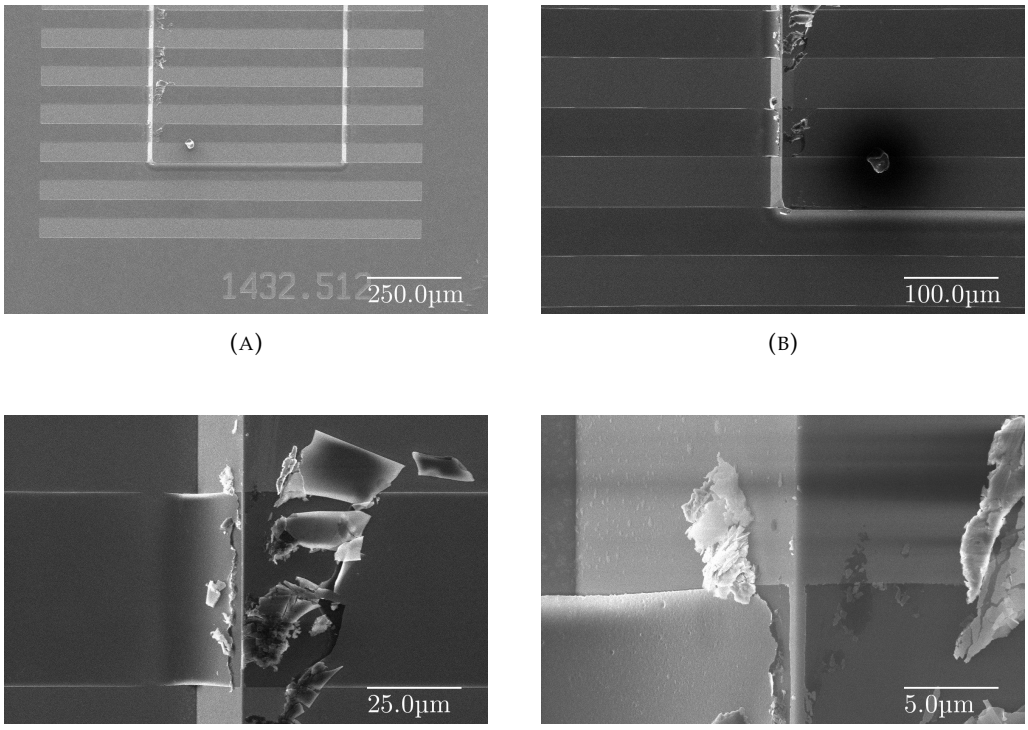

(A) (B)

(C) (D)

FIGURE G.7: SEM images of a metallised feature written in spray-coated resist, at various magnifications.

raised feature, indicating that no resist was present in this area. We propose that the resist has receded from the edge during soft-bake due to surface tension.

G.5.2 Discussion

The results presented in Figure G.7 were generated from a sample coated with optimal process parameters. At the limit of flow ratio permitted by the machine, we still observe pores in the as-deposited film. We have shown that soft-baking can mitigate this, but an overly aggressive bake has been shown to recess the film from feature edges. We have performed additional experiments to optimise the bake recipe, however it appears likely that an alteration in the resist/solvent mixture is required. We propose that the issues demonstrated here are caused by too little low volatility solvent. Increased proportions would allow for greater local re-flow of resist during deposition and reduce the required soft-baking time.

Bibliography

[1] E. S. Toberer, L. L. Baranowski, and C. Dames, "Advances in Thermal Conductivity," *Annual Review of Materials Research*, vol. 42, no. 1, pp. 179–209, 2012. DOI: 10.1146/annurev-matsci-070511-155040.

[2] W. J. Parker, R. J. Jenkins, C. P. Butler, and G. L. Abbott, "Flash Method of Determining Thermal Diffusivity, Heat Capacity, and Thermal Conductivity," *Journal of Applied Physics*, vol. 32, no. 9, pp. 1679–1684, 1961. DOI: 10.1063/1.1728417.

[3] M. Vollmer and K.-P. Möllmann, *Infrared Thermal Imaging*. Wiley and Sons, 2011. DOI: 10.1002/9783527630868.

[4] M Farzaneh, K Maize, D Lüerßen, J. A. Summers, P. M. Mayer, P. E. Raad, K. P. Pipe, A Shakouri, R. J. Ram, and J. A. Hudgings, "CCD-based thermoreflectance microscopy: principles and applications," *Journal of Physics D: Applied Physics*, vol. 42, no. 14, p. 143 001, 2009. DOI: 10.1088/0022-3727/42/14/143001.

[5] G Tessier, G Jerosolimski, S Holé, D Fournier, and C Filloy, "Measuring and predicting the thermoreflectance sensitivity as a function of wavelength on encapsulated materials," *Review of Scientific Instruments*, vol. 74, no. 1, pp. 495–499, 2003. DOI: 10.1063/1.1517153.

[6] D. G. Cahill, K. Goodson, and A. Majumdar, "Thermometry and Thermal Transport in Micro/Nanoscale Solid-State Devices and Structures," *Journal of Heat Transfer*, vol. 124, no. 2, p. 223, 2002. DOI: 10.1115/1.1454111.

[7] T. Beechem, S. Graham, S Graham, P. J. Hesketh, and B. C. Mems, "Temperature Measurement of Microdevices using Thermoreflectance and Raman Thermometry," Tech. Rep., 2008. DOI: https://doi.org/10.1007/978-0-387-46283-7_6.

[8] J. Christofferson and A. Shakouri, "Thermoreflectance based thermal microscope," *Review of Scientific Instruments*, vol. 76, no. 2, pp. 1–6, 2005. DOI: 10.1063/1.1850632.

[9] G Tessier, M.-L. Polignano, S Pavageau, C Filloy, D Fournier, F Cerutti, and I Mica, "Thermoreflectance temperature imaging of integrated circuits: calibration technique and quantitative comparison with integrated sensors and simulations," *J. Phys. D: Appl. Phys*, vol. 39, pp. 4159–4166, 2006. DOI: 10.1088/0022-3727/39/19/007.

[10] A. J. Schmidt, X. Chen, and G. Chen, "Pulse accumulation, radial heat conduction, and anisotropic thermal conductivity in pump-probe transient thermoreflectance," *Review of Scientific Instruments*, vol. 79, no. 11, p. 114 902, 2008. DOI: 10.1063/1.3006335.

[11] P. Jiang, X. Qian, and R. Yang, "Tutorial: Time-domain thermoreflectance (TDTR) for thermal property characterization of bulk and thin film materials," 2018. DOI: 10.1063/1.5046944.

[12] A. A. Wilson, "Scanning thermal probe calibration for accurate measurement of thermal conductivity of ultrathin films," *MRS Communications*, vol. 9, no. 02, pp. 650–656, 2019. DOI: 10.1557/mrc.2019.37.

[13] J. Očenášek and J. Voldřich, "Raman thermometry: Effective temperature of the nonuniform temperature field induced by a Gaussian laser," *Journal of Applied Physics*, vol. 118, no. 23, p. 233 104, 2015. DOI: 10.1063/1.4937904.

[14] C. D. Brites, P. P. Lima, N. J. Silva, A. Millán, V. S. Amaral, F. Palacio, and L. D. Carlos, "Thermometry at the nanoscale," *Nanoscale*, vol. 4, no. 16, pp. 4799–4829, 2012. DOI: 10.1039/c2nr30663h.

[15] P. L. Rossiter, *The electrical resistivity of metals and alloys*. Cambridge University Press, 1987, p. 434.

[16] T. T. Bechtold, J. G. J. G. Korvink, and E. B. E. B. Rudnyi, "Dynamic Electrothermal simulation of microsystems," in *Fast simulation of electro-thermal MEMS : efficient dynamic compact models*, Springer, 2007, p. 180.

[17] D. M. Rowe, *CRC handbook of thermoelectrics*. CRC Press, 1995.

[18] G. P. Szakmany, A. O. Orlov, G. H. Bernstein, and W. Porod, "Single-metal nanoscale thermocouples," *IEEE Transactions on Nanotechnology*, vol. 13, no. 6, pp. 1234–1239, 2014. DOI: 10.1109/TNANO.2014.2358532.

[19] D. D. Pollock, *Thermoelectricity : theory, thermometry, tool*. ASTM, 1985, p. 295.

[20] J. Altet, S. Dilhaire, S. Volz, J.-M. Rampnoux, A. Rubio, S. Grauby, L. David, P. Lopez, W. Claeys, and J.-B. Saulnier, "Four different approaches for the measurement of IC surface temperature: application to thermal testing," Tech. Rep.

[21] J. Altet, A. Rubio, E. Schaub, S. Dilhaire, and W. Claeys, "Thermal coupling in integrated circuits: Application to thermal testing," *IEEE Journal of Solid-State Circuits*, vol. 36, no. 1, pp. 81–91, 2001. DOI: 10.1109/4.896232.

[22] D. G. Cahill, "Thermal conductivity measurement from 30 to 750 K: The 3?? method," *Review of Scientific Instruments*, vol. 61, no. 2, pp. 802–808, 1990. DOI: 10.1063/1.1141498.

[23] A Majumdar, "Scanning Thermal Microscopy," 1999.

[24] Y. Martin and H. K. Wickramasinghe, "Study of dynamic current distribution in logic circuits by Joule displacement microscopy," *Applied Physics Letters*, vol. 50, no. 3, pp. 167–168, 1987. DOI: 10.1063/1.97650.

[25] J. M. Weaver, L. M. Walpita, and H. K. Wickramasinghe, "Optical absorption microscopy and spectroscopy with nanometre resolution," *Nature*, vol. 342, no. 6251, pp. 783–785, 1989. DOI: 10.1038/342783a0.

[26] S. Gomès, A. Assy, and P. O. Chapuis, "Scanning thermal microscopy: A review," *Physica Status Solidi (A) Applications and Materials Science*, vol. 212, no. 3, pp. 477–494, 2015. DOI: 10.1002/pssa.201400360.

[27] P. D. Tovee, M. Pumarol, D. Zeze, K. Kjoller, and O. V. Kolosov, "Nanoscale spatial resolution probes for scanning thermal microscopy of solid state materials," *Journal of Applied Physics*, vol. 112, no. 11, 2012. DOI: 10.1063/1.4767923.

[28] B. Gotsmann and M. A. Lantz, "Quantized thermal transport across contacts of rough surfaces," *Nature Materials*, vol. 12, no. 1, pp. 59–65, 2012. DOI: 10.1038/nmat3460.

[29] L. Ramiandrisoa, A. Allard, Y. Joumani, B. Hay, and S. Gomès, "A dark mode in scanning thermal microscopy," *Review of Scientific Instruments*, vol. 88, no. 12, 2017. DOI: 10.1063/1.5002096.

[30] A. Majumdar, J. Lai, M. Chandrachood, O. Nakabeppu, Y. Wu, and Z. Shi, "Thermal imaging by atomic force microscopy using thermocouple cantilever probes," *Review of Scientific Instruments*, vol. 66, no. 6, pp. 3584–3592, 1995. DOI: 10.1063/1.1145474.

[31] K. Luo, Z. Shi, J. Lai, and A. Majumdar, "Nanofabrication of sensors on cantilever probe tips for scanning multiprobe microscopy," *Applied Physics Letters*, vol. 325, no. 1996, p. 325, 1995. DOI: 10.1063/1.116074.

[32] Y. Ge, Y. Zhang, J. A. Booth, J. M. Weaver, and P. S. Dobson, "Quantification of probe–sample interactions of a scanning thermal microscope using a nanofabricated calibration sample having programmable size," *Nanotechnology*, vol. 27, no. 32, p. 325 503, 2016. DOI: 10.1088/0957-4484/27/32/325503.

[33] J. Martinek, P. Klapetek, and A. C. Campbell, "Methods for topography artifacts compensation in scanning thermal microscopy," *Ultramicroscopy*, vol. 155, pp. 55–61, 2015. DOI: 10.1016/j.ultramic.2015.04.011.

[34] P. Klapetek, J. Martinek, P. Grolich, M. Valtr, and N. J. Kaur, "Graphics cards based topography artefacts simulations in Scanning Thermal Microscopy," *International Journal of Heat and Mass Transfer*, vol. 108, pp. 841–850, 2017. DOI: 10.1016/j.ijheatmasstransfer.2016.12.036.

[35] R. Lambert, "Development of Commercial Style Pop-out AFM Probes," 2014.

[36] C. D. W. Wilkinson and M Rahman, "Dry etching and sputtering," *Philosophical Transactions of the Royal Society A*, vol. 362, pp. 125–138, 2004. DOI: 10.1098/rsta.2003.1307.

[37] T. A. Schoolcraft and B. J. Garrison, "Initial Stages of Etching of the Si{100}(2Xl) Surface by 3.0-eV Normal Incident Fluorine Atoms: A Molecular Dynamics Study," Tech. Rep., 1991, pp. 8221–8228.

[38] R. A. Wind and M. A. Hines, "Macroscopic etch anisotropies and microscopic reaction mechanisms: a micromachined structure for the rapid assay of etchant anisotropy," *Surface Science*, vol. 460, no. 1-3, pp. 21–38, 2000. DOI: 10.1016/S0039-6028(00)00479-9.

[39] S. Franssila, *Introduction to Microfabrication to Microfabrication Second Edition*. Wiley, 2010, p. 518.

[40] P. J. P. J. Hesketh, G. Barna, and H. G. Hughes, *Proceedings of the Third International Symposium on Microstructures and Microfabricated Systems*. The Electrochemical Society, 1997, p. 217.

[41] G. Yan, P. C. Chan, I. M. Hsing, R. K. Sharma, J. K. Sin, and Y. Wang, "Improved TMAH Si-etching solution without attacking exposed aluminum," *Sensors and Actuators, A: Physical*, vol. 89, no. 1-2, pp. 135–141, 2001. DOI: 10.1016/S0924-4247(00)00546-X.

[42] U. Munch, N. Schneeberger, O. Paul, H. Baltes, and E. Doering, "Thin film front protection of CMOS wafers against KOH," P. J. French and K. H. Chau, Eds., vol. 3514, International Society for Optics and Photonics, 1998, pp. 124–133. DOI: 10.1117/12.323880.

[43] O. Powell, D. Sweatman, and H. B. Harrison, "The use of titanium and titanium dioxide as masks for deep silicon etching," *Smart Materials and Structures*, vol. 15, no. 1, S81–S86, 2005. DOI: 10.1088/0964-1726/15/1/013.

[44] D. P. Burt, P. S. Dobson, L. Donaldson, and J. M. Weaver, "A simple method for high yield fabrication of sharp silicon tips," *Microelectronic Engineering*, vol. 85, no. 3, pp. 625–630, 2008. DOI: 10.1016/j.mee.2007.11.010.

[45] M Elwenspoek and H. V. Jansen, *Silicon Micromachining*, ser. Cambridge Studies in Semiconductors. Cambridge University Press, 2004.

[46] M. M. Abu-Zeid, "Corner Undercutting in Anisotropically Etched Isolation Contours," *Journal of The Electrochemical Society*, vol. 131, no. 100, p. 2138, 1984. DOI: 10.1149/1.2116035.

[47] B. Tang and K. Sato, "Formation of silicon nano tips in surfactant-modified wet anisotropic etching," *Applied Physics Express*, vol. 4, no. 5, pp. 4–7, 2011. DOI: 10.1143/APEX.4.056501.

[48] C.-R. Yang, P.-Y. Chen, Y.-C. Chiou, and R.-T. Lee, "Effects of mechanical agitation and surfactant additive on silicon anisotropic etching in alkaline KOH solution," *Sensors and Actuators A*, vol. 119, pp. 263–270, 2005. DOI: 10.1016/j.sna.2004.07.015.

[49] I. Zubel, M. Kramkowska, and K. Rola, "Silicon anisotropic etching in TMAH solutions containing alcohol and surfactant additives," *Sensors and Actuators, A: Physical*, vol. 178, pp. 126–135, 2012. DOI: 10.1016/j.sna.2012.02.018.

[50] Q. Jiao, X. Tan, J. Zhu, S. Feng, and J. Gao, "Effects of ultrasonic agitation and surfactant additive on surface roughness of Si (1 1 1) crystal plane in alkaline KOH solution," *Ultrasonics Sonochemistry*, vol. 31, pp. 222–226, 2016. DOI: 10.1016/j.ultsonch.2015.12.019.

[51] I. Zubel and M. Kramkowska, "The effect of isopropyl alcohol on etching rate and roughness of (100) Si surface etched in KOH and TMAH solutions," *Sensors and Actuators, A: Physical*, vol. 93, no. 2, pp. 138–147, 2001. DOI: 10.1016/S0924-4247(01)00648-3.

[52] O. Powell and H. B. Harrison, "Anisotropic etching of {100} and {100} planes in (100) silicon," *Journal of Micromechanics and Microengineering*, vol. 11, no. 100, pp. 217–220, 2001.

[53] I. Zubel and M. Kramkowska, "Etch rates and morphology of silicon (h k l) surfaces etched in KOH and KOH saturated with isopropanol solutions," in *Sensors and Actuators, A: Physical*, vol. 115, 2004, pp. 549–556. DOI: 10.1016/j.sna.2003.11.010.

[54] K. P. Rola and I. Zubel, "Effect of molecular structure of alcohols on wet anisotropic etching of silicon," *Sensors and Actuators, A: Physical*, vol. 242, pp. 18–26, 2016. DOI: 10.1016/j.sna.2016.02.032.

[55] I. Zubel and K. P. Rola, "The effect of monohydric and polyhydric alcohols on silicon anisotropic etching in KOH solutions," *Sensors and Actuators, A: Physical*, vol. 266, pp. 145–157, 2017. DOI: 10.1016/j.sna.2017.09.022.

[56] A. Boisen, O. Hansen, and S. Bouwstra, "AFM probes with directly fabricated tips," *Journal of Micromechanics and Microengineering*, vol. 6, no. 1, pp. 58–62, 1996. DOI: 10.1088/0960-1317/6/1/012.

[57] J. D. Li, J. Xie, W. Xue, and D. M. Wu, "Fabrication of cantilever with self-sharpening nano-silicon-tip for AFM applications," *Microsystem Technologies*, vol. 19, no. 2, pp. 285–290, 2013. DOI: 10.1007/s00542-012-1622-x.

[58] Jin-Huai Liu, Timothy M Betzner, and M Thurman Henderson, "Etching of self-sharpening (338) tips in (100) silicon," Tech. Rep.

[59] C. Liu, "Mass-producible monolithic silicon probes for scanning probe microscopes," in *IMTC/98 Conference Proceedings. IEEE Instrumentation and Measurement Technology Conference. Where Instrumentation is Going (Cat. No.98CH36222)*, vol. 2, IEEE, 1998, pp. 1381–1384. DOI: 10.1109/IMTC.1998.676980.

[60] D Resnik, D Vrtacnik, U Aljancic, M Mozek, and S Amon, "Different aspect ratio pyramidal tips obtained by wet etching of (100) and (111) silicon," *Microelectronics Journal*, vol. 34, pp. 591–593, 2003. DOI: 10.1016/S0026-2692(03)00056-9.

[61] M. A. R. Alves, D. F. Takeuti, and E. S. Braga, "Fabrication of sharp silicon tips employing anisotropic wet etching and reactive ion etching," 2004. DOI: 10.1016/j.mejo.2004.10.004.

[62] D. W. Tuggle, "Emission characteristics of the ZrO/W thermal field electron source," *Journal of Vacuum Science & Technology B: Microelectronics and Nanometer Structures*, vol. 3, no. 1, p. 220, 1985. DOI: 10.1116/1.583231.

[63] M Kamp, M Emmerling, S Kuhn, and A Forchel, "Nanolithography using a 100 kV electron beam lithography system with a Schottky emitter," *Measurement, and Phenomena*, vol. 17, p. 3094, 1999. DOI: 10.1116/1.585935.

[64] M. M. Greve and B. Holst, "Optimization of an electron beam lithography instrument for fast, large area writing at 10 kV acceleration voltage," *Journal of Vacuum Science & Technology B, Nanotechnology and Microelectronics: Materials, Processing, Measurement, and Phenomena*, vol. 31, no. 4, p. 043 202, 2013. DOI: 10.1116/1.4813325.

[65] M. Altissimo, "E-beam lithography for micro-/nanofabrication," *Biomicrofluidics*, vol. 4, no. 2, 2010. DOI: 10.1063/1.3437589.

[66] Leica Microsystems Lithography Ltd, "Leica Vectorbeam Series Vectorbeam Operator Manual,"

[67] S. Thoms and D. S. Macintyre, "Tilt-corrected stitching for electron beam lithography," 2007. DOI: 10.1016/j.mee.2007.01.127.

[68] Tanner, *L-Edit*, 2019.

[69] C. David and D. Hambach, "Line width control using a defocused low voltage electron beam," *Microelectronic Engineering*, vol. 46, no. 1-4, pp. 219–222, 1999. DOI: 10.1016/S0167-9317(99)00066-0.

[70] T. H. P. Chang, "Proximity effect in electron-beam lithography," *Journal of Vacuum Science and Technology*, vol. 12, no. 6, pp. 1271–1275, 1975. DOI: 10.1116/1.568515.

[71] C. Nien, L.-C. Chang, J.-H. Ye, V.-C. Su, C.-H. Wu, and C.-H. Kuan, "Proximity effect correction in electron-beam lithography based on computation of critical-development time with swarm intelligence," *Journal of Vacuum Science & Technology B, Nanotechnology and Microelectronics: Materials, Processing, Measurement, and Phenomena*, vol. 35, no. 5, p. 051 603, 2017. DOI: 10.1116/1.5001686.

[72] H. D. Young, R. A. Freedman, and A. L. Ford, *University Physics with Modern Physics*, 9. 2013, vol. 53, pp. 1689–1699.

[73] G. Owen and P. Rissman, "Proximity effect correction for electron beam lithography by equalization of background dose," *Journal of Applied Physics*, vol. 54, no. 6, pp. 3573–3581, 1983. DOI: 10.1063/1.332426.

[74] L. D. Jackel, R. E. Howard, P. M. Mankiewich, H. G. Craighead, and R. W. Epworth, "Beam energy effects in electron beam lithography: The range and intensity of backscattered exposure," *Applied Physics Letters*, vol. 45, no. 6, pp. 698–700, 1984. DOI: 10.1063/1.95361.

[75] E. Seo and O. Kim, "Dose and Shape Modification Proximity Effect Correction for Forward-Scattering Range Scale Features in Electron Beam Lithography," *Japanese Journal of Applied Physics*, vol. 39, no. Part 1, No. 12B, pp. 6827–6830, 2000. DOI: 10.1143/JJAP.39.6827.

[76] M. Stepanova and S. Dew, *Nanofabrication: Techniques and principles*. 2014, vol. 9783709104, pp. 12–41. DOI: 10.1007/978-3-7091-0424-8.

[77] M. Hatzakis, "Electron Resists for Microcircuit and Mask Production," *Journal of The Electrochemical Society*, vol. 116, no. 7, p. 1033, 1969. DOI: 10.1149/1.2412145.

[78] A Kokkinis, E. Valamontes, D Goustouridis, T. Ganetsos, K Beltsios, and I Raptis, "Molecular weight and processing effects on the dissolution properties of thin poly(methyl methacrylate) films," *Microelectronic Engineering*, vol. 85, no. 1, pp. 93–99, 2008. DOI: 10.1016/j.mee.2007.04.141.

[79] D. G. Hasko, S. Yasin, and A. Mumtaz, "Influence of developer and development conditions on the behavior of high molecular weight electron beam resists," *Journal of Vacuum Science & Technology B: Microelectronics and Nanometer Structures*, vol. 18, no. 6, p. 3441, 2002. DOI: 10.1116/1.1319834.

[80] F. Yaghmaie, J. Fleck, A. Gusman, and R. Prohaska, "Improvement of PMMA electron-beam lithography performance in metal liftoff through a poly-imide bi-layer system," *Microelectronic Engineering*, vol. 87, no. 12, pp. 2629–2632, 2010. DOI: 10.1016/j.mee.2010.07.030.

[81] Y. Zhang, Y. Zhang, J. Blaser, T. S. Sriram, A. Enver, and R. B. Marcus, "A thermal microprobe fabricated with wafer-stage processing," *Review of Scientific Instruments*, vol. 69, no. 5, pp. 2081–2084, 1998. DOI: 10.1063/1.1148902.

[82] G. Binnig, H. Rohrer, C. Gerber, and E. Weibel, "Vacuum tunneling," *Physica B+C*, vol. 109-110, pp. 2075–2077, 1982. DOI: 10.1016/0378-4363(82)90580-0.

[83] G Binnig and H Rohrer, "Scanning Tunneling Microscopy," *Surface Science*, vol. 126, pp. 236–244, 1983. DOI: 10.1016/0039-6028(83)90716-1.

[84] G. Binnig, H. Rohrer, C. Gerber, and E. Weibel, "Surface Studies by Scanning Tunneling Microscopy," *Physical Review Letters*, vol. 49, no. 1, pp. 57–61, 1982. DOI: 10.1103/PhysRevLett.49.57.

[85] S. Devasia, E. Eleftheriou, and S. O. R. Moheimani, "A Survey of Control Issues in Nanopositioning," *IEEE Transactions on Industrial Informatics*, vol. 15, no. 5, pp. 1211–1221, 2007. DOI: 10.1109/TII.2013.2272888.

[86] G. Binnig and D. P. Smith, "Single-tube three-dimensional scanner for scanning tunneling microscopy," *Review of Scientific Instruments*, vol. 57, no. 8, pp. 1688–1689, 1986. DOI: 10.1063/1.1139196.

[87] B Bhikkaji, M Ratnam, a. J. Fleming, and S. O. R. Moheimani, "High performance Control of Piezoelectric Tube Scanners," *IEEE Trans. Control Syst. Technol.*, vol. 15, no. 5, pp. 853–866, 2007. DOI: 10.1109/TCST.2007.902947.

[88] G. Binnig and C. F. Quate, "Atomic Force Microscope," *Physical Review Letters*, vol. 56, no. 9, pp. 930–933, 1986. DOI: 10.1103/PhysRevLett.56.930.

[89] D. Rugar and P. Hansma, "Atomic Force Microscopy," *Physics Today*, vol. 43, no. 10, pp. 23–30, 1990. DOI: 10.1063/1.881238.

[90] J. Goniakowski and C. Noguera, "Insulating oxide surfaces and nanostructures," *Comptes Rendus Physique*, vol. 17, no. 3-4, pp. 471–480, 2016. DOI: 10.1016/j.crhy.2015.12.007.

[91] S. Alexander, L. Hellemans, O. Marti, J. Schneir, V. Elings, P. K. Hansma, M. Longmire, and J. Gurley, "An atomic-resolution atomic-force microscope implemented using an optical lever," *Journal of Applied Physics*, vol. 65, no. 1, pp. 164–167, 1989. DOI: 10.1063/1.342563.

[92] A. Fujii, I. Misumi, S. Gonda, Q. Huang, T. Keem, T. Kurosawa, N. Hisata, T. Yamagishi, H. Fujimoto, K. Enjoji, S. Aya, and H. Sumitani, "Sub-hundred nanometre pitch measurements using an AFM with differential laser interferometers for designing usable lateral scales," *Meas. Sci. Technol*, vol. 16, pp. 2080–2090, 2005. DOI: 10.1088/0957-0233/16/10/025.

[93] C. A. Putman, B. G. de Grooth, N. F. van Hulst, and J. Greve, "A theoretical comparison between interferometric and optical beam deflection technique for the measurement of cantilever displacement in AFM," *Ultramicroscopy*, vol. 42-44, pp. 1509–1513, 1992. DOI: 10.1016/0304-3991(92)90474-X.

[94] F. Azcona, S. Royo, and A. Jha, "Towards atomic force microscopy measurements using differential self-mixing interferometry," *Proceedings of IEEE Sensors*, vol. 2014-Decem, no. December, pp. 4–8, 2014. DOI: 10.1109/ICSENS.2014.6985112.

[95] M Stark, B. N. Bercu, F Marchi, J Chevrier, and S Huant, "Marking the Difference: Interferometric Detection vs Optical Beam Deflection in AFM," vol. 696, p. 385, 2003. DOI: 10.1063/1.1639722.

[96] B. Voigtländer, "Scanning Probe Microscopy: Atomic Force Microscopy and Scanning Tunneling Microscopy," Tech. Rep.

[97] R. Garcia and R. Perez, "Dynamic atomic force microscopy methods," *Surface Science Reports*, vol. 47, no. 6-8, pp. 197–301, 2002. DOI: 10.1016/S0167-5729(02)00077-8.

[98] R. García and A. San Paulo, "Attractive and repulsive tip-sample interaction regimes in tapping-mode atomic force microscopy," *Physical Review B*, vol. 60, no. 7, pp. 4961–4967, 1999. DOI: 10.1103/PhysRevB.60.4961.

[99] G. Haugstad, *Atomic force microscopy : understanding basic modes and advanced applications*. John Wiley & Sons, 2012.

[100] P. J. Eaton and P. West, *Atomic force microscopy*. Oxford University Press, 2010, p. 248.

[101] J. E. Sader, J. W. M. Chon, and P. Mulvaney, "Calibration of rectangular atomic force microscope cantilevers," *Review of Scientific Instruments*, vol. 70, no. 10, pp. 3967–3970, 1999.

[102] J. E. Sader, J. A. Sanelli, B. D. Adamson, J. P. Monty, X. Wei, S. A. Crawford, J. R. Friend, I. Marusic, P. Mulvaney, and E. J. Bieske, "Spring constant calibration of atomic force microscope cantilevers of arbitrary shape," *Review of Scientific Instruments*, vol. 83, no. 10, 2012. DOI: 10.1063/1.4757398.

[103] J. E. Sader, "Parallel beam approximation for V-shaped atomic force microscope cantilevers," vol. 66, no. September, pp. 4–8, 1995.

[104] A Boisen, J. Rasmussen, O Hansen, and S Bouwstra, "Indirect tip fabrication for Scanning Probe Microscopy," *Microelectronic Engineering*, vol. 30, no. 1-4, pp. 579–582, 1996. DOI: 10.1016/0167-9317(95)00314-2.

[105] R. Barattin and N. Voyer, "Chemical Modifications of Atomic Force Microscopy Tips," in *Atomic Force Microscopy in Biomedical Research: Methods and Protocols*, P. C. Braga and D. Ricci, Eds. Totowa, NJ: Humana Press, 2011, pp. 457–483. DOI: 10.1007/978-1-61779-105-5_28.

[106] A.-L. Haag, Y. Nagai, R Lennox, and P. Grütter, "Characterization of a gold coated cantilever surface for biosensing applications," *EPJ Techniques and Instrumentation*, vol. 2, no. 1, p. 1, 2015. DOI: 10.1140/epjti/s40485-014-0011-5.

[107] M. Nonnenmacher, M. P. O'Boyle, and H. K. Wickramasinghe, "Kelvin probe force microscopy," *Applied Physics Letters*, vol. 58, no. 25, pp. 2921–2923, 1991. DOI: 10.1063/1.105227.

[108] C. C. Williams, W. P. Hough, and S. A. Rishton, "Scanning capacitance microscopy on a 25 nm scale," *Applied Physics Letters*, vol. 55, no. 2, pp. 203–205, 1989. DOI: 10.1063/1.102096.

[109] P. De Wolf, E. Brazel, and A. Erickson, "Electrical characterization of semiconductor materials and devices using scanning probe microscopy," *Materials Science in Semiconductor Processing*, vol. 4, no. 1-3, pp. 71–76, 2001. DOI: 10.1016/S1369-8001(00)00174-8.

[110] P. Girard, "Electrostatic force microscopy: principles and some applications to semiconductors," *Nanotechnology*, vol. 12, no. 4, pp. 485–490, 2001. DOI: 10.1088/0957-4484/12/4/321.

[111] M. Nakamura and H. Yamada, "Electrostatic force microscopy," in *Roadmap of Scanning Probe Microscopy*, Springer, 2007, pp. 43–51.

[112] E. Soergel, "Piezoresponse force microscopy (PFM)," *Journal of Physics D: Applied Physics*, vol. 44, no. 46, 2011. DOI: 10.1088/0022-3727/44/46/464003.

[113] R. M. Stockle, Y. D. Suh, V. Deckert, R. Zenobi, and S. Switzerland¨¨, "Nanoscale chemical analysis by tip-enhanced Raman spectroscopy," Tech. Rep., 2000, pp. 131–136.

[114] F. Huth, A. Govyadinov, S. Amarie, W. Nuansing, F. Keilmann, and R. Hillenbrand, "Nano-FTIR Absorption Spectroscopy of Molecular Fingerprints at 20 nm Spatial Resolution," *Nano Letters*, vol. 12, no. 8, pp. 3973–3978, 2012. DOI: 10.1021/nl301159v.

[115] F Zenhausern, M. P. O'Boyle, and H. K. Wickramasinghe, "Apertureless near-field optical microscope," *Applied Physics Letters*, vol. 65, no. 13, pp. 1623–1625, 1994. DOI: 10.1063/1.112931.

[116] M Radmacher, P. E. Hillner, and P. K. Hansma, "Scanning nearfield optical microscope using microfabricated probes," *Citation: Review of Scientific Instruments*, vol. 65, p. 2737, 1994. DOI: 10.1063/1.1144610.

[117] A. Bek, R. Vogelgesang, and K. Kern, "Apertureless scanning near field optical microscope with sub-10nm resolution," *Review of Scientific Instruments*, vol. 77, no. 4, p. 043 703, 2006. DOI: 10.1063/1.2190211.

[118] H. Muramatsu, K. Homma, N. Chiba, N. Yamamoto, and A. Egawa, "Dynamic etching method for fabricating a variety of tip shapes in the optical fibre probe of a scanning near-field optical microscope," *Journal of Microscopy*, vol. 194, no. 2-3, pp. 383–387, 1999. DOI: 10.1046/j.1365-2818.1999.00509.x.

[119] E. Oesterschulze, O. Rudow, C. Mihalcea, W. Scholz, and S. Werner, "Cantilever probes for SNOM applications with single and double aperture tips," *Ultramicroscopy*, vol. 71, no. 1-4, pp. 85–92, 1998. DOI: 10.1016/S0304-3991(97)00089-2.

[120] P. Menon, H. Zhou, B. Casey, L. Donaldson, W. Smith, J. M. Weaver, and Citation: "Cantilever based SNOM Probes with Structured Apertures," in *AIP Conference Proceedings*, vol. 696, AIP, 2003, pp. 242–246. DOI: 10.1063/1.1639702.

[121] C Lehrer, L Frey, S Petersen, T. Sulzbach, O Ohlsson, T. Dziomba, H. U. Danzebrink, and H Ryssel, "Fabrication of silicon aperture probes for scanning near-field optical microscopy by focused ion beam nano machining," Tech. Rep., 2001, pp. 721–728.

[122] M. Muranishi, K. Sato, S. Hosaka, A. Kikukawa, T. Shintani, and K. Ito, "Control of Aperture Size of Optical Probes for Scanning Near-Field Optical Microscopy Using Focused Ion Beam Technology," *Japanese Journal of Applied Physics*, vol. 36, no. Part 2, No. 7B, pp. L942–L944, 1997. DOI: 10.1143/JJAP.36.L942.

[123] Danzebrink, T. Dziomba, Sulzbach, Ohlsson, Lehrer, and Frey, "Nano-slit probes for near-field optical microscopy fabricated by focused ion beams," *Journal of Microscopy*, vol. 194, no. 2-3, pp. 335–339, 1999. DOI: 10.1046/j.1365-2818.1999.00505.x.

[124] L. A. Giannuzzi and F. A. Stevie, *Introduction to focused ion beams : instrumentation, theory, techniques, and practice*. Springer, 2005, p. 357.

[125] A. Sandhu, K. Kurosawa, M. Dede, and A. Oral, "50 nm Hall Sensors for Room Temperature Scanning Hall Probe Microscopy," *Japanese Journal of Applied Physics*, vol. 43, no. 2, pp. 777–778, 2004. DOI: 10.1143/JJAP.43.777.

[126] M. J. Vasile, D. Grigg, J. E. Griffith, E. Fitzgerald, and P. E. Russell, "Scanning probe tip geometry optimized for metrology by focused ion beam ion milling," *Journal of Vacuum Science & Technology B: Microelectronics and Nanometer Structures*, vol. 9, no. 6, p. 3569, 1991. DOI: 10.1116/1.585846.

[127] B. G. Konoplev, O. A. Ageev, V. A. Smirnov, A. S. Kolomiitsev, and N. I. Serbu, "Probe modification for scanning-probe microscopy by the focused

ion beam method," *Russian Microelectronics*, vol. 41, no. 1, pp. 41–50, 2012. DOI: 10.1134/S1063739712010052.

[128] A. Han, A. Kuan, J. Golovchenko, and D. Branton, "Nanopatterning on non-planar and fragile substrates with ice resists," *Nano Letters*, vol. 12, no. 2, pp. 1018–1021, 2012. DOI: 10.1021/nl204198w.

[129] N. P. N. Pham, J. N. J. Burghartz, and P. P. M. Sarro, "Spray coating of photoresist for pattern transfer on high topography surfaces," *Journal of Micromechanics and Microengineering*, vol. 15, no. 4, pp. 691–697, 2005. DOI: 10.1088/0960-1317/15/4/003.

[130] L. Yu, Y. Y. Lee, F. E. H. Tay, and C. Iliescu, "Spray Coating of Photoresist for 3D Microstructures with Different Geometries," *Journal of Physics: Conference Series*, vol. 34, pp. 937–942, 2006. DOI: 10.1088/1742-6596/34/1/155.

[131] G. B. Mills, H. Zhou, A. Midha, L. Donaldson, and J. M. Weaver, "Scanning thermal microscopy using batch fabricated thermocouple probes," *Applied Physics Letters*, vol. 72, no. 22, pp. 2900–2902, 1998. DOI: 10.1063/1.121453.

[132] L. Shi, S. Plyasunov, A. Bachtold, P. L. McEuen, and A. Majumdar, "Scanning thermal microscopy of carbon nanotubes using batch-fabricated probes," *Applied Physics Letters*, vol. 77, no. 26, p. 4295, 2000. DOI: 10.1063/1.1334658.

[133] L. Shi, O. Kwon, A. C. Miner, and A. Majumdar, "Design and batch fabrication of probes for sub-100 nm scanning thermal microscopy," *Journal of Microelectromechanical Systems*, vol. 10, no. 3, pp. 370–378, 2001. DOI: 10.1109/84.946785.

[134] C Mihalcea, W Scholz, S Werner, S Münster, E Oesterschulze, and R Kassing, "Multipurpose sensor tips for scanning near-field microscopy," *Applied Physics Letters*, vol. 68, no. 25, pp. 3531–3533, 1996. DOI: 10.1063/1.116520.

[135] M. Costa, J. Gaspar, R. Ferreira, E. Paz, H. Fonseca, M. Martins, S. Cardoso, and P. P. Freitas, "Integration of Magnetoresistive Sensors With Atomic Force Microscopy Cantilevers for Scanning Magnetoresistance Microscopy Applications," vol. 51, no. 11, 2015.

[136] D. Chu, W.-K. Wong, K. E. Goodson, and R. F. W. Pease, "Transient temperature measurements of resist heating using nanothermocouples," *Journal*

of Vacuum Science & Technology B: Microelectronics and Nanometer Structures, vol. 21, no. 6, p. 2985, 2003. DOI: 10.1116/1.1624255.

[137] E Oesterschulze, M Stopka, and R Kassing, "Photo-thermal characterization of solids and thin films by optical and scanning probe techniques," *Microelectronic Engineering*, vol. 24, no. 1-4, pp. 107–112, 1994. DOI: 10.1016/0167-9317(94)90060-4.

[138] K. Luo, "Sensor nanofabrication, performance, and conduction mechanisms in scanning thermal microscopy," *Journal of Vacuum Science & Technology B: Microelectronics and Nanometer Structures*, vol. 15, no. 2, p. 349, 1997. DOI: 10.1116/1.589319.

[139] K. Hwang, K. Kim, J. Chung, O. Kwon, B. Lee, J. S. Lee, S. Park, and Y. K. Choi, "Development of Robust Batch-Fabrication Process for High Performance SThM Probe and Quantitative Performance Evaluation," in *ASME 2009 Second International Conference on Micro/Nanoscale Heat and Mass Transfer, Volume 2*, ASME, 2009, pp. 421–425. DOI: 10.1115/MNHMT2009-18218.

[140] K. Kim, J. Chung, J. Won, O. Kwon, J. S. Lee, S. H. Park, and Y. K. Choi, "Quantitative scanning thermal microscopy using double scan technique," *Applied Physics Letters*, vol. 93, no. 20, pp. 17–20, 2008. DOI: 10.1063/1.3033545.

[141] K. Kim, W. Jeong, W. Lee, and P. Reddy, "Ultra-High Vacuum Scanning Thermal Microscopy for Nanometer Resolution Quantitative Thermometry," *ACS Nano*, vol. 6, no. 5, pp. 4248–4257, 2012. DOI: 10.1021/nn300774n.

[142] J. Chung, K. Kim, G. Hwang, O. Kwon, Y. K. Choi, and J. S. Lee, "Quantitative temperature profiling through null-point scanning thermal microscopy," *International Journal of Thermal Sciences*, vol. 62, pp. 109–113, 2012. DOI: 10.1016/j.ijthermalsci.2011.11.012.

[143] K. Kim, W. Jeong, W. Lee, S. Sadat, D. Thompson, E. Meyhofer, and P. Reddy, "Quantification of thermal and contact resistances of scanning thermal probes," Tech. Rep. 20, 2014, p. 203 107. DOI: 10.1063/1.4902075.

[144] A. Majumdar, J. P. Carrejo, and J. Lai, "Thermal imaging using the atomic force microscope," *Applied Physics Letters*, vol. 62, no. 20, pp. 2501–2503, 1993. DOI: 10.1063/1.109335.

[145] A. Bontempi, D. Teyssieux, J.-M. Friedt, L. Thiery, D. Hermelin, and P. Vairac, "Photo-thermal quartz tuning fork excitation for dynamic mode atomic force microscope," *Applied Physics Letters*, vol. 105, no. 15, p. 154 104, 2014. DOI: 10.1063/1.4896784.

[146] A. Bontempi, T. P. Nguyen, R. Salut, L. Thiery, D. Teyssieux, and P. Vairac, "Scanning thermal microscopy based on a quartz tuning fork and a micro-thermocouple in active mode (2ω method)," *Review of Scientific Instruments*, vol. 87, no. 6, 2016. DOI: 10.1063/1.4952958.

[147] T. Nguyen, L Thiery, D. Teyssieux, D Briand, and P. Vairac, "Recent improvements on micro-thermocouple based SThM," *Journal of Physics: Conference Series*, vol. 785, no. 1, p. 012 005, 2017. DOI: 10.1088/1742-6596/785/1/012005.

[148] R. Pylkki, P. Moyer, and P. West, "Scanning near-field optical microscopy and scanning thermal microscopy," *Japanese journal of applied ...*, vol. 3785, pp. 895–899, 1994.

[149] E. Puyoo, S. Grauby, J. M. Rampnoux, E. Rouvìre, and S. Dilhaire, "Thermal exchange radius measurement: Application to nanowire thermal imaging," *Review of Scientific Instruments*, vol. 81, no. 7, pp. 2–6, 2010. DOI: 10.1063/1.3455214.

[150] M Despont, J Brugger, U Drechsler, U Durig, M Lutwyche, H Rothuizen, and W Haberle, "VLSI-NEMS chip for parallel AFM data storage," pp. 100–107, 2000.

[151] M. Tortonese, H. Yamada, R. Barrett, and C. Quate, "Atomic force microscopy using a piezoresistive cantilever," in *TRANSDUCERS '91: 1991 International Conference on Solid-State Sensors and Actuators. Digest of Technical Papers*, IEEE, pp. 448–451. DOI: 10.1109/SENSOR.1991.148908.

[152] B. A. Nelson and W. P. King, "Thermal calibration of heated silicon atomic force microscope cantilevers," *TRANSDUCERS and EUROSENSORS '07 - 4th International Conference on Solid-State Sensors, Actuators and Microsystems*, vol. 140, pp. 607–610, 2007. DOI: 10.1109/SENSOR.2007.4300203.

[153] W. P. King, "Heat Transfer Between a Heated Microcantilever and the Substrate," pp. 1–11, 2015.

[154] B. A. Nelson and W. P. King, "Measuring material softening with nanoscale spatial resolution using heated silicon probes," *Review of Scientific Instruments*, vol. 78, no. 2, pp. 1–8, 2007. DOI: 10.1063/1.2435589.

[155] W. P. King, T. W. Kenny, K. E. Goodson, G. L. Cross, M. Despont, U. T. Dürig, H. Rothuizen, G. Binnig, and P. Vettiger, "Design of atomic force microscope cantilevers for combined thermomechanical writing and thermal reading in array operation," *Journal of Microelectromechanical Systems*, vol. 11, no. 6, pp. 765–774, 2002. DOI: 10.1109/JMEMS.2002.803283.

[156] M. Hinz, O. Marti, B. Gotsmann, M. A. Lantz, and U. Dürig, "High resolution vacuum scanning thermal microscopy of HfO2 and SiO2," *Applied Physics Letters*, vol. 92, no. 4, p. 043 122, 2008. DOI: 10.1063/1.2840186.

[157] J. Lee, T Beechem, T Wright, B. Nelson, S Graham, and W. P. King, "Electrical, Thermal, and Mechanical Characterization of Silicon Microcantilever Heaters," *Journal of Microelectromechanical Systems*, vol. 15, no. 6, pp. 1644–1655, 2006. DOI: 10.1109/JMEMS.2006.886020.

[158] K. J. Kim, K. Park, J. Lee, Z. M. Zhang, and W. P. King, "Nanotopographical imaging using a heated atomic force microscope cantilever probe," *Sensors and Actuators, A: Physical*, vol. 136, no. 1, pp. 95–103, 2007. DOI: 10.1016/j.sna.2006.10.052.

[159] W. P. King, B. Bhatia, J. R. Felts, H. J. Kim, and B. Kwon, "Heated Atomic Force Microscope Cantilevers and Their," *Annual Review of Heat Transfer*, vol. XVI, pp. 287–326, 2013. DOI: 10.1615/AnnualRevHeatTransfer.v16.100.

[160] H. Zhou, B. K. Chong, P. Stopford, G. B. Mills, A. Midha, L. Donaldson, and J. M. Weaver, "Lithographically defined nano and micro sensors using "float coating" of resist and electron beam lithography," *Journal of Vacuum Science & Technology B: Microelectronics and Nanometer Structures*, vol. 18, no. 6, p. 3594, 2000. DOI: 10.1116/1.1321271.

[161] H. Zhou, A. Midha, G. B. Mills, S. Thoms, S. Murad, and J. M. Weaver, "Generic scanned-probe microscope sensors by combined micromachining and electron-beam lithography," *Journal of Vacuum Science & Technology B: Microelectronics and Nanometer Structures*, vol. 16, no. 1, p. 54, 1998. DOI: 10.1116/1.589835.

[162] Y Zhang, K. Docherty, and J. M. Weaver, "Batch fabrication of cantilever array aperture probes for scanning near-field optical microscopy," *Microelectronic Engineering*, vol. 87, no. 5-8, pp. 1229–1232, 2010. DOI: 10.1016/j.mee.2009.11.140.

[163] G. B. Mills, "Scanning thermal microscopy using nanofabricated probes," 1999.

[164] K. Rudnicki, "MOSFET transistor fabrication on AFM tip by," 2014.

[165] M. Timofeeva, A. Bolshakov, P. D. Tovee, D. A. Zeze, V. G. Dubrovskii, and O. V. Kolosov, "Scanning thermal microscopy with heat conductive nanowire probes," *Ultramicroscopy*, vol. 162, no. January, pp. 42–51, 2016. DOI: 10.1016/j.ultramic.2015.12.006.

[166] J. Juszczyk, M. Wojtol, and J. Bodzenta, "DC experiments in quantitative scanning thermal microscopy," *International Journal of Thermophysics*, vol. 34, no. 4, pp. 620–628, 2013. DOI: 10.1007/s10765-013-1449-4.

[167] L. Ramiandrisoa, A. Allard, B. Hay, and S. Gomès, "Uncertainty assessment for measurements performed in the determination of thermal conductivity by scanning thermal microscopy," *Measurement Science and Technology*, vol. 28, no. 11, 2017. DOI: 10.1088/1361-6501/aa8892.

[168] J. L. Bosse, M. Timofeeva, P. D. Tovee, B. J. Robinson, B. D. Huey, and O. V. Kolosov, "Nanothermal characterization of amorphous and crystalline phases in chalcogenide thin films with scanning thermal microscopy," *Journal of Applied Physics*, vol. 116, no. 13, 2014. DOI: 10.1063/1.4895493.

[169] J. Bodzenta, J. Juszczyk, and M. Chirtoc, "Quantitative scanning thermal microscopy based on determination of thermal probe dynamic resistance," *Review of Scientific Instruments*, vol. 84, no. 9, 2013. DOI: 10.1063/1.4819738.

[170] A. Assy and S. Gomès, "Heat transfer at nanoscale contacts investigated with scanning thermal microscopy," *Applied Physics Letters*, vol. 107, no. 4, 2015. DOI: 10.1063/1.4927653.

[171] Y. Zhang, P. S. Dobson, and J. M. Weaver, "High temperature imaging using a thermally compensated cantilever resistive probe for scanning thermal microscopy," *Journal of Vacuum Science & Technology B: Microelectronics and Nanometer Structures*, vol. 30, no. 1, p. 010 601, 2012. DOI: 10.1116/1.3664328.

[172] Y. Ge, "Quantitative measurement using scanning thermal microscopy," 2016.

[173] J Spiece, C Evangeli, K Lulla, A Robson, B Robinson, and O Kolosov, "Improving accuracy of nanothermal measurements via spatially distributed scanning thermal microscope probes," *Journal of Applied Physics*, vol. 124, no. 1, p. 015 101, 2018. DOI: 10.1063/1.5031085.

[174] D. Necas and P. Klapetek, "Gwyddion: an open-source software for SPM data analysis," *Central European Journal of Physics*, vol. 10, no. 1, pp. 181–188, 2012. DOI: 10.2478/s11534-011-0096-2.

[175] C. J. Lasance, "Ten years of boundary-condition- Independent compact thermal modeling of electronic parts: A review," *Heat Transfer Engineering*, vol. 29, no. 2, pp. 149–168, 2008. DOI: 10.1080/01457630701673188.

[176] L. Shi and A. Majumdar, "Thermal Transport Mechanisms at Nanoscale Point Contacts," *Journal of Heat Transfer*, vol. 124, no. 2, p. 329, 2002. DOI: 10.1115/1.1447939.

[177] D. G. Cahill, W. K. Ford, K. E. Goodson, G. D. Mahan, A. Majumdar, H. J. Maris, R. Merlin, and S. R. Phillpot, "Nanoscale thermal transport," *Journal of Applied Physics*, vol. 93, no. 2, pp. 793–818, 2003. DOI: 10.1063/1.1524305.

[178] A. Vladimirescu, *The SPICE Book*. J. Wiley, 1994, p. 412. DOI: 10.978.0471/609261.

[179] R. Rohrer, "Circuit simulation-the early years," *IEEE Circuits and Devices Magazine*, vol. 8, no. 3, pp. 32–37, 1992. DOI: 10.1109/101.136783.

[180] A. Assy, S. Lefèvre, P.-O. Chapuis, and S. Gomès, "Analysis of heat transfer in the water meniscus at the tip-sample contact in scanning thermal microscopy," *Journal of Physics D: Applied Physics*, vol. 47, no. 44, p. 442 001, 2014. DOI: 10.1088/0022-3727/47/44/442001.

[181] J. Bodzenta, A. Kaźmierczak-Bałata, M. Lorenc, and J. Juszczyk, "Analysis of possibilities of application of nanofabricated thermal probes to quantitative thermal measurements," *International Journal of Thermophysics*, vol. 31, no. 1, pp. 150–162, 2010. DOI: 10.1007/s10765-009-0659-2.

[182] R. Pulavarthy and M. Haque, "A novel technique for Interfacial Thermal Resistance measurement for nanoscale thin films," *International Journal of Heat and Mass Transfer*, vol. 89, pp. 743–748, 2015. DOI: 10.1016/j.ijheatmasstransfer.2015.05.088.

[183] Z. Suszynski, "Thermal model based on the electrical analogy of the thermal processes," in *Proceedings of the 10th international conference on photoacoustic and photothermal phenomena*, vol. 463, ASCE, 1999, pp. 197–199. DOI: 10.1063/1.58045.

[184] V. Szekely and M. Rencz, "Thermal dynamics and the time constant domain," *IEEE Transactions on Components and Packaging Technologies*, vol. 23, no. 3, pp. 587–594, 2000. DOI: 10.1109/6144.868862.

[185] T. L. Bergman, A. S. Lavine, and F. P. Incropera, *Fundamentals of Heat and Mass Transfer*. 7th. Wiley, 2011, p. 1076.

[186] J. Holman, *Heat Transfer*, 10th ed. McGraw Hill Higher Education, 2010, p. 758.

[187] E. Puyoo, S. Grauby, J. M. Rampnoux, E. Rouvìre, and S. Dilhaire, "Scanning thermal microscopy of individual silicon nanowires," *Journal of Applied Physics*, vol. 109, no. 2, p. 024 302, 2011. DOI: 10.1063/1.3524223.

[188] Y. Ge, Y. Zhang, J. M. Weaver, H. Zhou, and P. S. Dobson, "Topography-free sample for thermal spatial response measurement of scanning thermal microscopy," *Journal of Vacuum Science & Technology B, Nanotechnology and Microelectronics: Materials, Processing, Measurement, and Phenomena*, vol. 33, no. 6, 06FA03, 2015. DOI: 10.1116/1.4933172.

[189] S. Volz, *Microscale and Nanoscale Heat Transfer*, C. E. Ascheron, Ed. Springer, 2005.

[190] E. T. Swartz and R. O. Pohl, "Thermal boundary resistance," *Reviews of Modern Physics*, vol. 61, no. 3, pp. 605–668, 1989. DOI: 10.1103/RevModPhys.61.605.

[191] L. D. Bellis, P. E. Phelan, and R. S. Prasher, "Variations of Acoustic and Diffuse Mismatch Models in Predicting Thermal-Boundary Resistance," *Journal of Thermophysics and Heat Transfer*, vol. 14, no. 2, pp. 144–150, 2000. DOI: 10.2514/2.6525.

[192] J. Cho, Z. Li, M. Asheghi, and K. E. Goodson, "Near-Junction Thermal Management: Thermal Conduction in Gallium Nitride Composite Substrates," *Annual Review of Heat Transfer*, vol. 18, no. July, pp. 7–45, 2015. DOI: 10.1615/AnnualRevHeatTransfer.2015011335.

[193] H. S. Carslaw and J. C. Jaeger, *Conduction of heat in solids*. Clarendon Press, 1959, p. 510.

[194] M. Yovanovich and E. Marotta, "Thermal Spreading and Contact Resistances," in *Heat transfer handbook*, 2003, ch. 4, pp. 261–393.

[195] R. Prasher, "Predicting the thermal resistance of nanosized constrictions," *Nano Letters*, vol. 5, no. 11, pp. 2155–2159, 2005. DOI: 10.1021/nl051710b.

[196] S. Lefèvre, S. Volz, and P. O. Chapuis, "Nanoscale heat transfer at contact between a hot tip and a substrate," *International Journal of Heat and Mass Transfer*, vol. 49, no. 1-2, pp. 251–258, 2006. DOI: 10.1016/j.ijheatmasstransfer.2005.07.010.

[197] J. C. Whitaker, *The electronics handbook*. CRC Press, 1996, p. 2575.

[198] H. Wang, Y. Xu, M. Shimono, Y. Tanaka, and M. Yamazaki, "Computation of Interfacial Thermal Resistance by Phonon Diffuse Mismatch Model," *Materials Transactions*, vol. 48, no. 9, pp. 2349–2352, 2007. DOI: 10.2320/matertrans.MAW200717.

[199] B. V. Derjaguin, V. M. Muller, and Y. U. P. Toporov, "Effect of contact deformation on the adhesion of particles.," *Journal of colloid and interface science*, vol. 52, no. 3, pp. 105–108, 1975. DOI: 10.1016/0021-9797(75)90018-1.

[200] M. Thompson Pettes and L. Shi, "A Reexamination of Phonon Transport Through a Nanoscale Point Contact in Vacuum," *Journal of Heat Transfer*, vol. 136, no. 3, p. 032 401, 2013. DOI: 10.1115/1.4025643.

[201] P. S. Dobson, J. M. Weaver, and G. B. Mills, "New methods for calibrated Scanning Thermal Microscopy (SThM)," *Proceedings of IEEE Sensors*, pp. 708–711, 2007. DOI: 10.1109/ICSENS.2007.4388498.

[202] B. C. Gundrum, D. G. Cahill, and R. S. Averback, "Thermal conductance of metal-metal interfaces," *Physical Review B*, vol. 72, no. 24, p. 245 426, 2005. DOI: 10.1103/PhysRevB.72.245426.

[203] P. C. Fletcher, B. Lee, and W. P. King, "Thermoelectric voltage at a nanometer-scale heated tip point contact," *Nanotechnology*, vol. 23, no. 3, p. 035 401, 2012. DOI: 10.1088/0957-4484/23/3/035401.

[204] K. Termentzidis, "Thermal conductivity anisotropy in nanostructures and nanostructured materials," *Journal of Physics D: Applied Physics*, vol. 51, no. 9, p. 094 003, 2018. DOI: 10.1088/1361-6463/aaa82e.

[205] B. Gotsmann, M. A. Lantz, A. Knoll, and U. Dürig, "Nanoscale Thermal and Mechanical Interactions Studies using Heatable Probes," in *Nanotechnology*, Weinheim, Germany: Wiley-VCH Verlag GmbH & Co. KGaA, 2010, pp. 121–169. DOI: 10.1002/9783527628155.nanotech066.

[206] B. Bhushan, "Nanotribology and nanomechanics of MEMS/NEMS and BioMEMS/BioNEMS materials and devices," *Microelectronic Engineering*, vol. 84, no. 3, pp. 387–412, 2007. DOI: 10.1016/j.mee.2006.10.059.

[207] G. E. Ewing, "Thin Film Water," vol. 108, p. 29, 2004. DOI: 10.1021/jp040378.

[208] E. Charlaix and M. Ciccotti, "Capillary Condensation in Confined Media," in *Handbook of Nanophysics: Principles and Methods*, K. D. Sattler, Ed., CRC Press, 2010, ch. 12, pp. 1–18.

[209] A. Assy and S. Gomès, "Temperature-dependent capillary forces at nano-contacts for estimating the heat conduction through a water meniscus," *Nanotechnology*, vol. 26, no. 35, p. 355 401, 2015. DOI: 10.1088/0957-4484/26/35/355401.

[210] L David, S. Gomès, and M Raynaud, "Modelling for the thermal characterization of solid materials by dc scanning thermal microscopy," *Journal of Physics D: Applied Physics*, vol. 40, no. 14, pp. 4337–4346, 2007. DOI: 10.1088/0022-3727/40/14/032.

[211] M. M. Sadeghi, S. Park, Y. Huang, D. Akinwande, Z. Yao, J. Murthy, and L. Shi, "Quantitative scanning thermal microscopy of graphene devices on flexible polyimide substrates," *Journal of Applied Physics*, vol. 119, no. 23, 2016. DOI: 10.1063/1.4953584.

[212] Y. Zhang, P. S. Dobson, and J. M. Weaver, "Batch fabricated dual cantilever resistive probe for scanning thermal microscopy," *Microelectronic Engineering*, vol. 88, no. 8, pp. 2435–2438, 2011. DOI: 10.1016/j.mee.2011.02.040.

[213] A. Bejan and A. D. Kraus, *Heat Transfer Handbook*. John Wiley & Sons, 2003, p. 1480.

[214] G Langer, J Hartmann, and M Reichling, "Thermal conductivity of thin metallic films measured by photothermal profile analysis," *Review of Scientific Instruments*, vol. 68, no. 3, pp. 1510–1513, 1997. DOI: 10.1063/1.1147638.

[215] X. Zhang and C. P. Grigoropoulos, "Thermal conductivity and diffusivity of free-standing silicon nitride thin films," *Review of Scientific Instruments*, vol. 66, no. 2, pp. 1115–1120, 1995. DOI: 10.1063/1.1145989.

[216] H. Ftouni, C. Blanc, D. Tainoff, A. D. Fefferman, M. Defoort, K. J. Lulla, J. Richard, E. Collin, and O. Bourgeois, "Thermal conductivity of silicon nitride membranes is not sensitive to stress," *Physical Review B*, vol. 92, no. 12, p. 125 439, 2015. DOI: 10.1103/PhysRevB.92.125439.

[217] G. Rizzoni, *Principals and Applications of Electrical Engineering*. 2004, p. 1134.

[218] Chung-Wen Ho, A. Ruehli, and P. Brennan, "The modified nodal approach to network analysis," *IEEE Transactions on Circuits and Systems*, vol. 22, no. 6, pp. 504–509, 1975. DOI: 10.1109/TCS.1975.1084079.

[219] R. A. DeCarlo and P.-M. Lin, *Linear Circuit Analysis: Time Domain, Phasor, and Laplace Transform Approaches*. Prentice Hall, 2001, p. 1024.

[220] Y. Zhou, R. Ramaneti, J. Anaya, S. Korneychuk, J. Derluyn, H. Sun, J. Pomeroy, J. Verbeeck, K. Haenen, and M. Kuball, "Thermal characterization of polycrystalline diamond thin film heat spreaders grown on GaN HEMTs," *Applied Physics Letters*, vol. 111, no. 4, p. 041 901, 2017. DOI: 10.1063/1.4995407.

[221] S. Lefèvre, S. Volz, J. B. Saulnier, C. Fuentes, and N. Trannoy, "Thermal conductivity calibration for hot wire based dc scanning thermal microscopy," *Review of Scientific Instruments*, vol. 74, no. 4, pp. 2418–2423, 2003. DOI: 10.1063/1.1544078.

[222] H. Fischer, "Quantitative determination of heat conductivities by scanning thermal microscopy," *Thermochimica Acta*, vol. 425, no. 1-2, pp. 69–74, 2005. DOI: 10.1016/j.tca.2004.06.005.

[223] M Chirtoc, J Gibkes, R Wernhardt, J Pelzl, and A Wieck, "Temperature-dependent quantitative 3ω scanning thermal microscopy: Local thermal conductivity changes in NiTi microstructures induced by martensite-austenite phase transition," *Review of Scientific Instruments*, vol. 79, no. 9, p. 093 703, 2008. DOI: 10.1063/1.2982235.

[224] R Bashir, A Gupta, G. W. Neudeck, M McElfresh, and R Gomez, "On the design of piezoresistive silicon cantilevers with stress concentration regions for scanning probe microscopy applications," *Journal of Micromechanics and Microengineering*, vol. 10, no. 4, pp. 483–491, 2000. DOI: 10.1088/0960-1317/10/4/301.

[225] T Sun, "Classical size effect in copper thin films: Impact of surface and grain boundary scattering on resistivity," p. 97, 2009.

[226] S. Thoms, Y. Zhang, and J. M. Weaver, "Improved alignment algorithm for electron beam lithography," *Journal of Vacuum Science & Technology B*, vol. 32, no. 6, 06F509, 2014. DOI: 10.1116/1.4901015.

[227] D. E. Davis, "Registration Mark Detection for Electron-Beam Lithography—EL1 System," *IBM Journal of Research and Development*, vol. 24, no. 5, pp. 545–553, 1980. DOI: 10.1147/rd.245.0545.

[228] E. ul Haq, Z. Liu, Y. Zhang, S. A. A. Ahmad, L.-S. Wong, S. P. Armes, J. K. Hobbs, G. J. Leggett, J. Micklefield, C. J. Roberts, and J. M. Weaver, "Parallel Scanning Near-Field Photolithography: The Snomipede," *Nano Letters*, vol. 10, no. 11, pp. 4375–4380, 2010. DOI: 10.1021/nl1018782.

[229] K. E. Docherty, K. A. Lister, J. Romijn, and J. M. Weaver, "High robustness of correlation-based alignment with Penrose patterns to marker damage in electron beam lithography," *Microelectronic Engineering*, vol. 86, no. 4-6, pp. 532–534, 2009. DOI: 10.1016/j.mee.2008.11.037.

[230] R. K. Dey and B. Cui, "Stitching error reduction in electron beam lithography with in-situ feedback using self-developing resist," *Journal of Vacuum Science & Technology B, Nanotechnology and Microelectronics: Materials, Processing, Measurement, and Phenomena*, vol. 31, no. 6, 06F409, 2013. DOI: 10.1116/1.4831769.

[231] A. Atkins, "Opposite paths in the tearing of sheet materials," *Endeavour*, vol. 19, no. 1, pp. 2–10, 1995. DOI: 10.1016/0160-9327(95)98887-L.

[232] E. Hamm, P. Reis, M. LeBlanc, B. Roman, and E. Cerda, "Tearing as a test for mechanical characterization of thin adhesive films," *Nature Materials*, vol. 7, no. 5, pp. 386–390, 2008. DOI: 10.1038/nmat2161.

[233] P. D. Tovee and O. V. Kolosov, "Mapping nanoscale thermal transfer in-liquid environment—immersion scanning thermal microscopy," *Nanotechnology*, vol. 24, no. 46, p. 465 706, 2013. DOI: 10.1088/0957-4484/24/46/465706.

[234] A. Kaźmierczak-Bałata, J. Juszczyk, D. Trefon-Radziejewska, and J. Bodzenta, "Influence of probe-sample temperature difference on thermal mapping contrast in scanning thermal microscopy imaging," *Journal of Applied Physics*, vol. 121, no. 11, p. 114 502, 2017. DOI: 10.1063/1.4977101.

[235] J Bodzenta, M Chirtoc, and J Juszczyk, "Reduced thermal quadrupole heat transport modeling in harmonic and transient regime scanning thermal microscopy using nanofabricated thermal probes," *Journal of Applied Physics*, vol. 116, no. 5, p. 054 501, 2014. DOI: 10.1063/1.4891872.

[236] L. Thiery, E. Gavignet, and B. Cretin, "Two omega method for active thermocouple microscopy," *Review of Scientific Instruments*, vol. 80, no. 3, 2009. DOI: 10.1063/1.3097183.

[237] P. S. Dobson, G. Mills, and J. M. R. Weaver, "Microfabricated temperature standard based on Johnson noise measurement for the calibration of micro- and nano-thermometers," *Review of Scientific Instruments*, vol. 76, no. 5, p. 054 901, 2005. DOI: 10.1063/1.1899463.

[238] W. J. Parker, R. J. Jenkins, C. P. Butler, and G. L. Abbott, "Flash Method of Determining Thermal Diffusivity, Heat Capacity, and Thermal Conductivity," *Journal of Applied Physics*, vol. 32, no. 9, pp. 1679–1684, 1961. DOI: 10.1063/1.1728417.

[239] B. Hay, J. Hameury, N. Fleurence, P. Lacipiere, M. Grelard, V. Scoarnec, and G. Davee, "New Facilities for the Measurements of High-Temperature Thermophysical Properties at LNE," *International Journal of Thermophysics*, vol. 35, no. 9-10, pp. 1712–1724, 2014. DOI: 10.1007/s10765-013-1400-8.

[240] P. S. Ho and T. Kwok, "Electromigration in metals," *Reports on Progress in Physics*, vol. 52, no. 3, pp. 301–348, 1989. DOI: 10.1088/0034-4885/52/3/002.

[241] J. Linden, C. Thanner, B. Schaaf, S. Wolff, B. Lägel, and E. Oesterschulze, "Spray coating of PMMA for pattern transfer via electron beam lithography on surfaces with high topography," *Microelectronic Engineering*, vol. 88, no. 8, pp. 2030–2032, 2011. DOI: 10.1016/j.mee.2010.12.106.